Volume exchange across the shelf edge: the role of the internal tide and other physical processes

Thesis submitted in accordance with the requirements of
the University of Liverpool for the degree of Doctor in Philosophy
by
Carl Spingys

September 2016

Abstract

The world ocean can broadly be split into two regimes, the shallow shelf seas up to a few hundred metres deep and the deep open ocean which is typically 4-5 km deep. These two regimes are separated by a narrow region of steep topography. This steep topography acts to limit the exchange to those processes that break the assumptions of geostrophy. This exchange, however, is important on both a local and global scale. The shelf seas are an important source of dense water masses, ventilating the deep ocean, control of the flux of mid-depth open ocean heat to glacial fronts, supply of nutrients from the open ocean to sustain enhanced productivity on the shelf, and export of the carbon drawn-down by this productivity into the deep ocean. This problem will be explored through two themes, one exploring the role of the bolus transport and one exploring an integral framework.

The bolus transport is defined as the transport as a result of co-variances in layer thickness and layer velocity. This has previously been extensively applied for the atmosphere and the action of eddies in the Southern Ocean. Here the bolus transport driven by the action of the internal tide near the shelf edge is considered. First we consider a sinusoidal internal wave on the interface of a two well mixed layer ocean. This leads to a theoretical scaling for the bolus transport of $(ca^2)/(2\overline{h_i})$ in the same direction as the propagation of the wave. The bolus transport was then calculated for eight moorings across four locations. For the surface layer these transports were in the range 1.09 to 0.1 $\mathrm{m^2s^{-1}}$ and for the bottom layer were in the range 1.06 to 0.04 $\mathrm{m^2s^{-1}}$. These observational estimates compare favourably with the estimates from the theory, with the theory within ± 40% of the observed values. This bolus transport is balanced locally by a time-mean velocity of equal magnitude but directed off shelf in both layers.

The Walin Framework is an integral framework describing the rate at which water crosses density surfaces. This is used to diagnose the formation, or destruction, rate of water within density classes across the European Shelf, bounded by the 200m isobath, the southern limit of the Celtic Sea and the Norwegian Coast. This formation rate makes the largest contribution to the exchange across the shelf edge. This reveals three distinct regimes: an off-shelf transport in the lightest classes of 0.5 Sv, an on-shelf transport in the middle density classes of 1.5 Sv, and an off shelf transport in the densest classes of 1 Sv. Mapping these along the shelf edge indicates that much of the shelf does not reach the lightest classes so only the intermediate and dense regime is applicable. The lightest regime primarily exists along the southern section of the Norwegian Trench. This implies two circulations: a down-welling circulation of 1 Sv across much of the European Shelf and an across shelf transport of 0.5 Sv, on-shelf across much of the shelf edge balanced by an off shelf transport in the Norwegian Trench. This down-welling circulation is similar to previous estimates of the total transport across the European Shelf Break.

Contents

List of Figures

List of Tables

Acknowledgements

First I must thank my supervisors Prof. Ric Williams, Prof. Jonathan Sharples and Dr Jo Hopkins for their guidance and patience. Specifically, I must thank Prof. Ric Williams for the support and advice he has offered me throughout the highs and lows of research and helping me maintain focus on the pertinent question. The time he always managed to find for me despite being busy, especially in the weeks leading up to the completion of this thesis, has been vital. Prof. Jonathan Sharples, thank you for sharing your knowledge and experience of shelf seas research with me. Dr Jo Hopkins, I owe a great debt to you for the data you have made available to me, saving me many hours hunting down data wrestling it into a useful format, and for helping me with many of the computational aspects of the work in this thesis. Additionally, I must thank Dr Mattias Green who has provided hugely valuable datasets and understanding of internal wave energetics.

I must also thank the colleagues I have worked alongside throughout my PhD for keeping me in good humour, answering my, sometimes stupid, questions and always being willing to share a scientific discussion. This includes: those I have shared an office with, those I have shared a ship with, and my fellow FASTNEters. I must particularly thank Calum, Juliane and Hannah, and those who have shared a board game or beer with us, for helping me maintain something approaching work-life balance.

My family also deserve much thanks for the support they have given me over the last 21 years of education - maybe it is finally time for me to get a real

job although there are no promises!

Finally I must thank Siobhan. Your support throughout my PhD has been unwavering even when it has meant me spending a considerable amount of time at sea or working all evening and weekend. You have kept me grounded throughout this process and helped me enjoy the successes and pick me up during the disappointments.

Thank you

Chapter 1

Introduction and Background

The ocean can generally be split into two distinct regimes. These are the shallow shelf seas, typically up to 200 metres deep, and the open ocean, typically 4 to 5 kilometres deep. Due to these large differences in depth the two regimes have significantly different physical, chemical and biological oceanographic features. These two regimes are separated by a narrow (approximately 50km) region of steep topography referred to as the shelf edge, shelf break or continental slope. It is in this region that the two substantially different regimes meet and communicate with each other.

1.1 Contrast between the shelf seas and open ocean

The primary physical differences between the open ocean and shelf seas are a result of the difference in depth. For the open ocean only a small portion of the water column is within the boundary, surface and bottom, layers. This results in an interior that is relatively quiescent with weak turbulence. The flows in the deep ocean show a large temporal and spatial scale, a month and 100 km for an eddy through to basin-wide gyre circulations. For the shelf seas the boundary layers take up a large portion of the water column and often meet. This leads to a highly turbulent regime where surface wind and bottom friction play an important role in setting the oceanographic conditions. The currents on the shelf are generally dominated by the tides which vary on the tidal period, 12.42

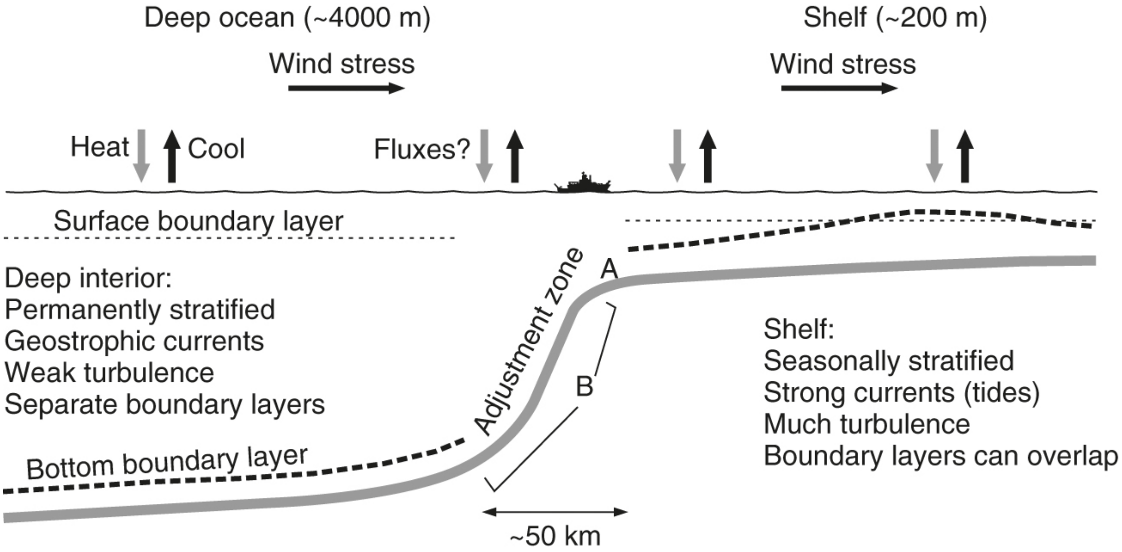

Figure 1.1: Summary of the different physical regimes between the open ocean and the shelf seas showing the narrow "adjustment zone" between these two. This figure is taken from Simpson and Sharples [2012]

hrs for the M2 period, and reach 1 m s^{-1} in parts of the European Shelf. These physical differences are summarised in Fig. 1.1. Shelf seas are also special in that they are the areas of the global ocean adjacent to land and thus human populations. This leads to an additional set of pressures on the shelf sea driven by human interaction, such as modification of the coastal boundary or use of the shelf seas for commercial or leisure activities.

These physical differences between the two regimes lead to different biogeochemical characters. The shelf seas, due to the elevated levels of pycnocline mixing and the seasonal breakdown in stratification, are more productive than an equivalent area of the open ocean. The shelf seas only occupy 9% of the ocean surface area however account for 16% of the global ocean primary production [Simpson and Sharples, 2012]. The effects of this enhanced productivity cascade through the shelf sea ecosystem with potentially important impacts on human activity [Sharples et al., 2013], for example 90% of global fish catches are made in shelf seas [Pauly et al., 2002].

1.2 Importance of open ocean - shelf exchange

The physical processes at the shelf edge are vital as they control the flux of volume and tracers between these two regimes and the strength of imprint they have on each other. Here four important impacts of shelf edge exchange will be briefly explored: the role of the shelf in forming water masses; the transport of heat from the open ocean onto ice adjacent shelves; the supply of nutrients from the open ocean supporting enhanced productivity on the shelf; and the export of carbon drawn down from the atmosphere on the shelf.

1.2.1 Formation of water masses

The shelf, due to its shallow depth and the presence of the land boundary, sees its physical properties changed more rapidly than those in the open ocean. This can be through surface cooling, evaporation or ice formation generating dense water or the run-off from land generating light water. These properties can then be exported from the shelf to form water masses filling large open ocean basins. This process plays an important role in the formation of bottom waters in the Arctic Ocean and Nordic Seas [Backhaus et al., 1997] as well as forming a cool halocline that blocks the heat from the Atlantic inflow reaching the ice [Aagaard et al., 1981] which must then be overcome by turbulent mixing [Rippeth et al., 2015]. The shelf seas adjacent to Antarctica are also thought to play a key role in the formation of the Antarctic bottom water that fills much of the deep ocean [Baines and Condie, 1998, Snow et al., 2016].

1.2.2 Mediating supply of heat to ice-adjacent shelves

The increased melting rate of glaciers in both Antarctica and Greenland have been, partly, related to an increase in basal melting due to an increase in the temperature of the adjacent shelf water [Schmidtko et al., 2014, Sutherland et al., 2013]. This increased temperature is often related to an increase in the supply of heat from the mid-depth open ocean, where the waters are less exposed to atmospheric cooling, to the shelf and ultimately the ice front [Walker et al., 2007, Straneo and Heimbach, 2013]. These warm waters however first need to pass over the topographic barrier of the continental slope.

1.2.3 Supporting enhanced productivity on-shelf

The shelf seas see enhanced productivity relative to the open ocean due to the unique physical environment. This enhanced productivity during the stratified period in the shallow shelf seas is limited by the availability of nutrients, such as nitrogen and phosphate [Hydes et al., 2001]. Rivers are able to supply high nutrient waters to the shelf seas, however, these waters are typically highly localised and, when considered over an entire shelf, are a small contribution. It is estimated that 80 - 90 % of the nitrogen and 50 - 60 % of the phosphate required to sustain the levels of primary production seen in the shelf seas is supplied from the open ocean [Liu et al., 2010]. These horizontal fluxes have previously been estimated, as the total nitrogen requirement minus the supply from the land-sea boundary, through regional budgeting and modelling as 2.44 Mt/year and 3.74 Mt/year respectively for the European Shelf. [Seitzinger and Giblin, 1996, Proctor et al., 2003].

1.2.4 Export of carbon from the shelf

The global ocean is a large component of the global carbon cycle which is estimated to remove 26% of anthropogenic carbon [Le Quere et al., 2009]. The European Shelf has been identified in a number of studies as making a significant contribution to this sink [Thomas et al., 2004, Frankignoulle and Borges, 2001]. This occurs through the process of enhanced productivity near the surface drawing carbon down from the atmosphere which then sinks into the bottom layer as particulate carbon[Tsunogai et al., 1999, Yool and Fasham, 2001]. That carbon is then re-mineralised and returned to the dissolved pool [Wollast and Chou, 2001]. Whilst this process will remove carbon over the stratified period it will only remove carbon from the atmosphere on inter-annual time-scales if the dissolved carbon is then transported into the open ocean below the main pycnocline.

1.3 Physics of the shelf edge

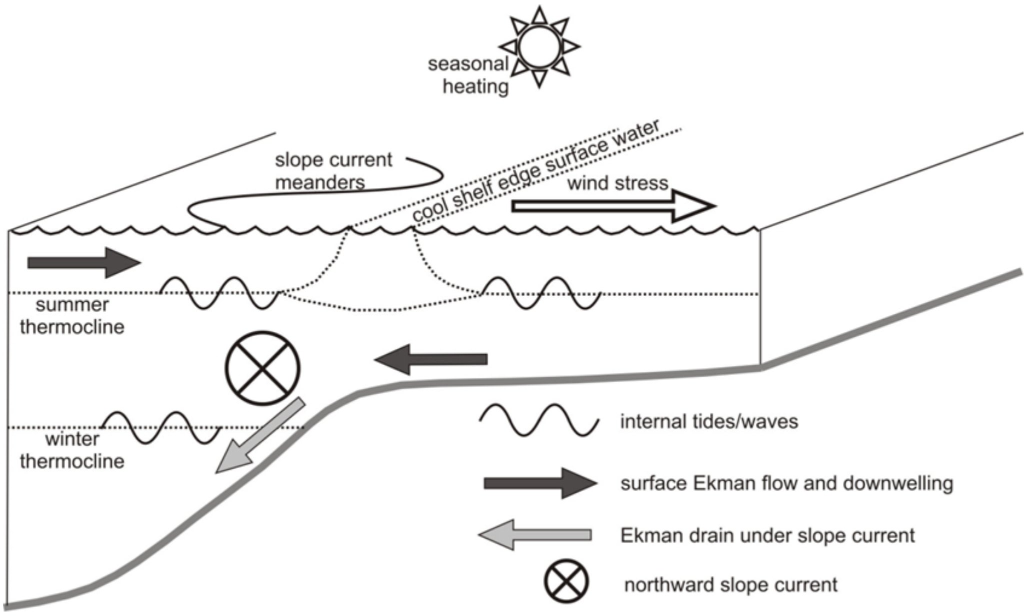

Figure 1.2: A schematic showing the range of physical processes occurring at the shelf break. This figure adapted from Huthnance et al. [2009]

Now we will explore the wide range of physical processes which occur at the shelf break and how they contribute to transport of volume across the shelf break. Some of the key physical processes are summarised in Fig. 1.2.

1.3.1 Why is exchange limited?

The steep topographic slope associated with the shelf edge is fundamental in understanding the flows, and thus across shelf exchange, in this region.

Taylor-Proudman Theorem

The combination of the topography and rotation of the earth applies a strong constraint on the flow. This constraint is referred to as the Taylor-Proudman theorem. Following the approach of Simpson and Sharples [2012] and Brink [1988] we start by taking the momentum equations with the steady and geostrophic assumptions,

$$fu = -\frac{1}{\rho}\frac{\partial p}{\partial y} \qquad -fv = -\frac{1}{\rho}\frac{\partial p}{\partial x}, \tag{1.1}$$

f is the Coriolis parameter,u and v are the horizontal components of the velocity, ρ is the density, p is the pressure field and x and y are the horizontal co-ordinates. Combining the differentials of Eqns. 1.1 with the continuity equation ($\frac{\partial u}{\partial x} + \frac{\partial v}{\partial y} + \frac{\partial w}{\partial z} = 0$) yields,

$$\frac{\partial w}{\partial z} = 0, \tag{1.2}$$

where w is the vertical velocity and z is the vertical co-ordinate. Since the vertical velocity at the surface equals zero, Eqn. 1.2 implies that the vertical velocity must be zero at all depths. Any across slope transport would require a non-zero vertical velocity and therefore the flow must be parallel to the isobaths.

This leads to the constraint that any steady geostrophic flow must be parallel to the topographic slope at the shelf edge and does not make a contribution to exchange across the shelf edge. This leads to the conclusion that exchange across the shelf edge can only occur when the assumptions of a steady geostrophic flow are relaxed. These assumptions are relaxed for: regions where friction plays an important role such as in the boundary layers; when the flow is unsteady such as tidal flows; and when the non-linear terms in the momentum equations become important such as when the flow interacts with sharp changes in the direction of the topography.

The slope current

A key physical component of the shelf edge system is a current that flows along isobaths [Burrows and Thorpe, 1999] with only a small cross-slope component

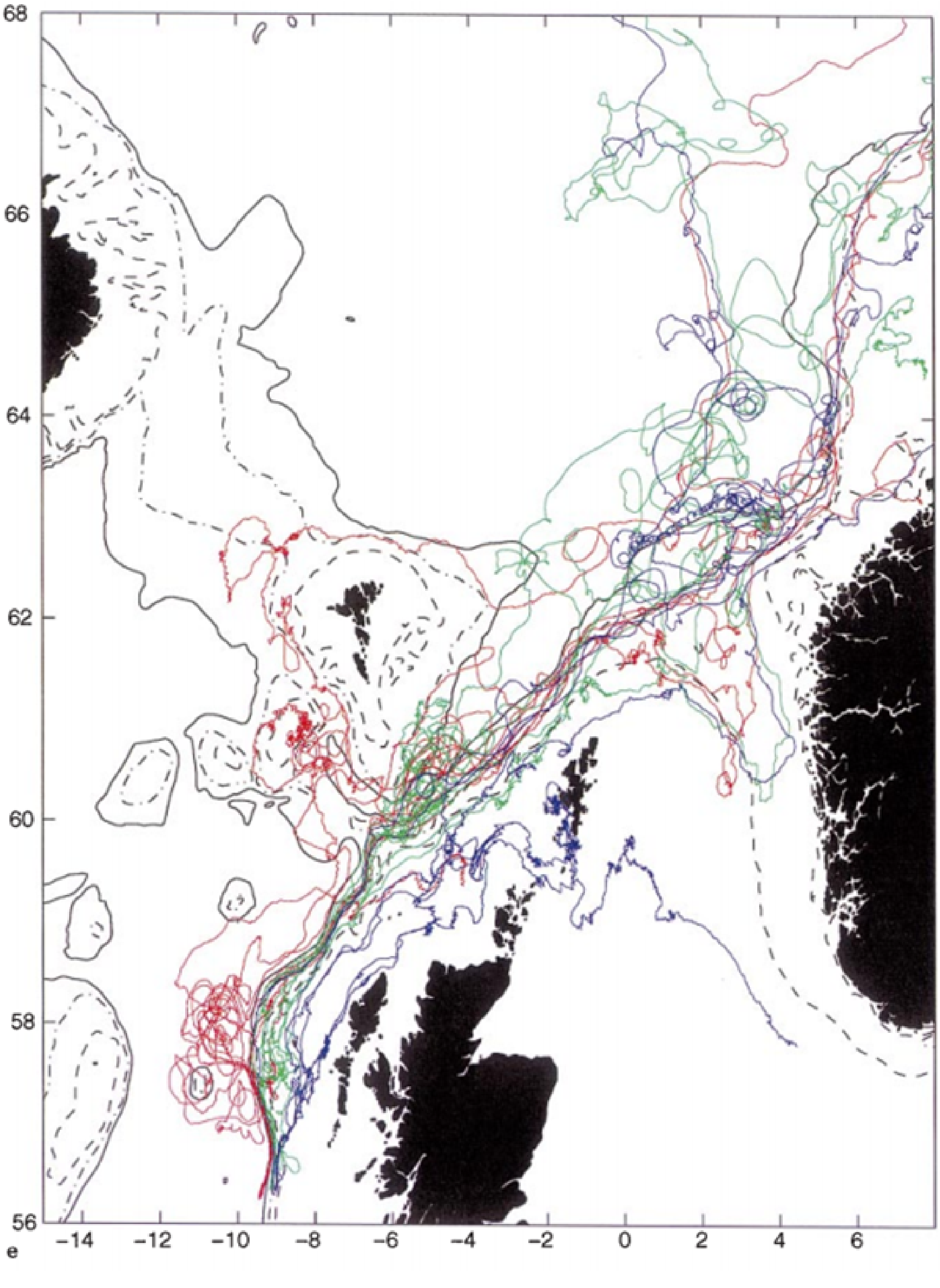

Figure 1.3: Tracks over 240 days of drifters released on December 1995. The colours represent the location of deployment: blue on the upper slope (200 - 400m), red on the mid-slope (500 - 700m), and green in the lower slope (1000 - 1200 m). This figure is from Burrows and Thorpe [1999]

over the mid and upper slope (Fig. 1.3). This demonstrates the tight topographic control discussed in the previous section. At the Hebridean Shelf edge in summer this current transports 1 Sv and in winter transports 2 Sv polewards and is predominantly barotropic [Souza et al., 2001]. Whilst much of the previous work above has taken place at the Hebridean and Malin Shelf, the current extends along the entire slope from the Bay of Biscay through to the Norwegian Trench [Pingree and Cann, 1989, Xu et al., 2015].

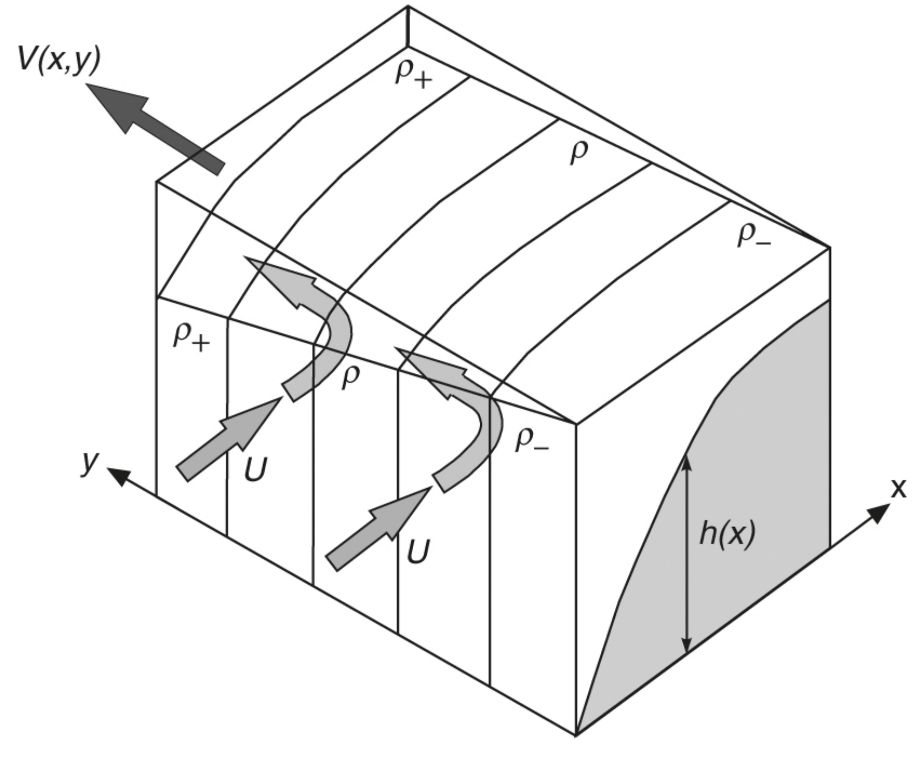

Figure 1.4: A schematic of the density and velocity associated with the JEBAR process in the Northern hemisphere. This figure is from Simpson and Sharples [2012]

At eastern boundaries, such as the European Shelf, this current is driven by a process known as JEBAR (Joint Effect of Baroclinicity and Relief) which was explored theoretically by Huthnance [1984]. This process is a result of the interaction between the northwards increase in surface density, as a result of the northwards decrease in surface temperature, and the topographic slope. A simplified model of the process is presented in Simpson and Sharples [2012] and will be followed here as a demonstration. Considering an ocean with a north-south orientated slope, in the same sense as the y-axis, separating a shallow shelf sea and deep open ocean. The density is taken as constant with depth but increases northwards, in the y direction, and the topography only varies in the east-west direction. So the equations of motion become,

$$fU = -gh\frac{\partial \eta}{\partial y} - \frac{gh^2}{2\rho_0}\frac{\partial \rho}{\partial y} \tag{1.3}$$

$$-fV = -gh\frac{\partial \eta}{\partial x} \tag{1.4}$$

where f is the Coriolis parameter, U and V are the vertically integrated velocities, g is the gravitational acceleration, η is the surface displacement, h is the depth of the water, ρ_0 is a reference density and ρ is the local density. Applying the differential of Eqns. 1.3 and 1.4 to the depth-integrated continuity equation yields,

$$\frac{\partial \eta}{\partial y} = -\frac{h}{\rho_0}\frac{\partial \rho}{\partial y} \tag{1.5}$$

This implies that, given the fact that the open ocean depth is much greater than the shelf depth ($h_{ocean} >> h_{shelf}$), the drop in sea surface height due to the density gradient will be greater in the open ocean than on the shelf. This difference between the two regimes implies that, as you move north-ward there will be an increasing sea surface slope between the shelf and the ocean (Fig. 1.4). This gradient in sea surface height drives a current in the y direction, i.e. parallel to the bathymetry. A more complete system is considered in Huthnance [1984] which derives the following expression for the strength of the slope current,

$$v = \frac{g}{2\rho_0 k}\frac{\partial \rho}{\partial y}h(H - h) \tag{1.6}$$

where H is the depth of the deep ocean and k is a drag coefficient. Using typical inputs for the European Shelf suggests an along slope current of O(0.1 ms^{-1}). This mechanism has since been supported by both numerical modelling and observations [Souza et al., 2001, Pingree and Cann, 1989].

1.3.2 Review of key processes

A number of the processes that have previously been identified as making a contribution to the transport across the shelf edge will now be explored. These processes all act outside the assumptions made in the Taylor-Proudman theorem and can potentially drive exchange across the shelf edge. First, two processes associated with the slope current will be explored, then the role of the winds will be considered and finally we will consider the effects of a density gradient between the shelf and open ocean.

Slope current meanders

The exchange potentially driven by flows interacting with sharp changes in topographic direction will now be considered. As discussed above any geostrophic flow is required to follow topographic contours provided they vary sufficiently slowly. When a flow meets a sharp change in the direction of topography relative to the speed of the flow the non-linear terms in the momentum equation become important and the Taylor-Proudman constraint no longer holds. The likelihood of a flow becoming separated from the effects of topographic steering can be summarised through the Rossby Number, Ro, which is the ratio of the inertial and Coriolis forcing,

$$Ro = \frac{V}{fL} \tag{1.7}$$

where V is the velocity and L is a horizontal length scale representing the deviation of the flow. When this number is greater than 0.1 the flow is considered to be out of geostrophic control and as a result no longer following contours.

A number of examples of this breakdown resulting in cross shelf edge exchange have been recorded in the literature. The Kuroshio current is deflected where the Rossby Number reaches 0.3 resulting in a large transport into the Sea of Japan and the South China Sea [Hsueh et al., 1996]. A further example is the deflection of a portion of the slope current as a result of topographic changes West of Ireland and on the Malin Shelf [Hill, 1995].

It was previously understood that the tight topographic control by the shelf break suppresses mesoscale eddies [Stewart and Thompson, 2013]. However, more recent work has demonstrated that under certain conditions, such as where isopycnals are steep and connect between the open ocean and the shelf, eddies can transport volume across the shelf [Thompson et al., 2014, Stewart and Thompson, 2015].

Bottom Ekman transport

Now the processes occurring within the bottom boundary layer, where friction controls the dynamics, will be explored. In this layer the approximately barotropic slope current is reduced to zero at the bed as a result of bottom friction. As a result of this bottom friction we expect the current to be deflected in the direction of the pressure gradient, for the European Shelf directed off-shelf, as the flow becomes weaker and thus the Coriolis force balancing the pressure gradient also becomes weaker [Simpson and Sharples, 2012]. This results in a bottom layer spiral typical of Ekman veering. The net depth integrated cross-isobath transport is,

$$T = \frac{\tau}{\rho_0 f} = \frac{kv^2}{f} \tag{1.8}$$

where T is the total transport, τ is the bottom stress, k is the bottom drag coefficient and v is the barotropic velocity above the bottom boundary layer. Using typical values for the European Shelf this transport is 0.8 $\mathrm{m^2s^{-1}}$ [Simpson and Sharples, 2012]. Observation studies on the Malin Shelf show a down slope

Ekman transport of 1.6 $\mathrm{m^2 s^{-1}}$ [Simpson and McCandliss, 2013].

Wind forcing

Now we will consider the effects of friction in the surface boundary layer. Here, rather than the friction between an oceanic flow and the boundary we will consider the response of the ocean when forced at the boundary. The initial forcing by the wind at the surface is perturbed by the Coriolis forcing as the momentum propagates down the water column, leading to the classic Ekman Spiral with the direction of the transport rotating to the right in the northern hemisphere. Depth integrating these velocities yields,

$$U = 0, \quad V = \frac{\tau_x}{f \rho_0} \tag{1.9}$$

where U and V are the transports in the x and y directions respectivly and τ_x is the wind-stress directed in the x direction.

These equations show that the depth integrated transport is at right angles to the direction of the wind stress. At the European Shelf edge the wind is predominantly to the north-east or east resulting in an Ekman transport onto the shelf in the surface Ekman layer. This transport, in combination with the Bottom Ekman transport, has previously been invoked in a down-welling circulation across the North-West European Shelf with important implications for the transport of carbon off the shelf [Holt et al., 2009, Huthnance et al., 2009, Painter et al., 2016].

Cascading

A further process that contributes to cross-shelf exchange is the density driven flows as a result of the differential cooling between the shelf and open ocean during winter. During winter the surface mixed layer in the open ocean drops deeper than the shelf edge and the shelf becomes well mixed with depth. As a result of this the surface cooling is occurring over a greater depth, and a larger

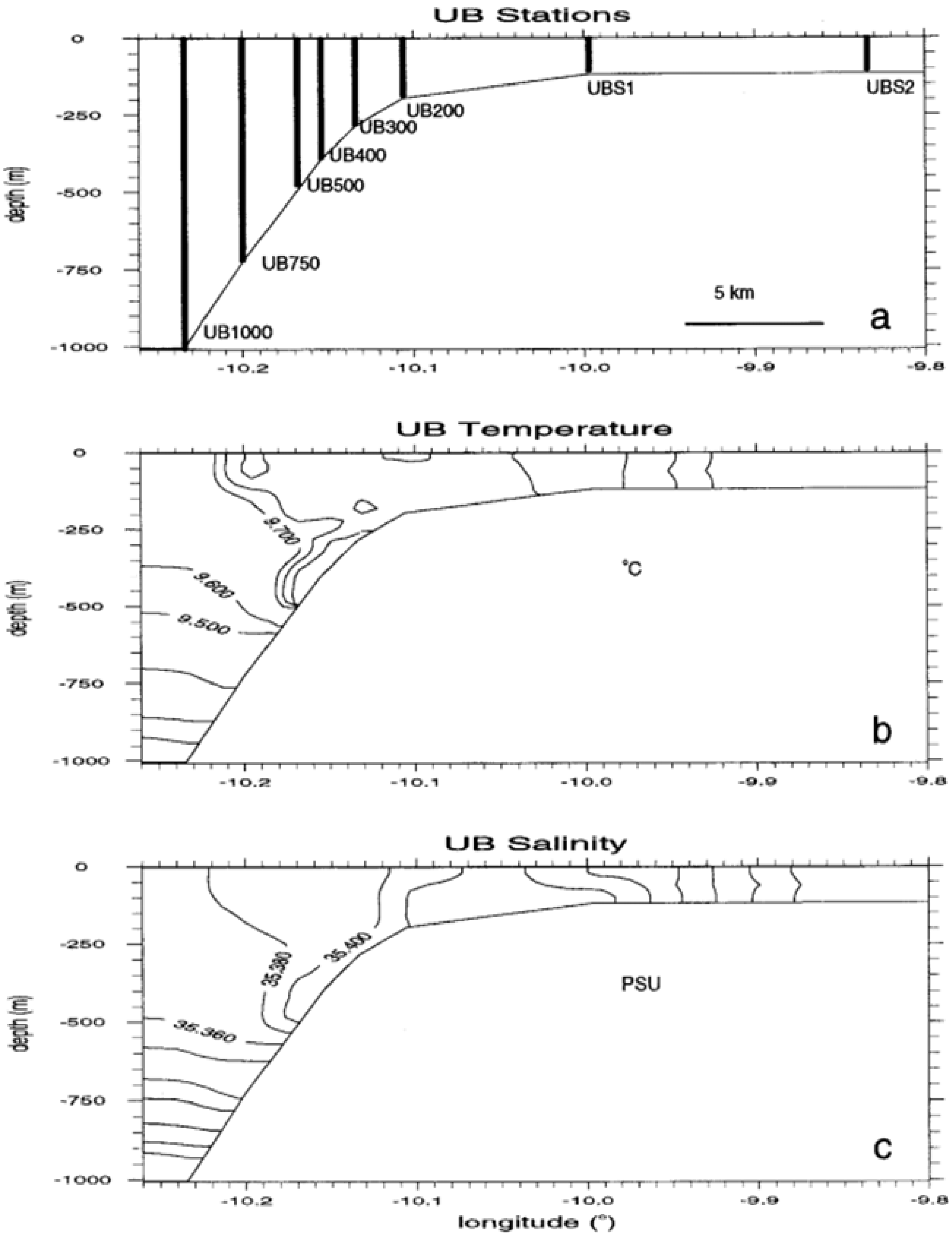

Figure 1.5: Hydrographic sections along a line in the Malin Shelf showing: (a) the positions of the stations, (b) the temperature (°C), and (c) the salinity. This figure is from Hill et al. [1998]

volume, on the open ocean side than the shelf. This leads to the shelf becoming cooler and denser than the adjacent ocean. Such a density gradient is unstable and results in a down slope flow. This down slope flow is partially modified by the Coriolis force however bottom friction stops the flow becoming geostrophic so it maintains a down slope component. Bowden [1960] explored this phenomenon theoretically and derived the following relations for such a density driven current, assuming that the angle of the slope relative to horizontal is small (<15°) [Simpson and Sharples, 2012],

$$tan\theta = \frac{r}{fh} \tag{1.10}$$

$$V = \frac{g'h\delta}{\sqrt{f^2h^2 + r^2}} \tag{1.11}$$

where θ is the angle of the angle of the flow relative to the bathymetry, r is the drag coefficient, h is the thickness of the cascading layer, g' is the reduced gravity, and δ is the angle of the topography relative to horizontal. Bowden [1960] applied these relations to the Iceland-Faroe ridge and calculated that the angle of the cascade relative to the topography is typically 5° to 10 °, although it can reach as high as 30 °. These features are only expected to occur infrequently, as they rely on the difference in density which only occurs towards the end of the cooling period and rapidly remove the instability that causes them. As a result these events are rarely observed with the inventory presented in Ivanov et al. [2004] only recording 61 cases. One of these cases is presented in Fig. 1.5 with a salty tongue of shelf water being present along the bottom boundary of the slope [Hill et al., 1998]. Using typical inputs for the Malin Shelf the cascade moves down slope at 7° relative to the topography leading to a down slope component of transport of 0.4 m^2s^{-1} [Simpson and Sharples, 2012]. This transport is of similar magnitude to the transports expected by other processes indicating that it may be important when occurring however the intermittent nature of this process suggests it is likely to only make a small contribution when averaged over a seasonal cycle. They may however, due to their high density, play an important role in the formation of dense water and the ventilation of deep layers within the open ocean.

Estimates of the magnitude of these processes

An estimate of the magnitude of the Ekman transport and the transport by eddies is provided in Table 1.1 with the values taken from Huthnance et al. [2009]. The transport by cascading is not including due to the lack of observations and its intermittent nature.

Table 1.1: Estimates of cross-shelf exchange per unit width (m^2s^{-1}) driven by various processes in the sectors of the European Shelf edge. This table is adapted from Huthnance et al. [2009]

Sector	Bottom Ekman	Eddies	Summer Wind	Winter Wind
	Off-shelf	Variable	Variable Average on-shelf	Variable Average on-shelf
Norway	0.5	1	0.9	1.48
North Sea	2			2
North Scotland	0.5	1	1.06	1.81
West Scotland	0.5		0.8	1.73
West Ireland	0.5		0.67	1.55
Celtic Sea	0.5		0.78	1.09

These estimates reveal that the two components of Ekman transport are of approximately the same magnitude, with the Bottom Ekman transport 0.5 m^2s^{-1} and the wind driven Ekman transport of 0.67 to 1.81 m^2s^{-1}. Whilst the estimate of the wind driven transport is somewhat larger than the estimate of the bottom Ekman transport, the latter is consistent in terms of direction whereas the surface wind forcing is likely to be more variable in direction and thus partially cancelling with itself. These process estimates will later be compared with the total exchanges calculated within this study.

1.3.3 Internal tides

A further important physical process at the shelf edge is the generation of internal waves of both tidal and higher frequency. These variations associated with the internal tide are sufficiently rapid that they are not constrained by geostrophy. These internal tides have not previously been viewed as making a contribution to transport across the shelf edge however they do generate important enhanced mixing both locally [Sharples et al., 2001, 2007] and as the wave propagates into the interior of the shelf [Pingree and Mardell, 1985]. Additionally, the internal tide can generate non-linear internal waves which have previously been studied as a source of cross-slope transport [Inall et al., 2001].

Internal tides are generated throughout the global ocean anywhere tides, a stratified water column and steep topography interact, primarily the continental slope and ridges in the ocean bed [Green and Nycander, 2013]. This generation is a result of convergence generated by the barotropic tide as it moves up the slope squeezing the water column and divergence as the tide moves down the slope stretching the water column (Fig. 1.6). This periodic forcing generates waves in the displacement of the stratification which then propagate away as waves parallel to the topography and in both directions.

The internal waves generated by these features then fill much of the global open ocean [Zhao et al., 2016] and are present in many shelf seas [Nash et al., 2012]. Whilst a portion of the energy propagates into the open ocean here we will primarily be interested in the portion propagating onto the shelf. There is some disagreement over how far onto the shelf the internal tide propagates with the combined observational and modelling work from Green et al. [2008] in the Celtic Sea showing the majority of internal tide energy being dissipated within 20-30 km whereas Inall et al. [2011] shows the internal tide propagating 170 km into the Celtic Sea. As the internal tide propagates onto the shelf shorter period

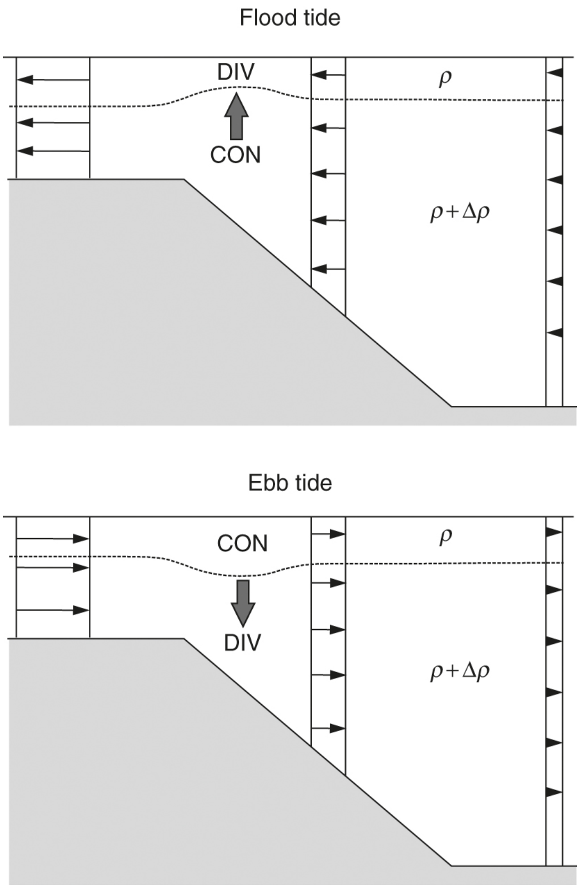

Figure 1.6: A schematic of the convergences and divergences generated by the barotropic tide. These convergences and divergences then displace the stratification generating the internal tide. This figure is from Simpson and Sharples [2012]

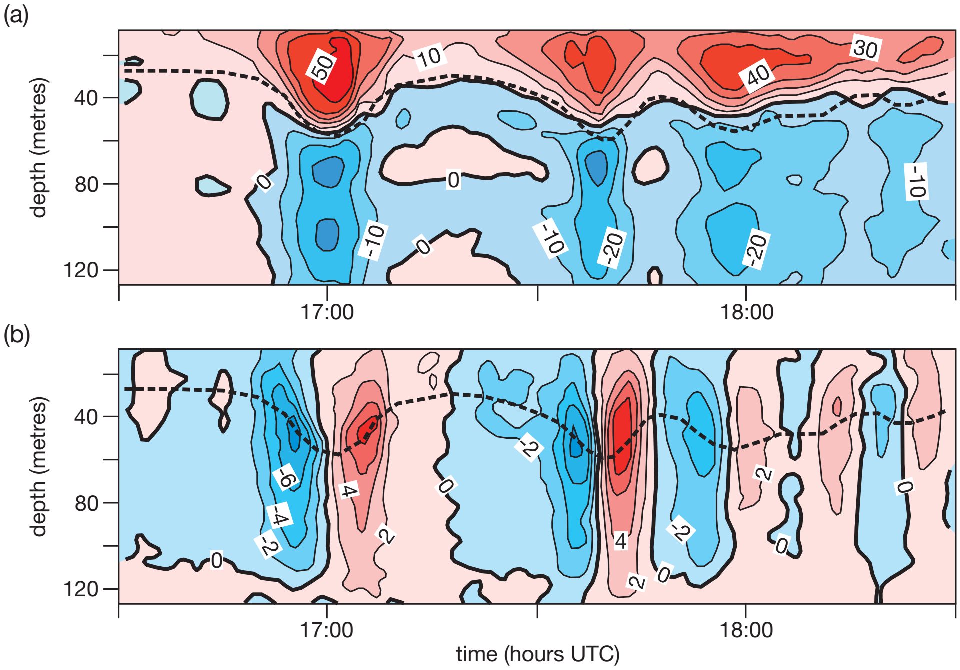

Figure 1.7: Observations from a bed mounted ADCP on the Hebredian Shelf showing (a) the horizontal velocity and (b) the vertical velocity (cm s^{-1}). The dashed line shows the displacement of a particle. This figure is from Simpson and Sharples [2012]

waves are generated as the internal tide interacts with the shallow sloping sea bed. In the shelf, where the stratification can be simplified to that of two well mixed layers separated by a thin thermocline, these propagating waves generate opposing horizontal velocities in the surface and bottom layers with maximum vertical velocities occurring at the pycnocline when the pycnocline is moving between elevated and depressed phases (Fig. 1.7)

1.4 Bolus transport

The first theme within this thesis explored the role of bolus transport in shelf edge exchange associated with internal waves. A detailed mathematical introduction to the bolus transport will be given in Chapter 2. It is sufficient at this point to think of the bolus transport as the effect of propagation of thickness anomalies in transport volume in addition to the mean transport. This process has previosuly been considered in the upper atmosphere [Plumb and Mahlman, 1987], Southern Ocean [Gent et al., 1995], Western Up-welling regions [Csanady, 1989], transport through the Strait of Gibraltar [Bryden et al., 1994] and near the coastal boundary [Lee et al., 1997].

This transport was initially considered for the problem of polewards transport of tracers, primarily ozone, in the upper atmosphere. Ozone is formed by photochemical reactions indicating a stronger source of ozone at low latitudes where solar radiation is strongest . Given this you would expect there to be high concentrations of ozone in the tropics and low concentrations at the poles. However the observed distribution of ozone is one of low concentration at the tropics and high concentration at the mid and high latitudes, particularly in the winter hemisphere, prior to anthropogenic impacts [London and Kelley, 1974, Cooper et al., 2014]. This distribution must thus be the result of transport redistributing the ozone, however, the time-average circulation does not match this distribution of ozone. Ultimately this redistribution was accounted for by considering the bolus transport in the upper atmosphere [Plumb and Mahlman, 1987, Andrews, 1990].

The initial application of this idea to the ocean was in parametrising the effect of ocean eddies, especially in the Southern Ocean [Gent and McWilliams, 1990, Danabasoglu et al., 1994, Gent et al., 1995]. The bolus transport was used to describe the meridional transport of water masses across the fronts in the Southern Ocean [Marshall, 1997]. This particularly applies to the subduction of the Antarctic Intermediate Water and Antarctic Bottom Water and entrainment of the North Atlantic Deep Water, all of which are opposed by the Eulerian velocity.

A further previous use of the bolus transport has been in the action of surface waves approaching a beach. Here the bolus transport is equivalent to the Stokes Drift for a simple surface wave [e.g. Lee et al., 1997] although in a more complete representation of the system the bolus transport may only be a contribution to the Stokes Drift. In this case the bolus transport associated with the surface waves are driving volume towards the coastal boundary. This leads to a strong localised return either through an off-beach directed bottom layer transport or through a return flow focussed into a narrow rip current.

This leads to two views of the bolus transport in the literature for the ocean: the open ocean case where the bolus transport makes an important contribution to the overall system wide circulation; and a coastal view where the bolus transport moves volume, however, it is returned locally such as in an undercurrent or a rip current.

1.5 Challenges of a synthesis of ocean-shelf exchange

A complete understanding of shelf edge exchange is difficult given the current limitations in observational or modelling data sets. There have been many previous observational efforts to understand shelf edge exchange, for example the SEEP I and II projects [Biscaye et al., 1994] on the Mid-Atlantic Bight and OMEX I [Wollast and Chou, 2001] and II [Huthnance et al., 2002] and SES [Souza et al., 2001] on the European Shelf. These studies have often had a strong observational component however it is difficult, in a system with such a wide range of processes occurring across a range of spatial and temporal scales, to understand how representative those observations are over a shelf edge of 2000 km and over a seasonal cycle. These problems might be resolved by using a numerical model to place an observational campaign into the wider context. Whilst the use of a numerical model is rather tempting, given the large-scale picture they are able to offer, it is important to note that, until very recently, it has not been possible to apply a model over the entire shelf with sufficient horizontal resolution to capture some important processes occurring at the shelf edge, such as internal tides.

1.6 Structure of this study

This study has two primary sections: firstly the proposal and evaluation of a new process that may contribute to the exchange across the shelf break, and secondly the use of an integral framework to evaluate the exchange of volume at the shelf edge. The first of these themes is explored across chapters two, three and four with the work split into an initial theoretical presentation of the process, evaluation of the process in a series of observational data sets and finally using model output to estimate the global magnitude of the process. The integral framework will then be explored in chapter five concluding with an estimate of the volume exchange and circulation implied by the calculation averaged over the entire shelf and over the full seasonal cycle.

1.7 Summary

- The deep ocean and shallow shelf seas have distinct physical, chemical and biological characters. This is largely due to the fact that shelf seas are much shallower than the open ocean and that they are adjacent to the land boundary.

- The exchange between these two regimes is important for a range of reasons, including: the formation of water masses such as the AABW which fills much of the deep ocean; the supply of warm water from the ocean to ice fronts modifying the basal melting; supplying the nutrients required to maintain enhanced productivity on the shelf; and exporting carbon that has been drawn down onto the shelf into the deep ocean.

- This exchange is limited due to the steep topography of the shelf edge which, through the Taylor-Proudman Theorem, requires all geostrophic flows to follow the topography. An example of such a steered flow is the slope current.

- A number of processes have previously been identified as potentially important in driving cross-shelf exchange. These processes include: slope current meanders and eddies, bottom Ekman transport, wind driven Ekman transport and cascading. These processes typically drive transports of 0.5 to 1.8 m^2s^{-1}.

- A further important process at the shelf edge is the generation of internal tides. These internal tides are generated by the interaction of steep topography and the barotropic tide. These internal tides have been observed to propagate a considerable distance onto the shelf, although some modelling work suggests a large portion of the energy is lost in the shelf edge region.

- A synthesis of ocean shelf exchange is difficult due to the wide range of spatial and temporal scales over which the exchange occurs, from the constant effects of the bottom Ekman transport to the highly intermittent and local effects of cascading.

- This thesis contains two primary themes. Firstly, we will investigate the role of the internal tide in generating thickness and velocity perturbations and their potential to drive a Bolus transport. Secondly, we will explore the application of a water-mass based integral framework to the shelf sea, specifically the European Shelf, and the implied circulations.

Chapter 2

Bolus Transport

2.1 Transport in a layer

In the ocean it is often useful to split the water column up into a series of layers defined by properties, typically potential density. These layers can often, if the step in property is sufficiently small, be treated as homogeneous layers with tracers and velocity not varying with depth within the layer. Here we discuss the expected transport of volume and tracer expected for such a layer.

2.1.1 Definition of bolus transport and transport velocity

The volume transport per unit length ($m^2 s^{-1}$) for a layer is given by the product of the velocity in the layer ($\mathbf{u}$) and the thickness of the layer (h). Here we think of the instantaneous layer velocity as the depth averaged velocity ($\mathbf{u}$) between two bounding surfaces, typically potential density surfaces, and the layer thickness as vertical distance between these two surfaces (h).

The velocity within the layer and its thickness can be split into a time-mean, denoted by an over bar, and a time-varying component, referred to as an eddy component and denoted by a prime:

$$h(x,y,t) = \overline{h}(x,y) + h'(x,y,t), \tag{2.1}$$

$$\mathbf{u}(x,y,t) = \overline{\mathbf{u}}(x,y) + \mathbf{u}'(x,y,t), \tag{2.2}$$

where the time mean is

$$\overline{h}(x,y) = \frac{1}{\Delta t}\int_0^{\Delta t} h(x,y,t)\ dt\ , \tag{2.3}$$

$$\overline{\mathbf{u}}(x,y) = \frac{1}{\Delta t}\int_0^{\Delta t} \mathbf{u}(x,y,t)\ dt\ , \tag{2.4}$$

and the time-varying or eddy component is given by

$$h'(x,y,t) = h(x,y,t) - \overline{h}(x,y), \tag{2.5}$$

$$\mathbf{u}'(x,y,t) = \mathbf{u}(x,y,t) - \overline{\mathbf{u}}(x,y), \tag{2.6}$$

These time varying components have, by definition, a zero time mean i.e. $\overline{h'(x,y,t)} = 0$ and $\overline{\mathbf{u}'(x,y,t)} = 0$. It is important to note that we use a purely mathematical definition of an eddy component, i.e. the deviation from the mean state, rather than referring to a specific coherent feature such as a mesoscale eddy.

Now taking the product of equations (2.1) and (2.2) gives a volume transport per unit length,

$$\mathbf{u}h = (\overline{h} + h')(\overline{\mathbf{u}} + \mathbf{u}') = \overline{h}\overline{\mathbf{u}} + \overline{h}\mathbf{u}' + h'\overline{\mathbf{u}} + h'\mathbf{u}', \tag{2.7}$$

where the dependences of each variable are taken as above.

Taking the time-mean volume transport and recalling that the time means of the time-varying components are zero gives

$$\overline{\mathbf{u}h} = \overline{\mathbf{u}}\overline{h} + \overline{\mathbf{u}'h'}, \tag{2.8}$$

showing the volume transport in a layer made up of a contribution from the time-mean velocity, $\overline{u}\overline{h}$, and an additional component driven by the covariance of the time-varying velocity and layer thickness, $\overline{u'h'}$. This additional component is often referred to as the eddy or bolus transport [McDougall, 1991]. This bolus transport is shown graphically in Fig. 2.1(a). The layer has oscillating horizontal velocity with the positive velocity, to the right, being co-located with the layer being thicker than average and the negative velocity, to the left, being co-located with the layer being thin. This leads to a time-mean transport of volume to the right, as more volume is moved to the right in the first phase than is returned in the second phase. By dividing (2.8) by the time mean thickness we obtain the transport velocity,

$$\frac{\overline{\mathbf{u}h}}{\overline{h}} = \overline{\mathbf{u}} + \frac{\overline{\mathbf{u}'h'}}{\overline{h}}, \tag{2.9}$$

where the bolus transport divided by the layer thickness may be viewed as an equivalent bolus velocity, often denoted by $\mathbf{u}^*$. The bolus transport requires velocity and thickness anomalies to vary in phase with each other. The bolus transport might be driven by a range of processes including, but not limited to, geostropic eddies generated by baroclinic instability, baroclinic internal waves and surface waves approaching the shore. The bolus transport is well established in the open ocean community and is often considered important in advecting tracer across contours of time-mean flow, for example in understanding the meridional transport in the Southern Ocean, described by Gent et al. [1995], Danabasoglu et al. [1994] and Lee et al. [1997].

Taking in phase layer thickness variations, h', of ± 10 m and velocity variation, u', of ± 10 cm s^{-1}, values that would be reasonable on the North-East Atlantic shelf, leads to instantaneous volume transports, $u'h'$, in the range 0 to 1 m^{2}s^{-1}. Assuming that these transports are evenly distributed, such as with a sinusoid, the time-mean bolus transport, $\overline{u'h'}$, is 0.5 m^{2}s^{-1} or, in a layer with a time-mean thickness, $\overline{h}$, of 100 m, a representative bolus transport velocity, u^*, of 0.5 cm s^{-1}. It would only require a mean velocity, $\overline{u}$, of 0.5 cm s^{-1} for an

(a) Eddy transport from the covariance of thickness and velocity

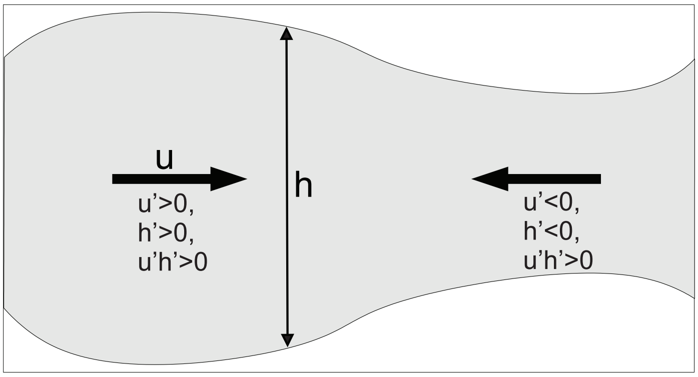

(b) Baroclinic tidal thickness and velocity variations

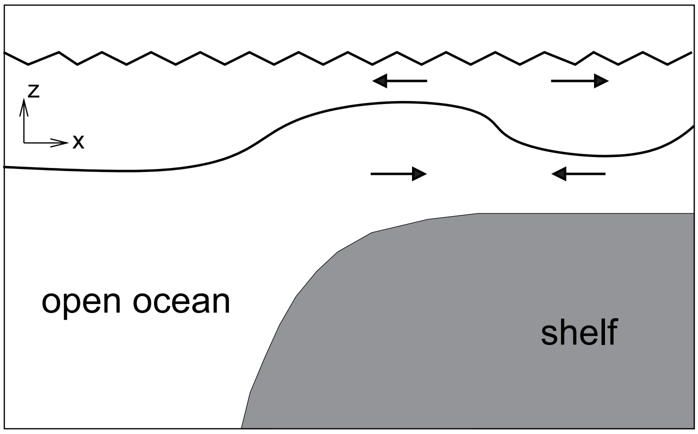

Figure 2.1: A schematic figure for (a) how the covariance of the temporal deviation of layer thickness, h', and layer velocity, u', leads to a volume transport, $u'h'$, and (b) how layer thicknesses and horizontal velocities are related for a simple linear baroclinic internal wave on the continental shelf in a two layer ocean.

equivalent mean transport, $\overline{u}\overline{h}$. This time-mean velocity is often constrained to following depth contours rather than transporting volume across topography. These transports are comparable to estimates of other processes acting at the shelf edge, such as wind or slope current driven Ekman transport or the effects of eddies and meanders, [Huthnance et al., 2009] indicating that the bolus transport could make up a significant component of the volume transport across the shelf edge.

2.1.2 Extension to tracer transport

Now we consider the transport of a tracer in a layer. The tracer transport is given by the product of the velocity in the layer, $\mathbf{u}$, the thickness of the layer, h, and the tracer concentration, c. Performing the same separation into time-mean and time-varying components, as discussed above gives a tracer transport per unit horizontal length,

$$h\mathbf{u}c = (\overline{h\mathbf{u}} + (h\mathbf{u})')(\overline{c} + c') = (\overline{h\mathbf{u}})\overline{c} + (\overline{h\mathbf{u}})c' + (h\mathbf{u})'\overline{c} + (h\mathbf{u})'c', \tag{2.10}$$

and again applying a time mean gives

$$\overline{h\mathbf{u}c} = (\overline{h\mathbf{u}})\overline{c} + \overline{(h\mathbf{u})'c'}, \tag{2.11}$$

and substituting in the expression for the time-mean volume transport given in (2.8)

$$\overline{h\mathbf{u}c} = \overline{h}\overline{u}\,\overline{c} + \overline{\mathbf{u}'h'}\overline{c} + \overline{(h\mathbf{u})'c'}, \tag{2.12}$$

which, as with the volume transport, can then be divided by the mean layer thickness

$$\frac{\overline{h\mathbf{u}c}}{\overline{h}} = \overline{\mathbf{u}}\,\overline{c} + \frac{\overline{\mathbf{u}'h'}}{\overline{h}}\overline{c} + \frac{\overline{(h\mathbf{u})'c'}}{\overline{h}} \tag{2.13}$$

The transport of a tracer consists of three components: (1) advection of the time-mean tracer by the time-mean velocity, (2) advection of the time-mean tracer by the bolus transport, and (3) a diffusive transport given by the covariance of the time-varying transport and tracer concentration. This is set out in Gent et al. [1995].

For both the volume and tracer transport per unit length calculations above, the integrated volume (m^3s^{-1}) or tracer transport is given by multiplying by an appropriate length scale perpendicular to the direction of the transport.

2.2 Two layer versus continuous stratification

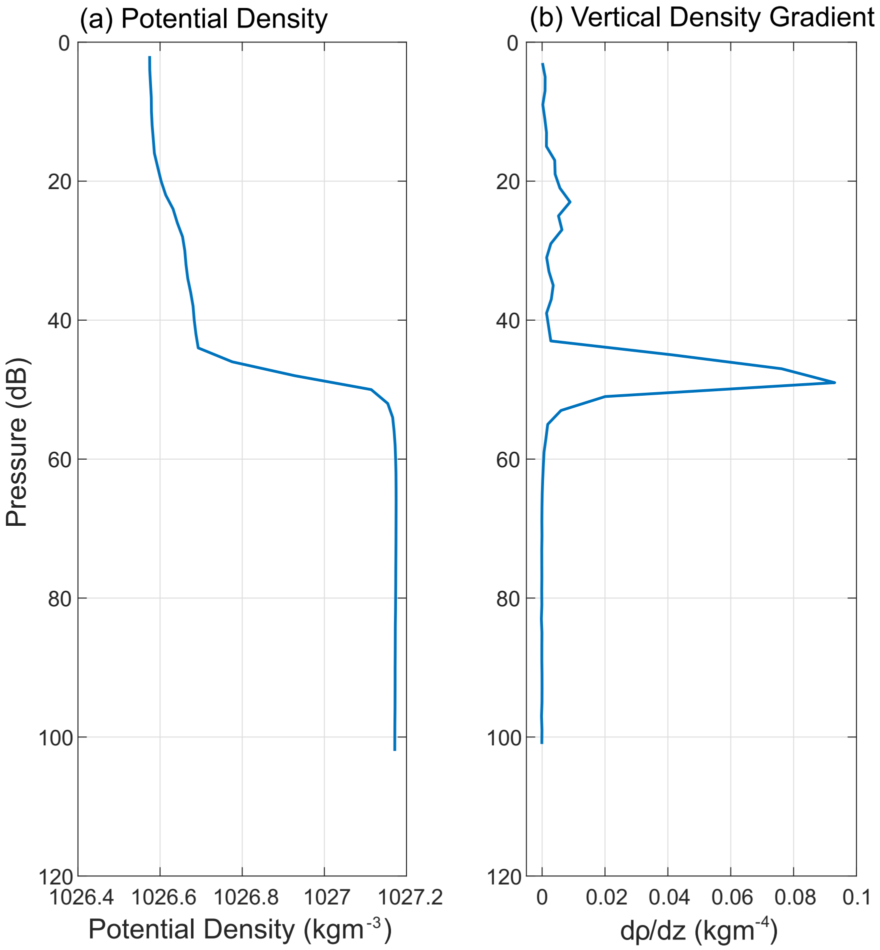

Figure 2.2: Profiles of (a) potential density (kg m^{-3}) and (b) the vertical gradient in potential density (kg m^{-4}) from a CTD cast near the Celtic Sea shelf break (49.2° N, 8.5° W). This profile is typical for the shelf sea.

In this work we view the shelf seas in the vertical as a simple system of two well mixed layers separated by an infinitesimal boundary, rather than a continuously stratified one. On the North-West European shelf this not an unreasonable simplification to make as boundary-driven processes, primarily surface wind forcing and bottom friction associated with the tide, drive enhanced mixing generating well mixed bottom and surface layers (Fig. 2.2(a)).

On some shelves, where the tide is weaker, the bottom layer mixing will be weaker resulting in a thicker and deeper pycnocline. These layers are then separated by a thin boundary layer where we see large vertical density gradients (Fig. 2.2(b)).

In a continuously stratified fluid, the total Stokes' drift can be written as the sum of two terms [McDougall and McIntosh, 2001],

$$u_{Stokes} = \overline{u\frac{\partial \zeta}{\partial z}} + \overline{\zeta\frac{\partial u}{\partial z}}, \tag{2.14}$$

where u is the horizontal velocity, z is the vertical co-ordinate and ζ is the vertical displacement of a density surface. The first term is the bolus transport, as the vertical derivative of ζ is the thickness variations. The second term is driven by the effect of a particle moving vertically through a water column, with vertically-sheared velocity, so that the particle will experience a velocity different to the velocity at its mean depth. Whilst this second term is important in a continuously stratified fluid, this term is zero in the two layer system considered here. In each layer the velocity is not varying with depth, i.e. $\frac{\partial u}{\partial z} = 0$, with the shear confined to the boundary between the two layers. In a system where the diabatic forcing and mixing is small, particles will not cross the interface and thus will not experience this shear and contribution to the Stokes' drift. Initially within this thesis we will use this well mixed layers with limited exchange assumption and evaluate the role of internal tide driven bolus transport. We will then, in Chapter 6 of this thesis, consider the role that the shear driven component of the Stokes' Drift could play in opposing or supporting the bolus component both within layers and in a depth integral sense. This will be considered from both theoretical arguments and a brief reanalysis of some of the observations presented in Chapter 3.

2.3 Bolus transport by an internal wave

The bolus transport provides a mechanism for breaking Taylor-Proudman constraints on volume transport across the topographic contours at the continental slope. The bolus transport has generally not been considered as playing an important role across continental slopes, since the baroclinic eddy activity is inhibited; bottom topography can stabilise a baroclinic front whenever the layer interfaces slope in the same sense as the bottom topography [Orlansky, 1969, Barth, 1989]. However, the mesoscale activity may still be important when there are large contrasts in layer thickness between the shelf and open ocean, such as for the Antarctic shelf break [Thompson et al., 2014].

While the mesoscale activity may be important in some regimes, we now explore the effect of another baroclinic process involving the time-dependent baroclinic waves and tide. For baroclinic waves and tides with periods less than a day there is not the same steering of the flow along bathymetric contours.

2.3.1 Derivation using layer-averaged velocities and continuity

Consider a two dimensional ocean consisting of two homogeneous layers with a sharp undulating interface and uniform horizontal velocity in each layer. For the baroclinic wave, assume a sinusoidal vertical displacement of the layer interface propagating in the x direction leading to layer thickness anomalies in each layer,

$$h_i'(x,t) = \wedge_i a \sin(kx - \omega t), \tag{2.15}$$

where a is the amplitude of the displacement, k is the wave number, x is the horizontal co-ordinate, ω is the angular frequency, t is time and $\wedge_i$ is used to identify the sign of the thickness anomaly for each layer; $\wedge_{i=1} = -1$ for the upper layer and $\wedge_{i=2} = 1$ for the lower layer.

Depth integrating the two dimensional continuity equation, $\frac{\partial u'}{\partial x} + \frac{\partial w'}{\partial z} = 0$, with the vertical velocities at the sea surface and the sea floor taken to be zero, gives

$$w'(h_i) = -h_i \frac{\partial u'}{\partial x}, \tag{2.16}$$

where $w'(h_i)$ is the vertical velocity at the layer interface. Thus the vertical velocity at the layer interface is balanced by the horizontal convergence of uniform horizontal velocity in each layer. Assuming the waves are small in amplitude compared to the time mean of the layer thickness, $h_i(t) \approx \overline{h_i}$, and then setting the vertical velocity such that there is adiabatic flow, $w'(h_i) = \frac{\partial h'}{\partial t}$, then gives the following continuity equation,

$$\frac{\partial h'_i}{\partial t} + \overline{h_i} \frac{\partial u'_i}{\partial x} = 0, \tag{2.17}$$

Substituting (2.15) into (2.17) leads to the layer-averaged velocity perturbation associated with the baroclinic wave,

$$u'_i(x,t) = \wedge_i \frac{\omega a}{k\overline{h_i}} \sin(kx - \omega t), \tag{2.18}$$

The bolus transport for the baroclinic wave is defined by the time mean of the product of the time-varying layer thickness (2.15) and horizontal velocity (2.18) perturbations, giving

$$u'_i h'_i = \frac{\omega a^2}{k\overline{h_i}} \sin^2(kx - \omega t), \tag{2.19}$$

then taking the time mean of (2.19) over a wave period yields

$$\overline{u'_i h'_i} = \frac{c a^2}{2\overline{h_i}}, \tag{2.20}$$

where $c = \omega/k$ is the phase speed. This expression for the bolus transport can be written as a bolus velocity by dividing by the time mean thickness,

$$u^* = \frac{c a^2}{2\overline{h_i}^2}, \tag{2.21}$$

The covariance of time-varying thickness and velocity leads to a rectified transport that is always positive and in the same direction as the propagation of the wave (Fig. 2.3) A similar derivation for the bolus transport by a shallow water, surface wave is given in Lee et al. [1997].

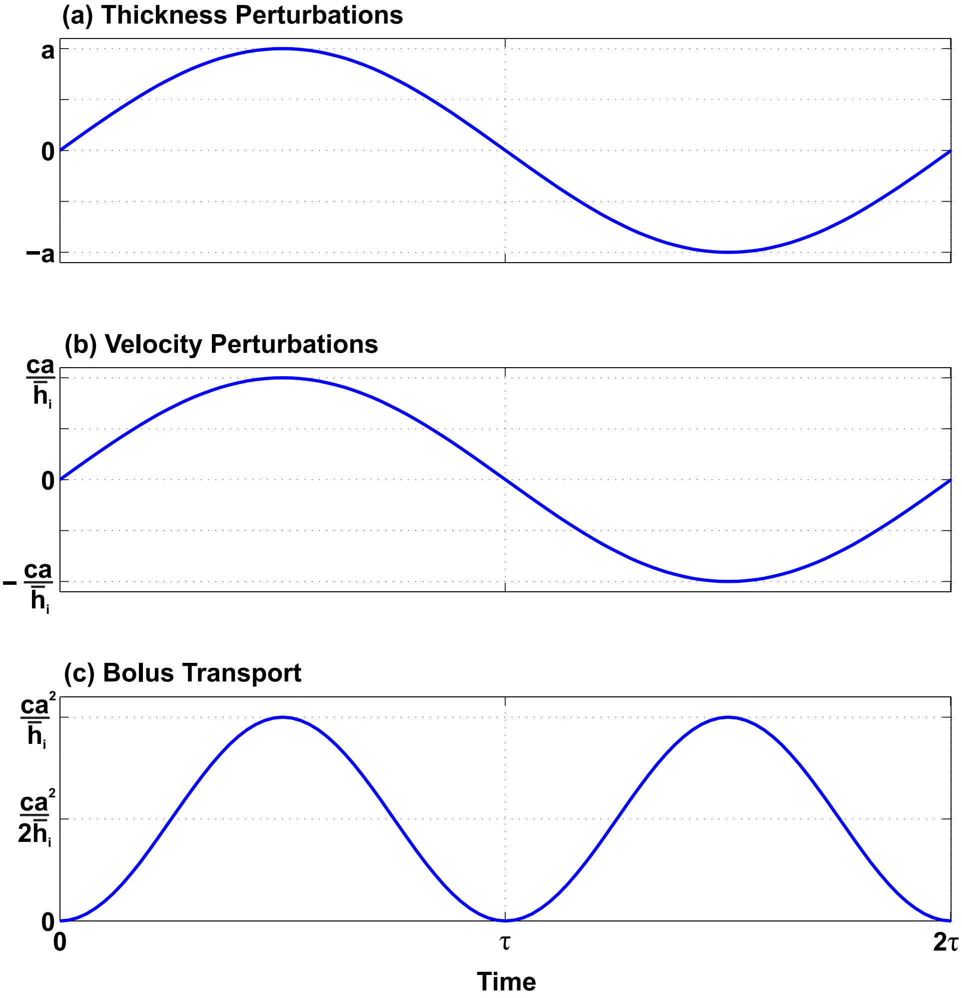

Figure 2.3: Theoretical time-series showing (a) velocity perturbations, (b) thickness perturbations and (c) bolus transport for the bottom layer over a wave period. Taken from equations (2.15), (2.18) and (2.19)

Typically in the global ocean, the phase speed changes by up to a factor of 5 and is typically in the region of 0.1 to 0.5 m s^{-1}, whilst both the internal wave amplitude and bottom layer thickness varies by a few orders of magnitude, typically 1 to 100m and 100 to 5000m. Using these values the bolus transport driven by an internal wave in the global ocean ranges from 0.00001 to 25 m^2 s^{-1}. We can limit these values to those typically seen in the shelf seas. Internal wave amplitudes are in the range 1 to 10 and bottom layer thickness in the range 10 to 100 m. The volume transport is then in the range 0.001 to 5 m^2 s^{-1}.

2.3.2 Derivation using continuous velocities and continuity

The same bolus transport, $\overline{u'h'}$, can be obtained from a depth-varying horizontal velocity in a strictly two layer ocean. The velocities will be derived using well established methods, such as in Simpson and Sharples [2012], which will then be used in a novel manner to derive the bolus transport, $\overline{u'h'}$. Here we take the interface displacement as

$$\zeta(x,t) = acos(kx - \omega t), \tag{2.22}$$

using Euler's formula, $e^{ix} = cos(x) + isin(x)$, and taking our solution as the real part allows us to write (2.22) as,

$$\zeta = Re(ae^{i(kx-\omega t)}), \tag{2.23}$$

where k is the wave number, x is the horizontal co-ordinate, ω is the angular frequency and t is time.

In order to solve this system we must make some simplifying assumptions. Firstly, we assume that we are working in an immiscible and inviscid ocean with a rigid boundary at the top and bottom. We also choose that each layer is irrotational so that there is a velocity potential function (Φ) such that its derivative is the velocity field, $u = \frac{\partial \Phi}{\partial x}$ and $w = \frac{\partial \Phi}{\partial z}$. Through volume conservation we require that the derivative of the velocity, or the second derivative of the velocity potential, is zero ($\nabla^2 \Phi = 0$), which is equivalent to the Laplace Equation. Now we define a separate velocity potential field for each layer, denoted by a subscript one, $0 < z < h_1$, and subscript two, $-h_2 < z < 0$, with zero defined as the mean position of the interface between the layers.

We need to find four boundary conditions and one initial condition for each layer. Two of these boundary conditions and the initial condition are behavioural, i.e. we require the solution to be periodic in the x direction and time. An additional boundary condition in each layer is requiring that the vertical velocity at the rigid boundaries goes to zero,

$$\frac{\partial \Phi_1}{\partial z}|_{z=h_1} = 0, \tag{2.24}$$

$$\frac{\partial \Phi_2}{\partial z}|_{z=-h_2} = 0, \tag{2.25}$$

Also, we set a dynamic boundary condition at the interface between the layers. Specifically, this consists of requiring that the displacement of the pycnocline, as set by equation (2.22), matches the vertical velocity, i.e. no fluid will cross the interface.

$$\frac{\partial \Phi_1}{\partial z}|_{z=0} = \frac{\partial \zeta}{\partial t}, \tag{2.26}$$

$$\frac{\partial \Phi_2}{\partial z}|_{z=0} = \frac{\partial \zeta}{\partial t}, \tag{2.27}$$

Now we can solve the Laplace Equation independently for each layer. Since we want the solutions to be periodic in the horizontal and time, the same as the interface displacement, we look for a solution of the form

$$\Phi_j = Re(Z_j(z)e^{i(kx-\omega t)}), \tag{2.28}$$

In order to avoid unnecessary clutter we will now drop the real part operator, Re, until it is applied in finding the velocity potential fields. By substituting equation (2.28) into the Laplace Equation, representing continuity, we obtain the second order differential equation for the vertical structure of the solution,

$$\frac{\partial^2 Z_j(z)}{\partial z^2} - k^2 Z_j(z) = 0, \tag{2.29}$$

which has two real roots, thus the general solution is of the form

$$Z_j(z) = C_j e^{kz} + D_j e^{-kz}, \tag{2.30}$$

where j is the layer index.

Now we can apply this to the equation (2.28) and substitute into the boundary conditions (Eqns. 2.24, 2.25, 2.26 and 2.27). This makes the four boundary conditions as follows

$$C_1 k e^{kh_1} - D_1 k e^{-kh_1} = 0, \tag{2.31}$$

$$C_2 k e^{-kh_2} - D_2 k e^{kh_2} = 0, \tag{2.32}$$

$$C_1 - D_1 = -\frac{ia\omega}{k}, \tag{2.33}$$

$$C_2 - D_2 = -\frac{ia\omega}{k}, \tag{2.34}$$

which we can now use to find the functions C_1, C_2, D_1 and D_2.

$$C_1 = \frac{ia\omega e^{-2kh_1}}{k(1 - e^{-2kh_1})}, \tag{2.35}$$

$$C_2 = \frac{ia\omega e^{2kh_2}}{k(1 - e^{2kh_2})}, \tag{2.36}$$

$$D_1 = \frac{ia\omega}{k(1 - e^{-2kh_1})}, \tag{2.37}$$

$$D_2 = \frac{ia\omega}{k(1 - e^{2kh_2})}, \tag{2.38}$$

which when substituted into into (2.30) for the top layer, j=1, yield,

$$Z_1 = \frac{ia\omega e^{-2kh_1} e^{kz}}{k(1-e^{-2kh_1})} + \frac{ia\omega e^{-kz}}{k(1-e^{-2kh_1})}, \tag{2.39}$$

if we now merge the fractions and multiply both the numerator and denominator by $2e^{-kh_1}$,

$$Z_1 = \frac{ia\omega}{k} \frac{(2e^{-kh_1})(e^{-2kh_1} e^{kz} + e^{-kz})}{(2e^{-kh_1})(1-e^{-2kh_1})}, \tag{2.40}$$

recalling that $sinh(x) = (1-e^{-2x})/(2e^{-x})$ allows the above equation to be written as,

$$Z_1 = \frac{ia\omega}{k} \frac{1}{sinh(kh_1)} \frac{e^{-2kh_1} e^{kz} + e^{-kz}}{2e^{-kh_1}}, \tag{2.41}$$

The last term can now be rearranged to show,

$$\frac{e^{-2kh_1} e^{kz} + e^{-kz}}{2e^{-kh_1}} = \frac{e^{k(z-h_1)} + e^{-k(z-h_1)}}{2} \tag{2.42}$$

Recalling that $cosh(x) = (e^x + e^{-x})/2$ and substituting into (2.28) gives,

$$\Phi_1 = Re(\frac{ia\omega}{k} \frac{cosh(k(z-h_1))}{sinh(kh_1)} e^{i(kx-\omega t)}), \tag{2.43}$$

and substituting in the Euler's formula, $e^{ix} = cos(x) + isin(x)$,

$$\Phi_1 = Re(\frac{a\omega}{k} \frac{cosh(k(z-h_1))}{sinh(kh_1)} (icos(kx-\omega t) - sin(kx-\omega t))), \tag{2.44}$$

Taking the real part then gives,

$$\Phi_1 = -\frac{a\omega}{k} (\frac{cosh(k(z-h_1))}{sinh(kh_1)}) sin(kx-\omega t), \tag{2.45}$$

The velocity potential for the second layer, j=2, can be obtained through a similar process giving,

$$\Phi_2 = \frac{a\omega}{k}(\frac{cosh(k(z+h_2))}{sinh(kh_2)})sin(kx-\omega t), \tag{2.46}$$

and the following equations for the horizontal and vertical velocities in each layer.

$$u_1 = -\frac{a\omega cosh(k(z-h_1))}{sinh(kh_1)}cos(kx-\omega t), \tag{2.47}$$

$$u_2 = \frac{a\omega cosh(k(z+h_2))}{sinh(kh_2)}cos(kx-\omega t), \tag{2.48}$$

$$w_1 = \frac{a\omega sinh(k(z-h_1))}{sinh(kh_1)}sin(kx-\omega t), \tag{2.49}$$

$$w_2 = -\frac{a\omega sinh(k(z+h_2))}{sinh(kh_2)}sin(kx-\omega t), \tag{2.50}$$

These show vertical velocities that are continuous between the two layers, with the sign matching the displacement of the interface, as expected (Fig. 2.4(b)). There are opposing horizontal velocities between the two layers, with the positive velocities co-located with the layer being thick (Fig. 2.4(a)).

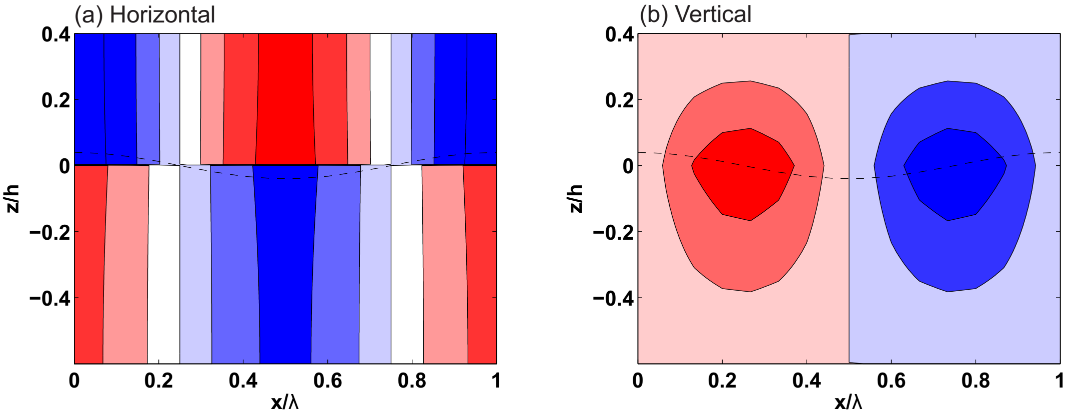

Figure 2.4: (a) Horizontal and (b) vertical velocities for a two layer internal wave for 10 m displacements in a water column with the surface layer 100 m thick and the bottom layer 150 m thick. Taken from Eqn. (2.47), (2.48), (2.49) and (2.50)

Now these previously published equations will be used in a novel manner to estimate the magnitude and direction of the bolus transport associated with an internal wave. As we know the displacement of the pycnocline (Equation 2.22) and the horizontal velocity field (Equations 2.47 and 2.48) the volume transport driven by the co-variance of layer thickness and velocity is given by solving the following equations,

$$\overline{u_1{}'h_1{}'} = \frac{1}{h_1\tau}\int_0^{\tau} -\zeta(\int_0^{h_1} u_1 dz)dt, \tag{2.51}$$

$$\overline{u_2'h_2'} = \frac{1}{h_2\tau}\int_0^{\tau} \zeta(\int_{-h_2}^{0} u_2 dz)dt, \tag{2.52}$$

which gives a persistent volume transport for the two layers as follows

$$\overline{u_1'h_1'} = \frac{a^2\omega}{2kh_1}, \tag{2.53}$$

$$\overline{u_2'h_2'} = \frac{a^2\omega}{2kh_2}, \tag{2.54}$$

which can be written as

$$\overline{u_i'h_i'} = \frac{ca^2}{2\overline{h_i}}, \tag{2.55}$$

where $c = \omega/k$ is the phase speed and i denotes the layer. This relationship for the bolus transport assuming continuous velocities is identical to the result given using the depth-integrated continuity equation (Eqn. 2.20). This is perhaps not surprising as most of the assumptions used in both methods are the same, for example no volume crossing the interface and a rigid lid and bottom, whilst the vertical shear of velocity within a layer is removed in the calculation of the bolus transport.

2.4 Comparison between bolus transport and Stokes' drift

2.4.1 Analytical Comparison

The average velocity following a moving parcel, the Lagrangian velocity, is given by the average velocity at a fixed position, the Eulerian velocity, plus the Stokes' drift velocity [Andrews and McIntyre, 1978]. The generic Stokes' drift for a propagating sinusoidal flow in a well mixed layer is given by $u_{Stokes} = u_0^2/(2c)$, where u_0 is the amplitude of the horizontal Eulerian velocity associated with the wave disturbance and $c = \omega/k$ is the wave speed. The Stokes' drift velocity and bolus velocity, $\overline{u_i' h_i'}/\overline{h_i'}$, are the same for shallow-water waves approaching the sea shore for simple geometries [Lee et al., 1997]: the velocity and thickness are in phase, providing a rectified transport towards the sea shore. For a simple two layer geometry, taking the amplitude of the wave velocity in each layer, $u_{0,i} = \omega a/(k\overline{h_i})$ from (2.18), provides an estimate of the Stokes' drift velocity averaged over each layer,

$$u_{Stokes,i} \equiv \frac{u_{0,i}^2}{2c} = \frac{ca^2}{2\overline{h_i}^2}, \tag{2.56}$$

which for this simple geometry is the same as the bolus velocity in each layer (2.20).

2.4.2 Particle Tracking

The bolus transport given above can also be compared to the Stokes' drift by tracking particles in the velocity fields given by Eqns. (2.47), (2.48), (2.49) and (2.50). It is important to note that these equations are derived assuming an infinitely long channel and thus there is no barrier to limit the transport or require a return flow. Particle tracking has been achieved using a 4th-order Runge-Kutta method to numerically integrate the velocity following the particles. The wave characteristics used have been selected to be similar to those expected for an M2 period internal tide slightly on-shelf of the shelf edge

(Table 2.1). Particles have been initialised at $1m$ vertical intervals throughout the water column. No particles have been initialised within $10m$ of the interface as this is the area affected by the small-wave assumption used above.

Table 2.1: Values used to calculate the velocity fields used in the particle tracking

Surface Thickness	h_1	50 m
Bottom Thickness	h_2	100 m
Wavelength	λ	35 km
Wave Period	τ	12.42 hr
Displacement Amplitude	a	10 m

The particles' tracks show the typical orbital movements associated with wave motions, over horizontal scales of order 100 to 1000 m with the surface layer showing larger excursions due to the stronger horizontal velocities in that layer (Fig. 2.5(a)). Whilst the primary feature of the particle tracks are these oscillatory motions it is clear that these do not close over a tidal cycle, leading to a particle being displaced from its initial position in the horizontal by 4263 m in the surface layer and 794 m in the bottom layer after 5 tidal cycles (Fig. 2.5(b)).

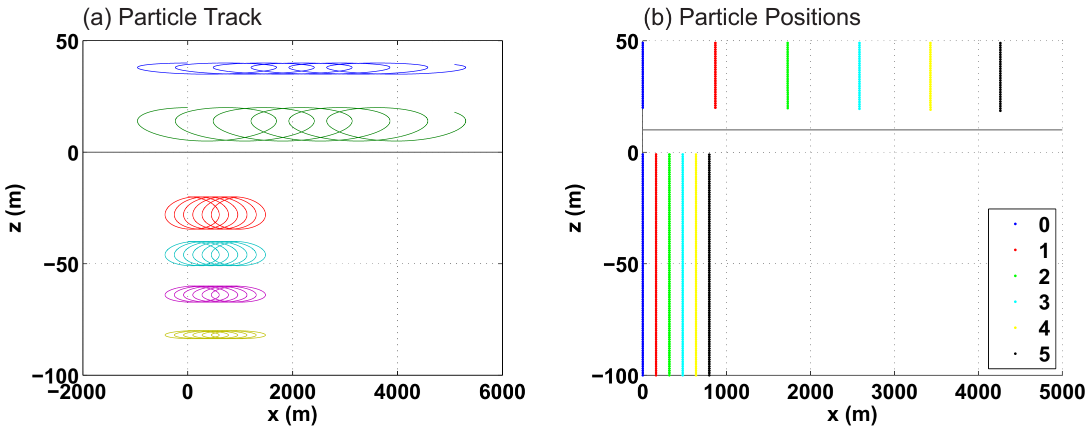

Figure 2.5: Particle tracking plots for a two layer internal wave showing (a) the tracks of selected particles throughout the water column and (b) the positions of all the particles at the start and after 1, 2, 3, 4 and 5 M2 periods

The average excursion of the particles in each layer has been taken and divided by 5 M2 periods to calculate the Lagrangian velocity of these particles. These velocities are then representative of the Stokes' drift experienced by these particles. In the surface layer the Lagrangian velocity of the particles is 1.9 cm s^{-1} whilst the bolus velocity is 1.6 cm s^{-1} and in the bottom layer these velocities are 0.35 cm s^{-1} and 0.39 cm s^{-1} respectively. The closeness of these two measures of the residual transport velocity indicate that, for the simple theoretical internal tide presented here, the Stokes' drift and bolus transport are very similar, supporting the analytical comparison made above.

Table 2.2: Comparison between the horizontal Lagrangian particle velocity calculated over 5 wave periods and the theoretical bolus velocity taken from Eqn. (2.20)

Layer	Particle Velocity (cm s^{-1})	Bolus Velocity (cm s^{-1})
Surface	1.9	1.6
Bottom	0.35	0.39

This equivalence may break down for more complicated geometries, more detailed stratification and different dynamical balances. Hence, the Stokes' drift velocity definition, $u_{0,i}^2/(2c)$ need not be the same as the bolus velocity, $\overline{u_i'h_i'}/\overline{h_i'}$. Thus, we view the bolus velocity as providing an important contribution to the Stokes' drift velocity.

2.5 Interaction between the barotropic and baroclinic tides

In addition to the baroclinic, two-layer, velocity, there is a one-layer barotropic tide with the same angular frequency. To account for this in the theory an additional term is added to the layer mean velocity given in Eqn. (2.18), here represented by $u_{baroclinic}$. The additional velocity has the same angular frequency as the internal tide, but with some phase shift (ϕ);

$$u_{depth-mean} = u_{baroclinic} + u_0 \sin(kx - \omega t + \phi) \tag{2.57}$$

where u_0 is the amplitude of the barotropic tidal velocity. We can then, in the same manner in section 2.3.1, calculate the volume transport for each layer associated with this more general velocity,

$$\overline{u_1 h_1} = \frac{a^2\omega}{2kh_1} - \frac{au_0}{2} cos(\phi) \tag{2.58}$$

$$\overline{u_2 h_2} = \frac{a^2\omega}{2kh_1} + \frac{au_0}{2} cos(\phi) \tag{2.59}$$

These equations are the same as for the purely baroclinic case, but with an additional term. This additional term has a sign dependent on the phase shift between the baroclinic and barotropic tides. This means that for the top layer with a phase shift $-90° < \phi < 90°$ the additional barotropic transport is in the opposite direction as the propagation of the wave, and for a phase shift $90° < \phi < 270°$ the additional barotropic transport is in the same direction to the wave propagation. Whilst the bottom layer shows a bolus transport of the same magnitude, but with the opposite sign. The opposing transports in the surface and bottom layers are a result of the fact that whilst the layer thicknesses variations, h_i', still have opposing signs in each layer the velocity variations driven by the barotropic tide have the same sign in each layer.

The relative importance of the term driven purely by the baroclinic thickness and velocity variations compared to the term driven by the baroclinic thickness variations and barotropic velocity variations can be neatly summed up by their ratio,

$$ratio = \frac{\frac{ca^2}{2h_i}}{\frac{au_0}{2}} = \frac{ca}{u_0 h_i} \tag{2.60}$$

where we have assumed a regime where the barotropic and baroclinic tides are in phase, which must be the case within half a wavelength of any location in the ocean. This maximises the effect of the barotropic-baroclinic interaction and thus this scaling gives the limit where the barotropic is most important, though locally the interaction could be significantly weaker. When this ratio is greater that 1 it means the baroclinic term dominates and when the ratio is less than 1 it indicates that the barotropic-baroclinic interaction is the primary driver of the bolus transport.

Take typical values for the phase speed (c) in the range 0.1 to 0.5 m s^{-1}, internal wave amplitudes (a) of 1 to 100 m, barotropic tidal velocity (u_0) 0.1 to 1 m s^{-1} and average bottom layer thickness (h_i) of 10 to 5000 m. These give an estimated ratio in the range $2x10^{-5}$ to 50 indicating that both regimes are likely to exist in the ocean. However, the barotropic interaction is dominant for more of the parameter space than the purely baroclinic term. Given the relatively small change in phase speed we can estimate the ratio on a global scale to be controlled, assuming mks units, by $ratio \approx a/(4u_0h_i)$ taking the phase speed fixed at 0.25 m s^{-1}. Focussing specifically on the region of the shelf sea close to the shelf break, we can treat the bottom layer thickness (h_i) as a constant 100 m, as a result of the fact it does not vary much in this region relative to the other terms. This leads to the ratio being reduced, again assuming mks units, to $ratio \approx= a/(400u_0)$. Now taking internal wave amplitudes (a) of 1 to 10 m and barotropic tidal velocity (u_0) 0f 0.1 to 1 m s^{-1} gives ratio range of $2.5x10^{-3}$ to 0.25 indicating that we would expect the bolus transport in the shelf sea to typically be dominated by the barotropic - baroclinic interaction although it is possible that there are some regions where values for the amplitude of the baroclinic tidal displacement and baroclinic tidal velocity are beyond the range considered here and the two terms are of approximately the same magnitude.

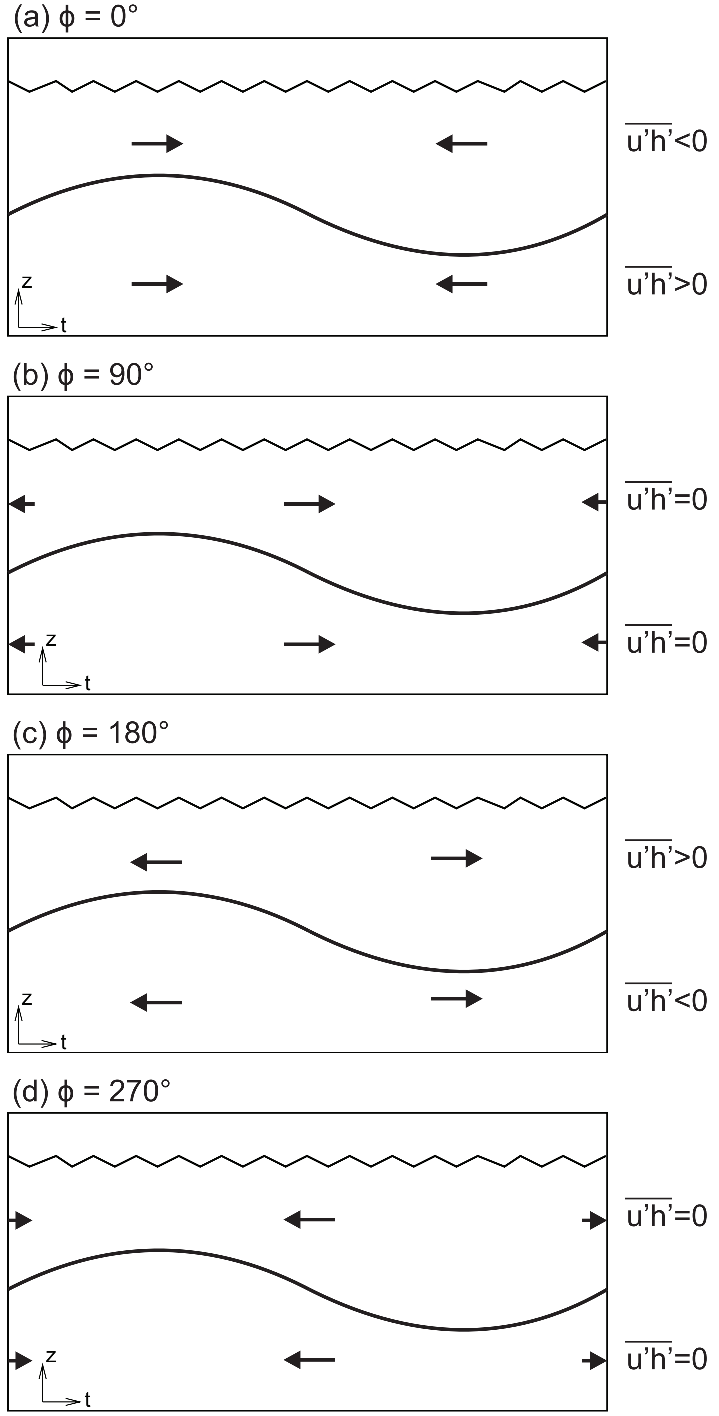

Figure 2.6: A schematic showing the interface displacement, barotropic velocity and associated bolus transport for (a) 0°, (b) 90°, (c) 180° and (d) 270° phase shift between the barotropic and baroclinic tides.

2.6 Spatial Pattern

Now we can now map an estimate of the volume transport for both the purely baroclinic and the baroclinic/barotropic interaction terms in the bottom layer. Here this has been done for North-East Atlantic, specifically the Celtic Sea, setting the wavelength and period to typical values for the internal tide for this region (35km and M2 respectively), using the GEBCO and WOA datasets for bottom layer thickness, the major axis of the M2 tide from POLCOMS model output for the barotropic velocity and setting the internal tide amplitude to decay linearly from the 200m isobath to reach zero at approximately 180km [Inall et al., 2011].

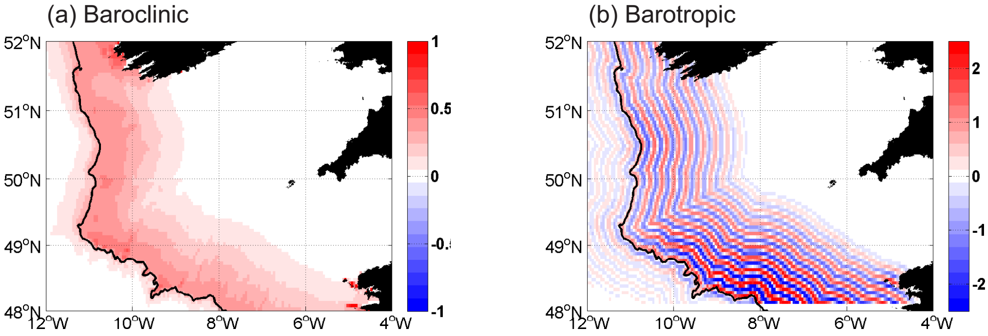

Figure 2.7: Maps showing the implied volume transport from the covariance of baroclinic tide thickness variations and (a) baroclinic tide velocity variations or (b) barotropic tide velocity variations. From Eqn. 2.59

The baroclinic and barotropic cases show very different spatial structure. The purely baroclinic case shows a positive, in the direction of propagation, transport in all locations, whilst the barotropic interaction case changes sign every half a wavelength from the shelf edge, assuming the barotropic tide occurs instantaneously over this length scale. The barotropic case tends to have a larger magnitude than the baroclinic, however due to the spatial structure it is unlikely to transport volume, and thus tracers, any considerable distance. Both of these transports are limited spatially by the decay of the internal tide away from the shelf edge. This means the bolus transport is unlikely to be important further on-shelf, but could play an important role in transporting volume and tracers away from the topographically controlled shelf edge.

2.7 Return of volume flux to the open ocean

On a shelf wide perspective this bolus transport onto the shelf at all locations, although with varying magnitude, must be balanced by an off shelf volume flux if the shelf seas are to maintain the same volume. This argument has been used previously to state that in an adiabatic model the cross slope volume transport is zero for all density classes at all locations [Wunsch, 1971, Ou and Maas, 1986]. One way of breaking the assumptions made in these models is to allow vertical mixing, effectively allowing volume to change its density class on the shelf. A further potential way of allowing a cross slope volume transport is to break the uniform along-shelf assumption. Relaxing this uniform assumption would allow an on-shelf transport at one location which is then balanced by an off-shelf transport at another location.This case is analogous with a rip current on a beach, where the on-beach transport of volume by waves in most locations is balanced by a strong local off-beach transport at a different location.

Whilst a wide range of processes could be driving an off-shelf volume transport we consider four simplified choices of the return flow.

(1) The first is the case discussed above, with limited mixing and along shelf transport, where the on-shelf transport is balanced by a local return transport of the same magnitude in each layer (Fig. 2.8(a)). This results in a zero net across shelf transport in all layers.

(2) The along slope transport is still small, but mixing allows volume to move between density classes on the shelf, here represented by a depth-mean return flow applied where the water column is well mixed (Fig. 2.8(b)). In this case the depth-integrated transport is still zero, but allows volume to change

density whilst on-shelf allowing the layers to have transports of equal magnitude but with opposing directions. This allows a convergence or divergence of tracers on the shelf if the two layers have different values for the selected tracer.

(3) and (4) A non-local return where, thinking about a 2D section running across the shelf, the volume is transported onto the shelf at the open ocean boundary and then is transported along the shelf and out of the section (Fig. 2.8(c) and (d)). This can further be separated into a case where mixing is small and the lateral transport is the same magnitude as the on-shelf transport in each layer (Fig. 2.8(c)) or the case where mixing is large and the lateral transport occurs in the well mixed region beyond the tidal mixing front (Fig. 2.8(d)). Again both of these cases allows the convergence or divergence of tracer in our 2D section where there is an across shelf gradient in the tracer.

(a) Local layered return

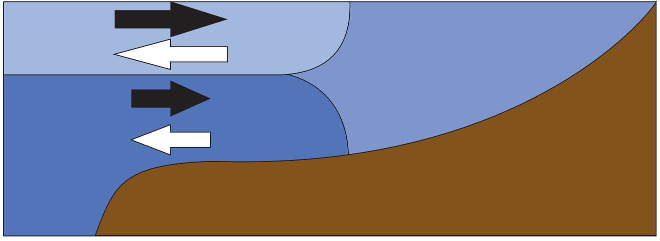

(b) Local depth mean return

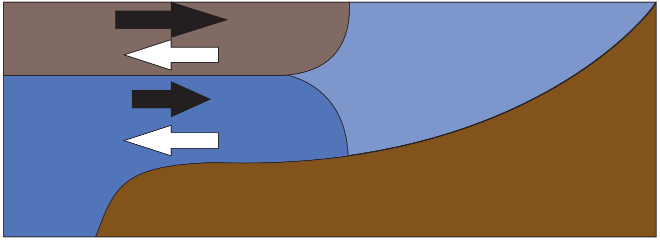

(c) Non-local layered return

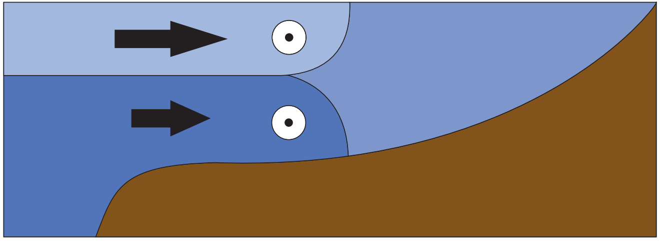

(d) Non-local depth mean return

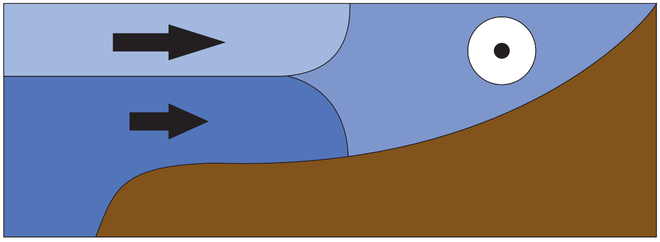

Figure 2.8: Schematics of the four possible return scenarios: (a) the case where mixing is small and domain is uniform in the along shelf direction; (b) the case where mixing is large and domain is uniform in the along shelf direction; (c) the case where mixing is small and the along shelf uniformity is relaxed; and (d) the case where mixing is large and the along shelf uniformity is relaxed. The black arrows indicate the bolus transport onto the shelf and the white arrows indicate the balancing volume flux.

2.8 Summary

- It is useful to consider the ocean as consisting of multiple layers where the properties and velocity of the water in that layer are broadly the same. These layers are often defined in density space. In the shelf seas, where the pycnocline tends to be thin,we can usefully think of the ocean as consisting of a less dense surface layer overlying a more dense bottom layer.

- The volume transport (m^2s^{-1}) in a layer is defined as the product of the thickness of the layer (m) and the velocity in that layer (ms^{-1}). The thickness and velocity in the layer can then be separated into time-mean and time-varying components. When this transport is time averaged there are two contributions, one from the time-mean velocity and another from co-variance of the time-varying thickness and velocity. This is usually referred to as the bolus transport or can be viewed in terms of a representative bolus velocity, dividing by the time-mean layer thickness.

- This bolus transport makes a contribution to the Stokes' Drift, with the other contribution being the effects of vertical shear. When considering well mixed layers where the velocity does not change in the vertical the shear contribution is small. This is the assumption we will be using initially within this thesis, although we will discuss the role of shear in Chapter 6.

- 2D propagating internal waves show in phase variations in layer thickness and velocity for both the bottom and surface layers. This bolus transport, driven by a linear internal wave, is given by $ca^2/2\overline{h_i}$ where i is the layer. This bolus transport is always directed in the direction of propagation of the wave for both the surface and bottom layer. This transport, when written as the bolus velocity $ca^2/2\overline{h_i}^2$, is identical to the Stokes' drift for this simple case without considering a return flow. This suggests that, if the internal tide propagates in the on-shore direction a significant distance [Inall et al., 2011], there would be a transport of volume from the open ocean onto the shelf.

- There is an additional term when the barotropic tide is added to the baroclinic tide. The sign of this term changes as the phase difference between the barotropic and baroclinic tides changes leading to a highly spatially variable structure. The depth-integrated bolus transport for this interaction is zero as the surface and bottom layers have opposing signs.
- The purely baroclinic term is generally smaller than the term given by the interaction of barotropic and baroclinic tides however is far less spatially variable so is likely to lead to a greater transport of tracers a significant distance onto the shelf.
- On a shelf wide scale, this bolus transport must be returned to the open ocean. In the simplest models the cross shelf exchange is zero for all density classes, however these models make a number of assumptions that may not apply in the real ocean. Relaxing these assumptions gives us four possible return scenarios. These are: (1) the return in the same location and the same density class; (2) the return in the same location but with volume having been exchanged between density classes; (3) return at a different location but in the same density classes; and (4) return at a different location and with volume having changed density class. Scenarios (2), (3) and (4) could all result in a convergence, or divergence, of tracer on the shelf.
- In the next chapter we use a number of mooring datasets to test if this process is taking place, if this theory provides a reasonable estimate of the magnitude, the direction of this transport and to try and identify the

nature of the return transport.

Chapter 3

Shelf-Edge Observations of Bolus Transport

3.1 Aims of this chapter

The aim of this chapter is, using observational data, to (i) identify whether there is a systematic bolus transport near the shelf edge and the dominant periods involved; (ii) identify how the strength and direction of the bolus transport varies spatially, both in an on-off shelf and along shelf direction; (iii) consider how well the two layer/mode one simplification works for these moorings; (iv) consider the role of locally generated internal tides on the shelf; and (v) identify if this volume flux is balanced locally.

This is achieved by calculating the various contributions to the volume transport from a series of moorings close to the shelf break and near an internal tide generating bank. These contributions are the bolus, $\overline{u_i' h_i'}$, and mean, $\overline{u}\overline{h}$, transport. These are then further broken up into contributions driven by the barotropic (depth-mean) and baroclinic (depth-varying) velocities. In total eight moorings are analysed across four locations, specifically the New Zealand shelf break, the Malin shelf break, the Celtic Sea shelf break and a bank in the Celtic Sea. We have assumed that in the shelf seas the water column can reasonably be approximated as consisting of two well-mixed layers separated by a thin pycnocline. These cases represent a range of regimes in terms of:

- the orientation of the shelf break, open ocean to the west for the Celtic Sea and Malin Shelf and to the east for New Zealand
- the strength of the internal tide, strong relative to other processes at the New Zealand shelf and Celtic Sea whilst weak at the Malin Shelf
- complexity of topography, smooth at the New Zealand shelf and Malin Shelf and more complex in the Celtic Sea
- internal tides generated at the shelf edge or an on-shelf bank, shelf edge for the New Zealand shelf, Malin shelf and Celtic sea shelf edge cases and an on-shelf bank in the Jones Bank case.

A subset of the analysis for each mooring is presented here with a full set of figures for each mooring available in the appendix. There are also a range of other processes that could be contributing to the bolus transport in these moorings, including but not limited to geostrophic eddies, surface waves and tides, and higher frequency internal waves.

3.2 Method of Analysis

3.2.1 Split into layers and trim time-series

The water column is partitioned into two layers with thicknesses, h_i, separated by a density interface defined by the zero crossing of the first baroclinic mode. This zero crossing is obtained by solving the eigenvalue problem from linear wave theory using the time-mean density structure observed at the mooring [Gill, 1982, MacKinnon and Gregg, 2003] using the Matlab tool developed by Klink [1999]. Whilst the modal structure changes when using the time-mean density profile, as opposed to a series of instantaneous density profiles, the position in density space of the zero crossing does not change significantly. The layer thicknesses are then calculated as the distance between the deepest observation and this density surface or the density surface and the upper most observation for the bottom and top layers respectively.

All the observational data sets used are trimmed at the end such that the remaining time-series are an integer number of M2 periods (12.42 hours) long. This is done in order to avoid any contribution to the transports from a truncation of the tidal cycle.

3.2.2 Baroclinic/Barotropic Split

The contributions to the bolus transport driven by the baroclinic and barotropic tides are separated by splitting the instantaneous velocity profiles into the baotropic and baroclinic velocities. The barotropic velocity is diagnosed as,

$$\mathbf{u}_{barotropic} = \frac{1}{h_{full}} \int_0^{h_{full}} \mathbf{u}\, dz \ , \tag{3.1}$$

where $\mathbf{u}$ is the velocity vector, z is now defined as positive upwards with $z = 0$ at the bed and h_{full} is the full depth of the water column. The baroclinic velocity is taken as the departure from the barotropic velocity,

$$\mathbf{u}_{baroclinic} = \mathbf{u} - \mathbf{u}_{barotropic}, \tag{3.2}$$

3.2.3 Layer Averaging

The baroclinic velocity time-series for each layer is then given by depth averaging the baroclinic velocities between the bed and the isopycnal or the isopycnal and the surface, in the same manner as the calculation of the layer thicknesses set out above.

$$\mathbf{u}_{baroclinic1} = \frac{1}{h_1} \int_{h_2}^{h_{full}} \mathbf{u}_{baroclinic}\, dz \ , \tag{3.3}$$

and,

$$\mathbf{u}_{baroclinic2} = \frac{1}{h_2} \int_0^{h_2} \mathbf{u}_{baroclinic}\, dz \ , \tag{3.4}$$

This leaves us with five time-series to consider: the layer thicknesses (h_1 and h_2), the barotropic velocity ($\mathbf{u}_{barotropic}$), and the layer averaged baroclinic velocities ($\mathbf{u}_{baroclinic1}$ and $\mathbf{u}_{baroclinic2}$).

3.2.4 Split into time-mean and bolus contributions

Each of the times series are now decomposed into their time-mean and time-varying components, $\mathbf{u}_i = \overline{\mathbf{u}}_i + \mathbf{u}'_i$ and $h_i = \overline{h}_i + h'_i$, where the overbar indicates a time mean and the prime indicates the deviations from this time mean. The bolus ($\overline{u'h'}$) and time-mean ($\overline{h}\overline{u}$) transports are then calculated using these decomposed time-series.

In addition to the full time-series, derived as explained above, we will consider the bolus transport having excluded the contribution to the bolus transport from high frequency variability. This is achieved by applying a low-pass Butterworth filter [Roberts and Roberts, 1978], with a 7 hour cut off, to the time series of thickness and layer averaged velocity.

3.2.5 Integral Constraint on baroclinic transport

These definitions introduce a constraint on the depth-integrated baroclinic transport.

The instantaneous transport for the surface layer is,

$$\int_{h_2}^{h_{full}} \mathbf{u}\; dz = h_1 \mathbf{u}_{barotropic} + \int_{h_2}^{h_{full}} \mathbf{u}_{baroclinic}\; dz, \tag{3.5}$$

and for the bottom layer,

$$\int_{0}^{h_2} \mathbf{u}\; dz = h_2 \mathbf{u}_{barotropic} + \int_{0}^{h_2} \mathbf{u}_{baroclinic}\; dz, \tag{3.6}$$

The depth-integrated transport then becomes the sum of these two equations (Eqns. 3.5 and 3.6),

$$\int_0^{h_{full}} \mathbf{u}\, dz = h_2 \mathbf{u}_{barotropic} + \int_0^{h_2} \mathbf{u}_{baroclinic}\, dz + h_1 \mathbf{u}_{barotropic} + \int_{h_2}^{h_{full}} \mathbf{u}_{baroclinic}\, dz, \tag{3.7}$$

which can then be simplified to,

$$\int_0^{h_{full}} \mathbf{u}\ dz = h_{full} \mathbf{u}_{barotropic} + \int_0^{h_{full}} \mathbf{u}_{baroclinic}\ dz, \tag{3.8}$$

Recalling the definition of the baroclinic transport (Eqn. 3.1 and 3.2) we can show that that,

$$\int_0^{h_{full}} \mathbf{u}_{baroclinic}\ dz = 0, \tag{3.9}$$

Using equations 3.8 and 3.9 we can show that the depth-integrated transport becomes,

$$\int_0^{h_{full}} \mathbf{u}\ dz = h_{full} \mathbf{u}_{barotropic}, \tag{3.10}$$

showing that only the barotropic velocity makes a contribution to the depth-integrated transport and that the transport to which the baroclinic velocity contributes is zero.

3.2.6 Transport Definitions

Throughout this chapter we will be using the bolus transport to refer to the time-mean of the bolus contribution, i.e. $\overline{u'h'}$, and time-mean transport to refer to the contribution driven by the time-mean velocity, i.e. $\overline{u}\overline{h}$. When referring to the bolus transport prior to the time-mean, i.e. $u'h'$, we will use the instantaneous bolus transport. When talking about the depth-integral we are refering to the sum of the transports in the top and bottom layer, i.e. the depth-integrated bolus transport is $\overline{u_1'h_1'} + \overline{u_2'h_2'}$. Finally, the total transport is the sum of the bolus and time-mean transports, $\overline{u'h'} + \overline{u}\overline{h}$.

3.3 New Zealand - NZ

This is a regime where the shelf break runs North-West to South-East with the open ocean to the east, the internal tide is strong relative to other processes, the topography is smooth and the internal tide is generated at the shelf break. One mooring was located off the North East coast of New Zealand near the shelf edge ($35°44.76'S, 174°43.59'E$). This mooring was deployed for approximately 7 days in 110 m of water in November and December 1998.

3.3.1 Mooring Details

This mooring consisted of a bed-mounted (5 metres above the bed) 500 kHz ADCP sampling every minute. There was also a string of 10 temperature loggers through the water column, with a 10 metre separation, also sampling every minute [Sharples et al., 2001]. The temperature and velocity data were both linearly interpolated onto a 1 minute x 5 metre resolution grid. There were no salinity instruments on the mooring so the salinity has been taken as constant from a single CTD station near the mooring location. The water column was stratified throughout the time-series, although the stratification was weakened by a strong wind mixing event midway through the time series. There is a strong internal tide (Fig. 3.1a), which is modified by the weakening stratification [Sharples et al., 2001].

3.3.2 Is there a bolus transport and what is its temporal signature?

On the New Zealand shelf there is a strong mode-1 dominated internal tide, with the position of the isopycnal moving through a large percentage of the water column. (Fig. 3.1). This mode-1 internal tide drives features similar to those expected from our schematic understanding, with the layers being thick when the velocity is in the direction of the mean bolus transport (the red colours in Fig. 3.1(b)). There are also higher frequency internal waves superimposed

(a) Potential Density (kg/m^3)

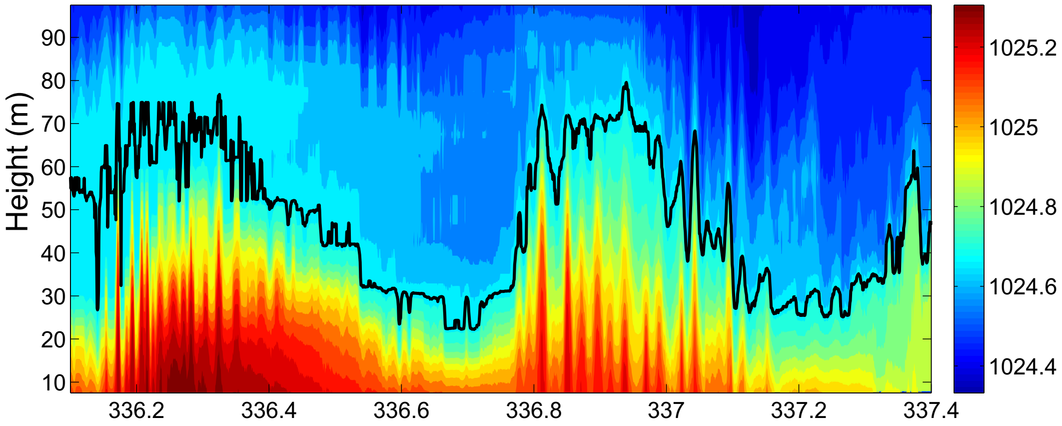

(b) Baroclinic Velocity (m/s)

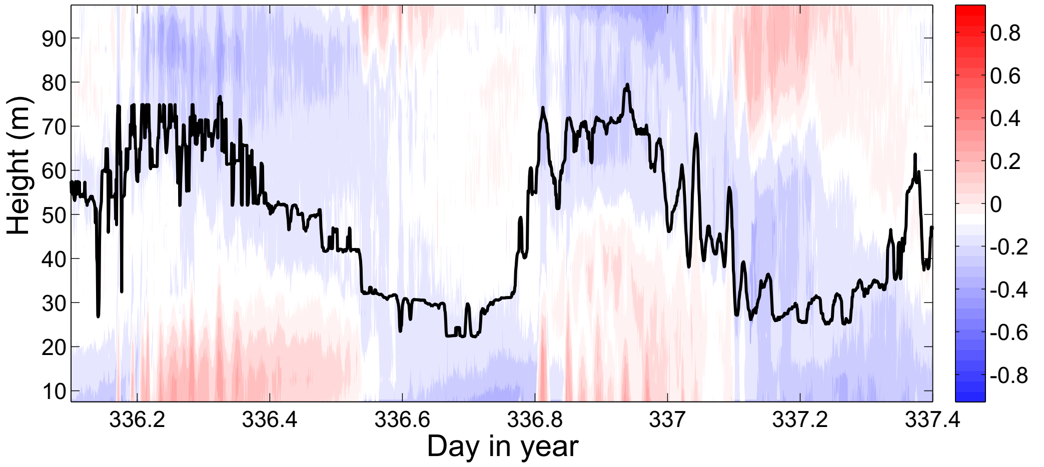

Figure 3.1: Sections of (a) Potential Density and (b) the Baroclinic velocity in the across shelf direction for mooring NZ on the New Zealand shelf. The black line indicates the isopycnal used to separate the surface and deep layers.

on the internal tide signal. The baroclinic velocities reach up to ± 0.8 ms^{-1} however these are where the internal tide is reinforced by the high frequency internal waves and the magnitude of the signal associated with the internal tide is typically a few cm s^{-1}.

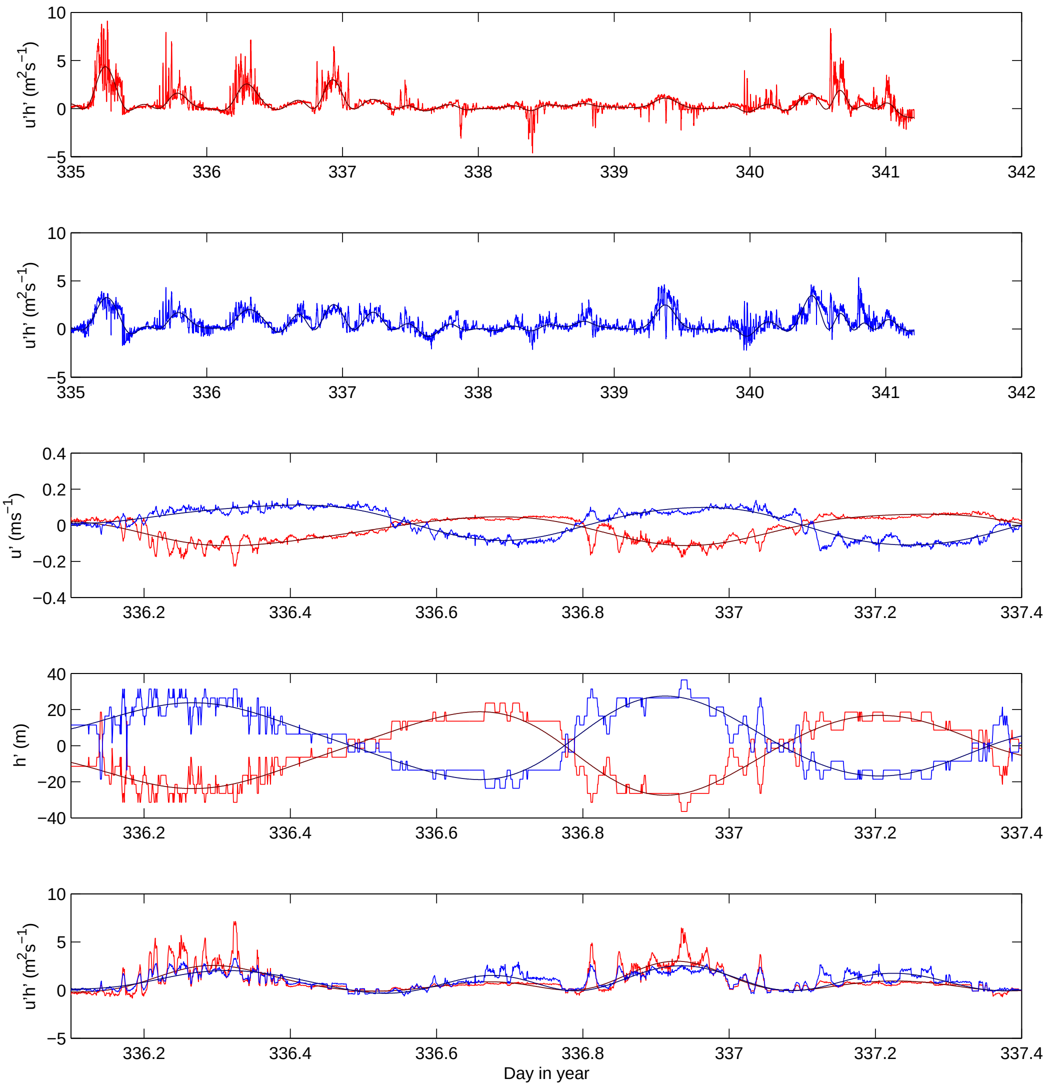

Figure 3.2: Time series from mooring NZ on the New Zealand shelf of (a and b) the full record of instantaneous bolus transport for the surface and bottom layers respectively and (c) the velocity perturbations, (d) thickness perturbations and (e) the bolus transport for a selected day. The lighter lines are the full observations and the dark lines are using the 7 hour low pass filtered time series of thickness and velocity.

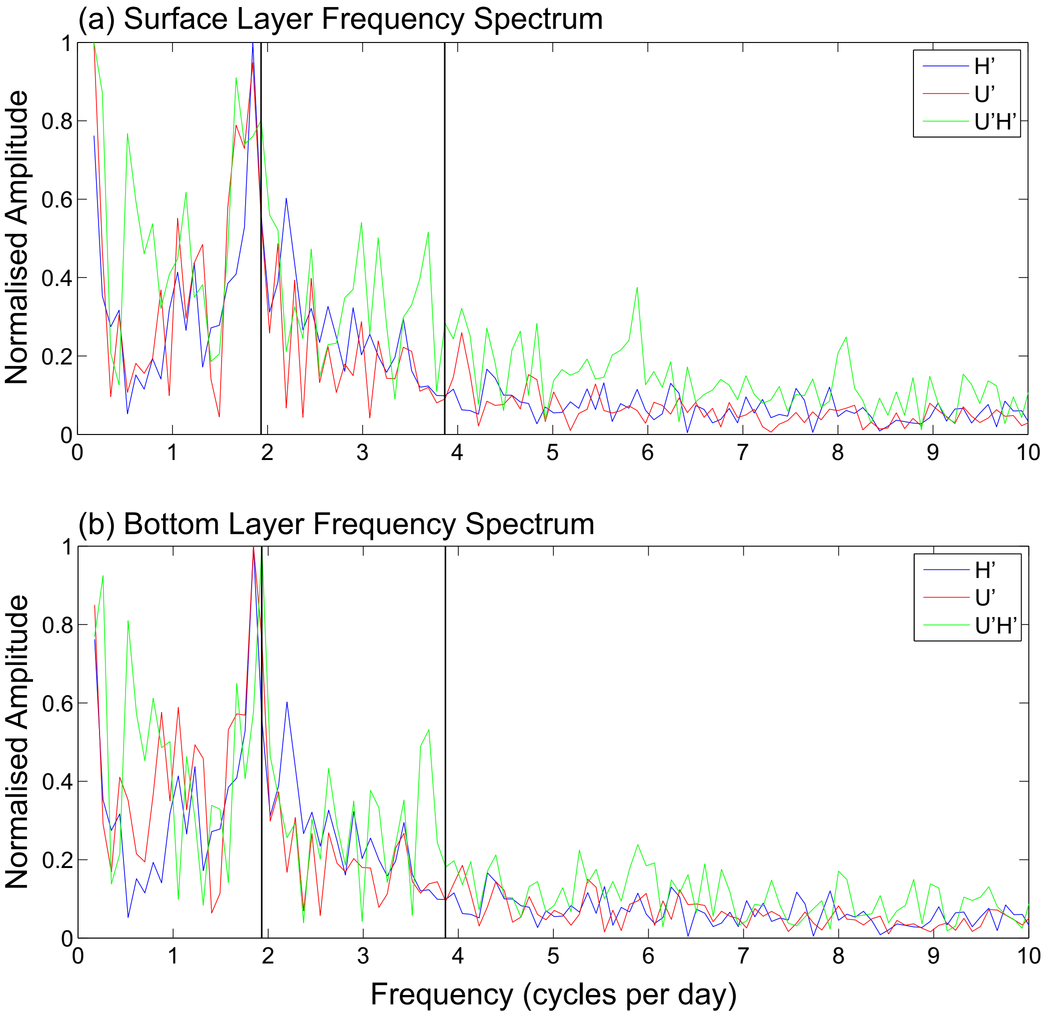

Figure 3.3: Frequency spectra from mooring NZ on the New Zealand shelf for (blue) thickness perturbations, (red) velocity perturbations and (green) bolus transport for (a) the surface and (b) the bottom layer.

The layer thickness and layer averaged baroclinic velocities both show M2 period variability, typical for an regime where the internal tide is large relative to other processes (Fig. 3.2(c and d)). The layer thickness perturbations show the same magnitude but opposite signs in each layer, which is necessarily the case when considering a water column with a fixed top and bottom boundary. The baroclinic velocity perturbations also show a similar magnitude but opposite signs between the layers, typical for a mode-1 dominated regime. These signals are also clear when the time series are converted into frequency space with both the surface (Fig. 3.3(a)) and bottom (Fig. 3.3(b)) showing a relatively noisy signal but with a clear peak in amplitude at the M2 frequency.

For a typical day during the period when the internal tide is more energetic, the velocity, in the direction of the mean bolus transport, varies by $\pm$ 0.1 m s^{-1} (3.2c) and the thickness varies by $\pm$ 20 m (3.2d) leading to peaks in bolus transport of 2 m^2 s^{-1} (3.2e) and a mean bolus transport of 1 m^2 s^{-1}.

In each layer these two M2 period signals are in phase (Fig. 3.2(c and d)). This is in line with the expectations from the theory and we would expect to see an M4 period signal in the resultant instantaneous bolus transport (Fig. 2.3). This is the case for both the surface and the bottom layers although the signal is not as clear as the M2 period in the component parts (Fig. 3.2(e) and Fig. 3.3). There is also a large M2 period in the instantaneous bolus transport signal in both the surface and bottom layers (Fig. 3.3) with the instantaneous bolus transport being a factor of two larger when the thermocline is elevated (Fig. 3.2(d and e)). This asymmetry is larger in the surface layer than the bottom. This could indicate that we are seeing waves of elevation propagating through the regime rather than a wave with equal elevation and depression.

3.3.3 Is this volume flux returned locally?

The direction and relative magnitude of the various terms driving the total transport will now be explored. The baroclinic bolus transport is directed onto

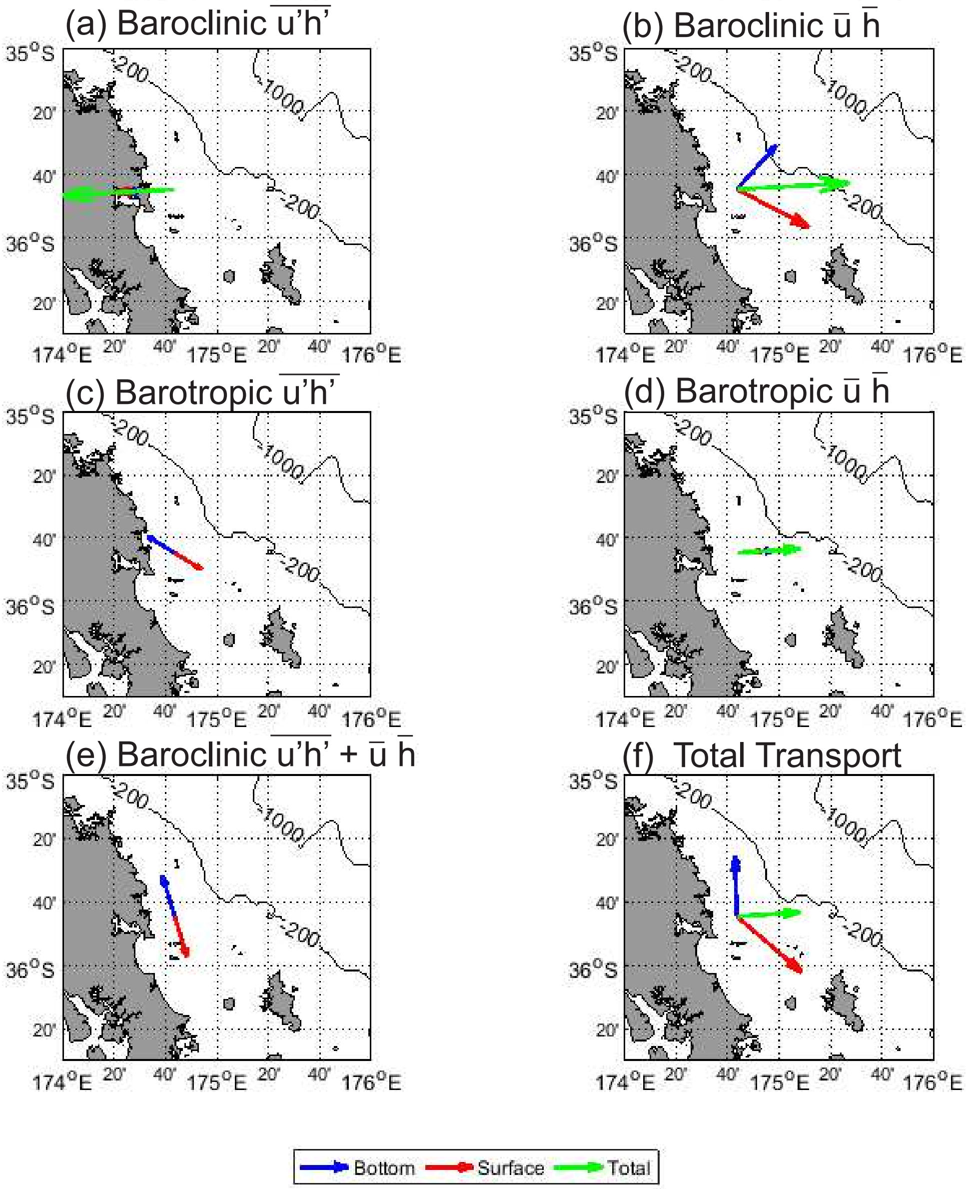

Figure 3.4: Plots showing the direction and relative magnitude of (a) the bolus transport driven by the baroclinic velocities, (b) the mean transport driven by the baroclinic velocities, (c) the bolus transport driven by the barotropic velocities, (d) the mean transport driven by the barotropic velocities, (e) the total, bolus plus mean, transport driven by the baroclinic velocities and (f) the total transport driven by both the baroclinic and barotropic velocities for the New Zealand shelf moorings.

the shelf, to the west, in both the surface and bottom layers. The bolus transport is larger in the relatively thin bottom layer (Fig. 3.4). This is consistent with our theoretical understanding where the baroclinic velocity, and thus the bolus transport, is scaled by the reciprocal of the layer thickness. This leads to a depth-integrated bolus transport also in the same direction and larger than either of the layer transports (Fig. 3.4(a)). The baroclinic time-mean flow has a more complicated depth structure with the bottom layer being directed to the North-East and the surface layer transport being to the South-East (Fig. 3.4(b)). The depth integrated baroclinic time-mean transport is to the East, opposed to the baroclinic bolus transport. The magnitude of the transport is slightly larger in the surface layer than the bottom with a depth-integrated time-mean transport larger than either of the individual layers.

The barotropic bolus transport is directed to the North-West in the bottom layer and to the South-East in the surface layer. These two transports are of equal magnitude and are directed in exactly opposing directions, leading to a zero depth-integrated bolus transport (Fig. 3.4(c)). This is consistent with our theoretical understanding for the barotropic bolus transport (Section 2.5). The barotropic mean transport is in the same direction in both layers, which is required by defining the barotropic velocity as not varying in depth, and is scaled by the mean layer thickness resulting in the surface layer having a larger transport than the bottom layer. In this case the barotropic transport is directed off shelf, to the East (Fig. 3.4(d)).

The total contribution to the transport from the baroclinic velocities, the addition of the baroclinic bolus and baroclinic time-mean terms, shows two opposing layers of equal magnitude, leading to zero depth-integrated transport of volume. The surface layer is directed to the north, whilst the bottom layer is to the south, with both approximately parallel to the depth contours indicating that the total baroclinic contribution to exchange of volume between the shelf and the open ocean is small.

The total depth-integrated volume transport at this mooring is identical to the depth integrated barotropic time-mean transport (Fig. 3.4(d and f)). This is a result of the fact that the barotopic bolus transport (Fig. 3.4(c)) and the total baroclinic transport both depth integrate to zero (Fig. 3.4(e)). The surface layer total transport is to the north whilst the bottom transport is to the south-east with the two having similar magnitude however they do not exactly cancel. Many of these features are present throughout the following moorings, although each mooring helps provide a more complete understanding of the baroclinic process and allows us to answer the questions posed in the opening of this chapter.

3.3.4 Summary for the New Zealand shelf

- Observational support for a two layer system with an onshore bolus transport/(schematic in Fig. 2.6(b)). The baroclinic horizontal velocity only shows small vertical variability within each layer relative to the shear at the interface. The sign of the velocity changes in phase with the variations in the position of the pycnocline.

- These variations in velocity and layer thickness occur with an approximately M2 period, although there are also higher frequency signals superimposed on this signal. Removing these higher frequency signals results in only a small change in the bolus transport.

- In the instantaneous bolus transport timeseries, there is a M4 period in both layers, as expected from the product of two in phase M2 period signals. There is also a M2 period signal, more prominent in the surface layer, with the bolus transport being larger when the thermocline is elevated relative to the depressed phase.

- The baroclinic bolus transport is in the same direction in both layers, with the bottom layer showing a larger transport than the surface layer.

- The depth-integrated baroclinic time-mean transport is in the opposite direction to the baroclinic bolus transport. When these two terms are added together the depth-integrated baroclinic transport is zero with the two layers showing opposing transport of equal magnitude. These two transports are parallel to the shelf edge indicating little exchange between the shelf and open ocean.

- The barotropic bolus transport results in two opposing layers, in agreement with the theory presented in Section 2.5.

- The barotropic mean transport is large and, by definition, in the same direction in all layers. This term makes the only non-zero contribution to the total depth integrated transport, although the individual layers have a response controlled by all the of the terms.

- Many of the features in the direction of the barotropic transport are replicated for the moorings that follow and make a limited contribution to answering the questions set out at the start of this chapter. As such the barotropic transport will only be considered briefly for the following moorings.

3.4 Jones Bank - MS1, MS2 and MS3

This is a regime where the internal tide is generated from an on-shelf bank leading to a strong internal tide relative to other processes. The layout of the moorings allows us to consider how the bolus transport varies near the generation zone. Three moorings were located on the slope of Jones Bank in the Celtic Sea: MS1, MS2 and MS3. These formed a line running from the top to the base of the slope with MS1 located furthest on-bank and MS3 located furthest off bank. MS1 was deployed for approximately 19 days in 78 m of water at $49°51.25'N, 7°56.94'W$. MS2 was deployed for approximately 18 days in 114 m of water at $49°53.90'N, 7°52.57'W$. MS3 was deployed for approximately 19 days in 122 m of water at $49°56.40'N, 7°49.00'W$.

3.4.1 Mooring Details

The mooring at MS1 consisted of a bed mounted ADCP and a string of CTD's and temperature loggers.. There were two CTD's located at the surface and the bottom and 26 temperature loggers between the bed and the surface with variable spacing, between 5 and 2 metres.

The mooring at MS2 consisted of a bed mounted ADCP and a string of CTD's and temperature loggers.. There were three CTD's located at the surface, 54 metres and the bottom and 39 temperature loggers between the bed and the surface with variable spacing, between 5 and 2 metres.

The mooring at MS3 consisted of a bed mounted ADCP and a string of CTD's and temperature loggers.. There were two CTD's located at the surface and the bottom and 30 temperature loggers between the bed and the surface with variable spacing, between 10 and 2 metres.

Full water column profiles of salinity were constructed from the 2 - 3 CTDs deployed at each location and used to calculate the density. All measurements were then linearly interpolated onto coincident 5 minute x 2 metre resolution grids for mooring MS1 and MS2 and a 5 minute x 4 metre grid for MS3. This difference in grids is used so that the vertical resolution of the grid matches the vertical resolution of the velocity data. Unfortunately the ADCP's at all three moorings failed part way through the deployment leading to useful data only being available for between 7 and 8 days.

3.4.2 Is there a bolus transport and what is its temporal signature?

The moorings at Jones bank show an exceedingly strong internal tide, with the displacements of the pycnocline taking up a large percentage of the water

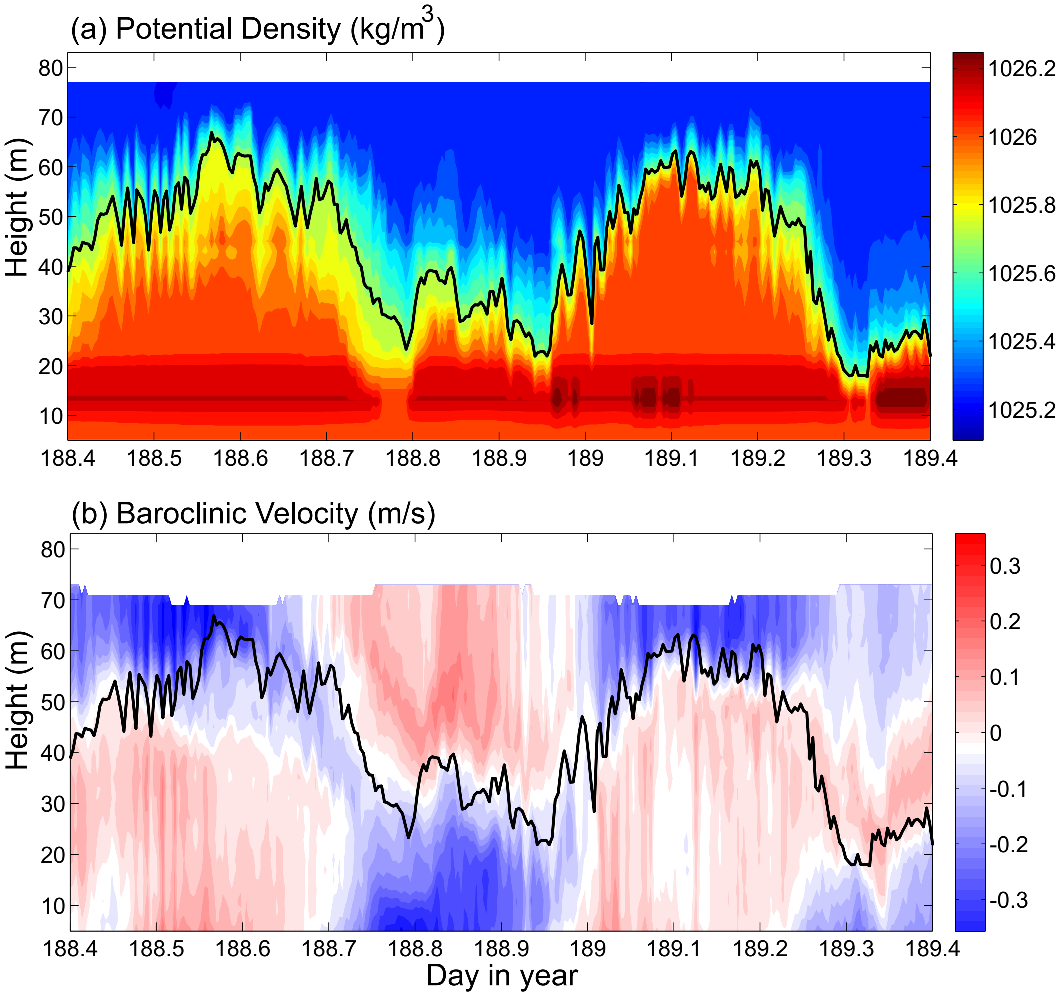

Figure 3.5: Sections of (a) Potential Density and (b) the Baroclinic velocity in the direction of the Baroclinic energy flux for mooring MS1 on the Jones bank. The black line indicates the isopycnal used to separate the surface and deep layers.

column, at MS1 the isopycnal selected for this analysis moves from 20m to 70m above the bed in only 78m water depth (Fig. 3.5(a)). These large vertical displacements of the pycnocline lead to strong horizontal baroclinic velocities typically ±20 - 30 cm s^{-1}, with little vertical shear within each layer but with a sign change in the pycnocline. This is typical of a mode-1 internal tide as discussed in Chapter 2. This internal tide is no longer one generated at the shelf edge but one generated by the barotropic tide interacting with local topography.

Both layers at mooring MS1 show in phase variations in layer thickness and horizontal baroclinic velocity (Fig. 3.6(c and d)) with an M2 period (Fig.3.7). These in phase variations lead to the instantaneous bolus transport being positive for the majority of the time series (Fig. 3.6(a and b)) and having the M4 period characteristic of an internal tide driven transport (Fig. 3.6(e) and 3.7).

3.4.3 How does the bolus transport vary between the moorings?

The bolus transport is directed to the north-east in all three moorings on Jones bank. The difference in direction between the two layers is larger than in some of the other moorings, with the bottom layer to the left of the depth integrated transport at MS1 and the bottom layer to the right of the depth integrated transport for the other two moorings. All three moorings show depth-integrated bolus transports of similar magnitude: 1 m^2s^{-1} for MS1; 0.7 m^2s^{-1} for MS2; and 1.5 m^2s^{-1} for MS3. This, in addition to the limited directional differences between the moorings, indicates that they are sampling the same internal tide and the bolus transport does not decay rapidly as the internal tide propagates.

3.4.4 Is this volume flux returned locally?

As with the New Zealand mooring, the depth integrated baroclinic time-mean transport (green in Fig. 3.8 (d), (e) and (f)) is in the opposite direction to the baroclinic bolus transport. Once again the total baroclinic transport shows two opposing layers of equal magnitude. These layers are directed approximatly

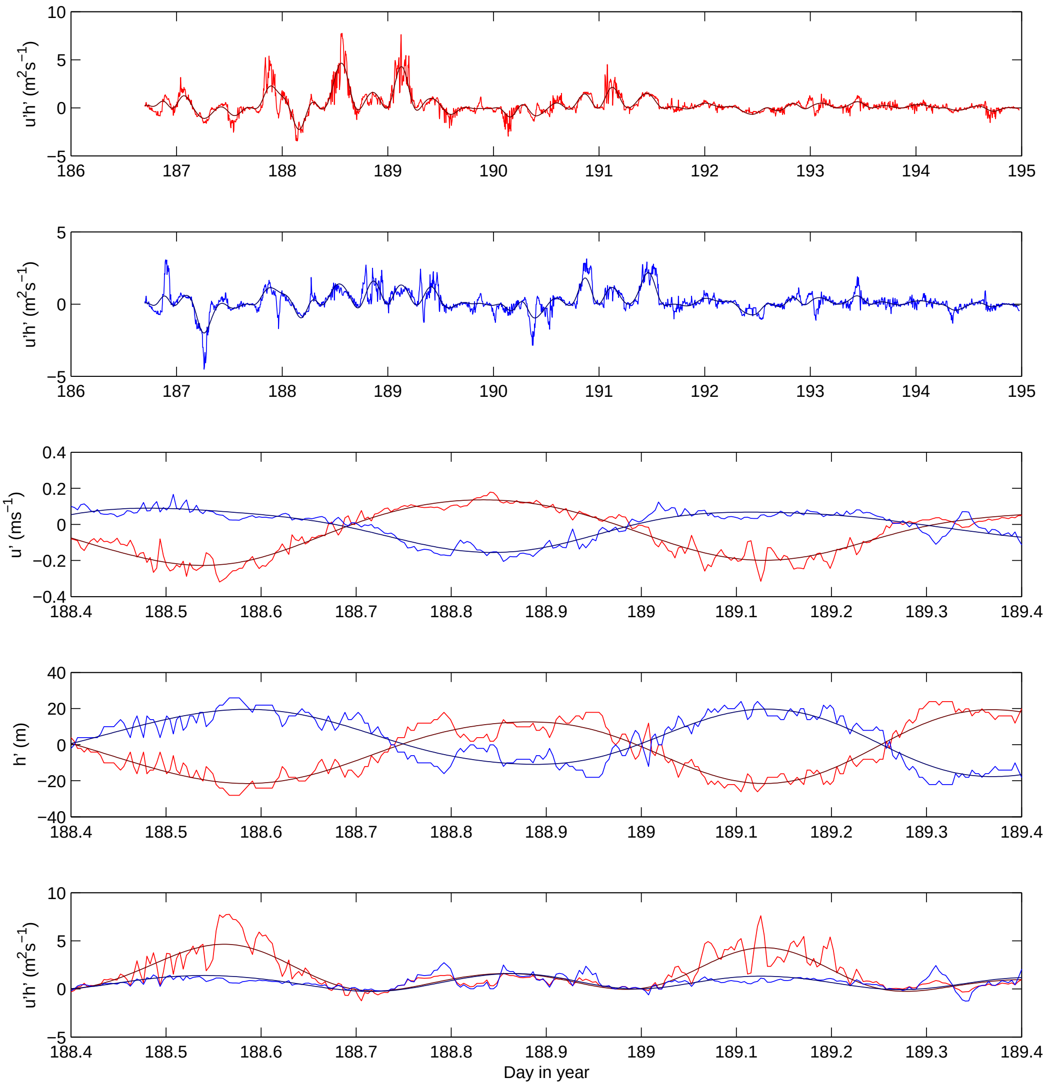

Figure 3.6: Time series from mooring MS1 on the Jones bank of (a and b) the full record of instantaneous bolus transport for the surface and bottom layers respectively and (c) the velocity perturbations, (d) thickness perturbations and (e) the bolus transport for a selected day. The lighter lines are the full observations and the dark lines are using the 7 hour low pass filtered time series of thickness and velocity.

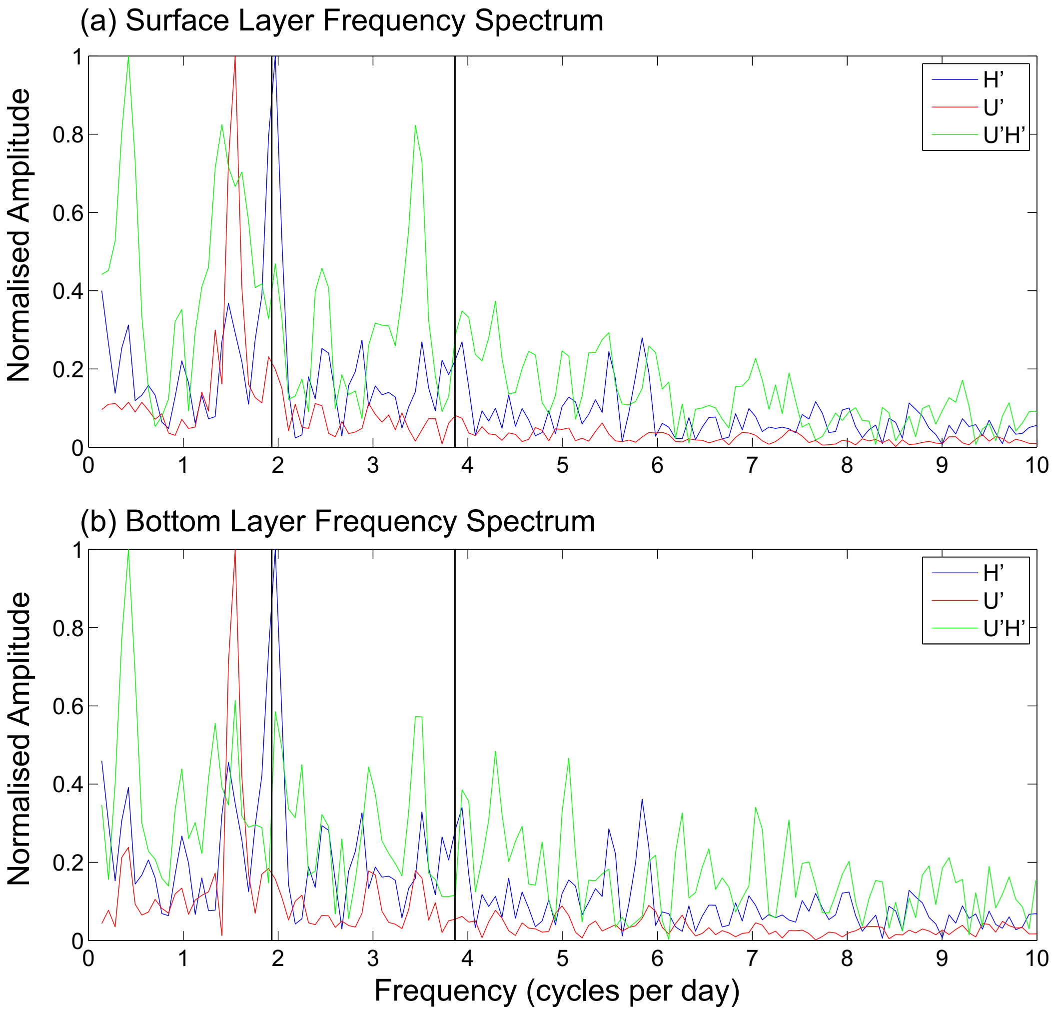

Figure 3.7: Frequency spectra from mooring MS1 on the Jones bank for (blue) thickness perturbations, (red) velocity perturbations and (green) bolus transport for (a) the surface and (b) the bottom layer.

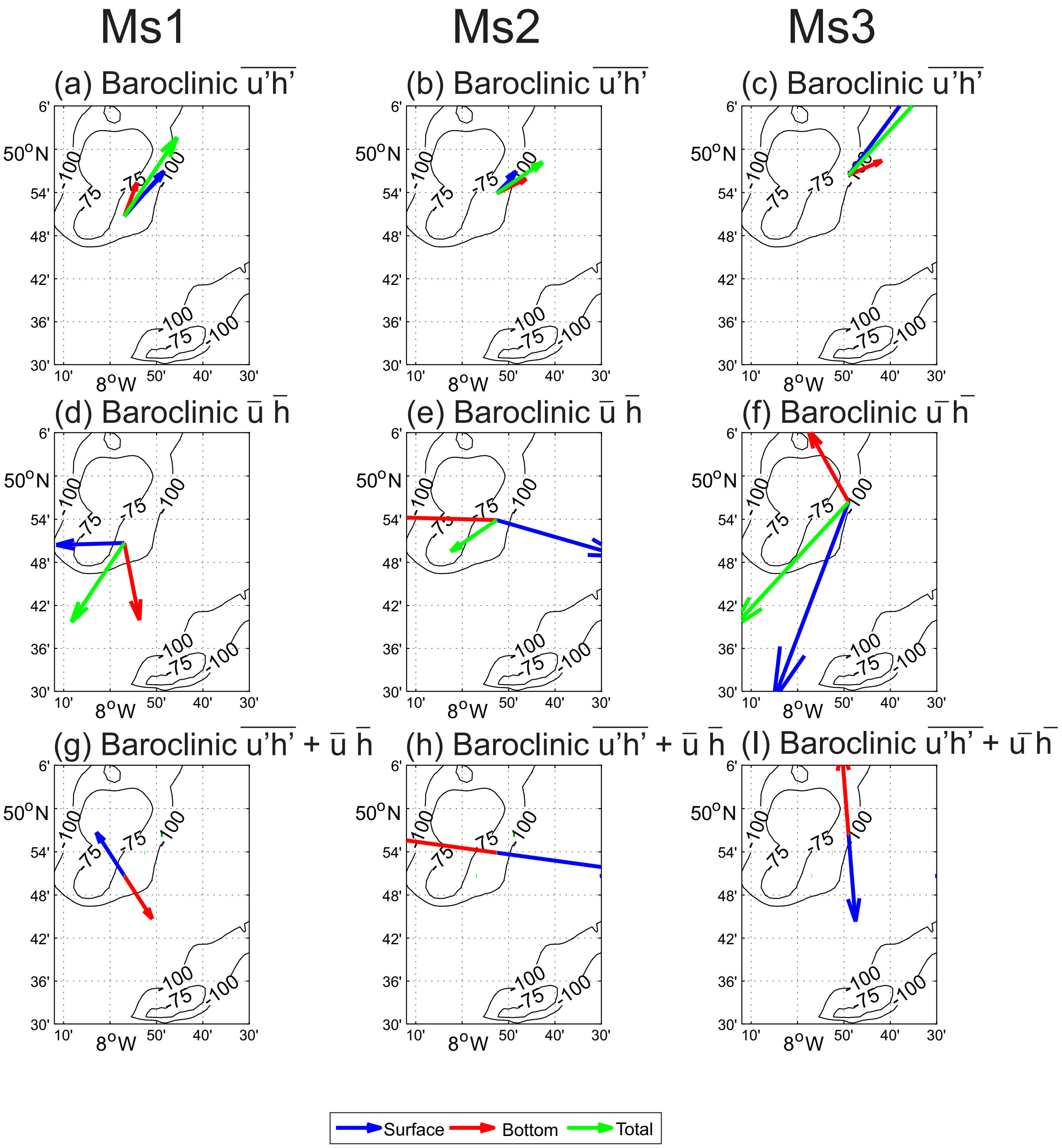

Figure 3.8: Plots showing the direction and relative magnitude of (a, b and c) the bolus transport driven by the baroclinic velocities, (d, e and f) the mean transport driven by the baroclinic velocities and (g, h and i) the total, bolus plus mean, transport driven by the baroclinic velocities i.e (a)+(d)=(g). For the moorings MS1 (a,d and g), MS2 (b, e and h) and MS3 (c, f and i).

perpendicular to the direction of the baroclinic bolus transport.

3.4.5 Summary for Jones Bank

- These moorings show a strong M2 period internal tide generated by local topography (Jones Bank). This leads to a transport typically away from the bank.

- The instantaneous bolus transport has a clear M4 period in both layers, driven by in phase M2 period variations in the thickness and velocity times series.

- All three moorings show a similar magnitude bolus transport, indicating that they are observing the same internal tide and that the bolus transport does not decay rapidly as we move away from the generation zone.

- As with the New Zealand mooring, the depth-integrated total baroclinic transport is zero. This is due to the fact the depth-integrated baroclinic bolus transport and depth-integrated baroclinic time-mean transport have the same magntiude but act in opposite direction. The two layers have opposing total baroclinic transports acting roughly perpendicular to the baroclinic bolus transport.

3.5 Malin Shelf - SE and SG

This is a regime where the open ocean is to the west, the topography is relatively smooth however the internal tide is weak. Two moorings were located on the Northwest European Malin Shelf, one near the shelf edge (SE) and one located further on shelf (SG). These moorings were deployed for 15 days during July 2013. SE was deployed in 149 m of water at $55°52.1'N, 9°3.7'W$. SG was deployed in 117 m of water at $55°47.8'N, 8°36.2'W$. The layout of moorings here again allows us to consider how the bolus transport varies as we move onto the shelf.

3.5.1 Mooring Details

The mooring at SE consisted of two 300kHz ADCPs: the first upward looking in a bottom frame and the second mounted in-line at 69 m above the bottom on a separate mooring. There was a string consisting of CTD's and temperature loggers. There were 5 CTD's located at 148 m, 135 m, 80 m, 48 m and 28 m depth, and 25 temperature loggers between 115 m and 18 m depth with a variable spacing, between 2 and 10 m [Short et al., 2013].

The mooring at SG consisted of one 150kHz ADCP upward looking from the bed. There were 6 CTD's located at 116 m, 96 m, 62 m, 54 m, 43 m and 29 m depth, and 20 temperature loggers again spaced by 2 to 10 m throughout the water column[Short et al., 2013].

Full water column profiles of salinity were constructed from the 5-6 CTDs deployed at each location [Hopkins et al., 2014] and used to calculate the density. All measurements were then linearly interpolated onto coincident 1 minute x 2 metre resolution grids. Both sites were well stratified throughout the observational period and show a weak, but persistent internal tidal signal, with a stronger internal tide at the near shelf edge mooring (SE).

3.5.2 Is there a bolus transport and what is its temporal signature?

On the Malin shelf, the instantaneous bolus transport, $\mathbf{u}'h'$, in both layers is intermittent and often weak (Fig. A1.2). This a result of the fact that the internal tide is significantly weaker here than at the previous moorings (on the New Zealand shelf and at Jones Bank), typical M2 period pycnocline displacements of 5 to 10m compared to 20m, and a range of other processes, with a range of temporal signatures , are of comparable magnitude. This is evidenced by the complex patterns in the displacement of the pycnocline and the baroclinic velocity (Fig. A1.1).

There are periods where there is an M2 period signal in the velocity and thickness (day 187.3 to 187.7 in Fig. A1.2(c and d)) however these are often short lived. The velocity perturbations are typically ± 0.05 m s^{-1} and the thickness variations are ± 10 m leading to peaks in bolus transport of 0.5 m^2 s^{-1} for SE, although because of the intermittent nature of the transport the average is considerably smaller. These periods of high bolus transport are often surrounded by periods where the velocity and thickness variations are small or show a wider range of periods. This suggests the strength of the internal tide at this location is highly variable. This sort of short-period variability has previously been seen on the European Shelf, for example where changes in the stratification modified the generation of the internal tide at the shelf edge [Stephenson Jr. et al., 2015].

These features are also seen in the power spectra, with the velocity and thickness both having peaks at the M2 period. However there are a lot of features with a range of periods of comparable magnitude (Fig. 3.9). This leads to a complex picture for the instantaneous bolus transport with some M4 period features (Fig. A1.2(e)), and other periods of little transport punctuated by large spikes in transport (Fig. A1.2(a, b and e)), likely associated with high frequency non-linear internal waves.

Mooring SG, further on-shelf, shows a diminished bolus transport, 0.094 m^2s at SE down to 0.057 m^2s at SG. This is consistent with an internal tide generated at the shelf edge losing energy as it propagates across the shelf. For the near shelf edge mooring, the low pass filtered transport is in the same direction as the mean transport, suggesting the dominant control over the time series is of tidal period or longer, however the magnitude of the transport is reduced as a result of these other processes being removed from the signal. The low pass filtered version of the on-shelf mooring shows a considerably smaller

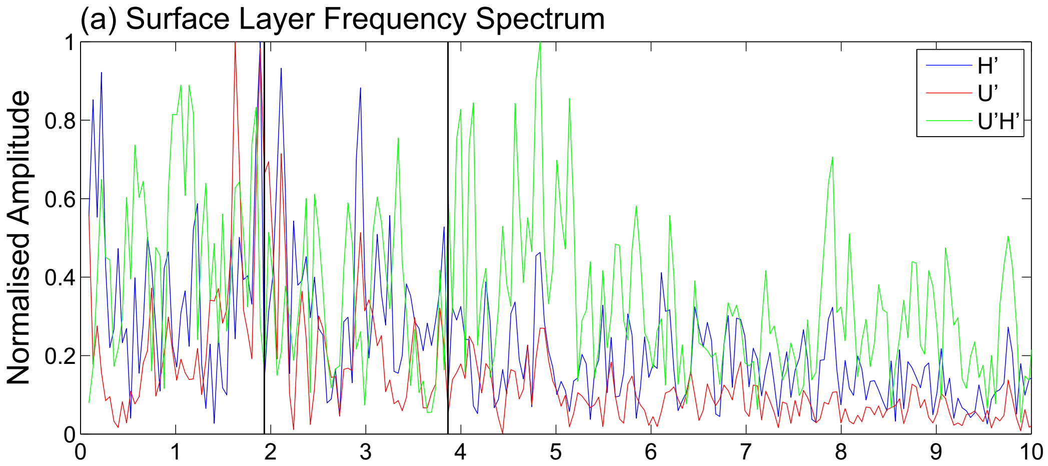
(a) Surface Layer Frequency Spectrum

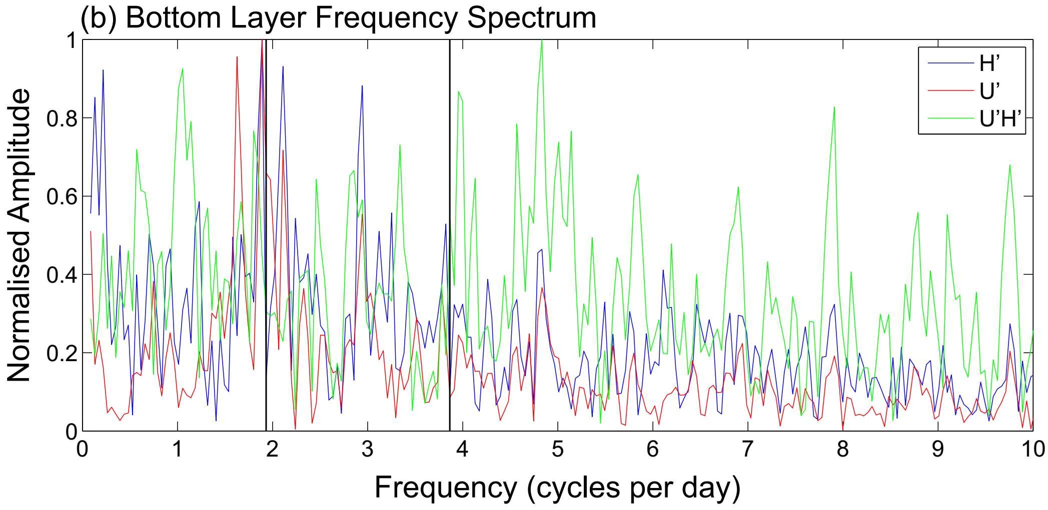
(b) Bottom Layer Frequency Spectrum

Figure 3.9: Frequency spectra from mooring SE on the Malin shelf for (blue) thickness perturbations, (red) velocity perturbations and (green) bolus transport for (a) the surface and (b) the bottom layer.

transport directed towards the shelf edge. I speculate that this is a result of the fact that locally generated internal tides, from on-shelf topographic features, have a cleaner and more coherent signature due to the relatively short distance they have propagated.

3.5.3 Is this volume flux returned locally?

Again, the bolus transport driven by the baroclinic velocity is directed on-shelf and is in the same direction in both layers for both moorings. This is also consistent with the schematic understanding presented in Section 2.3.1. The baroclinic mean transport shows large opposing transports between the layers with the transport at SE being to the north in the bottom and to the south at the surface whilst SG shows a bottom transport to the north-east and the surface transport to the south-west. Whilst the transports in the two layers are opposing they do not precisely cancel in the depth integral and result in a relatively small depth integrated off shelf transport. The sum of the two contributions to the transport driven by the baroclinic velocities depth integrate to zero, as also seen in the previous mooring, although there are large opposing transports in each layer which are dominated by the opposing transports seen in the time-mean baroclinic contribution. These are again directed along, rather than across, depth contours. This suggests limited cross shelf exchange at this location.

3.5.4 Summary for Malin Shelf

- In some regions, where the internal tide is weaker, the tidal bolus signal can be small and noisy, as a range of other processes can contribute. These processes are likely to be transient resulting in intermittent periods where the bolus transport is dominated by tidal processes and periods where other processes are important.

- As we move onto the shelf the internal tide signal becomes weaker, con-

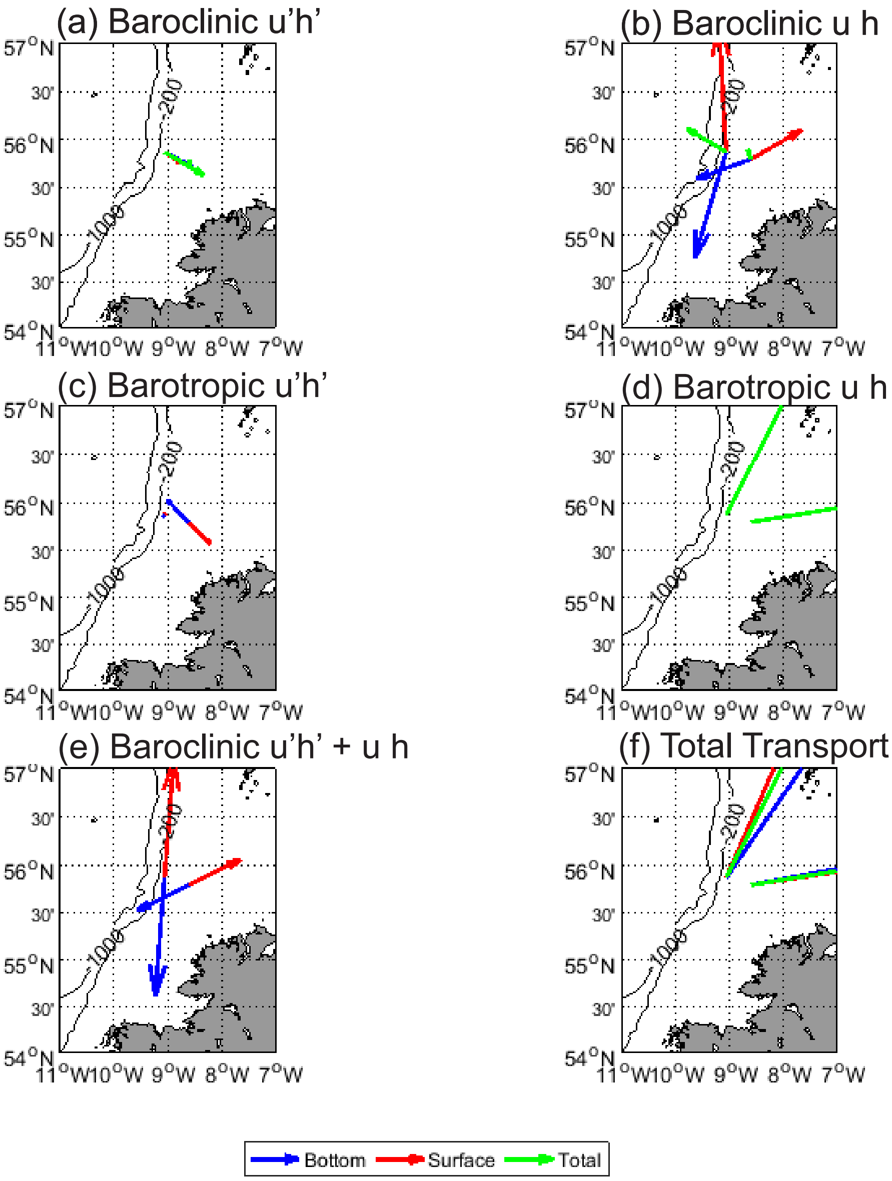

Figure 3.10: Plots showing the direction and relative magnitude of (a and b) the bolus transport driven by the baroclinic velocities, (c and d) the mean transport driven by the baroclinic velocities and (e and f) the total, bolus plus mean, transport driven by the baroclinic velocities i.e (a)+(c)=(e). For the moorings SE (a,c and e) and SG (b, d and f).

sistent with a shelf edge generated internal tide propogating across the shelf and dissipating energy as it goes.

- Away from the shelf edge there are likely to be internal tides generated by local topographic features, resulting in a more complicated mean transport.

- The depth-integrated total baroclinic transport is again zero with opposing layers directed parallel to the depth contours. This again indicated a limited contribution to the cross shelf exchange in the baroclinic transport.

3.6 Celtic Sea - ST4 and ST5

Here we investigate a regime where the internal tide is strong however the shelf edge has complex topography. Two moorings, labelled ST4 and ST5, were located in the Northwest European Celtic Sea as a part of the cruise D376. ST4 was deployed for approximately 12 days in 156 m of water at $48°38.91'N, 9°06.36'W$. ST5 was deployed for approximately 16 days in 169 m of water at $48°46.14'N, 9°24.38'W$.

3.6.1 Mooring Details

Each mooring consisted of a bed mounted 150 kHz ADCP and a string of temperature loggers and CTDs. At ST4 the string consisted of 6 CTD's located at 8, 30, 40, 50, 135 and 155 m depth, and 22 temperature loggers between 11 and 119 m depth with a separation of 2 - 10 m. At ST5 the string consisted of 6 CTD's located at 14, 38, 48, 58, 156 and 169 m depth, and 19 temperature loggers between 16 and 140 m depth with a separation of 2 - 20 m [Hopkins et al., 2014].

Full water column profiles of salinity were constructed from the 5-6 CTDs deployed at each location [Hopkins et al., 2014] and used to calculate the density. Observations were interpolated onto a full water column 1 minute x 1 metre grid. There was a strong wind event shortly after deployment that significantly modified the density structure of the water column [Hopkins et al., 2014, Stephenson Jr. et al., 2015] and drove strong residual surface currents. The time series is trimmed to the 8 days after the storm when the water column is stratified, as that period is more representative of typical summer conditions. In this region, the shelf break is heavily canyoned, which results in a strong and highly variable internal wave propagation [Vlasenko et al., 2014].

3.6.2 Is there a bolus transport and what is its temporal signature?

In the moorings ST4 and ST5 the baroclinic velocities again indicate a mode-one dominated regime, with both layers showing velocities that vary weakly with depth compared with at the interface (Fig. A1.4). These baroclinic velocity's vary in phase with the displacement of the pycnocline (Fig. A1.5(c and d)) with an M2 period (Fig. A1.6). This leads to an instantaneous bolus transport which shows both an M4 and M2 period in both layers (Fig. A1.6). The M4 period component of the instantaneous bolus transport occurs over a band between 3.5 and 4.2 cycles per day. This indicates that some of the M2 signal in the velocity and thickness time series is leaking into other nearby periods in the bolus transport which is potentially the result of a small, and possibly varying, phase offset between the two inputs.

In the Celtic Sea we see both a strong baroclinic and barotropic tide. Whilst the baroclinic tidal bolus transport is significant there is a large component from the interaction of the barotropic and baroclinic tide,15 times larger at ST4 and 19 times larger in ST5. This is a result of the fact that the velocities driven by the barotropic tide are significantly larger than those driven by the baroclinic, ± 0.5 m s^{-1} and ± 0.1 m s^{-1} respectively for ST4. The moorings also happen to be located where the barotropic and baroclinic tide are in phase for the bottom layer, a red stripe in Fig.2.7, as can be from the fact that bottom layer thickness is co-located in time with on shelf velocity.

3.6.3 How does the bolus transport vary along the shelf?

The direction of the baroclinic bolus transport in the Celtic Sea is complicated, directed along or off shelf for ST4 and more onto the shelf for ST5 (Fig. 3.11). Although the direction of the transport is not necessarily directed on-shelf, as we initially proposed this process would be, there is support for the bolus transport being driven by features of tidal, or longer period, from the fact that the 7 hour low-pass filtered time series still give transports of similar magnitude and direction as the full time series. The direction of the transport is also consistent with the direction of the M2 baroclinic energy flux as presented in Hopkins et al. [2014] This leads to the conclusion that the spatial variability seen here is a result of the complexity of the local topography, and thus generation and propagation characteristics of the internal tide. This view is supported by the variability seen between these two moorings in Hopkins et al. [2014] and the highly complex spatial picture given by numerical modeling of the internal wave field in this region [Vlasenko et al., 2014].

3.6.4 Is this volume flux returned locally?

The baroclinic time-mean transport again shows two large but opposing transports in the two layers. The depth-integrated time-mean baroclinic transport leaves a relatively small residual in the opposite direction to the baroclinic bolus transport (Fig. 3.11(c) and (d)). The total baroclinic transport shows a zero depth mean with two opposing layers dominated by the contribution from the mean velocity (Fig. 3.11(e) and (f)). These layers are again directed approximately parallel to the isobaths and thus indicate limited exchange between the open ocean and shelf sea.

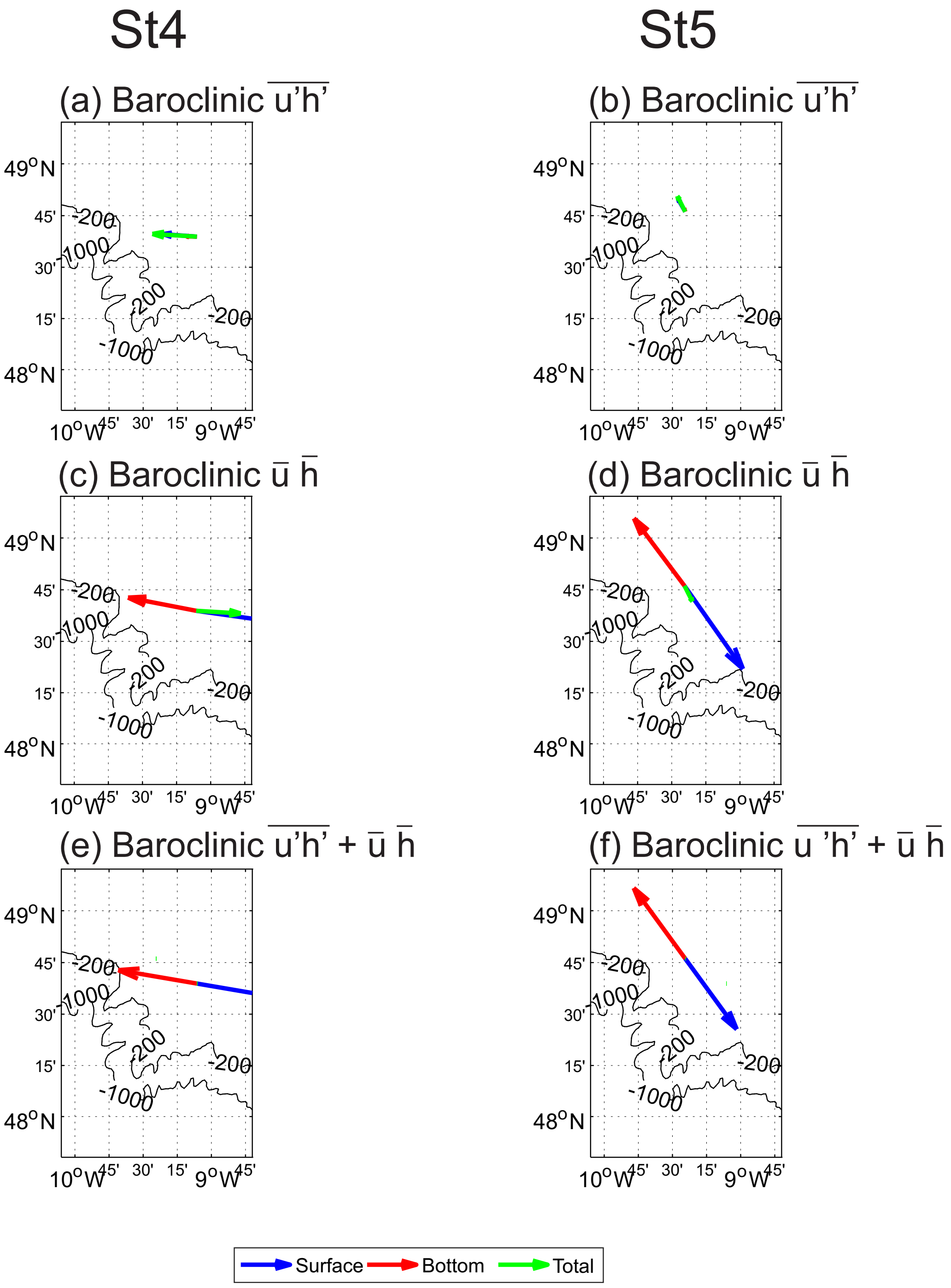

Figure 3.11: Plots showing the direction and relative magnitude of (a and b) the bolus transport driven by the baroclinic velocities, (c and d) the mean transport driven by the baroclinic velocities and (e and f) the total, bolus plus mean, transport driven by the baroclinic velocities i.e (a)+(c)=(e). For the moorings ST4 (a,c and e) and ST5 (b, d and f).

3.6.5 Summary for Celtic Sea

- There is an M2 period in the variations in layer thickness and velocity for both layers leading to a bolus transport with large M2 and M4 components.

- The direction of the bolus transport can be complicated by a complex internal tide field. In this case complex local topography leads to an internal tide propagating parallel to the depth contours in ST4 however propagating more on shore at ST5.

- Again, the two terms of the baroclinic transport cancel in the depth integral and lead to opposing layer transports generally directed parallel to the depth contours. This leads to a limited amount of exchange between the open ocean and shelf.

3.7 Discussion of the return flow

The moorings presented above all show a baroclinic bolus transport driven by tidal processes which would tend to move volume from the open ocean onto the shelf and ultimately towards the coast. As discussed in section 2.7, for a shelf sea bounded by the coast and the shelf edge, this bolus transport onto the shelf must be balanced by an equal return flow to the ocean. The exact nature of this return flow is vital in understanding the potential for the bolus transport to lead to an exchange of tracer. We previously considered four possible return flows (Fig. 2.8). Whilst it is not possible to give a definitive answer to how the volume is returned to the open ocean using the mooring data presented here, the moorings have all shown a cancellation in the depth integrated transport between the baroclinic bolus transport and the baroclinic mean transport, i.e. $\overline{u_1'h_1'} + \overline{u_2'h_2'} + \overline{u_1}\,\overline{h_1} + \overline{u_2}\,\overline{h_2} = 0$.

If the return flux is non-local we would expect to see a net on-shelf transport at the mooring locations. This is not seen in the moorings suggesting that, at these locations, the on-shelf bolus transport is being balanced by a local return flow, i.e. happening in the same cross-shelf 2D section. This is to be expected as a result of the integral constraint on the baroclinic depth-integrated transport as discussed in Section 3.2.5. This is a result of the fact that the baroclinic velocity is defined such that its depth-mean is zero and, as a result, its depth-integrated transport is also zero. It is difficult to identify a layered versus depth mean response in these moorings as other processes are making large contributions to the time-mean baroclinic flow, driving opposing layer transports typically parallel to depth contours. These large transports hide the relatively small differences between complete cancellation in each layer and opposing transports as a result of volume moving between density classes on the shelf.

3.8 Discussion of different regimes

3.8.1 Shelf-edge Orientation

Open ocean to the west The relevant locations for this condition are: the Celtic Sea and Malin Shelf.

Open ocean to the east The relevant location for this condition is: the New Zealand Shelf.

Discussion There is limited differences between the cases where the open ocean is to the west and to the east. In both cases the baroclinic bolus transport is typically directed on-shelf and is cancelled by the baroclinic time-mean transport. The total baroclinic transport has two opposing layers directed parallel to the isobaths, suggesting limited exchange, for both regimes.

3.8.2 Strength of the internal tide

Strong relative to other processes The relevant locations for this condition are: the New Zealand Shelf, Jones Bank and Celtic Sea.

Weak relative to other processes The relevant location for this condition is: the Malin Shelf.

Discussion The strength of the internal tide does not change the overall picture of on-shelf baroclinic bolus transport being cancelled by the baroclinic time-mean transport. The tidal signal is however much clearer in the strong internal tide cases and the M4 period matching the theoretical understanding (Fig. 2.3) is present in frequency space. For the Malin Shelf the tidal signal in the baroclinic bolus transport is intermittent and often has large contributions from other processes, masking the tidal signal. As a result it is hard to identify an M4 period in the instantaneous bolus transport.

3.8.3 Complexity of topography

Smooth topography The relevant locations for this condition are: the New Zealand Shelf and Malin Shelf.

Complex topography The relevant location for this condition is: Celtic Sea.

Discussion Again the overall picture of a baroclinic bolus transport in the same direction as the propagation of the internal tide is not modified by the complexity of the topography however the on-shelf assumption does not seem to hold when the topography is complex. This is due to the complexity of the shelf resulting in a complex internal tide field. This complexity is clear in the Celtic sea where one mooring shows the expected on-shelf transport whilst another mooring, only a short distance away, shows a transport along the shelf.

3.8.4 Location of generation

Generated at the shelf edge The relevant locations for this condition are: the New Zealand Shelf, Celtic Sea and Malin Shelf.

Generated at a bank The relevant location for this condition is: Jones Bank.

Discussion There is little difference in the bolus transport generated by the shelf edge and an on-shelf bank. The transport is in the same direction in both layers and shows a tidal period for both regimes. This is perhaps to be expected, as whilst the topography is different, both regimes are generating propagating internal waves with tidal period so will have very similar characteristics.

3.9 Summary

- We considered a range of moorings that span a range of regimes: the orientation of the shelf, the strength of the internal tide, the complexity of the generating topography; and whether the internal tide is generated at the shelf edge or by an on-shelf bank.

- Sections of density and baroclinic velocity taken from a series of near shelf edge moorings show, in most cases, two layers with opposing horizontal velocities. The signs of these velocities change in phase with the variations in the position of the pycnocline. This supports the schematic understanding presented in Figure 2.6.

- The variations in layer thickness and velocity typically occur with M2 period. This leads to an instantaneous bolus transport ($\mathbf{u}'h'$) which is preferentially positive and which contains both M2 and M4 period variability.

- The bolus transport ($\overline{\mathbf{u}'h'}$) is in the same direction in both layers. This is consistent with the theoretical understanding presented in Section 2.3.1. The baroclinic time-mean transport ($\overline{u}\overline{h}$) typically has two opposing layers leading to a small residual, relative to the layer transports, in the depth integral. This small residual is in the opposite direction to the baroclinic bolus transport. These two contributions cancel, leading to zero depth-integrated total volume transport from the baroclinic terms.

- This cancellation indicates that the volume fluxed onto the shelf in the bolus term is returned locally. This suggests that the combination of baroclinic processes is unlikely to play a significant role in exchanging volume or tracers between the open ocean and the shelf. There is still the potential for some convergence of tracers, if volume is moved between the two density classes whilst on the shelf. It is impossible to identify this from the available observations due to the presence of other large contributions to the baroclinic mean flow.

- In some regimes, particularly where the internal tide is weak, the bolus transport is small and often dominated by processes other than the internal tide.

- The direction of the bolus transport ($\overline{\mathbf{u}'h'}$) is set by the internal wave field in the area of interest. Where this is complicated, for example by complex topography, the bolus transport may not be directed onto the shelf and could be directed along the shelf or even off shelf.

- The internal tides driving this bolus transport ($\overline{\mathbf{u}'h'}$) can be dominated by locally generated internal tides, particularly away from the shelf edge and near large topographic features.

Chapter 4

Comparison between observed bolus transport and theoretical scaling for the internal tide

The observationally derived estimate of the bolus transport from the mooring data is now compared to the theoretical bolus transport expected from a baroclinic tide as derived in Section 2.3.1, $ca^2/(2\overline{h_i})$. Estimates of the inputs to this theoretical scaling will then be used to consider how we expect this bolus transport signal to change initially on a European shelf scale and then on a global scale.

4.1 Agreement between internal tidal theory and observed bolus transport

4.1.1 Methods

The baroclinic bolus transport is also compared with that predicted from our theoretical scaling for the baroclinic tide (2.20). Recalling from Chapter 2, we consider a two layer ocean with an infinitesimal interface and vertical displacements in the interface of,

$$h_i'(x,t) = \wedge_i a \sin(kx - \omega t), \tag{4.1}$$

where a is the amplitude of the displacement, k is the wave number, x is the horizontal co-ordinate, ω is the angular frequency, t is time and $\wedge_i$ is used to identify the sign of the thickness anomaly for each layer; $\wedge_{i=1} = -1$ for the upper layer and $\wedge_{i=2} = 1$ for the lower layer. We can then use depth-averaged continuity, $\frac{\partial u'}{\partial x} + \frac{\partial w'}{\partial z} = 0$, along with taking the vertical velocity as zero at the surface and setting the vertical velocities at the interface such that fluid does not cross the interface, $w'(h_i) = \frac{\partial h'}{\partial t}$, gives,

$$u_i'(x,t) = \wedge_i \frac{\omega a}{k\overline{h_i}} \sin(kx - \omega t), \tag{4.2}$$

Then, taking the product of the thickness (fig. 4.1) and velocity (fig. 4.2) and then averaging over a wave periods gives,

$$\overline{u_i' h_i'} = \frac{ca^2}{2\overline{h_i}}, \tag{4.3}$$

The amplitude of the interface displacement, a (m), is diagnosed from the time series for layer thickness; a M2 period sinusoid over a sliding window is fitted to allow for the changing amplitude of the internal tide. This window is two M2 periods long, allowing the fitting to account for the fact other processes may be present on top of the internal tide and to allow for the fact some moorings see significant changes in the strength of the internal tide. The layer thicknesses, $\overline{h_i}$, are diagnosed from the moorings by again taking the time-mean distance between the bed and an isopycnal or the isopycnal and the surface, as discussed above. The phase speeds, c, are diagnosed from linear internal wave theory [Gill, 1982, MacKinnon and Gregg, 2003] applied to the time-mean density structure in the mooring data [Klink, 1999]. A range is supplied for all the variables by performing the calculation over discrete M2 periods, to account for the fact that we expect to see M2 and M4 period variability in the signal.

This comparison is applied to all of the moorings presented in Chapter 3.

This allows us to test this theoretical understanding for a range of regimes including for: the orientation of the shelf break; the strength of the internal tide; complexity of topography; and internal tides generated at the shelf edge or an on-shelf bank.

New Zealand The diagnostics of the bolus transport compare reasonably well with the predictions made using our theory at the New Zealand mooring. For the surface layer the 7 hours low-passed observed bolus transport has a time-mean of 0.75 m^2 s^{-1} with a range from 0.18 to 1.9 m^2 s^{-1} whilst the theoretical scaling predicts a transport of 0.42 m^2 s^{-1} with a range from 0.01 to 1.8 m^2 s^{-1} (Table 4.1). For the bottom layer the 7 hours low-passed observed bolus transport has a time-mean of 0.84 m^2 s^{-1} with a range from 0.32 to 1.6 m^2 s^{-1} whilst the theoretical scaling predicts a transport of 0.61 m^2 s^{-1} with a range from 0.01 to 2.6 m^2 s^{-1} (Table 4.1). The first order control on this wide range is the amplitude of the displacement of the thermocline associated with the internal tide. The mean amplitude is 14 m however the range is from 2.4 to 25 m (Table 4.1) where the minimum is approximately 5 times smaller than the mean leading to the bolus transport being a factor of 25 smaller, due to the fact the amplitude is squared. This reduction in the magnitude of the internal tide is co-located with the a time when the stratification is weakened and the internal wave activity has decreased and moved towards higher frequency.

Celtic Sea - ST4 and ST5 For ST4 the mean filtered surface layer bolus transport is 0.38 m^2 s^{-1} with a range from 0.14 m^2 s^{-1} to 0.73 m^2 s^{-1} which compares well with the bolus transport from the theory, with a mean value of 0.41 m^2 s^{-1} and a range from 0.12 to 0.73 m^2 s^{-1}. The bottom layer also shows good agreement, with observations of 0.13 m^2 s^{-1} and a range of 0.04 to 0.23 m^2 s^{-1} and a mean theoretical estimate of 0.16 m^2 s^{-1} ranging from0.05 to 0.26 m^2 s^{-1}. For ST5 the mean surface layer observed transport, 0.18 m^2 s^{-1}

Table 4.1: Comparison between the theory and observations (with the 7-hour low passed bolus transports in brackets) for the bolus transport for ten different shelf moorings and input parameters for phase speed, displacement and layer thickness for both the surface and bottom layers.

Location		Phase Speed	Disp Ampl	Bott Thick	Surf Thick	Theo Bolus Surf	Obs Bolus Surf	Theo Bolus Bott	Obs Bolus Bott
New Zealand(NZ)	Min	0.185	2.44	31	44.5	0.00862	0.182(0.184)	0.0109	0.525(0.315)
	Avg	0.233	14.2	38.6	56.4	0.418	0.907(0.749)	0.612	1.06(0.844)
	Max	0.262	24.7	50.5	64	1.79	2.04(1.94)	2.57	2.17(1.58)
Celtic Sea(ST4)	Min	0.319	5.54	95.6	34.6	0.121	0.0885(0.135)	0.0483	0.0409(0.0385)
	Avg	0.338	9.57	98.5	37.5	0.413	0.44(0.375)	0.157	0.143(0.125)
	Max	0.356	11.9	101	40.4	0.726	0.906(0.725)	0.263	0.3(0.234)
Celtic Sea(ST5)	Min	0.304	0.894	98.9	35	0.00296	0.128(0.0348)	0.00116	0.00705(0.0124)
	Avg	0.33	5.81	102	38.4	0.145	0.249(0.182)	0.0547	0.0726(0.0635)
	Max	0.344	8.64	105	41.1	0.366	0.452(0.437)	0.13	0.188(0.185)
Malin Shelf(SE)	Min	0.259	0.428	72.3	52.5	0.000385	0.0218(0.0143)	0.000291	0.0297(0.00911)
	Avg	0.276	4.9	77.9	56.1	0.0591	0.123(0.0736)	0.0426	0.0941(0.0514)
	Max	0.292	10.2	81.5	61.7	0.292	0.255(0.204)	0.212	0.272(0.135)
Malin Shelf(SG)	Min	0.243	1.1	61.8	31.2	0.00366	0.0192(0.00649)	0.00208	0.00498(0.00496)
	Avg	0.251	3.68	65.1	36.9	0.046	0.0977(0.0865)	0.0261	0.0572(0.0516)
	Max	0.26	5.83	70.8	40.2	0.141	0.27(0.218)	0.0714	0.18(0.131)
Jones Bank(MS1)	Min	0.264	3.02	30.8	22	0.0323	0.0768(0.0638)	0.0262	0.0424(0.0361)
	Avg	0.302	8.98	36.1	32.1	0.379	0.644(0.598)	0.337	0.42(0.396)
	Max	0.336	16.2	46.1	37.4	2.01	1.79(1.63)	1.44	0.992(1.01)
Jones Bank(MS2)	Min	0.301	3.24	62.7	29.5	0.0382	0.0391(0.0561)	0.0211	0.035(0.0319)
	Avg	0.339	9.08	70	34	0.412	0.43(0.452)	0.2	0.315(0.294)
	Max	0.364	14.1	74.5	41.3	1.23	0.781(0.771)	0.576	0.703(0.688)
Jones Bank(MS3)	Min	0.324	0.335	19.9	34.8	0.000212	0.206(NaN)	0.000254	0.0154(NaN)
	Avg	0.343	17.6	40.8	64.8	0.821	1.09(NaN)	1.3	0.485(NaN)
	Max	0.354	33.4	71.3	85.4	5.69	3.79(NaN)	9.94	1.55(NaN)
Celtic Sea(IM1)	Min	0.387	0.344	87.3	12.8	0.00137	0.0139(NaN)	0.00025	0.00444(0.00552)
	Avg	0.409	2.31	89.2	14.8	0.0736	0.123(NaN)	0.0122	0.0402(0.0303)
	Max	0.426	4.37	91.2	16.7	0.317	0.413(NaN)	0.0466	0.137(0.108)
Celtic Sea(IM3)	Min	0.39	0.222	88.7	18.7	0.000411	0.00416(0.0105)	0.000103	0.00168(0.00341)
	Avg	0.416	2.9	90.3	21.7	0.0807	0.111(0.0999)	0.0194	0.0338(0.0287)
	Max	0.434	6.03	93.3	23.3	0.424	0.346(0.304)	0.0891	0.138(0.104)

and range 0.03 to 0.44 m^2 s^{-1}, also compares favorably with the theoretical scaling, mean 0.15 m^2 s^{-1} with range 0.003 to 0.37 m^2 s^{-1}. For the bottom layer the observed bolus transport is 0.06 m^2 s^{-1} with a range of 0.01 to 0.19 m^2 s^{-1}. This compares well with the theoretical estimates of 0.05 m^2 s^{-1} and a range from 0.001 to 0.13 m^2s^{-1}.

Malin Shelf The mean bolus transport for the surface layer at near shelf edge mooring (SE) is 0.0736 m^2s^{-1} with a range from 0.0143 to 0.204 m^2s^{-1}. These fall within the range given from our theoretical scaling, with the mean 0.0591 m^2s^{-1} and the range 0.0004 to 0.292 m^2s^{-1}. For the bottom layer the comparison is similar, with an observed mean bolus transport of 0.0514 m^2s^{-1} and range from 0.009 and 0.135 m^2s^{-1} and theoretical transport of 0.0426 m^2s^{-1} ranging from 0.0003 and 0.212 m^2s^{-1}. For the mooring further on-shelf (SG), the mean surface bolus transport is 0.0865 m^2s^{-1} with a range of 0.0065 m^2s^{-1} to 0.218 m^2s^{-1}. The theoretical scaling falls below the observations, with the mean transport 0.046 m^2s^{-1} and a range from 0.0037 to 0.141 m^2s^{-1}. This could be a result of the fact that internal tide is weak at this location and other processes could make equally large contributions, masking the tidal contribution. In the bottom layer the theory is closer to the average transport in the observations, 0.0261 and 0.0516 m^2s^{-1} respectively. The bottom layer is relatively isolated from external forcing meaning the other potential contributions to the bolus transport are likely to be smaller.

Jones Bank At Jones Bank the moorings all show a good agreement between the observed transport and that expected from theory. For MS1, at the top of the bank, the surface layer transports are 0.598 and 0.379 m^2s^{-1} and for the bottom they are 0.396 and 0.337 m^2s^{-1} respectively. For MS2 the surface layer observed transport is 0.452 m^2s^{-1} and the theory would predict 0.412 m^2s^{-1} and the bottom layer observed transport is 0.295 m^2s^{-1} and the theoretical transport would be 0.2 m^{2}s^{-1}. For the mooring at MS3 the filtering process was not possible, due to the gaps in the data, so a direct comparison between the theory and a bolus transport without the high frequency component is not possible.

Celtic Sea - IM1 and IM3 For IM1 the surface layer time series have gaps, similar to the Jones Bank moorings, meaning the filtered time series is not available. As such we will only consider the bottom layer at this location. The observed bolus transport is 0.0303 m^{2}s^{-1} with a range of 0.006 m^{2}s^{-1} to 0.108 m^{2}s^{-1} and the theoretical scaling is 0.0122 m^{2}s^{-1} with a range from 0.0003 to 0.0466 m^{2}s^{-1}, showing reasonable agreement despite the more complicated horizontal velocity profile. The mooring at IM3 also shows good agreement, with the surface layer having transports of 0.0999 and 0.0807 m^{2}s^{-1} for the observations and theory respectively and 0.0287 and 0.0338 m^{2}s^{-1} for the bottom layer.

Discussion of agreement between theory and observations The average difference between the theory estimate and the observed bolus transport is 46.6% of the observed value. Excluding the moorings IM1 and IM3, where the baroclinic velocities suggest that the assumptions in the theory do not hold, this drops to 40.4%. This indicates that the theoretical scaling presented in Chapter 2 represents the process occurring at these locations well, although there is some error. There are a number of different possible explanations for the errors seen including: inaccuracies in the estimates of the input terms, for example the M2 fitting for displacement not well representing the real tide; other processes contributing to the bolus transport; or some of the simplifications used in deriving the theory, for example the two layer or sinusoidal assumptions.

4.2 Estimates of internal tide driven bolus velocity away from these mooring locations

Given the reasonable correspondence between our bolus transports estimated from baroclinic theory and that diagnosed directly from our observations, we now consider the implied bolus signal from baroclinic tides at the shelf break on firstly a regional then global scale. This is achieved by exploiting diagnostics from a global barotropic tidal model and global climatologies.

4.2.1 Inputs

The bolus velocity is estimated using our theory for the baroclinic tide,

$$\overline{u_i'h_i'} = \frac{ca^2}{2\overline{h_i}}, \tag{4.4}$$

Each term is estimated for the shelf break, defined by the 300 m isobath.

Phase Speed (c) and Layer Thickness ($\overline{h_i}$)

The phase speed is calculated using linear internal wave theory [Gill, 1982, MacKinnon and Gregg, 2003] which is applied to the stratification data from the World Ocean Atlas (WOA; Locarnini et al. [2013], Zweng et al. [2013]) using the code of [Klink, 1999]. The layer thickness is calculated using the same theoretical basis and input data to calculate the vertical mode structure. The boundary between the surface and deep layers is then defined as the zero crossing of this mode structure.

Internal Tidal Amplitude (a)

The internal tide amplitude, a in m, is estimated from an energetics argument. We take the depth integrated supply of energy to the baroclinic tide m (W m^{-2}) to be equal to the energy lost by the barotropic tide. Near the shelf edge this is a reasonable assumption as friction, the other major contribution to the dissipation of the barotropic tide, is generally confined to very shallow near coast regions. We have taken these barotropic dissipation rates from Green and Nycander [2013] using the parameterisation of Nycander [2005]. If we then distribute this energy over some depth h_N (m) and integrate over a wave period τ (s) the total supply of potential energy to a single baroclinic tidal wave PE (J m^{-3}) becomes,

$$PE = m\tau / h_N \tag{4.5}$$

From linear wave theory we know the amplitude of a linear internal wave is related to its potential energy by,

$$PE = \rho N^2 a^2. \tag{4.6}$$

Now, by equating these two expressions, the vertical displacement amplitude can be estimated from,

$$a^2 = \frac{m\tau}{\rho N^2 h_N}, \tag{4.7}$$

Two choices were made about the calculation of N^2 and h_N based on different assumptions about how the depth-integrated energy supplied to the baroclinic is distributed in the vertical. The first assumption is that the energy is distributed evenly over the water column,with the depth averaged N^2 being used and h_N being taken as the full depth. This tends to underestimate the amplitude of the internal tide and can be treated as a lower bound. The second assumption is that the energy is focused around the pycnocline, with the maximum value of N^2 being used and the relevant depth h_N being the vertical resolution of the input data [Stigebrandt and Aure, 1989]. This method tends to over estimate the amplitude of the internal tide and should be treated as an upper bound. The buoyancy frequency is diagnosed using the closest climatological mean density profile in the World Ocean Atlas (WOA; Locarnini et al. [2013], Zweng et al. [2013]).

The amplitude of the internal tide calculated from the moorings, as described above, compares favorably with the estimate from the barotropic dissipation (Table 4.2). The five moorings considered here have been selected as they are the closest examples to the shelf edge. In the three of the five moorings considered here, NZ, ST4 and ST5 , the mooring values lie within the upper and lower bounds calculated. In mooring SG the observed value is slightly larger than the value from the modeling, 3.7 and 3.1 m respectively. For the mooring SE the observed value is smaller than the lower bound derived from the model. Some disagreement between the mooring and model values is to be expected as the energy supply to the internal tide is averaged over a large box, possibly capturing hot-spots in generation not relevant to the mooring location, and there is no estimation of the dissipation of the internal tide between the site of the internal tide generation and the location of the observations.

Table 4.2: Comparison of the observed M2 period vertical displacement from five shelf moorings with modeled vertical amplitude in the same location calculated from (4.7)

Mooring	Observed (m)	a_{avg} (m)	a_{max} (m)
New Zealand (NZ)	13	4.7	15.6
Malin Shelf (SE)	4.0	8.4	30.6
Malin Shelf (SG)	3.7	1.1	3.1
Celtic Sea (ST5)	4.9	2.1	9.8
Celtic Sea (ST4)	9.6	6.3	31.7

4.2.2 European Shelf Estimates of Bolus Velocity

The bolus velocity predicted from the baroclinic tide depends on the phase speed, c, the bottom layer thickness h_2, and the amplitude of the internal tide, a. For the European shelf, the phase speed is typically around 0.3 m s^{-1} over most of the shelf break, increasing to 0.5 m s^{-1} along the Norwegian shelf (Fig. 4.1(a)). The bottom layer thickness typically varies from 100 to 200 m along the shelf break (Fig. 4.1(b)). The amplitude of the baroclinic tide varies

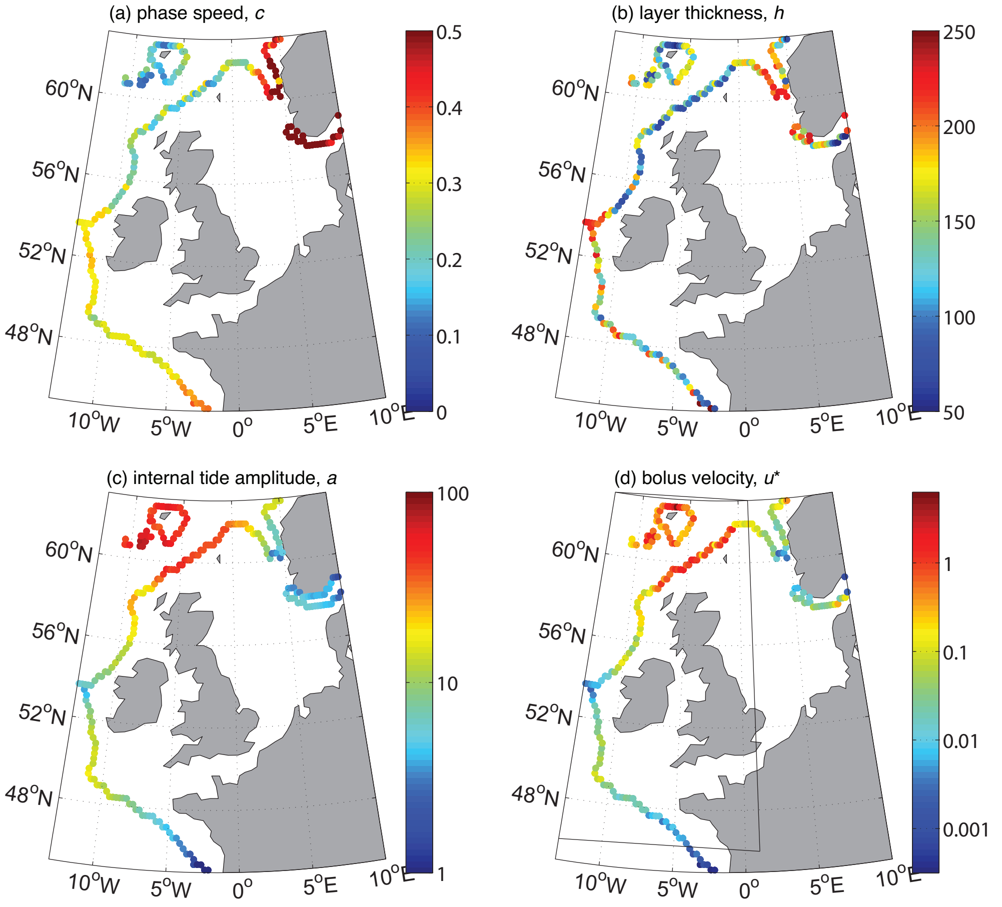

Figure 4.1: Maps of the European Shelf showing (a) the phase speed, c (m s^{-1}), (b) the bottom layer thickness, h_2 (m), (c) the amplitude of the internal tide at generation, a (m), and (d) the implied bolus velocity, $ca^2/(2\overline{h_2}^2)$ (cm s^{-1}).

from typically 1 to 100 m along the shelf break with higher values to the north of Scotland (Fig. 4.1(c)). The resulting bolus velocity varies from typically 0.01 to 1 cm s^{-1} along the shelf break (Fig. 4.1(d)), its pattern mainly determined by the amplitude of the baroclinic tide. This is due to the fact that the amplitude changes by a factor of 10^2 which is then squared meaning the bolus transport is modified by a factor of 10^4. The other two terms, phase speed and layer thickness, vary by approximately a factor of 5.

4.2.3 Global Estimates of Bolus Velocity at the Shelf Edge

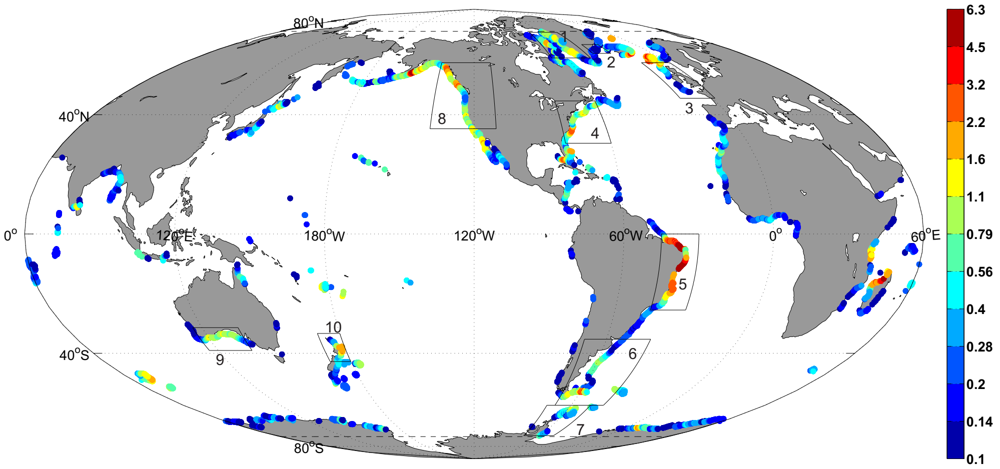

Figure 4.2: Global map of the implied bottom layer bolus velocity, $ca^2/(2\overline{h_2}^2)$ (cm s^{-1}), at a depth of 300 m at the top of the continental slope around the globe. Values less than 0.1 cm s^{-1} have not been plotted. The boxes represent the continental slope regions over which the integrated bolus transport is evaluated in Table 4.3.

The bolus velocity is then estimated at a depth of 300 m at the top of the continental slope around the globe using a similar procedure. The bolus velocity is typically ranging from 0.01 to 1 cm s^{-1} for continental slopes adjoining the open ocean (Fig. 4.2), but reduces to less than 0.001 cm s^{-1} where there are weak tides, for example in the Mediterranean or Arctic.

The integrated bolus transport has been calculated for a number of shelves where the internal tide is energetic and thus leads to significant transports (Fig.

Table 4.3: Bolus velocity and bolus volume flux across the 300m isobath for a range of shelf edge sectors. The error is estimated as ± 40% based on the average percentage difference between the observed and theoretical transports presented in Table **??**

	Box	Bolus velocity	Shelf-edge length	On-shelf bolus transport
Atlantic Sector		cm s^{-1}	km	Sv
West Greenland	1	0.5	5547	2.9
East Greenland	2	0.1	2257	0.3
European	3	0.3	2507	0.7
NE America	4	0.9	2400	1.0
SE America	5	2.8	3812	2.0
Patagonian	6	0.7	4574	1.9
Antarctic Peninsula	7	0.3	5036	1.2
Pacific Sector				
NW America	8	1.1	2534	1.8
S Australia	9	0.8	2167	0.8
N New Zealand	10	0.4	2386	0.7

4.2, boxes; Table **??**). For example, for the Northwest Atlantic, there is an on-shelf bolus velocity of 0.9 cm s^{-1}, which when integrated over the local depth and a shelf edge leads to an on-shelf transport of 1 Sv; for the European Shelf, there is an on-shelf bolus velocity of 0.3 cm s^{-1} and an on-shelf transport of 0.7 Sv; for the Patagonian shelf, there is a bolus velocity of 0.7 cm s^{-1} and a transport of 1.9 Sv; for the Southwest Atlantic, there is a bolus velocity of 2.8 cm s^{-1} and on-shelf transport of 2 Sv; and for the Northeast Pacific, there is a bolus velocity of 1.1 cm s^{-1} and an on-shelf transport of 1.8 Sv. for the South Australia shelf, there is a bolus velocity of 0.8 cm s^{-1} and a transport of 0.8 Sv; for the Northern New Zealand shelf, there is a relatively weak bolus velocity of 0.4 cm s^{-1} and a transport of 0.7 Sv.

4.3 Summary

- The observationally derived bolus transports compare favourably with the theoretical scaling derived in Chapter 2, $ca^2/(2\overline{h_i})$. The average difference between the 7-hour low passed observations and theory is 40%. This comparison is good for all of the regimes explored through the range of mooring locations.

- Using an energetics argument we have estimated the vertical displacement of the pycnocline by the internal tide using the energy converted from the barotropic tide and simple linear internal wave theory.

- This vertical displacement amplitude, in addition to estimates of the phase speed and layer thickness calculated using a global climatology, have been used to estimate the bolus transport for the European Shelf edge and on a global scale.

- On the European Shelf the primary control on the magnitude of the bolus transport is the vertical displacement amplitude, modifying the transport by a factor of 10^4 compared to a factor of 5 for the other terms.

- On a global scale the bolus transport velocity is larger than 0.1 cm s^{-1} for a large proportion of the global shelf edge, although regions with weak barotropic tides, such as the Mediterranean Sea, have very small bolus transports.

- For the majority of the regions used for averaging the bolus transport is in the range 0.1 to 1 cm s^{-1} leading to cross shelf edge transports of 0.3 to 3 Sv.

Chapter 5

Walin Transformation and Nutrient Implications

5.1 Introduction to Walin Framework

The Walin framework was first proposed by Walin [1982] as a way of calculating the transformation of water between temperature classes in the open ocean. It consists of a balance between the surface heat flux and the diffusion of heat across isotherms in order to calculate the total flux of water into, or out of, a particular temperature range. This flux can then be interpreted as a physical flow of water over stationary isotherms, the migration of isotherms or, more realistically, some combination of the two. Since this initial formulation it has been applied over a wide range of regimes and with a number of tracers, such as with density in the open ocean [Speer and Tziperman, 1992, Nurser et al., 1999], salinity in an estuarine environment [MacCready et al., 2002] and nutrients across a tidal mixing front [Badin et al., 2010]. It is formulated from a simple volume budget and tracer budget for the region between two surfaces in tracer space.

5.1.1 Derivation

The Walin framework consists of taking a volume and tracer budget between two tracer surfaces. Here the Walin framework is derived using potential density as the tracer, following Nurser et al. [1999].

Considering the volume between two surfaces in density space, ρ and $\rho{+}\Delta\rho$, we write the rate of change of volume between those two surfaces as a function of the volume flux through the sea surface, through the lateral boundaries and through the density surfaces (Fig. 5.1(a)),

(a) Volume Budget

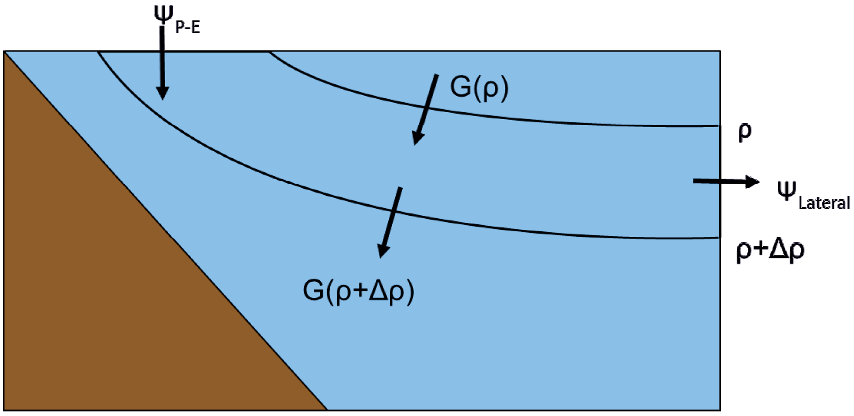

(b) Mass Budget

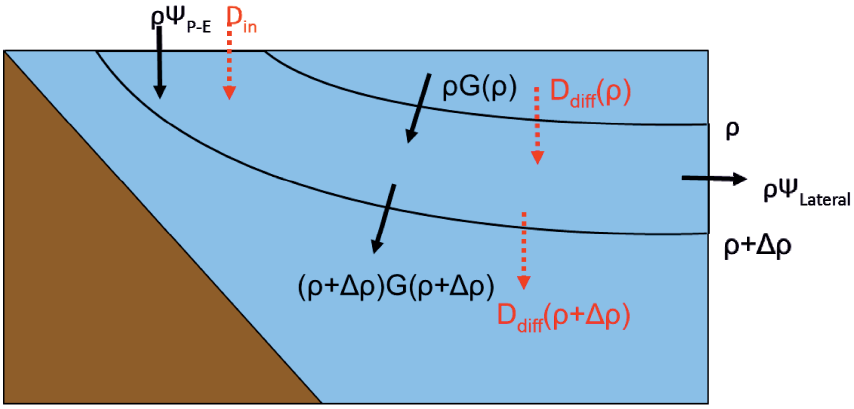

Figure 5.1: Schematic sections showing the terms for (a) the volume budget and (b) the mass budget between two density surfaces, ρ and $\rho + \Delta\rho$, used in the derivation of the Walin Framework. The volume budget is controlled by the flux of volume across the density surfaces, G, and through the boundaries of the domain, Ψ. The mass budget is also influenced by these terms, again shown in black, plus terms specific to the mass budget, shown in red, specifically the modification of density through surface forcing and through the diffusive density flux through the density surfaces.

$$\frac{\partial \Delta V}{\partial t} - \Psi_{P-E} + \Psi_{lateral} = G(\rho) - G(\rho + \Delta\rho) = -\Delta\rho \frac{\partial G}{\partial \rho}, \qquad (5.1)$$

where ΔV is the volume between these two surfaces (m^3), t is time (s), Ψ_{P-E} is the flux of volume between the surface of the ocean and the atmosphere (m^{3}s^{-1}), $\Psi_{lateral}$ is the flux of volume through the vertical side boundaries of the domain (m^{3}s^{-1}) and G is the diapycnal volume flux at ρ and $\rho + \Delta\rho$ (m^{3}s^{-1}). The convergence of diapycnal volume flux, G, in a density class is the rate of water mass formation, M,

$$M = -\Delta\rho \frac{\partial G}{\partial \rho}, \tag{5.2}$$

Using equations 5.1 and 5.2 we can write the water mass formation as,

$$M = \frac{\partial \Delta V}{\partial t} - \Psi_{P-E} + \Psi_{lateral}, \tag{5.3}$$

Now considering a mass budget for the volume between the same two isopycnals,

$$\rho(\frac{\partial \Delta V}{\partial t} - \Psi_{P-E} + \Psi_{lateral}) + \Delta\rho \frac{\partial(\rho G)}{\partial \rho} = -\Delta\rho \frac{\partial D_{diff}}{\partial \rho} + \int_{outcrop} D_{in} \quad \partial A \tag{5.4}$$

where D_{diff} is the integrated dispycnal diffusive mass flux (kg s^{-1}), D_{in} is the mass flux through the ocean surface (kg m^{-2} s^{-1}) and *outcrop* is the area on the ocean surface with density between ρ and $\rho + \Delta\rho$ (m^2). The left hand side of this equation is the mass added (or removed) through the addition (or subtraction) of volume. The right hand side has terms specific to the mass budget. The first term on the right hand side represents the convergence (or divergence) of the diapycnal mass flux and the second term represents the effect of the surface forcing on the mass.

The surface mass flux is,

$$\int_{outcrop} D_{in} \quad \partial A = \int_{outcrop} -\frac{\alpha}{C_p}\mathcal{H} + \beta\rho_0 S(\mathcal{E} - \mathcal{P}) \quad \partial A \tag{5.5}$$

where α is the thermal expansion coefficient ($^{\circ}\mathrm{C}^{-1}$), C_p is the specific heat capacity of seawater (J kg^{-1} $^{\circ}$C^{-1}), $\mathcal{H}$ is the surface heat flux defined as positive downwards (W m^{-2}), β is the saline contraction coefficient (psu^{-1}), ρ_0 is a reference density (kg m^{-3}), S is the salinity (psu), $\mathcal{E}$ is the evaporation rate (m s^{-1}) and $\mathcal{P}$ is the precipitation rate (m s^{-1}). The diffusive flux is,

$$D_{diff} = \int_{densitysurface} K_z \frac{\partial \rho}{\partial z} \quad \partial A \tag{5.6}$$

where $densitysurface$ is the surface area of the density surface (m^2) and K_z is the vertical eddy diffusivity (m^{2}s^{-1}). This flux, as with all fluxes in this work, is defined as positive directed towards denser waters.

Now, taking the mass budget (Eqn. 5.4) and substituting in the volume budget (Eqn. 5.1), we can write,

$$\rho(-\Delta\rho\frac{\partial G}{\partial \rho}) + \Delta\rho\frac{\partial(\rho G)}{\partial \rho} = -\Delta\rho\frac{\partial D_{diff}}{\partial \rho} + \int_{outcrop} D_{in} \quad \partial A \tag{5.7}$$

Using the product rule we can state,

$$\frac{\partial(\rho G)}{\partial \rho} = \rho\frac{\partial(G)}{\partial \rho} + G\frac{\partial \rho}{\partial \rho}, \tag{5.8}$$

which, using $\partial\rho/\partial\rho = 1$ and dividing by $\Delta\rho$, becomes,

$$G = -\frac{\partial D_{diff}}{\partial \rho} + \frac{1}{\Delta\rho}\int_{outcrop} D_{in} \quad \partial A \tag{5.9}$$

Thus, the transformation of volume to a lighter density requires either a divergence of diffusive density fluxes or a lightening through surface forcing. This dispycnal volume flux can be viewed as either the physical movement of water across stationary isopycnals or the movement of the isopycnals. In reality the output is likely to be some combination of these two views.

5.1.2 Example for the North Atlantic

The transformation will now be calculated for the North Atlantic as an illustration of the application of the Walin framework. This will be performed using only the surface heat and freshwater flux and ignoring the diapycnal diffusion term. This simplification is in the same spirit as the original Walin [1982] and has also been followed in subsequent studies [Speer and Tziperman, 1992]. The NOCS surface flux climatology version 1.1 is used for the surface heat and freshwater fluxes with the 2001 version of the World Ocean Atlas climatology used for the surface temperature and salinity needed to calculate the surface density field.

In the North Atlantic there is a strong positive surface density flux, acting to increase the density, over the Gulf Stream (Fig. 5.2). This is a result of relatively warm, and thus light, water being swept northwards from the tropics to cooler latitudes. The maximum negative surface density flux, acting to reduce the density, is in the tropics where there is strong radiative forcing and addition of fresh water.

Seasonal Transformation

In the winter the surface forcing drives an increase in density for all classes. The transformation rate is largest at 1026 kg m^{-3} with 110 Sv of water crossing that isopycnal (Fig. 5.3(b)). In spring the picture changes as increased surface heating leads to a transformation of water to lighter density classes. We still see a transformation of water into denser classes at the dense end, with a maximum flux at 1027.5 kg m^{-3} of 10 Sv. However in lighter classes, with density less than 1026 kg m^{-3}, we see water transformed into less dense classes, with a maximum flux at 1023 kg m^{-3} of 25 Sv (Fig. 5.3(c)). In summer water is transformed into less dense classes at all densities. This negative diapycnal volume flux is at a maximum between 1023 and 1025.5 kg m^{-3} where the flux reaches 50 Sv (Fig. 5.3(d)). In Autumn, water is again transformed into denser

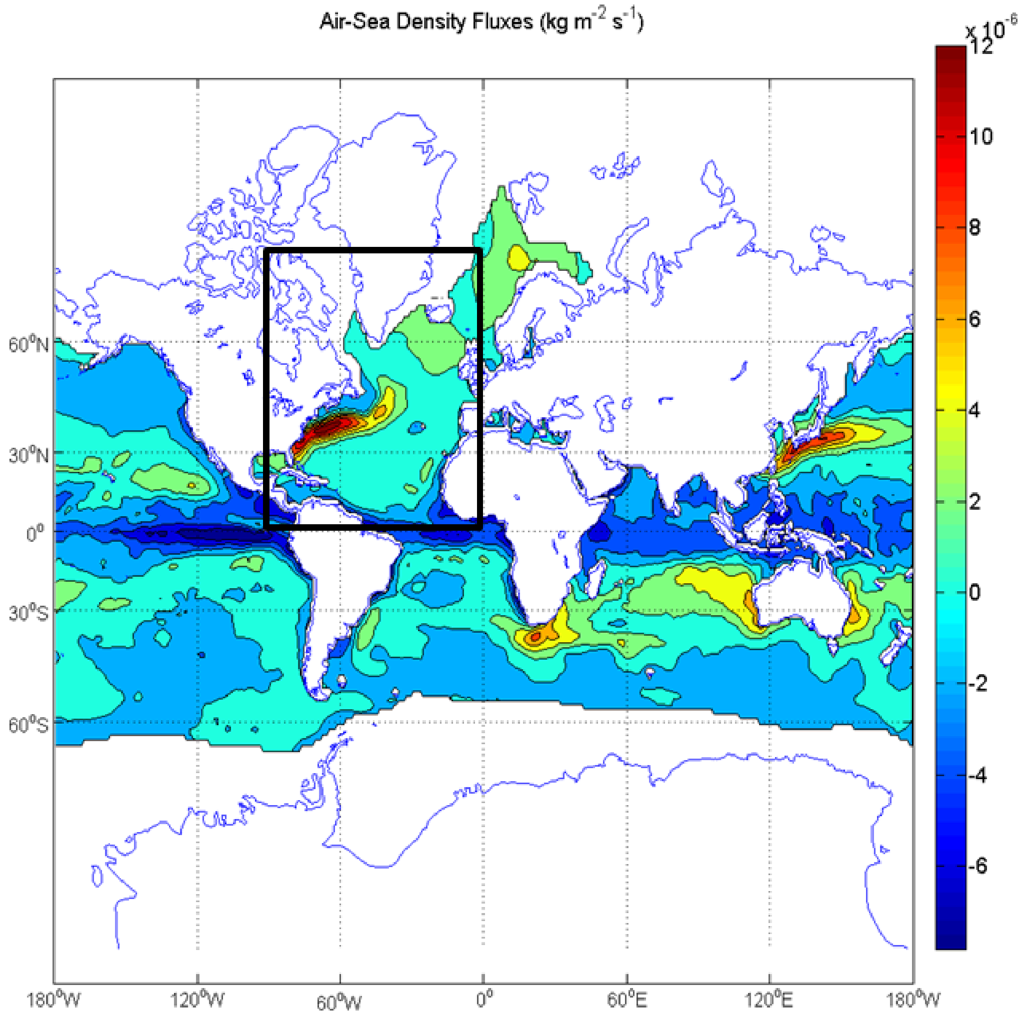

Figure 5.2: Plot of global annual average air-sea density flux (kg m^{-2} s^{-1}). The black box indicates the area over which the North Atlantic case is calculated.

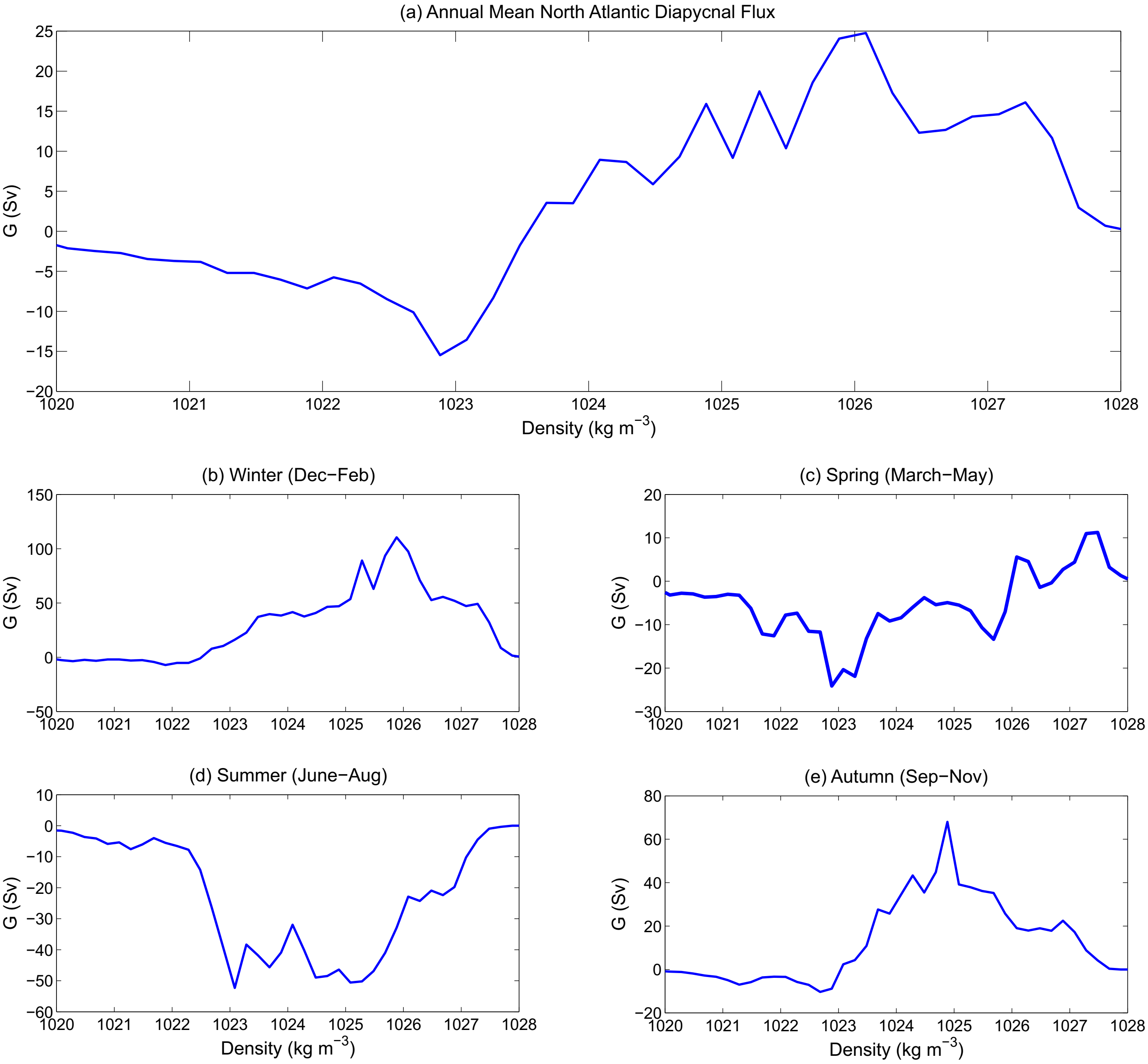

Figure 5.3: Transformation rates (Sv) over the North Atlantic averaged over: (a) the full year, (b) Winter, (c) Spring, (d) Summer and (e) Autumn

classes. The maximum diapycnal volume flux is at 1025 kg m^{-3} where the flux is 65 Sv towards more dense classes.

The overall picture given by the seasonal transformations is that of water transformed to less dense classes in the spring and summer, when the surface heat flux is positive, and water transformed into denser classes during the autumn and winter, when the ocean is losing heat to the atmosphere. This is consistent with the formation of a seasonal thermocline increasing the volume in light classes during the heating period and that seasonal thermocline breaking down during the cooling period and returning the volume to the more dense classes. As a result it is reasonable to interpret these transformations as being primarily driven by the movement of isopycnals through the water and as primarily resulting in changes in the budgeting of volume within the domain, rather than indicating a transport through the boundaries of the domain.

Annual Transformation and Formation

The annual average transformation in the North Atlantic shows maximum transformation towards lighter density classes of 16 Sv at 1023 kg m^{-3} (Fig. 5.4(a)). The maximum transformation to denser classes is 25 Sv at 1026 kg m^{-3} (Fig. 5.4(a)). The transformation is close to zero at 1020 kg m^{-3} and 1028 kg m^{-3}(Fig. 5.4(a)). This leads to: a weak formation of volume in classes less than 1023 kg m^{-3}; annual loss of volume for densities between 1023 kg m^{-3} and 1026 kg m^{-3}; finally a formation of volume for densities between 1026 kg m^{-3} and 1028 kg m^{-3} (Fig. 5.4(b)).

Assuming that the inter-annual variability in the portioning of volume between density classes is small, the annual average transformation cannot represent a change in volume within the domain. As the formation cannot result in volume changes within the domain it must be balanced by either internal diffusive fluxes of density or the lateral transport of the volume out of the domain. This formation of dense water resulting in a lateral transport may be viewed

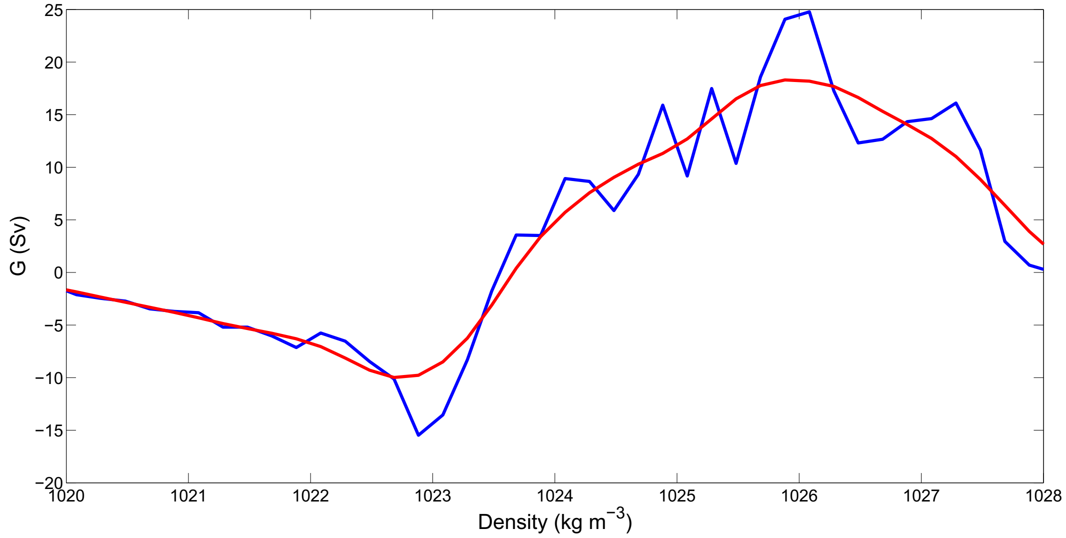

(a) Annual Mean North Atlantic Diapycnal Flux

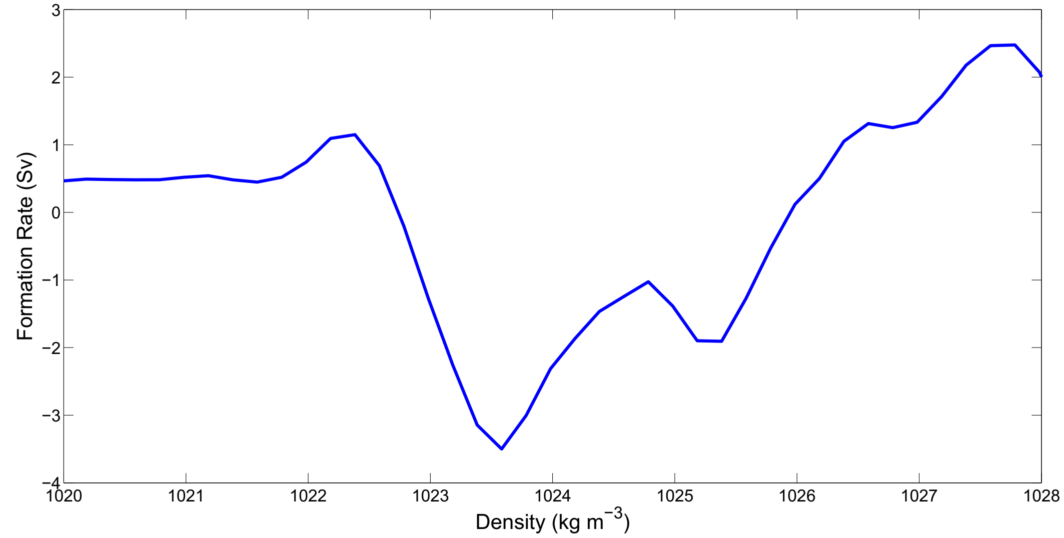

(b) Annual Mean Formation Rates (Smoothed)

Figure 5.4: (a) Annual average transformation rate (Sv), the full data in blue and smoothed data in red. (b) The formation rate (Sv) in 0.2 kg m^{-3} density classes calculated from the smoothed transformation rate.

as the lower limb of the Atlantic Meridional Overturning. The total formation rate of water denser than 1026 kg m^{-3} is 25 Sv which is larger than other estimates of the overturning the the North Atlantic, for example 17.6±3.1 Sv in Lumpkin and Speer [2007], indicating that diapycnal diffusive transfers not included in this calculation are also important.

5.1.3 Using the Walin Framework for the shelf seas and the associated complexities

The Walin Framework is useful for work on shelf edge exchange. Shelf edge exchange is driven by a range of processes which occur over a range of spatial and temporal scales. These processes include the short time scale variability driven by the tide and the highly intermittent effects of cascading, alongside longer time scale processes such as the Ekman transport associated with the slope current. Any individual observation of shelf edge exchange is likely to only catch the small proportion of processes occurring at that time and location. The strength of the Walin Framework in shelf edge exchange is that it integrates across this spatial and temporal variability to give an estimate of the total transport across this boundary in density classes. Unfortunately, because this calculation is integrated across all scales it is not possible to elucidate the various contributions from various processes.

The Walin Framework provides a useful tool to allow us to understand and evaluate the formation of water masses on the shelf. For the shelf seas the air-sea flux term is likely to be relatively straightforward to evaluate, based upon well established and high resolution reconstructions of surface heat and freshwater fluxes as well as surface density fields. In the shelf seas, unlike the deep ocean case considered in Section 5.1.2, we cannot make the assertion that the mixing is taking place somewhere away from the areas of formation. This assumption is not valid due to the considerably enhanced mixing on the shelf and the relative proximity of isopycnals to the boundary driven turbulence.

It is likely to be difficult to get a clear estimate of the diffusive mixing on the shelf at all locations so we will consider a range of potential options and provide some bounds for the transformation related to estimates of the diffusive flux.

In the temperate shelf seas, where the full water column is mixed during winter, it is possible to calculate the budgeting of volume within density classes purely from the surface density and depth. This in combination with the formation rate may be used to estimate the annual average lateral transport of water through the boundaries of the domain (Eqn. 5.1), in this case the shelf edge.

5.2 Inputs

The Walin Framework itself, as derived in Section 5.1.1 is mathematically rigorous and exact, although some of the inputs are not trivial to estimate. The calculation will be performed individually for the years 1979 to 2014 for the North-West European Shelf, here defined by 45°N to 63 °N and 13°W to 10°E. The year used here is defined as running from March to February, such that the start of the year is approximately at the end of the cooling period, and will be labelled using the the year it starts in, i.e. the year labelled 2014 runs from March 2014 to February 2015. The calculations are performed on a 1/4 degree horizontal resolution grid with the grid cells coinciding with the grid used for the ECMWF ERA-Interim 1/4 degree dataset. The domain is defined by the 200m isobath, resulting in the lateral boundaries being the 200 m isobath and the coast.

5.2.1 Surface Forcing

The surface forcing from surface heat flux and surface volume flux are calculated from the ECMWF ERA-Interim reanalysis data set. These surface fluxes are applied at 12 hour temporal resolution and a 1/4 degree horizontal resolution. These fluxes are all defined as positive downward. The heat fluxes, integrated over 12 hour time steps in units of J m^{-2}, are supplied split into multiple components: the sensible heat flux; latent heat flux; net solar radiation; and net thermal radiation. The volume flux, also integrated over the 12 hours in units of m^3m^{-2}, is supplied split into the evaporation and precipitation.

5.2.2 Surface Density

The surface density field is calculated from the ERA-Interim surface field for the sea surface temperature, also applied to 12 hours averages and a 1/4 degree horizontal resolution, with the World Ocean Atlas 2013 version 2 surface field for the the sea surface salinity. The World Ocean Atlas data used is the annual average climatological field calculated using the full time-series also supplied at 1/4 degree resolution. The World Ocean Atlas grid is offset by 1/8 degree from the ERA-Interim grid so the WOA data was linearly interpolated onto the ERA-Interim grid. The density was then calculated using the Sea Water toolbox developed by CSIRO [Morgan and Pender, 2010].

5.2.3 Diffusive flux

The diffusive flux is the most difficult term to get a clear estimate of for the shelf seas. This is due to the fact it is patchy in both space and time with variability of a few orders of magnitude which, when combined with the limited observations of this parameter, means that a whole shelf estimate of this parameter is difficult. A potential solution would be to apply the mixing from model output, however this will only give an estimate of the cross-shelf exchange that matches the model output and thus will give us limited new understanding. As a result we will simplify the problem and make a range of estimates, of increasing complexity, likely to represent the possible structure of mixing in the European Shelf.

We will use the turbulent kinetic energy (TKE) dissipation rate rather than eddy diffusivity (as discussed next in Eqns. 5.10 to 5.13) and then apply a single value representing mid-water column mixing, an observed vertical profile of TKE dissipation, and a spring-neap cycle using observed profiles.

Using Turbulent Kinetic Energy Dissipation rate

Recalling from Section 5.1.1 the equation for the density flux across an isopycnal is,

$$D_{diff} = \int_{densitysurface} K_z \frac{\partial \rho}{\partial z} \quad \partial A \tag{5.10}$$

when $densitysurface$ is the surface area of an isopycnal (m^2), K_z is the eddy diffusivity (m^{2}s^{-1}), ρ is the density (kg m^{-3}), and z is the vertical coordinate (m). We now take the Osborn relation [Osborn, 1980] linking the eddy diffusivity and the turbulent kinetic energy dissipation,

$$K_z = 0.2 \frac{\epsilon_m}{N^2} \tag{5.11}$$

where 0.2 is a mixing efficiency coefficient, ϵ_m is the turbulent kinetic energy dissipation rate (W kg^{-1}), and N is the buoyancy frequency (s^{-1}) defined as,

$$N^2 = -\frac{g}{\rho_0} \frac{\partial \rho}{\partial z} \tag{5.12}$$

where g is the gravitational constant which is taken as 9.81 m s^{-2} and ρ_0 is the reference density (kg m^{-3}). Taking equations 5.10, 5.11 and 5.12 and converting ϵ_m defined in terms of mass to ϵ_v defined in terms of volume such that it is in units of W m^{-3} gives,

$$D_{diff} = \int_{densitysurface} -0.2 \frac{\epsilon_v}{g} \quad \partial A \tag{5.13}$$

This allows us to estimate the diffusive flux of density across a surface by simply knowing the surface area of the isopycnal in question and the turbulent kinetic energy dissipation rate. This reduces the number of assumptions needed to evaluate the Walin Framework transformation rate by one.

5.2.4 Isopycnal surface area

The estimate of the isopycnal surface area, over which the diffusive flux will be integrated, is performed assuming that its horizontal extent is much larger than its vertical extent. This assumption allows us to simplify the problem to that of knowing, for each position in the grid, which isopyncals exist and the surface area of the grid cell. The lightest isopycnal present is straightforward to evaluate as it is the same as the surface density. The densest isopycnal is equivalent to the bottom density and is more difficult to estimate.

For the bottom density, we will make the assumption that once the water column is stratified the bottom density is fixed throughout the stratified period. Here the Potential Energy Anomaly (PEA) will be used as the measure of the stratification of the water column to denote periods when the water column is well mixed or stratified.

Potential Energy Anomaly

The PEA is defined as the difference between the potential energy of the water column and the potential energy of the water column if it was mixed [Simpson and Bowers, 1981],

$$\Phi = \frac{1}{h}\int_{-h}^{0} (\overline{\rho} - \rho(z))gz \quad \partial z \tag{5.14}$$

where Φ is the potential energy anomaly, h is the water depth, $\overline{\rho}$ is the depth mean density, $\rho(z)$ is the full density profile, g is the gravitational acceleration and z is the vertical coordinate. The PEA represents the amount of energy needed to fully mix a water column, with zero representing a well mixed water column and typically reaching O(10^2) J m^{-2} in the well stratified parts of the European Shelf.

The rate of change of the PEA can be expressed as a balance between the effects of surface heating attempting to stratify the water column and turbulence driven by tidal friction acting to break down stratification [Simpson and Sharples, 2012],

$$\frac{\partial \Phi}{\partial t} = \frac{\alpha g Q_i}{2 c_p} - \frac{e k_b \rho_0 |\hat{u}|^3}{h} \tag{5.15}$$

where t is time, α is the thermal expansion coefficient, Q_i is the surface heat flux, c_p is the specific heat capacity of seawater, e is the mixing efficiency, k_b is the bottom drag coefficient, and $|\hat{u}|$ is depth mean tidal current averaged over a tidal cycle. Here the first term represents the effects of surface heating on stratification and can be negative or positive depending on the sign of the surface heat flux. The second term represents the mixing by the tide and is always negative, i.e. the tidal mixing always acts to break down stratification. The wind input of mechanical energy and the surface volume input through precipitation and evaporation are neglected here.

This equation has been integrated forward in time separately for each year, defined here as running from March to February in order to make the start of year closer to the end of the cooling period and thus the minimum in stratification, assuming that the PEA is zero at the start of the year. The constants in Eqn. 5.15 have been derived using the CSIRO SeaWater toolbox [Morgan and Pender, 2010], the surface flux has been calculated as described in section 5.2.1 and the depths taken from the GEBCO bathymetry dataset and interpolated onto the same grid as the ERA-Interim data.

Tidal Amplitude

The tidal amplitude required to estimate the potential energy anomaly has been calculated using the Matlab implementation, Tidal Model Driver, of the OSU Tidal Inversion Software. This software allows the extraction of individual harmonic constituents from the OSU tidal solutions. Here we have used the European Shelf 1/30° resolution solution which has been calculated using GEBCO 1' bathymetry data and Topex Poseidon and Topex Tandem satellite altimetry data and validated using 126 tide gauges. The details of the generic solution are presented in Egbert and Erofeeva [2002] whilst the specific European Shelf case is presented in Egbert et al. [2010]. The amplitude of the M2 period barotropic tide amplitude is extracted at the centre point of each grid cell.

PEA Results

The Celtic Sea typically begins to stratify towards the end of March and the start of April building to a maximum PEA of 250 J m^{-2} by July and remaining high for approximately 2 months (Fig. 5.5(a)). Following this peak the stratification weakens until November where the PEA returns to being close to zero, indicative of a well mixed water column (Fig. 5.5(a)).

In the middle of summer, the water column is well stratified in the Celtic Sea, on the Malin Shelf and the Northern North Sea, with these regions typically having PEA above 100 J m^{-2} and in places reaching 300 J m^{-2} (Fig. 5.5(b)). The Irish Sea, English Channel and Southern North Sea are all mixed with PEA close to 0 J m^{-2}. These stratified and well-mixed regions are separated by tidal mixing fronts, controlled by the spatial distribution of tidal velocity and depth. The position of these fronts predicted by our PEA calculations compare well with the positions published previously (Simpson and Pingree [1977] and [Holt and Umlauf, 2008]). This gives confidence in the use of the PEA, with these inputs, as a measure of the stratification on the European Shelf.

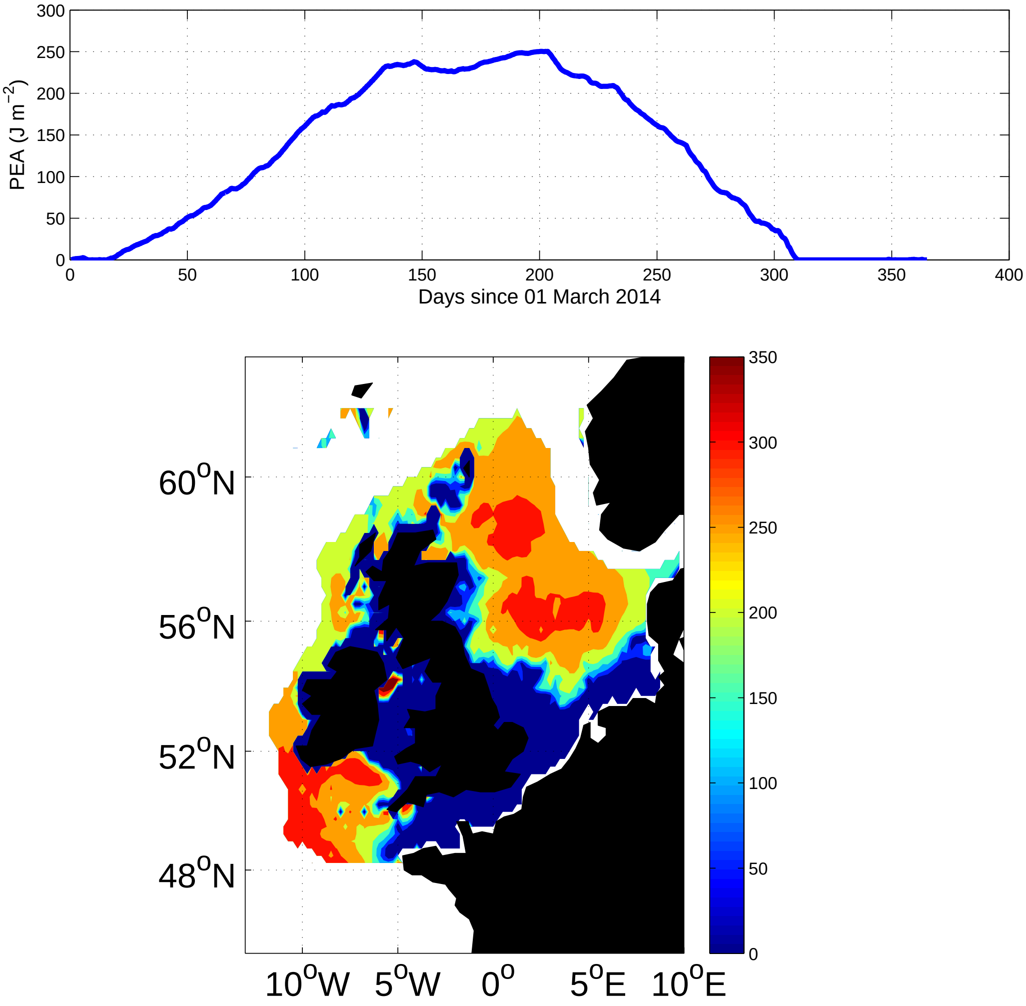

Figure 5.5: Figure showing: (a) the annual cycle of Potential Energy Anomaly (J m^{-2}) for the centre of the Celtic Sea (7°W 50°N) in year 2014; and (b) the spatial distribution of Potential Energy Anomaly (J m^{-2}) for day 200, time of maximum stratification, for the year 2014.

5.3 Air-Sea Transformation

Now we will consider the contribution to transformation on the shelf driven by air-sea fluxes of heat and salt exploring both seasonal and annual transformation rates using the inputs in section 5.2.

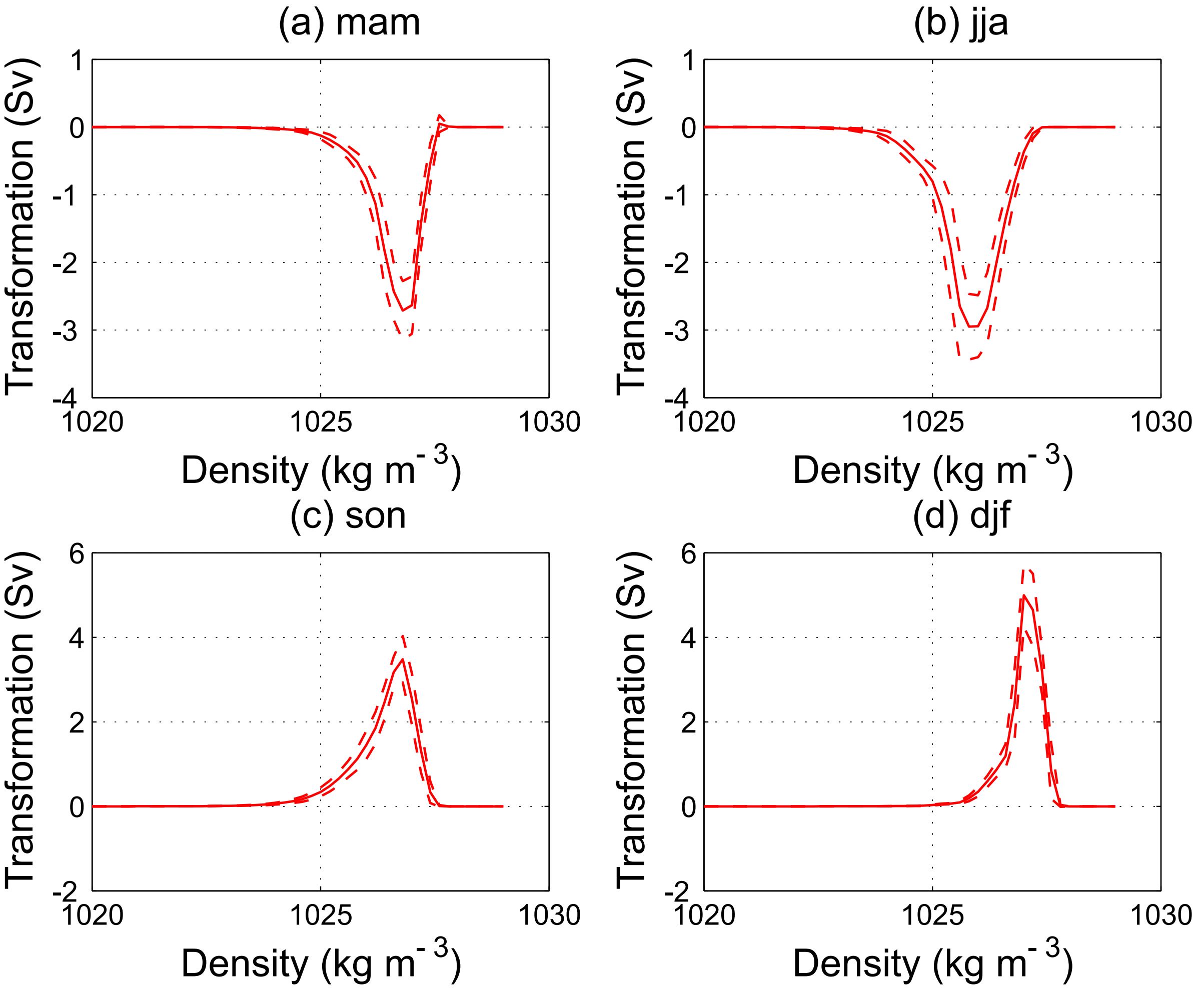

Figure 5.6: Transformation rates driven by Air-Sea forcing. The transformation rates are averaged over: (a) Spring: March, April and May; (b) Summer: June, July and August; (c) Autumn: September, October and November; and (d) Winter: December, January and February (equivalent to Fig. 5.3). The solid lines represent the mean transformation over the period 1979 to 2014 with the dashed lines showing the mean plus and minus the standard deviation over the same period.

In the spring (March to May) the air-sea driven transformation is negative and largest at 1026.5 kg m^{-3} driving a transformation towards lighter waters of 2.6 Sv (Fig. 5.6(a)). In summer (June to August) the air-sea term is again negative, indicating increasing stratification, reaching 3 Sv (Fig. 5.6(b)). In the autumn (September to November) the sign of the surface heat flux changes, as the ocean is losing heat to the atmosphere. As a result of this the transformation driven by air-sea forcing is moving volume towards more dense classes peaking at 3 Sv at 1027 kg m^{-3} (Fig. 5.6(c)). Finally, in winter the air-sea forcing drives a transformation peaking at 5 Sv directed towards denser water (Fig. 5.6(d)). These signals are consistent with the seasonal cycle in stratification seen on the European Shelf. In the spring and summer the transformation is negative, towards lighter water, consistent with the generation of less dense water in the upper water column during the stratified period . In the autumn and winter the transformation is positive, towards denser water, represnting the loss of heat from the surface ocean resulting in the breakdown of stratification and the light surface layer becoming dense water. The inter-annual variability in this signal is small, with the standard deviation reaching only ± 0.5 Sv, and is considerably smaller than the seasonal signal. This is unsurprising as the cycle in stratification is seen every year in the shelf although there is some variability in the timing and strength of stratification [Sharples et al., 2006], consistent with the inter-annual variability seen in the transformation.

The annual average transformation driven by air-sea forcing shows a negative peak, towards lighter waters, of 0.5 Sv at 1025.8 kg m^{-3} and a positive peak of 1.1 Sv at 1027 kg m^{-3} (Fig. 5.7). These transformations show the effect of air-sea forcing in reinforcing the contrast by making light waters lighter and dense waters denser. This signal of air-sea forcing generating more contrast is consistent with previous studies in other open ocean regions [Badin et al., 2013, Marshall et al., 1999, Speer and Tziperman, 1992] and is perhaps to be

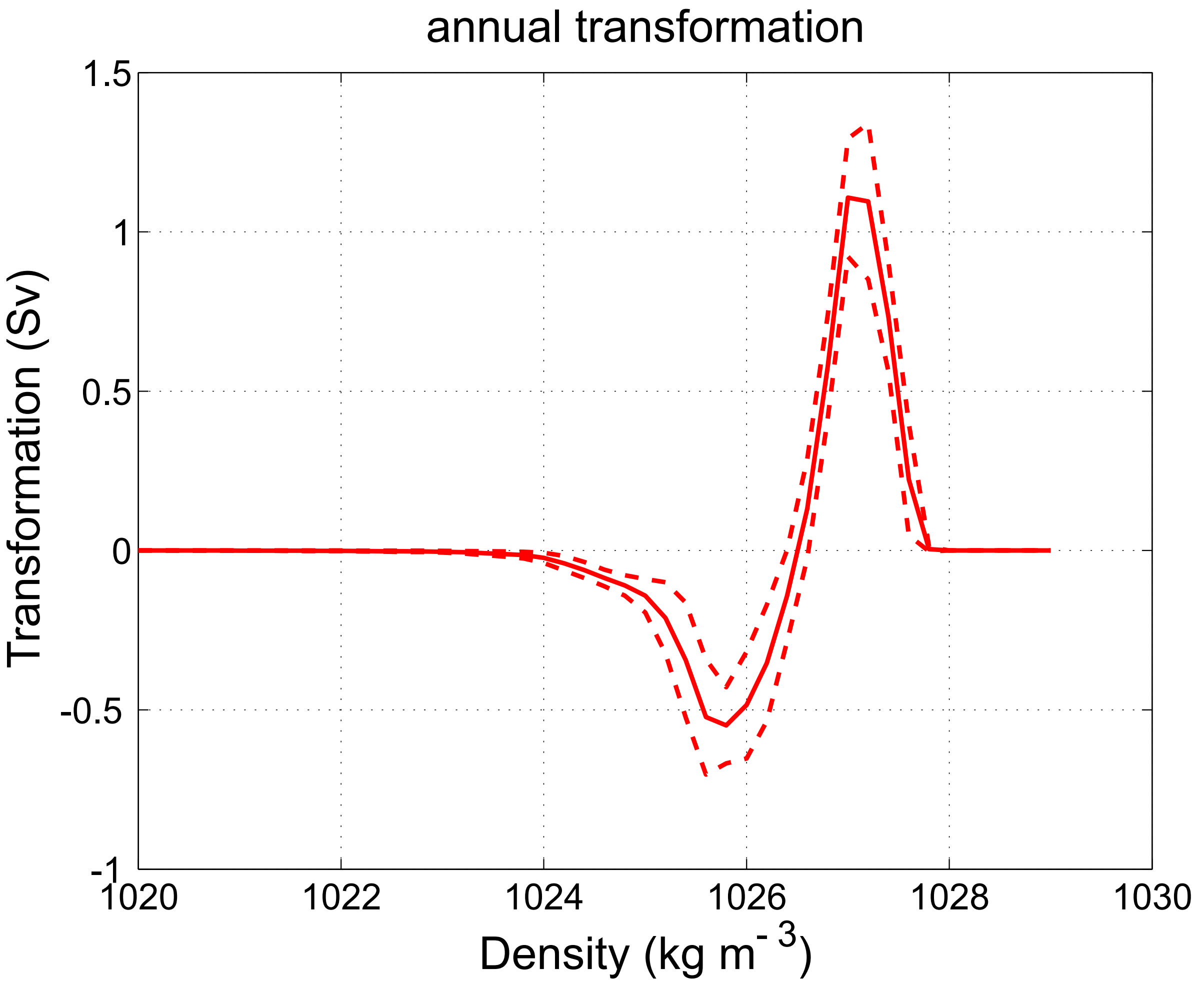

Figure 5.7: Transformation rates driven by Air-Sea forcing. The transformation rates are averaged over the full annual cycle. The solid lines represent the mean transformation over the period 1979 to 2014 with the dashed lines showing the mean plus and minus the standard deviation over the same period.

expected as mixing is considered to play an important role in setting the stratification of shelf seas [Holt and Umlauf, 2008] and is likely to act to reduce contrast.

5.4 Idealised closure: zero transport

Now we will make an estimate of the mixing required to balance the air-sea fluxes discussed above. Three assumptions will be made: firstly that the shelf seas are in a steady state on an annual time scale, $\frac{\partial \Delta V}{\partial t} = 0$; secondly the surface volume flux is small, $\Psi_{P-E} = 0$; and thirdly that the transport across the shelf edge is small, $\Psi_{lateral} = 0$. These assumptions lead to Eqn 5.3 becoming equal to zero,

$$M \Delta \rho = \frac{\partial \Delta V}{\partial t} - \Psi_{P-E} + \Psi_{lateral} = 0, \tag{5.16}$$

implying that the formation rate must be zero, $M = 0$, as $\Delta \rho$ is non-zero. Recall that the formation rate is defined as $M = -\frac{\partial G}{\partial \rho}$. The transformation rate, G, must go to zero at densities less than the minimum, or greater than the maximum, density within the region, as the surface outcrop required for air-sea forcing and the isopycnal area required for diffusive transformation are both zero. Given these assumptions and the constraint on transformation at very low and high density classes we know that the transformation rate must be zero everywhere, $G = 0$ and the diffusive transformation must balance the air-sea forcing.

These requirements mean that we would expect to see a transformation driven by diffusion that is 0.5 Sv at 1025.8 kg m^{-3} and -1.1 Sv at 1027 kg m^{-3} in order to balance the air-sea fluxes discussed in Section 5.3. The diffusive flux is defined as,

$$G_{diff} = -\frac{\partial D_{diff}}{\partial \rho}, \tag{5.17}$$

where,

$$D_{diff} = \int_{densitysurface} -0.2\frac{\epsilon_{m^3}}{g} \quad \partial A \tag{5.18}$$

Then making the simplification that the turbulent kinetic energy dissipation rate (ϵ) is constant throughout the regime Eqn. 5.18 becomes,

$$D_{diff} = -\frac{0.2\epsilon A(\rho)}{g} \tag{5.19}$$

where $A(\rho)$ is the surface area of the isopycnal ρ. Substituting into Eqn. 5.17 gives,

$$G_{diff} = \frac{0.2\epsilon}{g}\frac{\partial A}{\partial \rho} \tag{5.20}$$

We will now take an idealised view of the isopycnal surface area (A) for a shelf sea. The area of isopycnals must go to zero at very large and very small densities, as these density values will not exist in the domain. Further, thinking about a shelf sea reaching to a tidal mixing front, we would expect middle values of density to have the largest surface area, as these will extend from the tidal mixing front to the shelf break (Fig. 5.8(a)). The differential of these areas with respect to density give a positive result from light to mid density classes, as the area is increasing from zero to the maximum, and a negative result from mid to high density classes, as the area drops from the maximum back to zero (Fig. 5.8(a)). As the other terms in the diffusive transformation are scalars and positive (Eqn. 5.20) the transformation from diffusion will have the same sign as the differential of the area, i.e positive at low values of density and negative at high values of density, which is consistent with the signs required to balance the air-sea forcing.

Taking the total stratified area of the European Shelf as $\Delta A = 10^{11}\text{m}^2$; assuming that the distance in density space between the minimum density and the value of density with maximum area is $\Delta\rho = 1$ kg m^{-3}; taking gravitational

(a) Idealised Area of Isopycnals

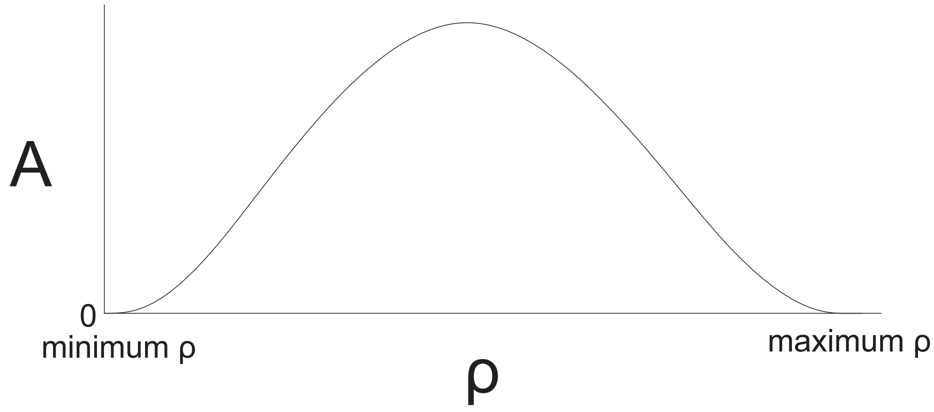

(b) Differential of Isopycnal Areas

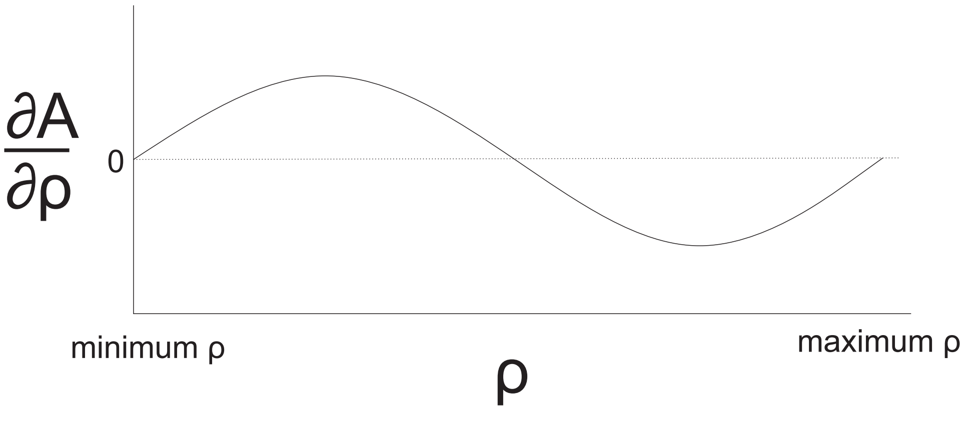

Figure 5.8: Plots of: (a) the expected distribution of the surface area of isopycnals, with low densities having zero area followed by increasing areas until some middle value of density after which the area returns to zero; and (b) the differential of the isopycnal areas as drawn in (a) showing a positive differential at lower densities and a negative differential at high values of density.

acceleration as $g = 10$ m s^{-2} and the required transformation as $G = 10^6$ m^{3}s^{-1} the required value for turbulent kinetic energy dissipation is $\epsilon = 5\text{x}10^{-4}$ W m^3.This value for turbulent kinetic energy dissipation is within the range of dissipations observed within the shelf seas [Palmer et al., 2013]. This estimate is, however, larger than observational estimates of dissipation within the pycnocline and away from topographic features (Table 5.1).

Table 5.1: Observational estimates of the pycnocline TKE dissipation rate in the literature. Estimates (4) and (5) are also taken from Inall et al. [2011].

	Study	Location	Dissipation (W m^3)
(1)	Palmer et al. [2008]	Celtic Sea	$6.7\text{x}10^{-5}$
(2)	Palmer et al. [2008]	Celtic Sea	$5.3\text{x}10^{-5}$
(3)	Inall et al. [2011]	Celtic Sea	$2.08\text{x}10^{-4}$
(4)	Sharples et al. [2009]	Celtic Sea	$2.15\text{x}10^{-4}$
(5)	Inall et al. [2000]	Malin Shelf	$1.8\text{x}10^{-5}$
(6)	Rippeth and Inall [2002]	Malin Shelf Edge	$4.9\text{x}10^{-5}$
(7)	Rippeth and Inall [2002]	Malin Shelf Edge	$2.2\text{x}10^{-4}$
(8)	Rippeth and Inall [2002]	Malin Shelf	$2.7\text{x}10^{-5}$
(9)	Rippeth and Inall [2002]	Malin Shelf	$2.13\text{x}10^{-5}$

This indicates that it is possible that a large proportion of the annual air-sea transformation seen in Section 5.3 can be accounted for through vertical mixing on the shelf, although the fact the estimate is slightly higher than some observation estimates indicates that air-sea forcing is potentially balanced by a combination of diapycnal diffusion and lateral exchange.

5.5 Realistic closure for zero transport

Here a more accurate estimate of the mixing required to balance the air-sea forcing is presented. This is calculated using the same equation as the previous section (Eqn. 5.20) in combination with the surface area of the isopycnals calculated using the method described in Section 5.2.4. This method yields a time-series of isopycnal areas. The high density classes maintain the same

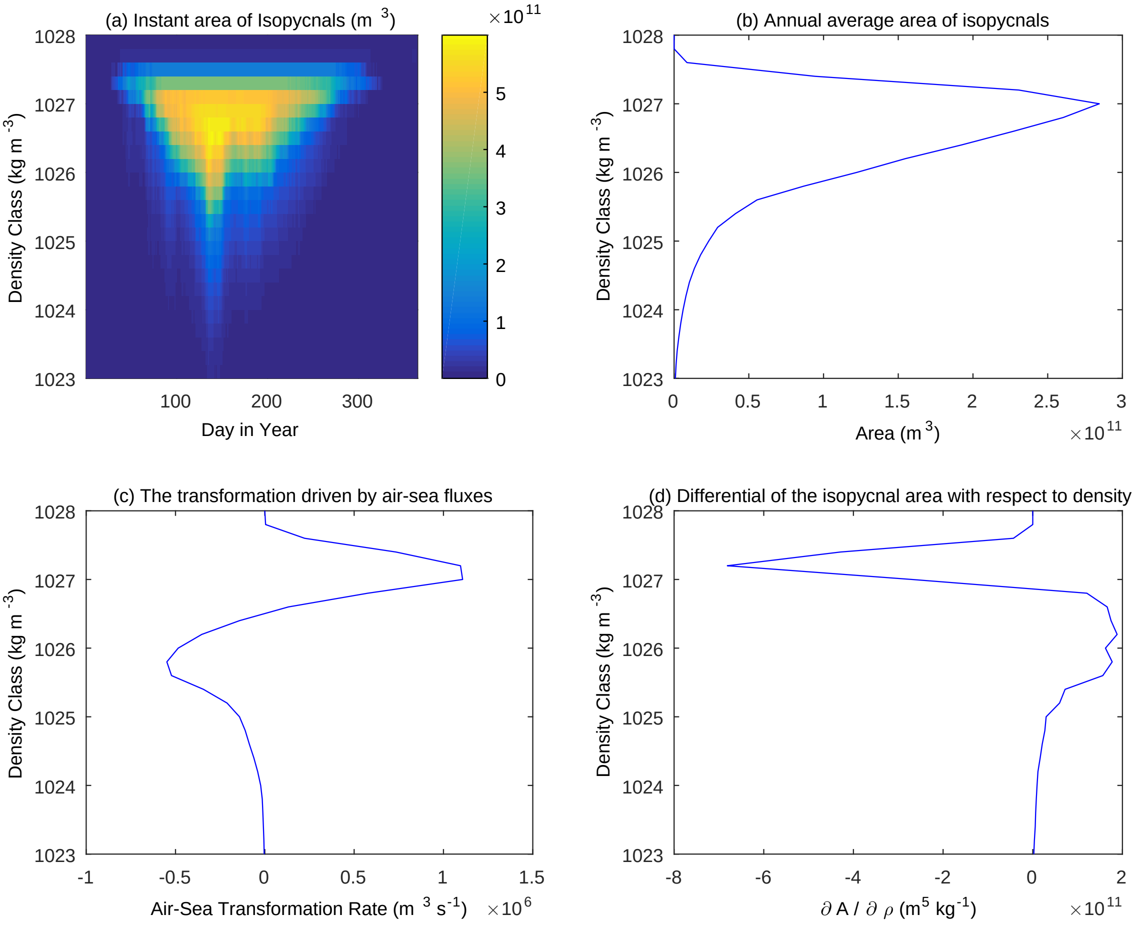

Figure 5.9: Plots showing various aspects of the calculated area of isopycnals for the year 2015 as used in the calculation of the TKE dissipation required to balance air-sea fluxes. (a) The instantaneous area of each isopycnal for each 12 hour step, (b) the annual average area of the isopycnals, (c) the annual average transformation driven by air-sea forcing and (d) the differential of isopycnal area with respect to density.

surface area throughout the stratified period, which is to be expected as once isolated from the surface forcing the bottom layer only undergoes slow warming driven by mixing at the pycnocline. The lighter isopycnals grow as stratification takes hold and then lose surface area as stratification is broken down (Fig. 5.9(a)). This difference between the behaviours of the denser and lighter isopycnals leads to a skewed distribution of area in the annual average, with the maximum annual average area towards the denser classes with a long tail of lighter isopycnals with a small, but non-zero, annual average area (Fig. 5.9(b)). The differential of the surface area of the isopycnals has a similar structure to the air-sea forcing although with the opposite sign (Fig. 5.9(c) and (d)). This reinforces the suggestion that diffusive transformation can, at least partially, cancel the air-sea forced transformation as set out in Fig. 5.8.

Applying the simplified equation for the diffusive transformation (Eqn. 5.20) to each density class individually such that it exactly balances the air-sea transformation yields values of turbulent kinetic energy dissipation rate in the range 2.3x10^{-4} to 3.9x10^{-5} W m^{3} . Whilst these give a range of possible values for the turbulent kinetic energy dissipation the application of Eqn. 5.20 in this manner does break the simplification of a constant ϵ through the regime. A constant value of epsilon has also been calculated, which does not break the assumption, such that it minimises the total cross shelf exchange, which is defined as $\sum_{\rho_{min}}^{\rho_{max}} |(G_{AS} + G_{diff})|$. This gives a value of turbulent kinetic energy dissipation of 1.5x10^{-4} W m^{3}. This is similar to the value derived using a more idealised area distribution presented in Section 5.4 and is again larger than some observational estimates of mid-water column mixing indicating a role for lateral exchange.

The annual transformation driven by this value of TKE dissipation is not zero for all density classes (Fig.5.10). It is representative of a minimum possible transformation and thus transport given the assumption that the TKE

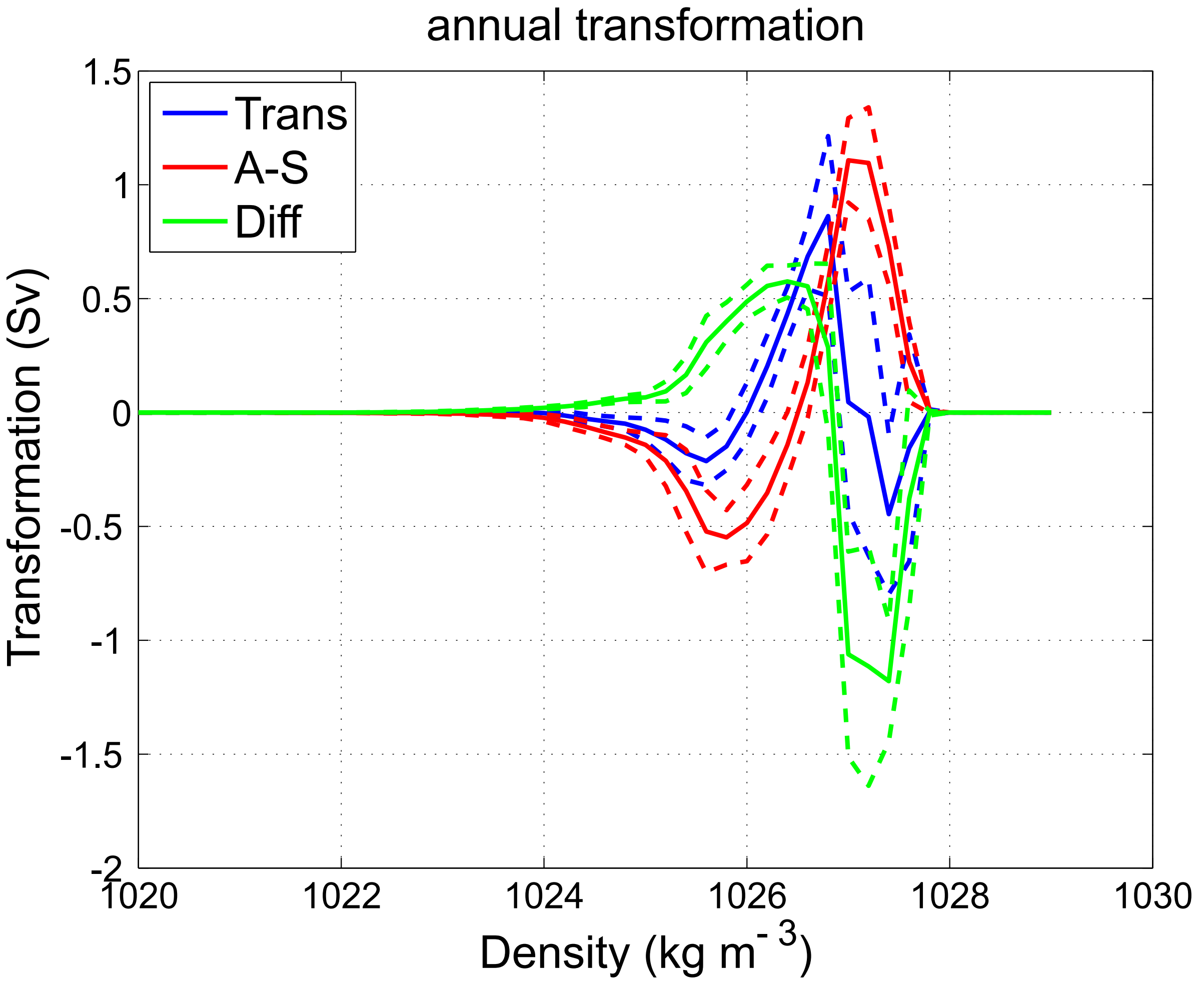

Figure 5.10: Transformation (Sv) rates for $\epsilon = 1.5\text{x}10^{-4}$ W m³ driven by (Red) Air-Sea forcing, (Green) Diffusion across density surfaces, and (Blue) their sum. The transformation rates are averaged over the full annual cycle. The solid lines represent the mean transformation over the period 1979 to 2014 with the dashed lines showing the mean plus and minus the standard deviation over the same period.

dissipation does not vary in space or time. The fact that the transformation is non-zero in many classes is due to the offset between the air-sea forcing and diffusive forcing, with diffusion being offset slightly towards denser classes. This can be understood by considering the fact that, at any location, the air-sea forcing is only applicable to the lightest classes present as that is the class that will be at the surface, whilst the diffusive forcing acts on every density class present at the location. This offset leads to a negative, towards lighter waters, transformation of 0.2 Sv at 1025.5 kg m^{-3} and 0.5 Sv at 1027.5 kg m^{-3} either side of a positive transformation, towards denser waters, of 0.8 Sv at 1026.7 kg m^{-3} (Fig.5.10). This would represent an annual loss of volume between 1025.5 kg m^{-3} and 1026.7 kg m^{-3} and a gain of volume between 1026.7 kg m^{-3} and 1027.5 kg m^{-3} (Fig.5.10).

5.6 Realistic value for Turbulent Kinetic Energy dissipation rate

In the previous sections the values of TKE Dissipation needed to balance the air-sea forcing, and result in small exchange across the shelf edge, were explored. Now we will use observational evidence to set the value of TKE Dissipation to a feasible value for the European Shelf with three levels of complexity: a single value applied throughout the regime; an observed profile of TKE dissipation scaled to the local density range; and a profile which varies with a spring-neap cycle.

The inputs for these will be taken from two Vertical Microstructure Profiler (VMP) time-series in the Celtic Sea during the summer of 2012. These two time-series were collected at a spring tide, days 171.8 to 173.5, and at the subsequent neap tide, days 177.4 to 178.0. These two time-series show a typical distribution of TKE dissipation for the shelf seas, with enhanced turbulence near the surface and bottom boundary, in both depth and density space, driven by shear generated by the wind and bottom friction associated with the tide

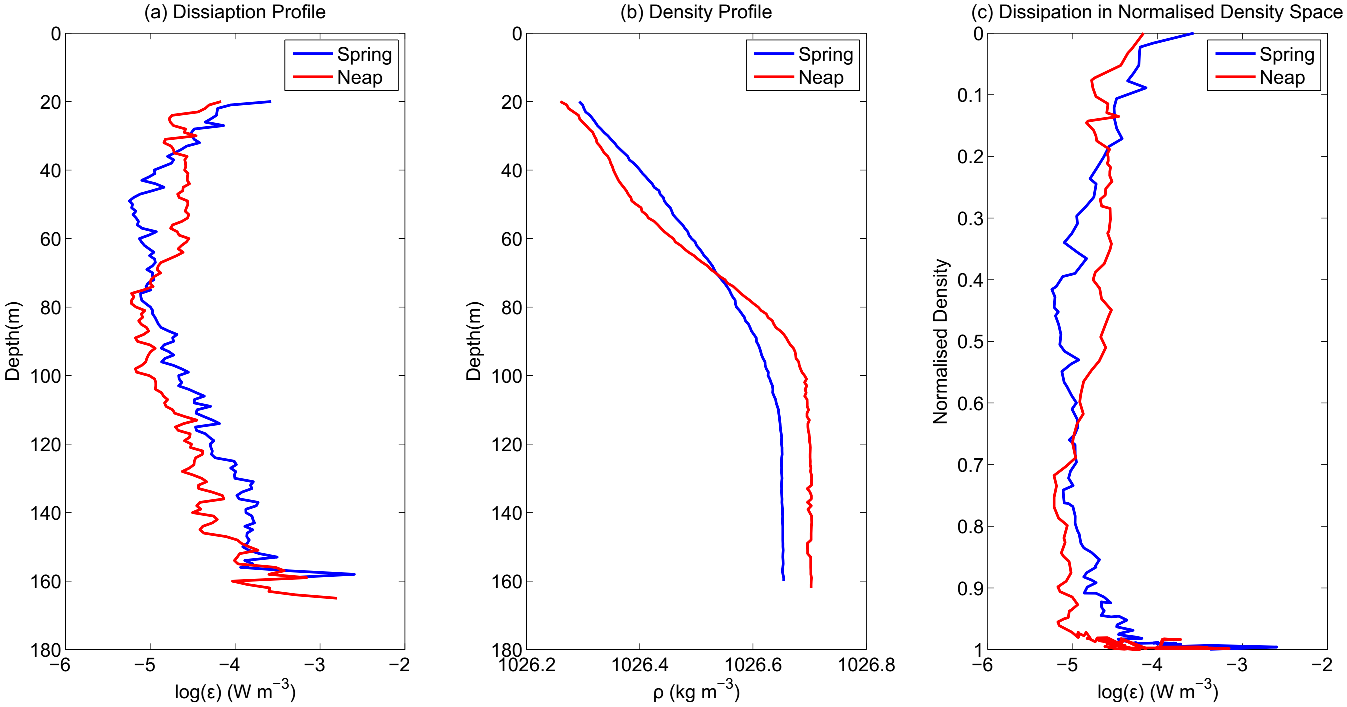

Figure 5.11: Observational data from the Celtic Sea taken from a Vertical Microstructure Profiler in the summer of 2012. Two observation periods are presented; one at a a spring tide (blue); and one at a neap tide (red). Profiles of: (a) the TKE dissipation rate derived from VMP observations against depth and averaged over the observation period, (b) the vertical density structure averaged over the observation period and (c) the TKE dissipation plotted in normalised density space where 0 is the minimum density observed and 1 is the maximum density observed.

respectively (Fig. 5.11 (a) and (c)). In the boundary layers the TKE dissipation can reach 10^{-3} to 10^{-2} W m^{-3} however it is typically 10^{-5} W m^{-3} in the mid-water column (Fig. 5.11 (a) and (c)).

5.6.1 Single Value

The most simple application of mixing to the Walin Framework is to assume a constant value for TKE dissipation throughout the regime, in space and time. The appropriate value has been calculated using the profiles presented in Fig. 5.11 by averaging the TKE dissipation from the bottom of the surface well mixed layer to the top of the bottom well mixed layer, both diagnosed here as being 0.05 kg m^{-3} from the minimum, or maximum, observed density. This gives a value for TKE dissipation of $\epsilon = 2.8\text{x}10^{-5}$ W m^{-3}.

The seasonal transformation driven by air-sea fluxes is identical to that discussed in Section 5.3, where the transformations match that expected from the annual cycle in stratification seen in many parts of the European shelf. The seasonally averaged transformation due to diffusion is generally weaker than the air-sea forcing. In spring, the diffusion only reaches ± 0.1 Sv compared to an air-sea transformation of -2.6 Sv, indicating that the air-sea forcing is dominant and generates stratification. In summer, the air-sea forcing is again dominant and generates stratification although towards denser classes the diffusion becomes important, also driving a transformation towards lighter classes, which is consistent with mixing transferring heat from the surface into the bottom layers. In autumn, the air-sea forcing is reinforced by diffusion, although the diffusion is much weaker than the air-sea forcing, driving light classes of water towards denser classes, indicating a role for both processes in the breakdown of stratification. Finally in winter, the transformation driven by diffusion is close to zero as the shelf is well mixed everywhere and as a result the surface area of isopycnals is small (Fig. 5.12). These general features of the seasonal transformation are seen throughout the following estimates of TKE dissipation,

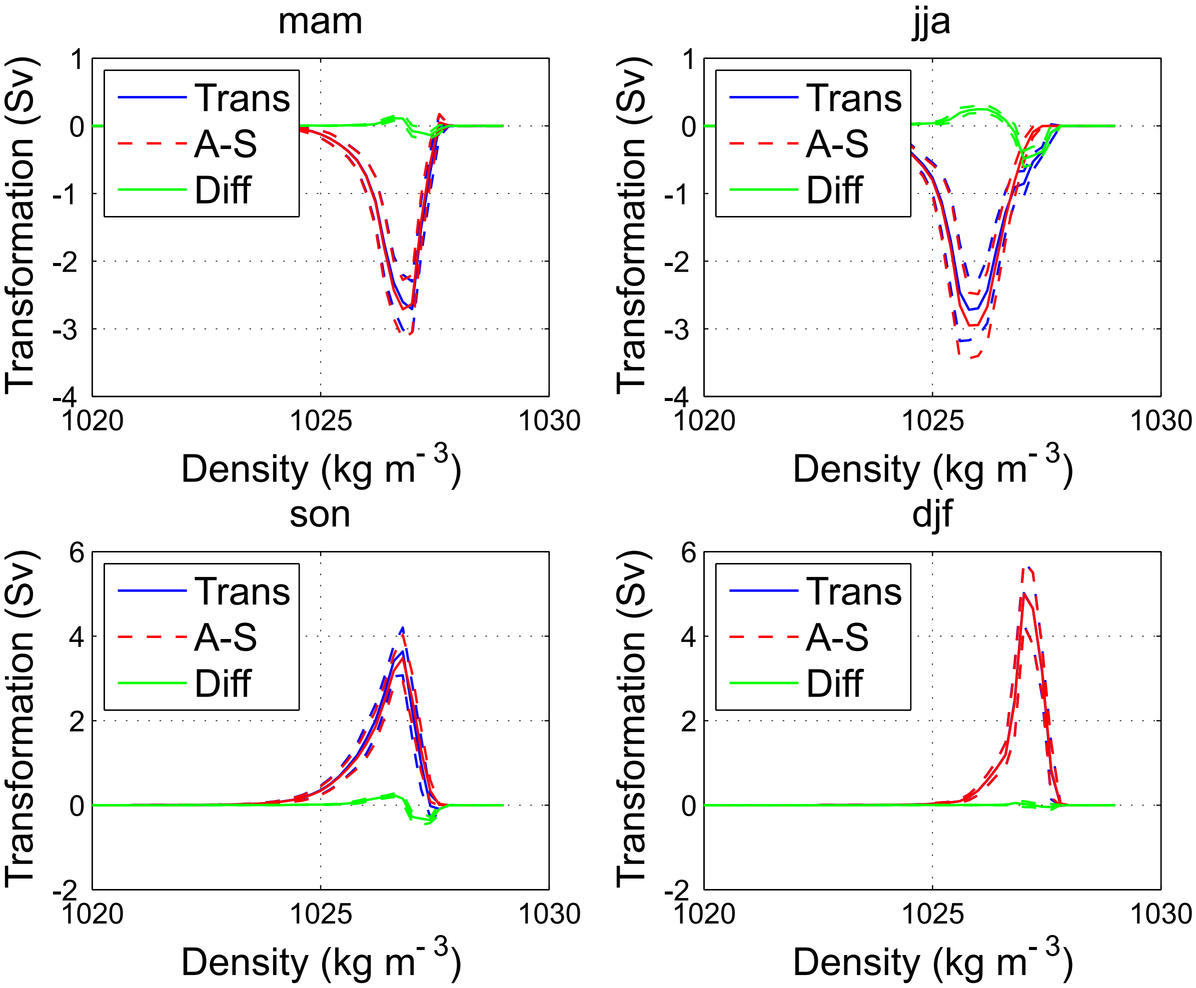

Figure 5.12: Transformation rates (Sv) for $\epsilon = 2.8 * 10^{-5}$ W m^{-3} driven by (Red) Air-Sea forcing, (Green) Diffusion across density surfaces, and (Blue) their sum. The transformation rates are averaged over: (a) Spring: March, April and May; (b) Summer: June, July and August; (c) Autumn: September, October and November; and (d) Winter: December, January and February. The solid lines represent the mean transformation over the period 1979 to 2014 with the dashed lines showing the mean plus and minus the standard deviation over the same period.

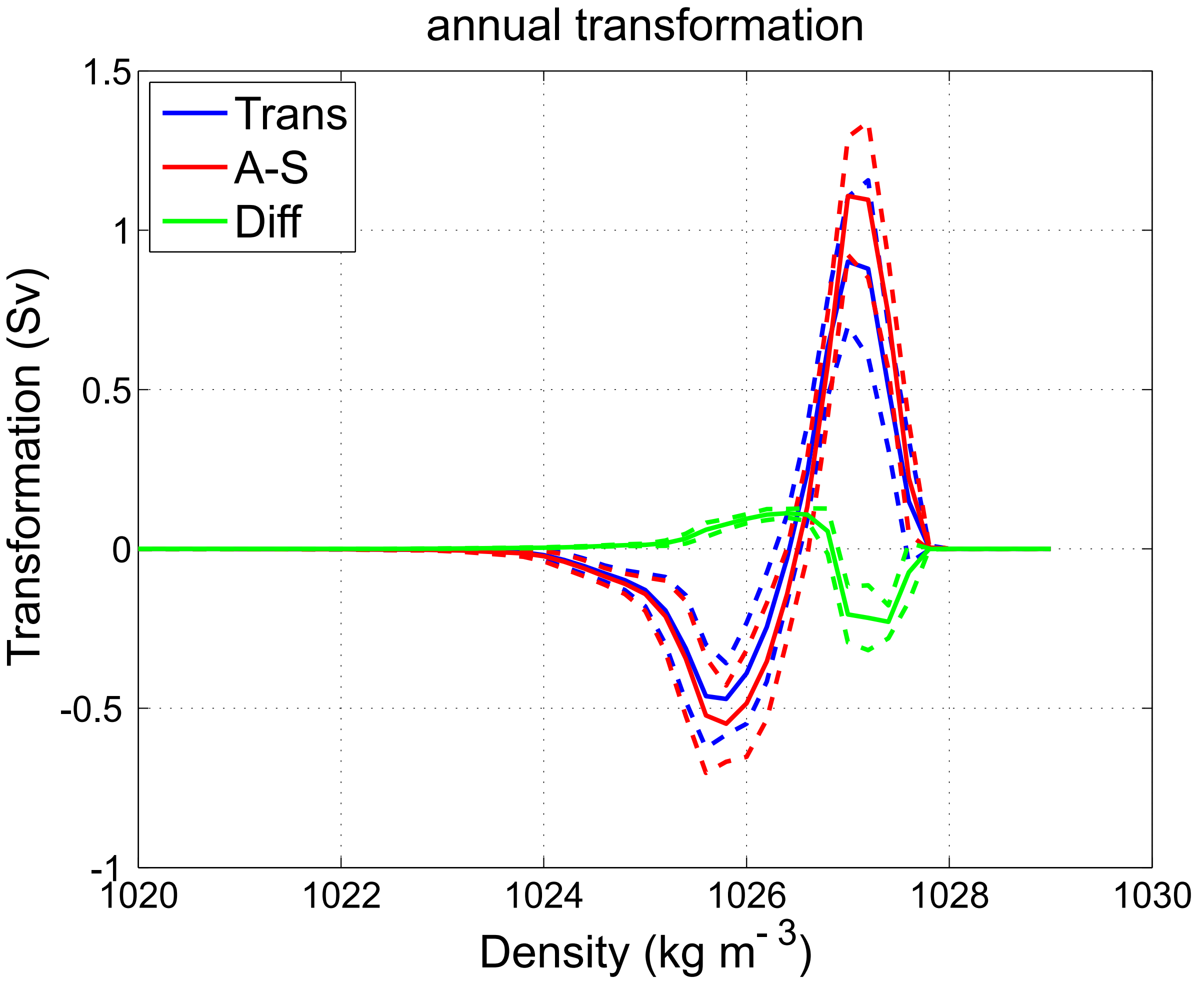

Figure 5.13: Transformation rates (Sv) for $\epsilon = 2.8 * 10^{-5}$ W m^{-3} driven by (Red) Air-Sea forcing, (Green) Diffusion across density surfaces, and (Blue) their sum. The transformation rates are averaged over the full annual cycle. The solid lines represent the mean transformation over the period 1979 to 2014 with the dashed lines showing the mean plus and minus the standard deviation over the same period.

although of course the precise ratio of mixing to air-sea forcing changes, so will not be repeated for every case.

The largest contribution to the annual transformation is as a result of the air-sea forcing, with the air-sea forcing generating contrasts in density. This air-sea forcing is opposed by the diffusive forcing. However, the diffusive forcing is weaker than the air-sea forcing, 0.1 Sv compared to 0.5 Sv at low densities and 0.2 compared to 1.1 Sv at high densities (Fig. 5.13). This would result in an overall gain of volume at the highest, centred around 1027.5 kg m^{-3}, and lowest classes, centred around 1024.5 kg m^{-3}, and a loss of volume at middle classes, centred around 1026.5kg m^{-3}.

5.6.2 Vertical Profile

Here the mixing has been applied using the average of the two profiles, in normalised density space, presented in Fig. 5.11(c). This profile has been scaled to match the maximum and minimum density values, calculated as in Section 5.2.4, at each position in space and time. The value of TKE dissipation has then been taken by linearly interpolating the isopycnal density onto this scaled profile.

The largest contribution to the annual average transformation is air-sea forcing, as in the previous case. The diffusive transformation is again weak, reaching a maximum magnitude of 0.2 Sv, and opposing the contrast being generated by the air-sea forcing. In this case the transformation in lighter classes is reduced relative to the single value of TKE dissipation case although denser classes are similar. This is a result of the depth averaged TKE dissipation rate, used in the previous section, capturing some of the enhanced dissipation at the boundaries. This results in the enhanced boundary dissipation being partially applied throughout the water column rather than being limited to the denser classes.

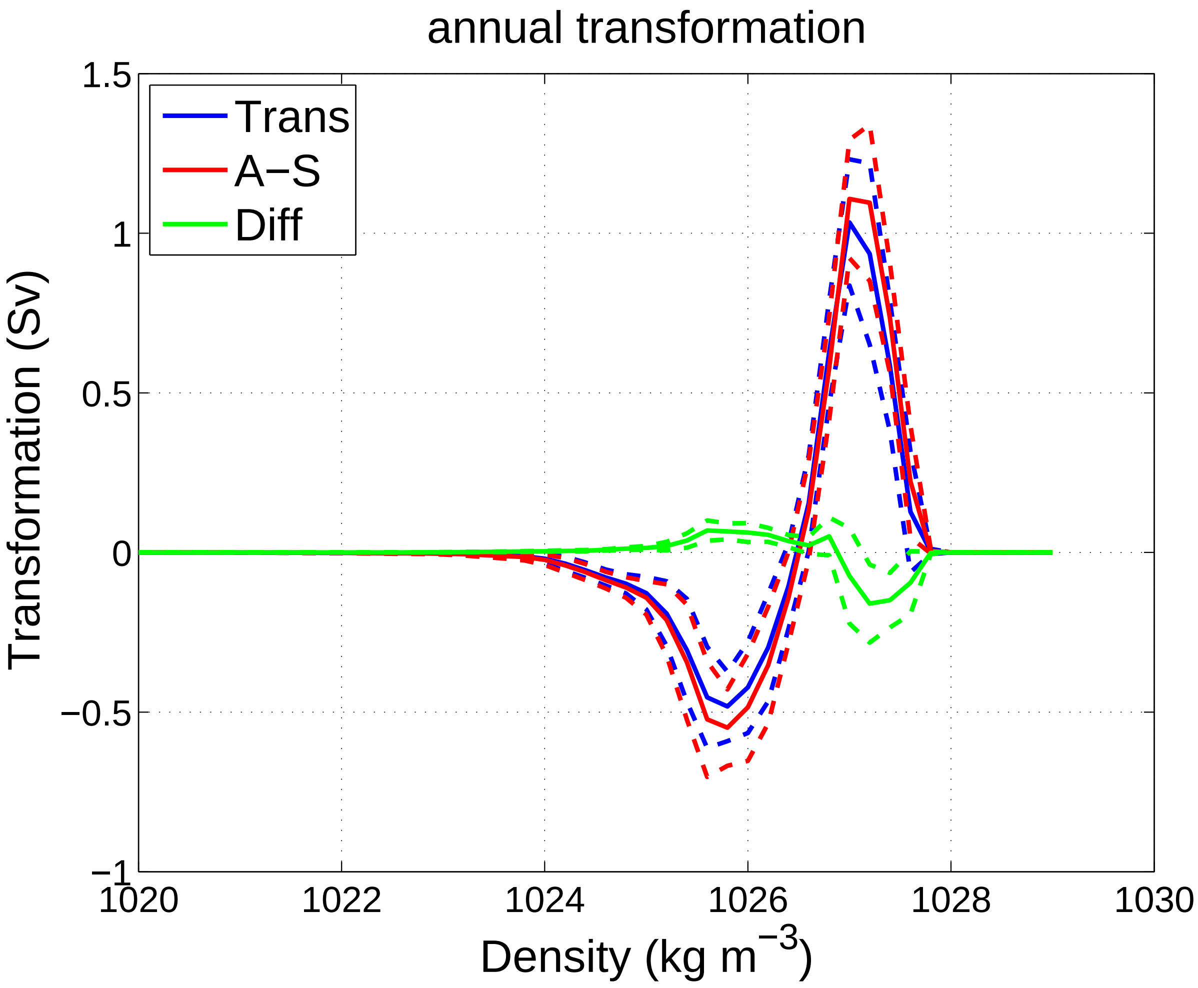

Figure 5.14: Transformation rates (Sv) using the TKE dissipation profile in Fig. 5.11 driven by (Red) Air-Sea forcing, (Green) Diffusion across density surfaces, and (Blue) their sum. The transformation rates are averaged over the full annual cycle. The solid lines represent the mean transformation over the period 1979 to 2014 with the dashed lines showing the mean plus and minus the standard deviation over the same period.

5.6.3 Spring-Neap Cycle

Now the mixing is applied again using the observed profiles presented in Fig. 5.11(c), however, this time including a spring-neap cycle. This has been achieved by taking the spring and neap profiles as the two end limits and then applying a sinusoidal variation between the two with a spring-neap period,

$$\epsilon(z,t) = F_{spring}(z) cos(\omega t + \phi) + F_{neap}(z)(1 - cos(\omega t + \phi)) \tag{5.21}$$

where F_{spring} and F_{neap} are piecewise linear functions describing the vertical structure seen in Fig. 5.11(c) for the spring and neap profiles respectively, ω is the angular frequency of the spring-neap cycle and ϕ is the phase at the start of the year.

In this final case the transformation is again dominated by the air-sea forcing and has only minor differences from the previous two cases (Fig. 5.15). This indicates that, whilst it is important on shorter time scales, when applied over an entire year the effect of the spring-neap cycle on water-masses is small. This would not necessarily be the case for all tracers however, for example nutrients where periodic cycling between more and less turbulent states could be advantageous for phytoplankton growth [e.g., Pingree et al., Sharples, 2008]. This calculation for the transformation rate will be used through the following sections.

5.7 Implied cross shelf edge transport

We can now calculate the formation rate of volume, which is the convergence of the transformation, using the equation 5.2. This shows a dominance of air-sea forcing generating contrast on the shelf. There are positive formation rates, volume gain, in classes centred on 1025.6 kg m^{-3} and 1027.5 kg m^{-3} reaching 0.15 Sv ad 0.45 Sv within a density class (0.2 kg m^{-3}) respectively and a volume

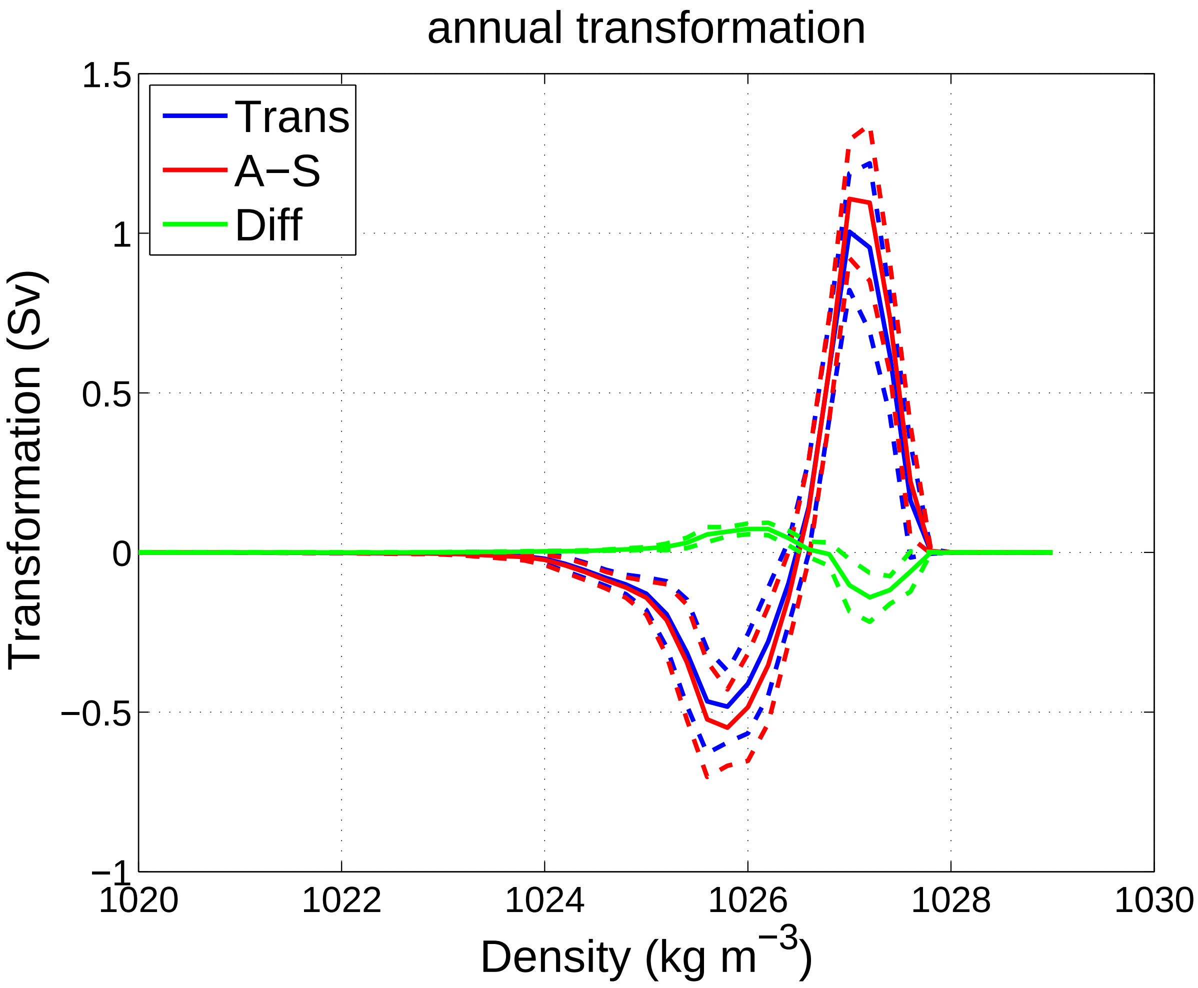

Figure 5.15: Transformation rates (Sv) using the TKE dissipation profile in Fig. 5.11 with a spring-neap cycle driven by (Red) Air-Sea forcing, (Green) Diffusion across density surfaces, and (Blue) their sum. The transformation rates are averaged over the full annual cycle. The solid lines represent the mean transformation over the period 1979 to 2014 with the dashed lines showing the mean plus and minus the standard deviation over the same period.

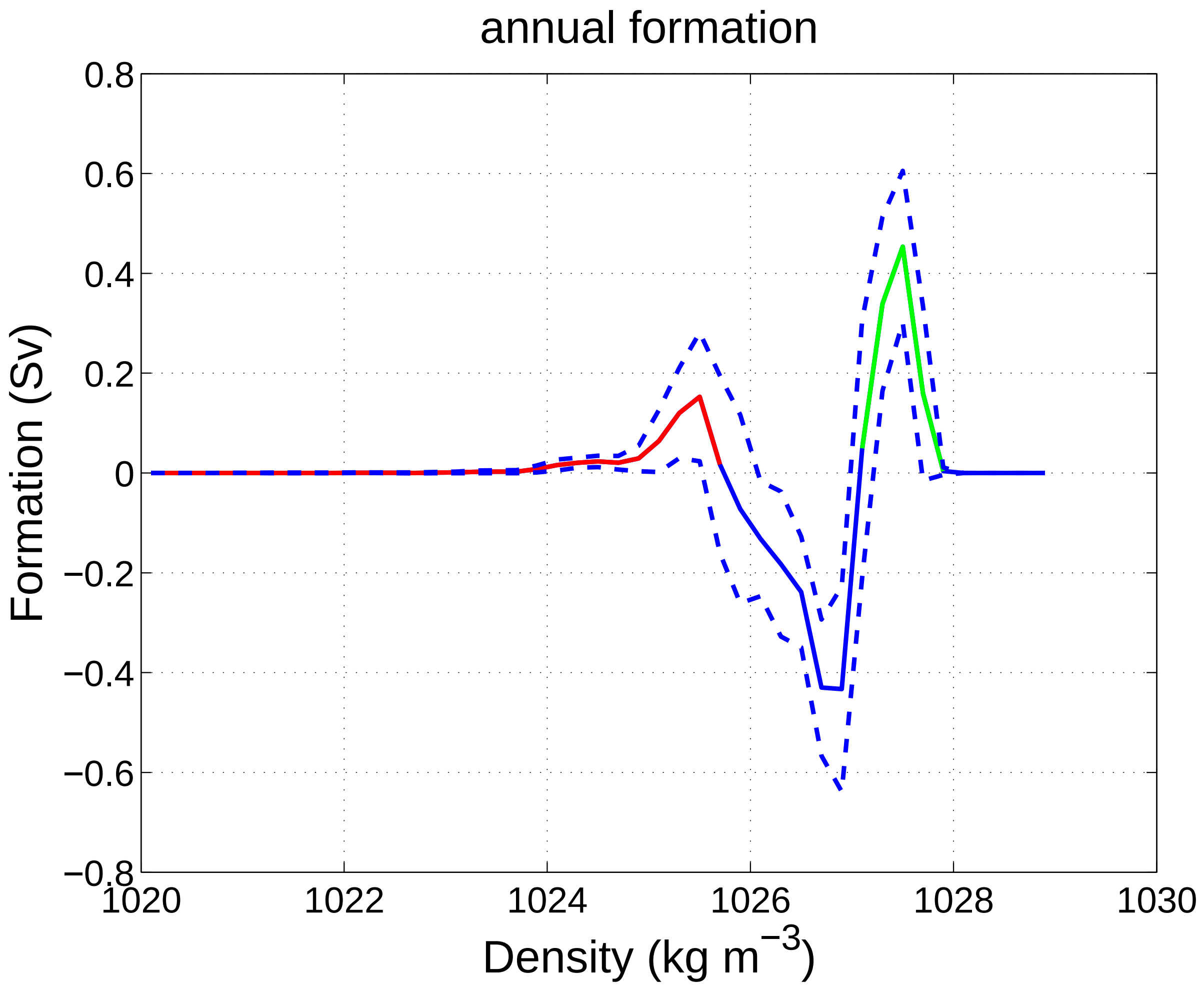

Figure 5.16: Formation rates (Sv) within 0.2 kg m^{-3} using the TKE dissipation profile in Fig. 5.11 with a spring-neap cycle. The transformation rates are averaged over the full annual cycle. The solid lines represent the mean formation over the period 1979 to 2014 with the dashed lines showing the mean plus and minus the standard deviation over the same period.

loss in the intermediate class centred on 1026.6 kg m^{-3} reaching 0.45 Sv within a density class (Fig. 5.16).

Recalling equation 5.3 we can evaluate the lateral transport of the volume in density space ($\Psi_{lateral}$) as a function of the formation rate ($M\Delta\rho$), rate of change of volume in a density class on the shelf ($\frac{\partial \Delta V}{\partial t}$), and the surface volume flux (Ψ_{P-E}),

$$\Psi_{lateral} = -M\Delta\rho + \frac{\partial \Delta V}{\partial t} - \Psi_{P-E}, \tag{5.22}$$

So far, the terms for formation rate ($M\Delta\rho$) and surface volume flux (Ψ_{P-E}) have been evaluated. The change of volume within a class ($\frac{\partial \Delta V}{\partial t}$) is evaluated over the whole year based on the assumption that the shelf is well mixed with depth in the winter. Using this assumption, the volume within each density class is,

$$\Delta V = \int_{outcrop} h \quad dA \tag{5.23}$$

where ΔV is the volume within a density class at the end of winter, *outcrop* is the regions where the surface density is between ρ and $\rho + \Delta\rho$, and h is the water depth.

The annual average surface volume flux (Ψ_{P-E}) is considerably smaller than the annual formation rate, only reaching a flux of 7x10^{-4} Sv, directed into the ocean, compared to a formation rate of 1 Sv (Fig. 5.17). This shows that the volume flux from the surface plays a small role in the volume budget of the shelf, although of course the associated modification of surface salinity along with the surface heat forcing are key in driving transformation.

There is large interannual variability in the density composition of the shelf (Fig. 5.18). The annual volume change ($\frac{\partial \Delta V}{\partial t}$) over any individual year is large, ranging between a 24 Sv gain of volume and 26 Sv loss of volume within a density class (Fig. 5.19(a)) which in some years represents a change in excess

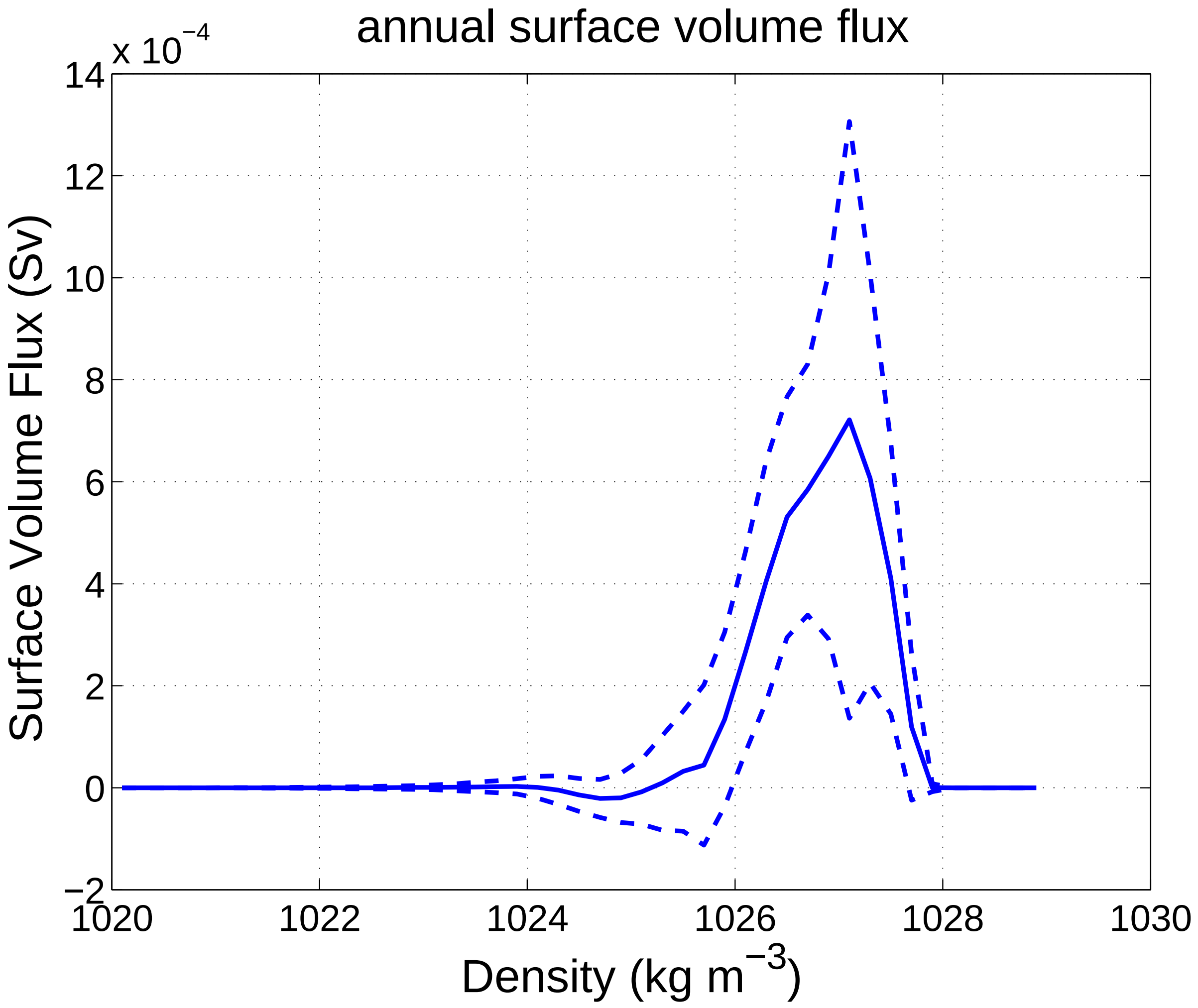

Figure 5.17: Annual average surface volume flux (Sv) in 0.2 kg m^{-3} density classes. The solid lines represent the mean volume flux over the period 1979 to 2014 with the dashed lines showing the mean plus and minus the standard deviation over the same period.

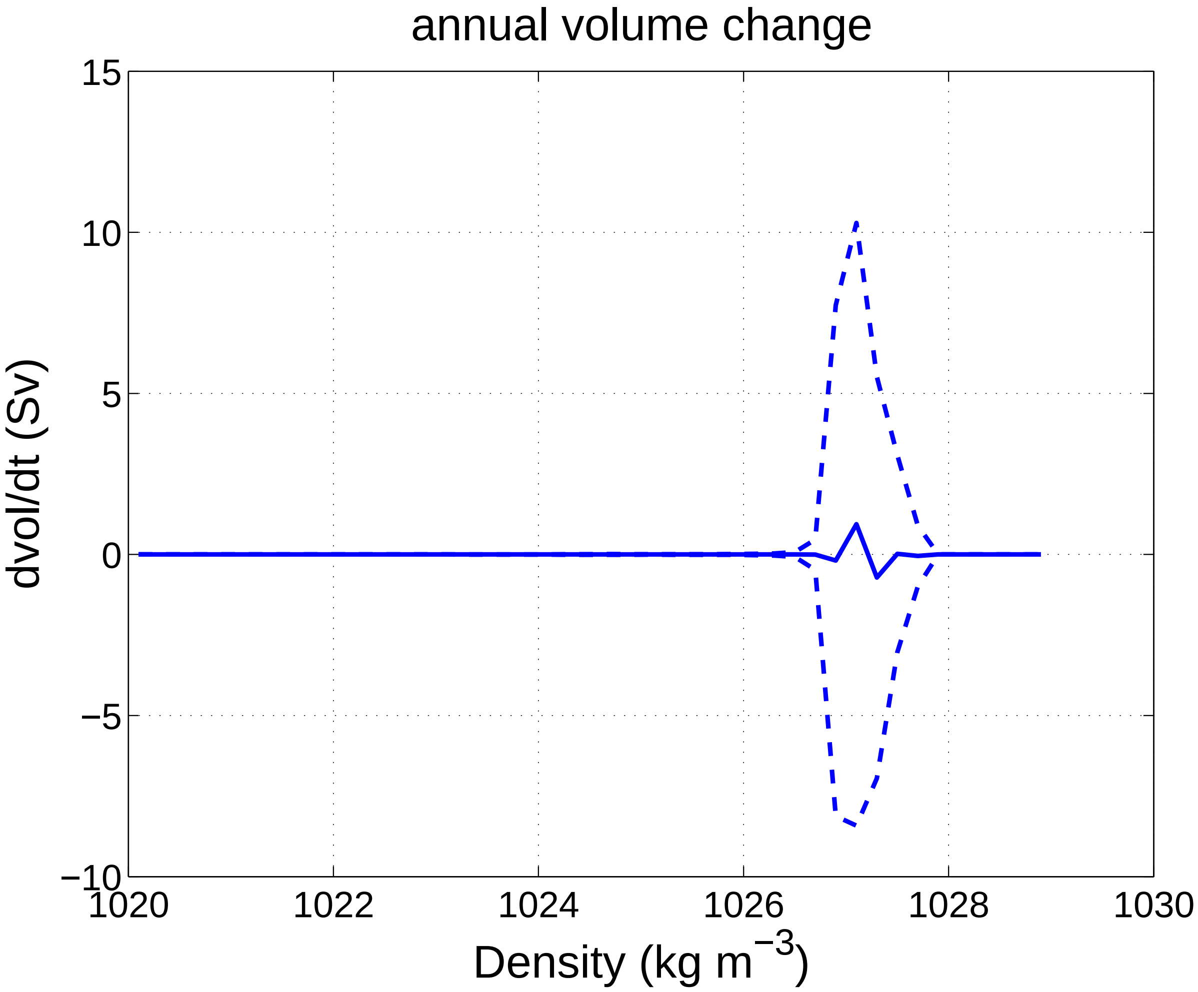

Figure 5.18: Volume change rates over a year. The volume change rates are averaged over the full annual cycle. The solid lines represent the mean annual volume change over the period 1979 to 2014 with the dashed lines showing the mean plus and minus the standard deviation over the same period.

(a) Rate of volume change for the density range 1027.0 to 1027.2 kg m^{-3}

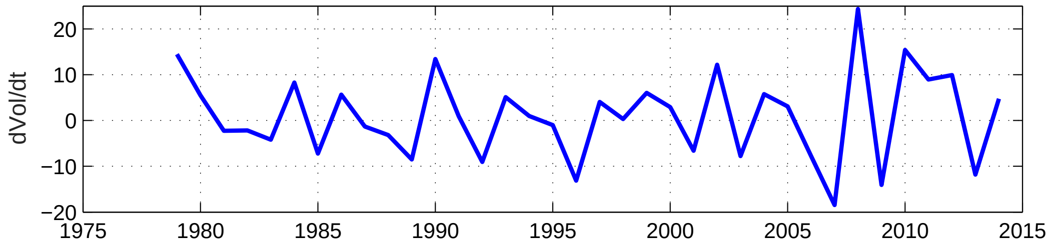

(b) Percentage volume change for the density range 1027.0 to 1027.2 kg m^{-3}

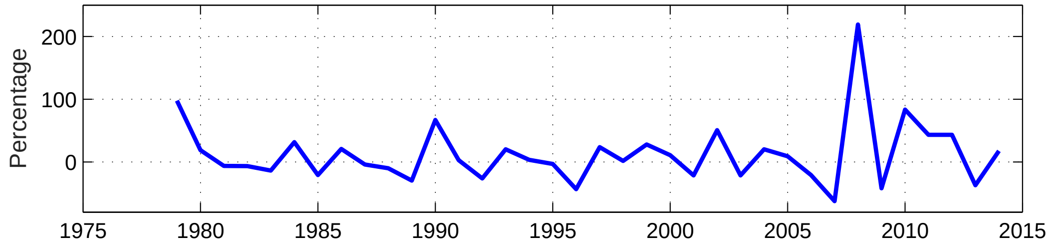

(c) Rate of volume change for the density range 1026.8 to 1027.4 kg m^{-3}

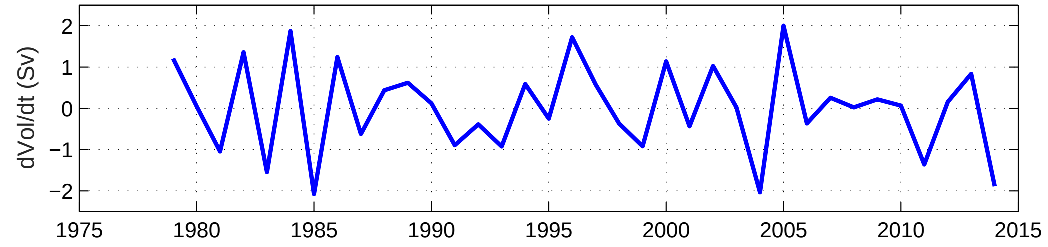

(d) Percentage volume change for the density range 1026.8 to 1027.4 kg m^{-3}

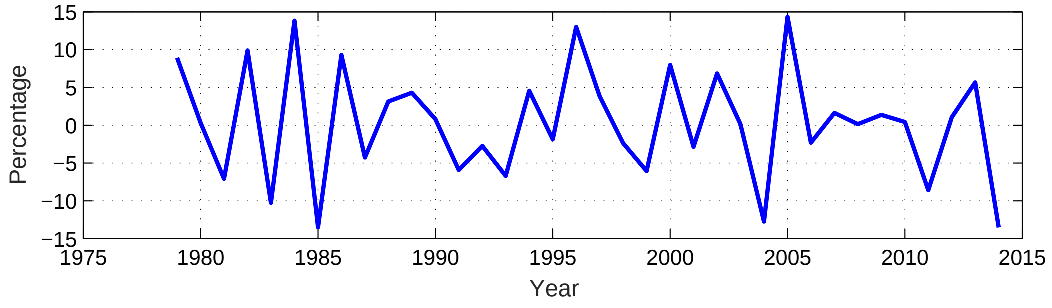

Figure 5.19: Time series of volume change over a year. The volume change rates are averaged over the full annual cycle. Two density bins are considered: 1027.0 to 1027.2 kg m^{-3} for (a) and (b), and 1026.8 to 1027.4 kg m^{-3} for (c) and (d). These changes are presented as: (a) and (c) the rate of volume change (Sv) normalised to a bin of 0.2 kg m^{-3} and (b) and (d) as the percentage change.

of 100%. Taking the volume change over a larger window leads to significantly smaller volume changes over the year, typically 10 to 15 %, indicating that the larger variability seen here is a result of using a small density class size. Despite this inter annual variability, the average volume change over the whole period 1979 to 2014 is small relative to these, reaching a maximum gain of 0.9 Sv and maximum loss of 0.7 Sv. Given the large variability around these mean values it is not possible to say with confidence that these means represent a real and systematic annual change in volume partitioning rather than simply being a small residual associated with such large, and noisy, inter annual variability.

Using Eqn. 5.22 with the inputs taken as in Figs. 5.16. 5.17 and 5.18 the implied lateral transport has been calculated (Fig. 5.20).

The volume exchange slightly modifies the implied lateral transport however it does not change the overall picture and has large variability. As such, and given that the surface volume flux is small, we will simply treat the lateral transport to be equivalent to the formation rate in the following sections. The lateral transport will now be considered integrated across three ranges: the off-shelf transport in light classes (1023.9 to 1025.7 kg m^{-3}); the on-shelf transport in intermediate classes (1025.7 to 1027.1 kg m^{-3}); and the off-shelf transport in dense classes (1027.1 to 1027.9 kg m^{-3}). When integrated over these ranges the transports are: 0.5 Sv off-shelf, 1.5 Sv on-shelf and 1 Sv off-shelf respectively. The transport across the whole range of density classes integrates to zero, which is to be expected as the volume of water on the European shelf does not change and thus the on-shelf transport must always be balanced by an equivalent off-shelf transport when integrated over all density classes.

Now we will explore a physical understanding for these formations, and thus lateral exchanges. This will be achieved by considering where the three density ranges considered above exist along the shelf edge through a seasonal cycle, and thus where these lateral transports are occurring.

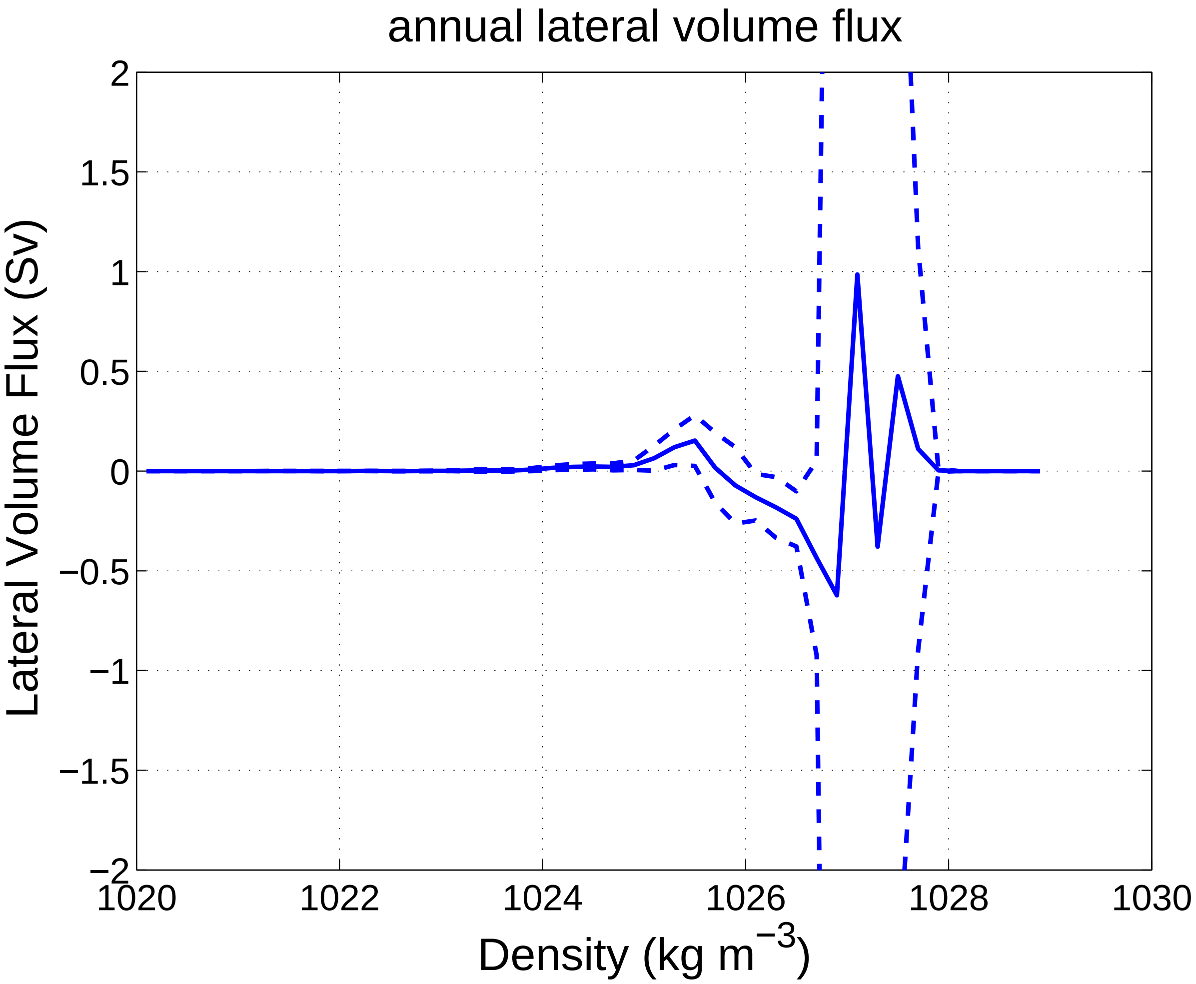

Figure 5.20: Implied lateral exchange (Sv) in 0.2 kg m^{-3} density classes from Eqn. 5.22. The solid lines represent the mean lateral exchange over the period 1979 to 2014 with the dashed lines showing the mean plus and minus the standard deviation over the same period.

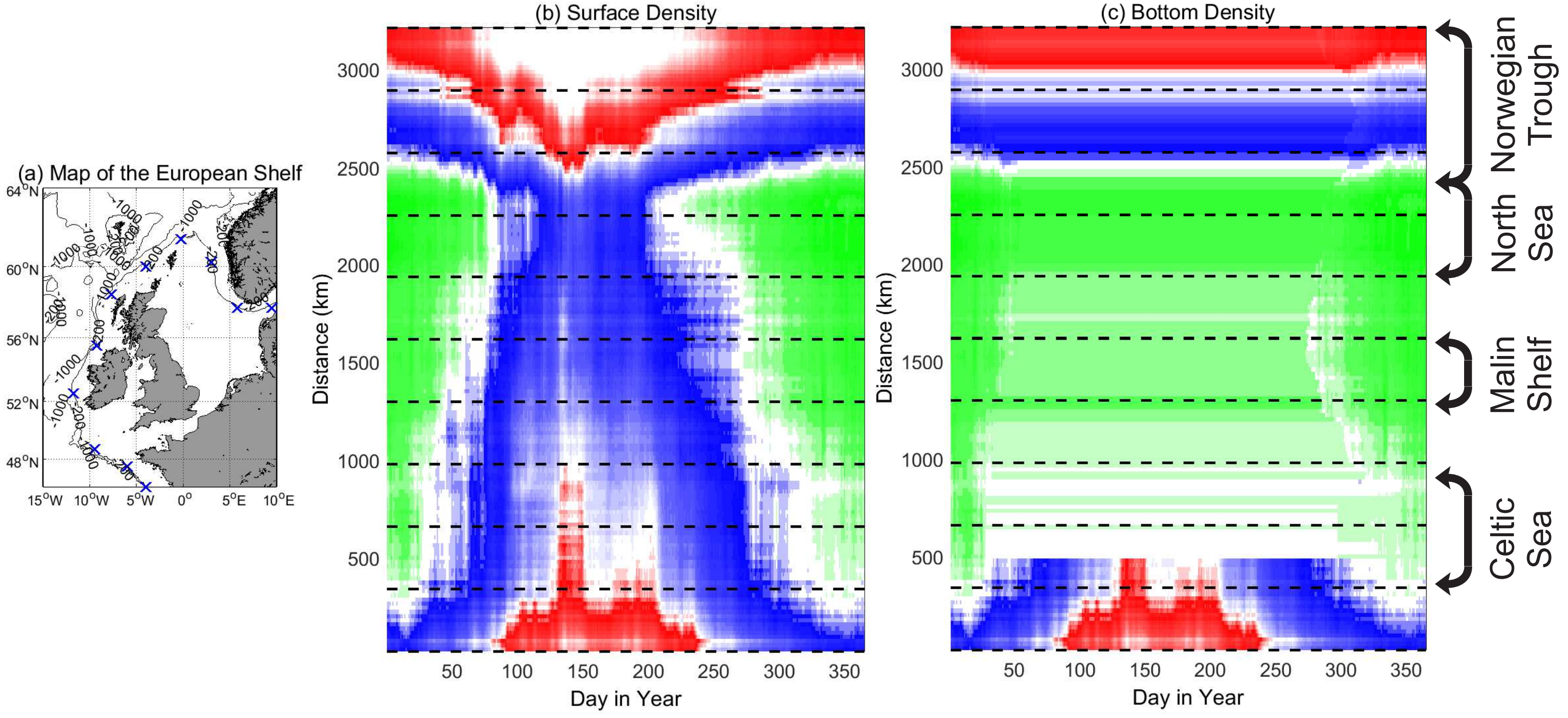

Figure 5.21: Figure showing the evolution of density along the shelf edge, defined as the 200m contour, through the year 2014 at (b) the surface and (c) the bottom. The horizontal dashed lines in (b) and (c) map to the locations indicated by the crosses in (a) with distance being measured from the location the 200m contour meets the southern boundary of the domain. The colours indicate the three regimes in Fig. 5.16 with red indicating the lightest off-shelf transport, blue indicating the on-shelf transport at intermediate densities and green indicating the off-shelf transport in the densest classes. The white regions indicate densities close to the boundary of a regime and with a small implied lateral exchange.

The bottom density is generally in the densest off-shelf class throughout the year at the shelf edge other than for a small number of locations at the southern boundary and during the summer in the well mixed southern North Sea(Fig. 5.21(c)). During the winter, when the water column is well mixed and at its coolest, the water surface is also generally in the densest classes, other than a small number of locations at the southern extremes (Fig. 5.21(b)). For much of the summer we see that for a large portion of the shelf edge the surface is in the intermediate density class with only a short period in the lightest class in the Celtic Sea and, more persistently, in the southern North Sea boundary with the Norwegian Trough (Fig. 5.21(b)).

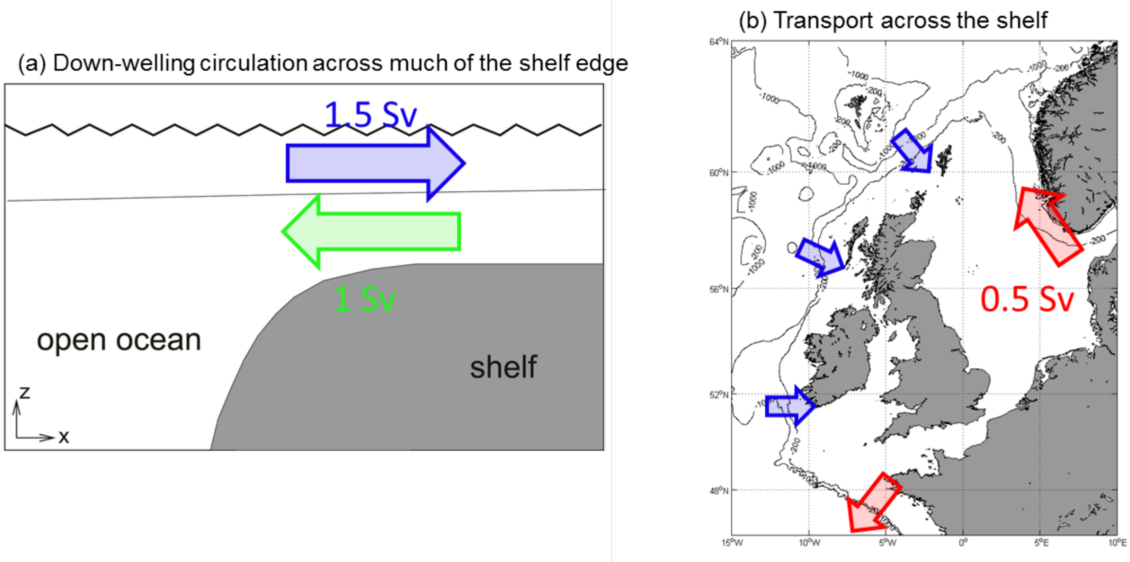

Figure 5.22: Schematics showing the general circulation indicated by the formation rates and the density distribution at the shelf edge. (a) The down-welling circulation indicated across much of the shelf edge, with a depth integrated on shelf transport. (b) The depth-integrated transport onto the shelf in many parts of the shelf edge balanced by an off-shelf transport in the southern Celtic Sea and the Norwegian Trough.

These density distributions indicate that for the majority of the shelf edge the transport is down-welling in nature, with an on-shelf transport of 1.5 Sv in the surface layer and upper pycnocline and an off-shelf transport of 1 Sv in the bottom layer and lower pycnocline (Fig. 5.22(a)). Thus there is an overall down-welling circulation of 1 Sv and a depth-integrated on-shelf transport of 0.5 Sv. This depth-integrated on-shelf transport is balanced by an equivalent off-shelf transport focussed on either the southern Celtic Sea or through the Norwegian Trough (Fig. 5.22(b)).

5.8 Inter-annual Variability

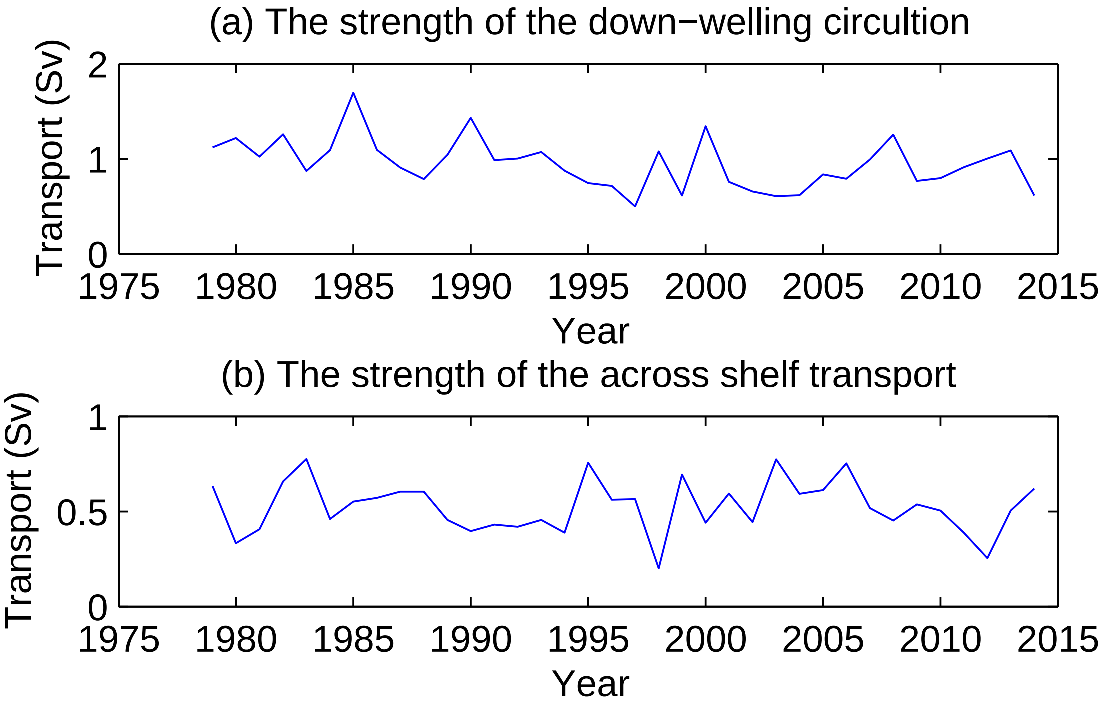

Figure 5.23: Time-series showing the inter-annual variability in (a) the down-welling circulation and (b) the across shelf transport.

The inter-annual variability will now be explored in terms of these two modes of the shelf edge transport, the down-welling and the across shelf transport. These two modes have been defined by the magnitude of their off-shelf component, as these are distinct whilst the on-shelf component of both circu-

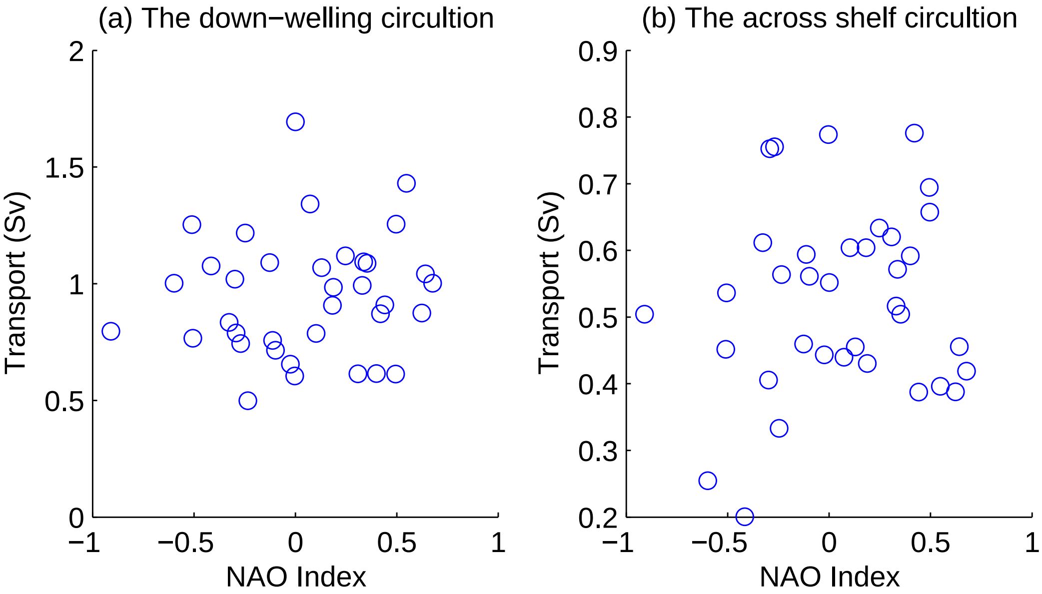

Figure 5.24: Plots of the strength of (a) the down-welling circulation and (b) the across shelf transport versus the North Atlantic Oscillation Index.

lations occur in the same density classes.

The down-welling circulation varies from 1.7 Sv to 0.5 Sv across the 35 year period examined here whilst the across shelf transport varies from 0.8 Sv to 0.2 Sv (Fig. 5.23). The down-welling and total, sum of down-welling and across shelf, transport both show downwards trends of 0.010 Sv yr^{-1} and 0.011 Sv yr^{-1} respectively however these linear trends only explain a small percentage of the total variability, R^2 of 0.17 and 0.22 respectively.

The strength of these circulations are not strongly affected by the North Atlantic Oscillation, with the annual average NAO Index having R^2 values of 0.01 and 0.02 for the down-welling and across shelf circulations (Fig. 5.24). When using seasonally averaged NAO Index the correlation is still weak, with $R^2 < 0.15$ for all four seasonal averages against both circulations.

The inter-annual variability is also not strongly affected by wind along the shelf edge. The R^2 values between the strength of these circulations and the wind stress averaged along the shelf edge throughout the year and decomposed into the along and across shelf edge components are in the range 0.04 to 0.01.

5.9 Summary of cross shelf exchange and comparison with other estimates

The overall picture of the exchange on the European Shelf given by the Walin Framework is that of two circulations. The first is a down-welling circulation across much of the shelf of 1 Sv, with volume moving onto the shelf in the surface layer and moving off the shelf in the bottom layer. The second circulation is a net on-shelf transport across much of the shelf edge which is balanced by an off-shelf transport through the Norwegian Trough of 0.5 Sv. These circulations lead to a total exchange, the sum of both the on and off shelf components of these circulations, of 3 Sv. The estimates of transport given by the Walin Framework are integrated within density classes and thus do not give an indication of the exchange occurring within the same density class. This means the transport derived by this method is likely to be biased towards the summer circulation, as during winter the range of densities over the shelf is limited.

Estimates of the total exchange are limited in the literature, with many studies of shelf edge exchange focusing on the transport in a limited spatial and temporal window and studying a limited subset of the processes contributing to the transport across the shelf edge. There are however some modelling studies that have estimated the total transport across the shelf edge. For example Holt et al. [2009] and Huthnance et al. [2009] discuss generally down-welling circulations of 0.9 ± 0.6 Sv and 1.2 Sv with a total exchange of 2.5 Sv (Fig. 5.25). These studies also show a net transport out of the Norwegian trench. These features are similar in both general features, i.e. overall down-welling with transport out of the Norwegian Trench, and magnitude to those calculated using the Walin framework here.

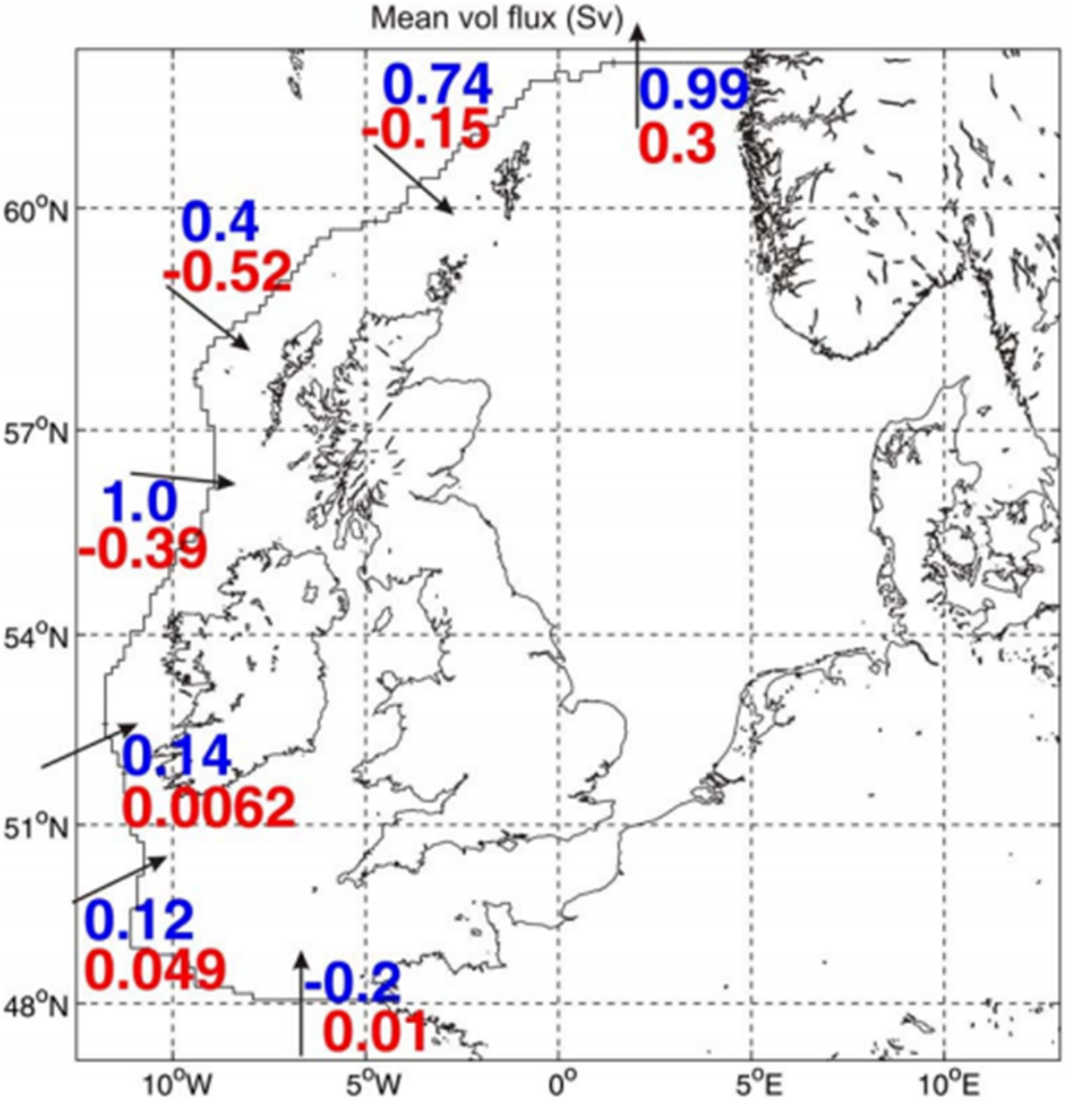

Figure 5.25: Modelled transports across the 200m isobath above 150m (blue) and below 150 m (red). Positive is directed onto the shelf other than next to Norway. This figure is taken from Huthnance et al. [2009]

5.10 Implied nutrient transport

The annual average volume flux calculated in Section 5.4 is now combined with climatological nutrient and density data to estimate the convergence, or divergence, of nutrients from volume exchange between the open ocean and shelf seas.

5.10.1 Methods

The nutrient transport, in density classes, has been evaluated by assuming the annual average transformation rate (Fig. 5.16) represents the transport of water across the shelf edge and then multiplying this transport by a relevant nutrient, in this case Nitrate, concentration.

The Nitrate concentrations will be calculated using the World Ocean Atlas seasonal climatologies for nitrate, temperature and salinity. The data used here is at 1 degree horizontal resolution, the highest resolution available for nutrient data, and 25 depth levels in the top 200m and 37 in the top 500m, the deepest available nitrate data. Here we will again define the boundary between the shelf and the open ocean as the 200m isoobath. Linear interpolation will be used to evaluate the nitrate concentration on each of the density surfaces used to evaluate the volume formation rate. This local value for nitrate on an isopycnal will be averaged, and the standard deviation calculated, across all positions and seasons on the shelf and off the shelf separately. This allows the calculation of a Nitrate flux however it does assume that the changes to the Nitrate structure in density space are not largely affected which is rather a crude assumption in a seaosnally stratifying shelf sea.

5.10.2 Nutrient contrast in density classes

The nutrient profiles in density space fit with the general expectation of lower nutrients at lighter density classes and increasing nutrients in denser classes (Fig. 5.26). This is a result of stratification holding phytoplankton in the

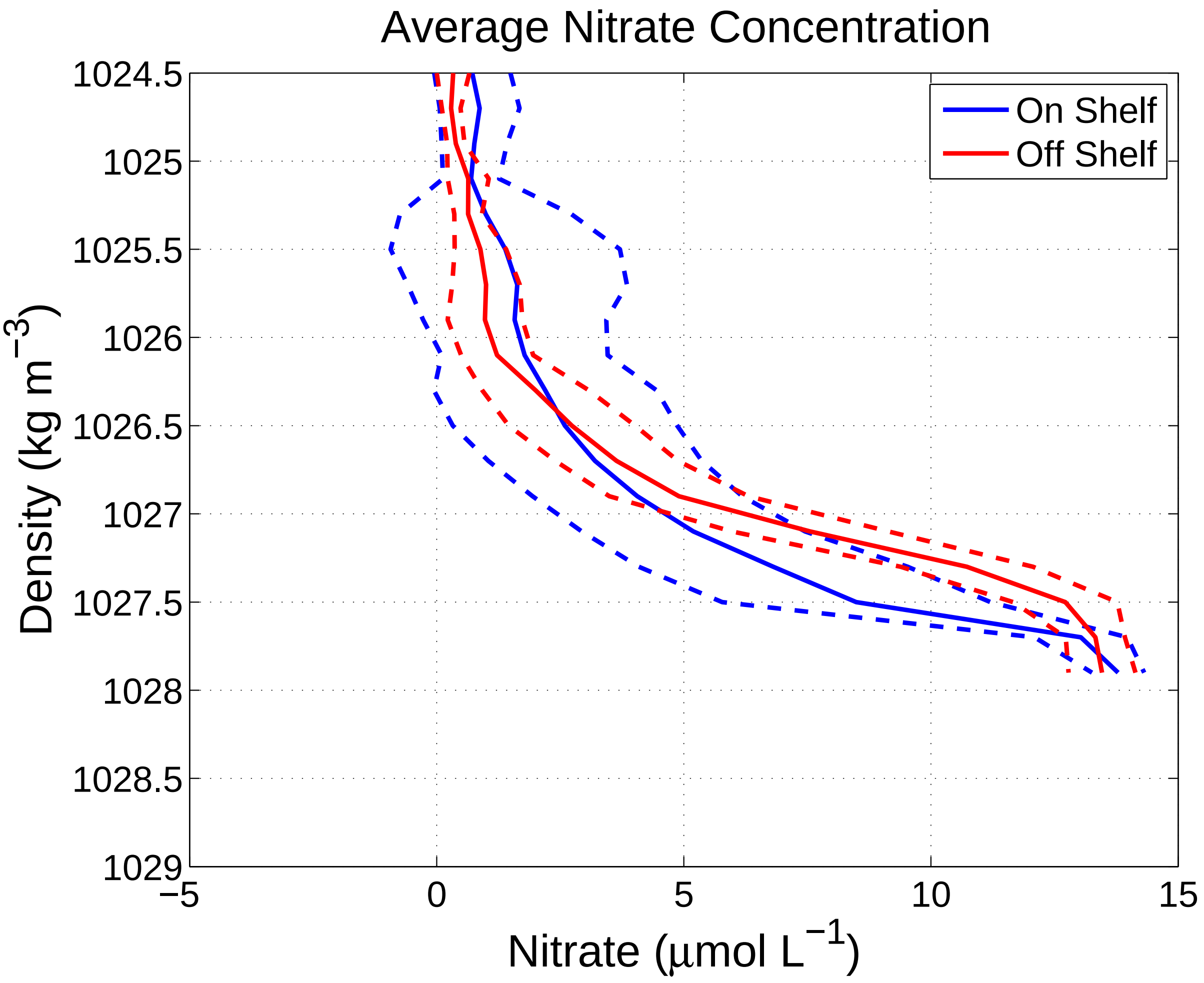

Figure 5.26: Nitrate concentration averaged within density classes over the full year. The calculations are performed separately over the shelf, less than 200m deep, and the open ocean, deeper than 200m.The solid lines represent the mean nutrient concentration over the domain with the dashed lines showing the mean plus and minus the standard deviation.

well lit surface layer causing increased productivity and depletion of surface nutrients. In the lighter classes the on-shelf waters typically have a higher nutrient concentration than off shelf, 1 μ mol L^{-1} on shelf and 0.5 μ mol L^{-1} off shelf. This is consistent with enhanced mixing at the pycnocline on the shelf driving nutrients from the bottom layer into the surface. In the denser classes, those associated with the bottom layer during summer and the well mixed shelf water column in winter, the off-shelf waters have a higher nutrient concentration than those on the shelf, 13 μ mol L^{-1} compared to 8 μ mol L^{-1} respectively. This is consistent with enhanced productivity on the shelf leading to an overall deficit which, it has been hypothesized, is replenished by exchange with the open ocean.

5.10.3 Implied nutrient convergence

Multiplying these nutrient concentrations by the transport, and accounting for the direction of transport in the choice of open ocean or shelf nutrient concentration, gives a nutrient supply that reaches 1.8 Kmol NO_3^- s^{-1} directed onto the shelf in the range 1026.8 to 1027 kg m^{-3} and 5.8 Kmol NO_3^- s^{-1} directed off the shelf in the range 1027.4 to 1027.6 kg m^{-3}. Integrating the nitrate transport across all density classes leads to an off-shelf directed annual average flux of nitrate of 7.7 Kmol NO_3^- s^{-1}. This is due to the enhanced nutrient concentrations in the bottom layer, where the down-welling circulation is transporting water off the shelf, relative to the surface layer, where volume is being transported onto the shelf. This divergence, driven by the down-welling circulation in combination with the vertical structure in nitrate, is dominant over the convergence that would be driven by the horizontal structure in nitrate concentrations. This divergence of nitrate leads to a loss of nitrate on the shelf through processes captured by the Walin Framework. Hence the required nitrate supply must come from lateral diffusion, an on-shelf transport balanced within the same density class or local biological recycling of nitrate.

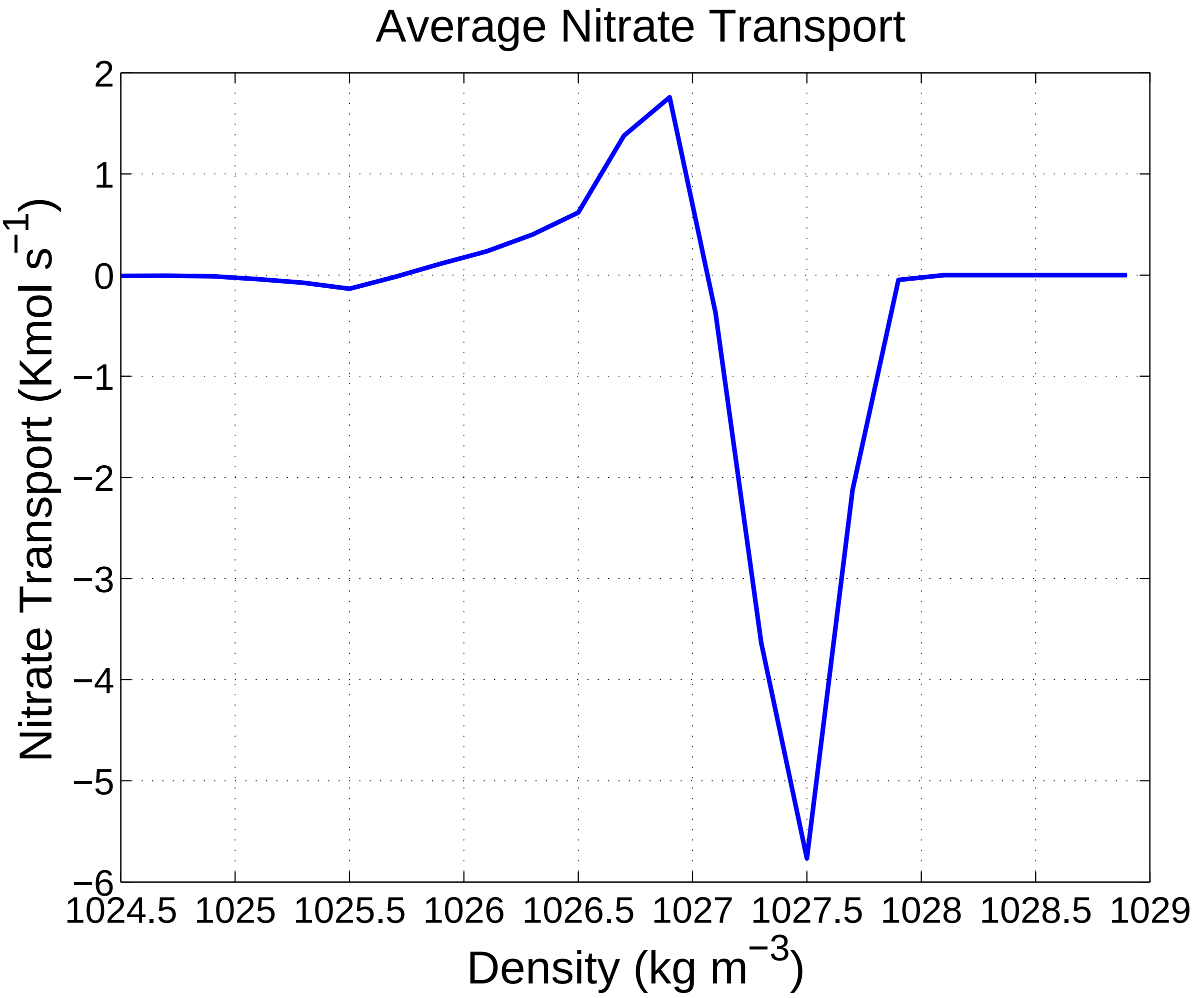

Figure 5.27: The transport of Nitrate on or off the shelf driven by the lateral exchange implied by the formation rate and Nitrate concentration within 0.2 kg m^{-3} density classes. The transport is defined as positive onto the shelf and negative off the shelf.

5.11 Summary

- The Walin Framework is a mathematically rigorous way of calculating the transformation of water across density surfaces which is derived from the combination of a volume and mass budget between two density surfaces.
- This transformation can instead be viewed, by taking its derivative with density, as the formation of volume within a density class. This formation can then be used as a contribution to a volume budget which also includes the lateral exchange through the boundaries of the domain.
- The Walin transformation has been evaluated for the European Shelf using surface data from the ECMWF ERA-Interim and World Ocean Atlas and making a series of plausible estimates of the diffusion driven transformation based on observations. These choices are specifically: a single value throughout the domain, a single vertical profile throughout the domain, and the application of vertical profiles varying with the spring-neap cycle however not varying spatially.
- The air-sea forcing has the same strength in all three cases. The seasonal picture from the air-sea fluxes is the formation of light water during the spring and summer as surface heating generates stratification and the formation of dense water in autumn and winter as the stratification is broken down. In the annual average the air-sea forcing drives a transformation towards lighter waters at 1026 kg m^{-3} and a transformation towards denser water at 1027 kg m^{-3}.
- This air-sea forcing is generally opposed by the diapycnal diffusion driven transformation. However, for all three diffusion cases tested here the air-sea transformation is larger, typically by a factor of 5, than the diffusive forcing and, as a result, the total transformation is similar to the air-sea driven transformation.

- The lateral transport can be calculated by taking the formation rate, the surface volume flux from precipitation and evaporation and the total change in volume over the year. The precipitation term is small, 10^{-4} Sv compared to a formation of 1 Sv, so has a very small effect on the calculation of lateral transport. The total volume change over any individual year can be large however averaged over the whole time-series the volume change is smaller than the transformation. These combine to give a transport that is similar to that given by the formation rate alone, although with a contribution from the volume change.

- The lateral transport has three components: an off-shelf transport of 0.5 Sv from 1024 to 1025.6 kg m^{-3}; on-shelf transport of 1.5 Sv between 1025.6 and 1027 kg m^{-3}; and off shelf transport of 1 Sv between 1027 and 1027.8 kg m^{-3}.

- Mapping these density classes indicates: that the lightest class only exists in the southern North Sea and, for a short period, in the summer in the Celtic Sea; the intermediate density classes exist in the surface layer for much of the shelf during summer ; and that the densest classes exist for all of the year, in either the well mixed winter water column or the bottom layer during summer.

- This density distribution suggests a down-welling circulation across much of the European Shelf of 1 Sv and an across shelf circulation of 0.5 Sv, with an on-shelf transport across much of the shelf edge and an off-shelf transport through the Celtic Sea and Norwegian Trench. This circulation is similar to the model diagnostics by Holt et al. [2009] and Huthnance et al. [2009].

- This down-welling circulation drives an off-shelf transport of nitrate of 7.7 Kmol NO_3^- s^{-1}. Hence the lateral exchange is acting to remove inorganic nitrate from the shelf rather than supply the nitrate. This implies that the nitrate requirments of the production on the shelf must be supplied by physical processes the Walin Framework fails to capture or by the local biology.

Chapter 6

Discussion

Through this thesis we have explored the transport across the shelf edge through two themes. The first of these is the consideration of the role of internal tides in driving bolus transport across the shelf edge and the potential cancelling transports. The second is considering the system wide circulation by applying a water-mass focussed integral framework. This has been achieved through the combination of theory and observational data sets. In this chapter these two themes will be summarised and some additional thought given to the implications of the results presented in the previous chapters.

6.1 Summary of bolus transport

In Chapter 2 we introduced the idea of the bolus transport. This can be considered by splitting the total transport into a component driven by the Eulerian velocity and a component driven by the covariance of layer thickness and velocity within the layer. There are two alternative views of how important the bolus transport in the ocean is. For the upper atmosphere and the Southern Ocean, the bolus transport makes a significant contribution to the total, or residual, transport and as a result a large contribution to the system wide circulation. For the coastal case, the bolus transport is driven by surface waves approaching a beach. Here a larger volume is transported towards the beach in the crests of the waves than is transported off the beach in the troughs. In this case the on beach bolus transport is locally returned either through an undercurrent or a rip current.

The work presented in this thesis suggests that for the shelf edge system we see a bolus transport directed in the same direction as the propagation of the internal tide, typically onto the shelf. This transport is balanced in the same horizontal and vertical position by an opposing time-mean transport. This suggests that we are in a system similar to the coastal system discussed above. This is perhaps to be expected for narrow shelf seas, such as those on the west coast of North America, where the coastal boundary is close to the shelf edge. The European Shelf however is much wider, reaching up to 500 km width in the Celtic Sea. This provides some separation between the boundary and the shelf edge and as a result allows a more complex and dynamic velocity field to form [Brown et al., 2002] on the shelf itself with velocities reaching 0.2 m s^{-1} [Holt and Proctor, 2008]. One would perhaps expect such a dynamic regime to allow a more complex circulation pattern, with volume potentially moving onto the shelf at some locations being balanced by a focussed off shelf transport such as the transport seen through the Norwegian Trench. The observational evidence presented here, however, shows that the return is local with only a small cross shelf edge residual.

Work similar to the bolus transport work presented here has been recently been presented in Henderson [2016]. In this work, Henderson explores the role of internal waves in the velocity field on the sloping bed of a lake. There is a Stokes' drift driving an up-slope transport of water which is balanced by a down-slope directed Eulerian velocity. This is similar in spirit to the coastal example discussed above and the results presented in this thesis. The paper does not however rule out any net advection of particles but discusses them as the small residual from two larger and opposing transports. In the paper he calculates this residual following an "isothermal mean" transport method which

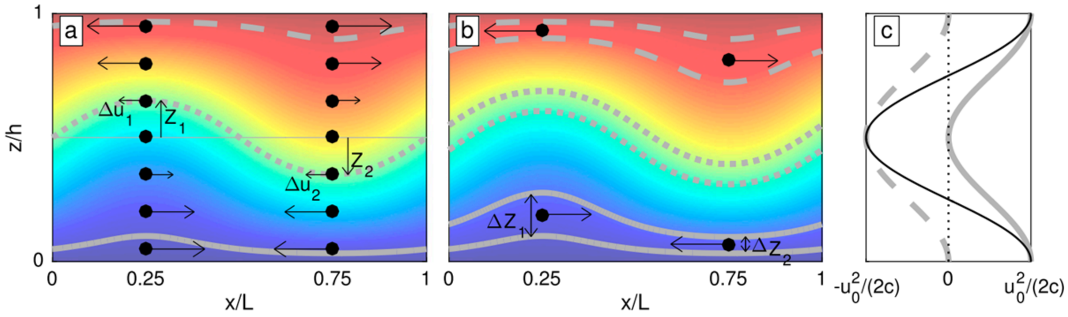

Figure 6.1: The Stokes drift for a linear mode-1 internal wave for a water column with stratification not changing with depth. (a) The contribution to the Stokes drift from a particle moving vertically through a sheared water column. (b) The bolus transport contribution to the Stokes drift. In these figures the colours represent the temperature, the grey lines represent isotherms and the arrows represent the velocity. (c) The vertical structure in these terms averaged over a wave period. The shear contribution is the dashed grey line, the bolus contribution is the solid grey line, and the total Stokes drift is the black solid line. This figure is taken from Henderson [2016]

is similar to the bolus transport applied in temperature space. In addition the full Stokes drift is calculated from the observations following the methods of Middleton and Loder [1989]. Here they take the total Stokes drift as,

$$u_{ST} = \frac{\partial < u'Z' >}{\partial z} \tag{6.1}$$

where u_{ST} is the full Stokes velocity, u' is the fluctuations in velocity and Z' is the displacement of a particle in the vertical. This last term is estimated as,

$$Z' = \frac{1}{c}\int_{z=0}^{z} u' \quad \partial z \tag{6.2}$$

where c is the phase speed and the wave is assumed to be linear and only slowly changing form as they propagate. This definition of the Stokes drift implies that the depth integrated transport must be zero, if we assume a rigid lid, although it does not imply zero Stokes drift at all depth with previous theoretical work implying reversals in the Stokes drift with depth [Thorpe, 1968]. These vertical reversals are explained in Henderson [2016] by splitting Eqn. 6.1 into two terms, one giving the bolus transport ($< u'\frac{\partial Z'}{\partial z} >$) and another giving the effect of the vertical displacement of a particle within a sheared flow field ($< Z'\frac{\partial u'}{\partial z} >$). The bolus term gives a positive contribution, in the direction of propagation of the wave, which reaches a maximum at the boundaries (Fig. 6.1). This is opposed by the shear term which gives a negative, against the direction of propagation, transport which reaches a maximum at mid-depth (Fig. 6.1). The combination of these two gives a vertical structure of positive transport near the boundaries and a negative transport at mid-depths, as implied by other theoretical work [Thorpe, 1968]. These theoretical results are generic to all linear internal waves, whether tidal, inertial or with some other period.

It is shown in Henderson [2016] that, given certain assumptions such as limited vertical mixing, the transport calculated within a density class around an isopycnal is equivalent to the sum of the time-mean Eulerian velocity at the mean depth of the density class, the shear term generated by the vertical displacement of a density class and the bolus transport within the density class. This isopycnal velocity can then be decomposed into the time-mean and time-varying contributions. The time-mean contribution will contain the Eulerian velocity at the time-mean depth of the density class plus the transport driven by the vertical shear. This can be understood for the two layer system considered in this thesis by considering the volumes above and below the mid-water column isotherm in Fig. 6.1. The depth-mean velocity when the layer is thick will be in the direction of propagation of the wave but will be reduced as the layer includes the zero crossing and reversal of the horizontal velocity. When the layer is thin the layer mean velocity will be against the direction of propagation and larger in magnitude than when the water column is thick as the layer only contains the stronger velocities near the boundary. When a wave average is applied this will skew the time-mean velocity within the layer in the opposite direction to the propagation. This is different to the theoretical system considered in this thesis as we have taken the view, previously used in the open ocean, that the velocity can be taken as constant within a layer.

6.1.1 Application of this method to the mooring data

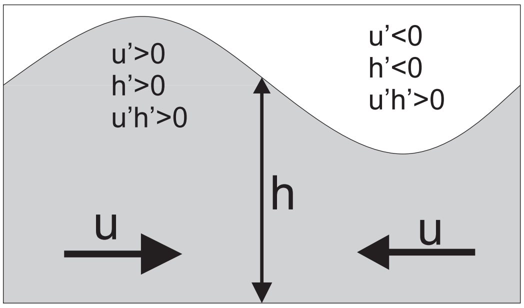
(a) Eddy transport from the covariance of thickness and velocity

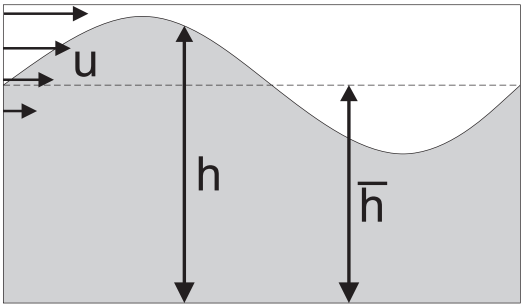
(b) Vertical extents used for averaging velocity

Figure 6.2: Schematics of (a) the bolus transport and (b) the vertical extents used for averaging the velocities.

We will now reconsider the mooring data in light of this work. Here the transport at the moorings will again be calculated however now the transport will be considered in three layers, consistent with the theoretical understanding of internal wave driven Stokes' Drift, and performing an additional split of the mean transport. The averaging of velocities within a layer is now performed over two vertical extents. The first of these extents is limited by the instantaneous positions of the bounding isopycnals (or physical boundary), $\mathbf{u}$, in the same manner as performed in Chapter 3 whilst the other is limited by the mean depth of the isopycnals (Fig. 6.2(b)), $\mathbf{u}_{\overline{h}}$. We can then define the contribution to the layer averaged velocity as a result of displacements of the boundaries, $\mathbf{u}_{h'}$.

$$\mathbf{u} = \mathbf{u}_{\overline{h}} + \mathbf{u}_{h'}, \tag{6.3}$$

This new split of the velocity is then used to split the mean transport, $\overline{\mathbf{u}}\overline{h}$, into a component driven by the mean depth of the isopycnals, $\overline{\mathbf{u}_{\overline{\mathbf{h}}}}\overline{h}$, and a component driven by the isopycnals moving through shear, $\overline{\mathbf{u}_{h'}}\overline{h}$. So the full transport becomes,

$$\overline{\mathbf{u}h} = \overline{\mathbf{u}_{\overline{\mathbf{h}}}}\overline{h} + \overline{\mathbf{u}_{h'}}\overline{h} + \overline{\mathbf{u}'h'} \tag{6.4}$$

where the first term on the RHS represents the Eulerian transport and the second and third terms together represent the Stokes' transport.

Now we will apply this new split across three layers for the mooring located on the New Zealand Shelf. This shows a bolus transport directed onto the shelf in the surface and bottom layers with the middle layer showing a weak bolus transport directed off shelf (Fig. 6.3(a)). In the depth integral the bolus transport is directed onto the shelf (Fig. 6.3(a)). Whilst the component of the transport driven by the vertical shear is directed off the shelf for the middle layer with weak transport in the surface and bottom layers (Fig. 6.3(c)). The depth integrated shear driven transport is directed off the shelf (Fig. 6.3(c)). When these two terms are added, representing the full Stokes' Drift, the depth integrated transport is small however this does not apply within density layers (Fig. 6.3(d)). The surface and bottom layers, where the bolus transport dominates, are directed onto the shelf whilst the middle layer, where the shear dominates, is directed off the shelf (Fig. 6.3(d)).

Reconsidering the results presented earlier in this thesis suggests the on shelf bolus transport is consistent with the effects of the internal tide. However the bolus transport alone does not fully represent the Stokes' Drift. The addi-

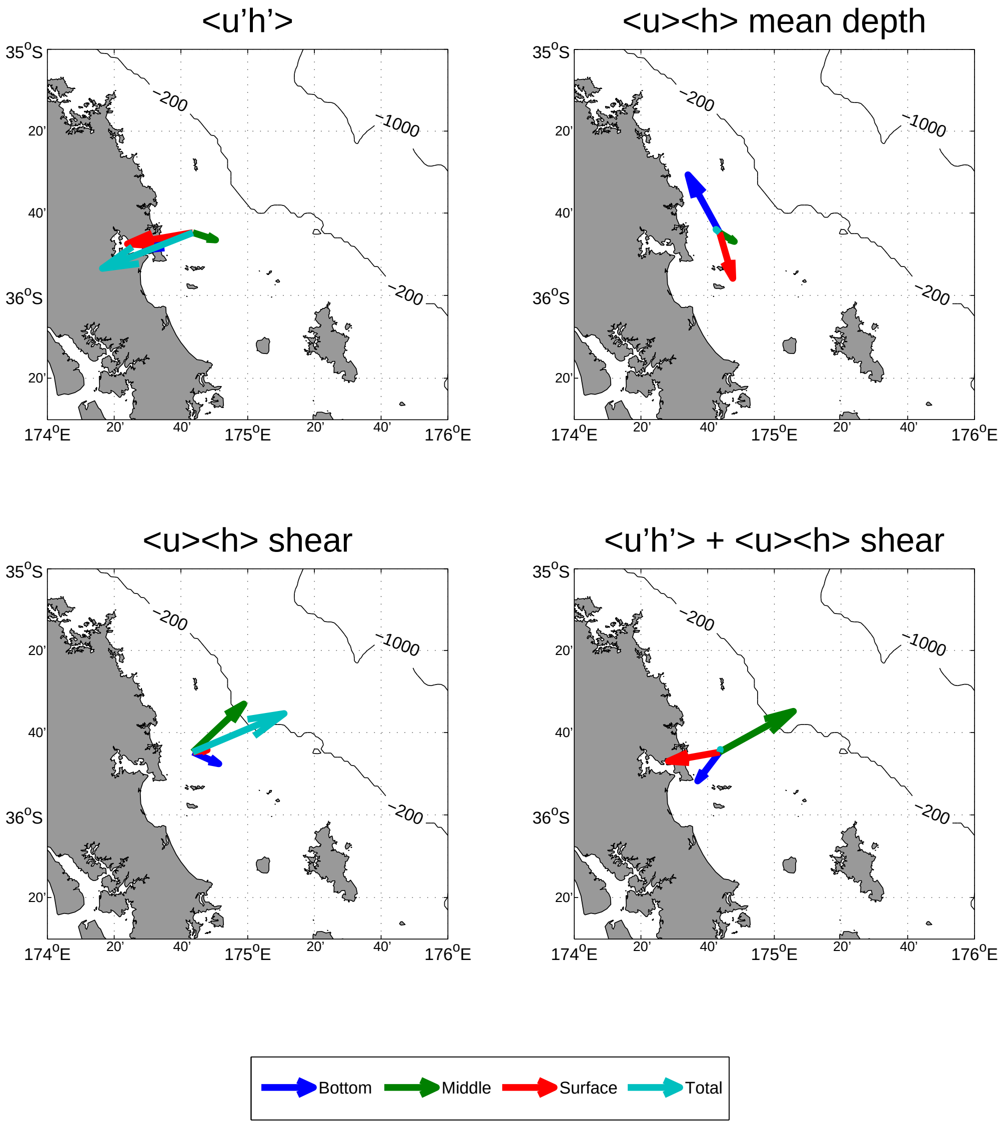

Figure 6.3: Transports on the New Zealand Shelf driven by (a) the bolus transport, (b) the mean transport evaluated over the mean depth of isopycnals, (c) the mean transport evaluated over the departures from the mean isopycnal depth, and (d) the sum of the bolus transport and the sum of the bolus transport and transport evaluated over the departures from the mean isopycnal depth.

tional shear term cancels the effects of the bolus transport when viewed in the depth integral however the transport within layers is not canceled resulting in exchange of volume and potentially, dependent on the vertical structure, a net tracer flux.

6.2 Summary of Walin Framework

In Chapter 5 we applied the Walin Framework to the European Shelf. The Walin Framework is a mathematically rigorous method for calculating the total volume crossing an interface in tracer space, either through water crossing stationary surfaces or surfaces migrating. Here it has been applied using potential density as the tracer for the European Shelf. The inputs required for this case were the surface heat and freshwater forcing and the diapycnal diffusion.

6.2.1 Importance of spatial variability in application of Walin Framework

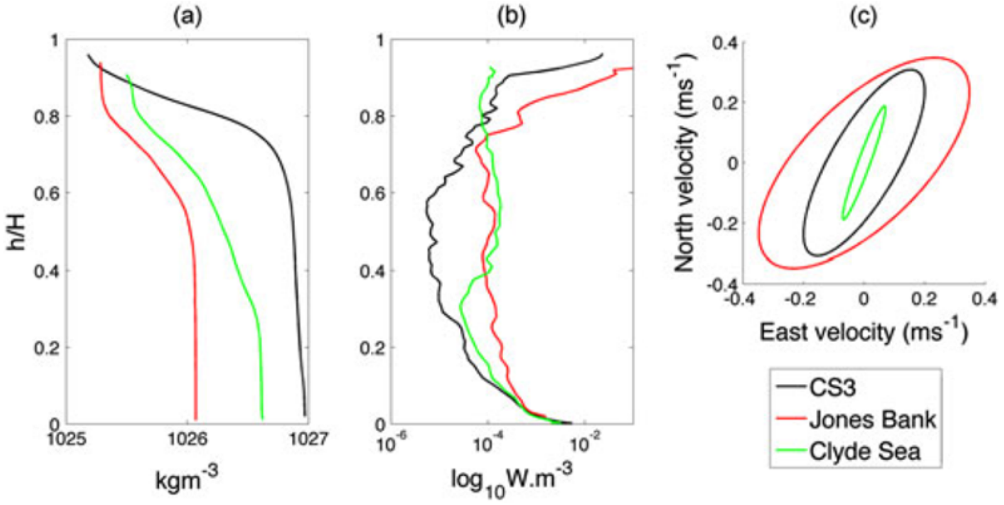

Figure 6.4: Profiles of (a) density, (b) the TKE dissipation rate and (c) the tidal ellipses for three locations across the European Shelf. This figure is taken from Palmer et al. [2013]

The surface forcing data was easily acquired using well established reanalysis data sets. The diapycnal diffusion data however was considerably more difficult. The primary problem was the lack of data available for this parameter across the shelf in combination with the high spatial and temporal variability observed within the shelf seas (Fig. 6.4) [Palmer et al., 2013, Sharples et al., 2007]. In this case we took two datasets of turbulent kinetic energy dissipation collected at the same location at a spring and a neap tide. We then made the assumption that these profiles were representative of the whole shelf dissipation. The result of using this profile was that the effects of diffusion were much smaller than the effects of the air sea forcing (5 to 10 times smaller). If we make alternative assumption that the diffusion is an order of magnitude larger over 10% of the area of the European Shelf, such as regions near topographic features, the total effect of the diffusive term will increase by a factor of two. This still results in a system dominated by the air-sea forcing and the density distribution of transformation and formation rates will be largely the same although the magnitude will be smaller.

6.2.2 Comparison between derived circulation and processes

The Walin Framework implied a down welling circulation across much of the European Shelf. This down-welling feature has previously been discussed in relation to either the effects of the bottom Ekman layer alone [Painter et al., 2016] or through the combination of surface wind forced Ekman and bottom Ekman layers [Holt et al., 2009, Huthnance et al., 2009]. Referring back to Table 1.1 in Section1.3.2, there have been previous estimates of the transport across the European Shelf edge driven by various processes, collated by Huthnance et al. [2009]. The typical transport per unit width of the shelf driven by the bottom Ekman layer is 0.5 m^2 s^{-1} which is equivalent to an off shelf bottom layer transport of 1 Sv when integrated over a 2000 km shelf edge length. This estimate is in agreement with the 1 Sv down welling circulation implied by the Walin calculation. The second important process to consider is the surface wind forcing. For comparison with the Walin calculation we are only going to consider the wind forced transport during the summer months as the relevant density classes only exist when the water column is stratified. For the summer wind forcing the transports per unit width are estimated from 0.67 to 1.06 m^2 s^{-1} Huthnance et al. [2009] which are equivalent to 1.34 to 2.12 Sv over the 2000 km shelf edge. The Walin estimate for the on shelf surface transport, as a component of both the down welling and across shelf circulations, is 1.5 Sv. This Walin estimate is again comparable with the wind-driven estimate. Hence, the surface wind forcing is driving an on-shelf transport of water in the surface layer which is then returned to the open ocean either through an off shelf transport in the bottom layer or through the Norwegian Trench. The partitioning of the return between these two options may be controlled by the strength of the bottom Ekman transport driven by the strength of the slope current.

6.2.3 Processes missing from the Walin Framework

Whilst the Walin Framework is mathematically rigorous and provides a good integrated view of the circulation of the European Shelf, some local processes contributing to cross shelf exchange of both volume and tracers are omitted. These processes include the transport of tracers along density surfaces or the transport of any volume onto the shelf which is balanced by an equivalent off shelf transport occurring within the same density class. Additionally the Walin calculations are applied using density as the tracer. As such the diffusion of any other tracers across the surfaces of the tracer, such as the diffusion of nutrients across nutrient surfaces, is not present in the calculation unless the nutrient surface happens to align with density surfaces. This coincidence is the case for the vertical structure of nutrients within the shelf seas as the stratification controls the boundary between the low nutrient surface layer and high nutrient bottom layer. This alignment is not, however, the case for the horizontal distribution of nutrients and the effects of the horizontal diffusion of nutrients are not captured within the calculation. This horizontal transfer can be achieved by considering the Walin Framework using a nutrient as the tracer [e.g Badin et al., 2010] however this required much more data then is readily available about the nutrient distribution and estimates of the sources and sinks meaning it is only feasible using the output of models.

6.3 Closing the nutrient budget

One of the key motivating points for this study was the estimates that the shelf seas require a supply of nutrients from the open ocean in order to maintain their enhanced productivity. In this thesis we have shown that the bolus transport is opposed by a time-mean flow resulting in a small total transport of volume and tracer. We have also shown that much of the European Shelf edge has a down welling circulation. This down welling results in a net loss of nutrients from the shelf, as the nutrient deplete surface water is transported onto the shelf and the nutrient rich deep water is transported off the shelf. This indicates that nutrients must be supplied to the shelf via a process missing from the Walin calculation. The missing process may be transfer along density surfaces which is balanced by an opposite and equivalent transport along the same density surface in a different location. This form of transport can be simply modelled by a horizontal diffusion,

$$F = LH\kappa_h \frac{\partial N}{\partial x} \tag{6.5}$$

where F is the flux of nitrate integrated over the whole shelf edge, L is the along slope length scale, H is the depth of the water column, κ_h is the horizontal diffusivity, N is the nitrate concentration, and x is the across shelf edge coordinate. Taking the across shelf nitrate gradient as $\Delta N = 5\mu molL^{-1} = 5\text{x}10^{-3} molm^{-3}$ over an across shelf distance of $\Delta x = 100$ km, a shelf edge length of $L = 2000$ km, a shelf depth of $H = 200$ m and requiring the total supply of nitrate to match the shelf edge supply estimate of Proctor et al. [2003], 3.7 Mtonnes N yr^{-1} = 8x10^3 mol NO$_3$ s^{-1}, yields a horizontal diffusivity of κ_h = 4x10^2 m^2 s^{-1}. This estimate is similar to previous estimates of the horizontal diffusivity over the shelf break, such as Burrows et al. [1999] estimate an across slope diffusivity of 3.6x10^2 m^{2}s^{-1} over the Hebridies Slope. This implies that much, if not all of the nutrient supply required on the shelf could be obtained from diffusive, rather than advective, processes.

6.4 Potential future work

The work presented here raises a number of questions which could be the focus of future studies.

6.4.1 Further investigation of the cancellation of the bolus transport

The cancellation between the bolus and mean transport in the depth integral and in a two layer ocean is somewhat surprising. Whilst the Stokes' Drift for an internal wave has been shown to depth-integrate to zero in a theoretical environment this does not imply close to zero transport in individual layers as seen here. This extension could consist of the application of the methods described in Henderson [2016] to the internal tide on the shelf. This would be best implemented in a region where the internal tide is strong compared to other processes, to avoid the complications of other processes masking the small residual that would be expected. Additionally the mooring investigated would preferably have a clean propagating internal tide signal that has been generated by a smooth topographic feature with the majority of the energy still in the tidal frequency and linear wave.

6.4.2 Application of the Walin Method to other shelf seas

The Walin Framework for understanding the transformation of water masses in density space is a mathematically rigorous framework. In this thesis the application of the framework to the European Shelf has implied circulations that are similar both in their pattern, in this case down-welling, and magnitude to previous studies. This supports the use of the method presented here in considering the circulations on other shelves across the globe which follow the requirements set out in the chapter. Primarily these are: that the shelf is seasonally stratified, there is sufficient range in density to determine a range of density bins, and there is an estimate of the structure and magnitude of the TKE dissipation rate. This could yield new estimates of the circulation for many shelves around the world, either providing the first estimate for the region or building on previous estimates of the circulation integrated in space and time.

6.4.3 Investigation of isopycnic transfers or nutrients

The application of the Walin Framework to the European Shelf implied a down-welling circulation across much of the shelf edge. This implies an off shelf transport of inorganic nutrients as they typically have a higher concentration in the bottom layer. This leaves open the question of how nutrients are supplied to the European Shelf but somewhat narrows down the range of processes that could be responsible to those that are not captured by the Walin calculation. This is specifically processes that are diffusive or that involve exchanges along density surfaces that are not constrained by the Taylor-Proudman Theorem.

6.5 Conclusions

In this thesis we have explored the volume exchange occurring at the topographically controlled shelf edge. This has occurred through two main themes.

The first of these themes was considering the role of bolus transport, the co-variance between layer thickness and velocity, generated by the internal tide in transporting volume near the shelf break. The bolus transport was always in the same direction as the propagation of the internal tide, typically onto the shelf, driving volume onto the shelf. This bolus transport was, however, in the two layer limit, balanced by the mean transport within the layer. This result can be explained through the recently published paper by Henderson [2016] through the fact that the bolus transport is only a partial representation of the Stokes drift for this problem and in fact the additional term, in our calculations a component of the time-mean transport, balances the bolus transport when considering the depth mean or the transport within layers defined by zero crossings in the horizontal velocity mode structure, as considered here.

The second theme was the application of the integral Walin Framework to the European Shelf. The air-sea forcing inputs were obtained using the ECMWF ERA-Interim product of reanalysis data. The diapycnic forcing was diagnosed using a pair of observational data sets collected at the same location for a spring and a neap tide, which was then assumed to be representative of the whole shelf. This showed formation rates dominated by the effects of air-sea forcing with slight modification by the diffusive forcing. These formation rates mapped into two distinct circulations. The first of these circulations was a down welling across much of the shelf edge of 1 Sv, which is similar to modelling calculations of the mean transport [Holt et al., 2009, Huthnance et al., 2009]. The second circulation was an across shelf circulation, with volume coming onto the shelf in the surface layer across much of the shelf edge which is balanced by a return flow through the Norwegian Trench. Hence, the Walin application to the European Shelf provides plausible transport estimates and a planned extension is to apply the same approach to other shelves.

Bibliography

Knut Aagaard, L. K. Coachman, and Eddy Carmack. On the halocline of the arctic ocean. *Deep-Sea Research*, 28A:529 – 545, 1981.

D. G. Andrews and M. E. McIntyre. An exact theory of nonlinear waves on a Lagrangian-mean flow. *J. Fluid Mech.*, 89:609–646, 1978.

David G. Andrews. On the forcing of time-mean flows by transient, small-amplitude eddies. *Journal of the Atmospheric Sciences*, 47:1837 – 1844, 1990.

Jan O. Backhaus, Hermann Fohrmann, Jochen Kampf, and Angelo Rubino. Formation and export of water masses produced in arctic shelf polynyas - process studies of oceanic convection. *ICES Journal of Marine Science*, 54: 366 – 382, 1997.

Gualtiero Badin, Richard G. Williams, and Jonathan Sharples. Water-mass transformation in the shelf seas. *Journal of Marine Research*, 68(2):189–214, 2010.

Gualtiero Badin, Richard G. Williams, Zhao Jing, and Lixin Wu. Water mass transformations in the southern ocean diagnosed from observations: Contrasting effects of air-sea fluxes and diapycnal mixing. *Journal of Physical Oceanography*, 43:1472 – 1484, 2013.

P. G. Baines and S. Condie. Observations and modeling of antarctic downslope flows: A review. In S. Jacobs and R. Weiss, editors, *Ocean, Ice, and*

Atmosphere: Interactions at the Antarctic Continental Margin, number 75 in Antarctic Research Series, pages 29 – 49. 1998.

J.A. Barth. Stability of a coastal upwelling front: 2. Model results and comparison with observations. *J. Geophys. Res*, 94:10857–10883, 1989.

P.E. Biscaye, C. N. Flagg, and P. G. Falkowski. The shelf edge exchange processes experiment, seep-ii: an introduction to hypotheses, results and conclusions. *Deep-Sea Research II*, 41:231 – 252, 1994.

K. F. Bowden. The dynamics of flow on a submarine ridge. *Tellus*, 12:418 – 426, 1960.

K.H. Brink. Deep-sea forcing and exchange processes. In K.H Brink and A.R. Robinson, editors, *Chap 6 In: The Sea, The Global Coastal Ocean: Processes and Methods*, volume 10, pages 151–167. John Wiley & Sons, New York, 1988.

J Brown, L Carrillo, L Fernand, K J Horsburgh, A E Hill, E F Young, and K J Medler. Observations of the physical structure and seasonal jet-like circulation of the celtic sea and st. georges channel of the irish sea. *Continental Shelf Research*, 23:533 – 137, 2002.

Harry L. Bryden, Julio Candela, and Thomas H.Kinder. Exchnage through the strait of gibraltar. *Progress in Oceanography*, 33:201 – 248, 1994.

M. Burrows and S. A. Thorpe. Drifter observations of the hebrides slope current and nearby circulation patterns. *Annales Geophysicae*, 17:280 – 302, 1999.

M. Burrows, S. A. Thorpe, and D. T. Meldrum. Dispersion over the hebridean and shetland shelves and slopes. *Continental Shelf Research*, 19:49 – 55, 1999.

O. R. Cooper, D. D. Parrish, J. Ziemke, N. V. Balashow, M.Cupeiro, I. E. Galbally, S. Gilge, L. Horowitz, N. R. Jensen, J. F. Lamarque, V. Naik, S. J.

Oltmans, J. Schwab, D. T. Shindell, A. M. Thompson, V. Thouret, Y. Wang, and R. M. Zbinden. Global distribution and trends of tropospheric ozone: An observation-based review. *Elementa*, 2, 2014.

G. T. Csanady. Energy dissipation and upwelling in a western boundary current. *Journal of Physical Oceanography*, 19:462 – 473, 1989.

G. Danabasoglu, J. C. McWilliams, and P. R. Gent. The role of mesoscale tracer transports in the general ocean circulation. *Science*, 264:1123–1126, 1994.

Gary D. Egbert and Svetlana Y. Erofeeva. Efficient inverse modeling of barotropic tides. *Journal of Atmospheric and Oceanic Technology*, 19:183 – 204, 2002.

Gary D. Egbert, Svetlana Y. Erofeeva, and Richard D. Ray. Assimilation of altimetry data for nonlinear shallow-water tide: Quater-diurnal tides of the northwest european shelf. *Continental Shelf Research*, 30:668 – 679, 2010.

Michel Frankignoulle and Alberto V. Borges. European continental shelf as a significant sink for atmospheric carbon dioxide. *Global Biogeochemical Cycles*, 15:569 – 576, 2001.

Peter R. Gent and James C. McWilliams. Isopycnal mixing in ocean circulation models. *Journal of Physical Oceanography*, 20:150 – 155, 1990.

Peter R. Gent, Jurgen Willebrand, Trevor J. McDougall, and James C. McWilliams. Parameterizing eddy-induced tracer transports in ocean circulation models. *Journal of Physical Oceanography*, 25:463 – 474, 1995.

A. E. Gill. Atmosphere-Ocean Dynamics. In *International Geophysics Series*, volume 30. Academic Press, 1982.

J.A. Mattias Green and Jonas Nycander. A comparison of tidal conversion parameterizations for tidal models. *Journal of Physical Oceanography*, 43: 104 – 119, 2013.

J.A. Mattias Green, John H. Simpson, Sonya Legg, and Matthew R. Palmer. Internal waves, baroclinic energy fluxes and mixing at the European shelf edge. *Continental Shelf Research*, 28:937–950, 2008.

Stephen M. Henderson. Upslope internal-wave stokes drift, and compensating downslope eulerian mean currents, observed above a lakebed. *Journal of Physical Oceanography*, 46:1947 – 1961, 2016.

A. Edward Hill. Leakage of barotropic slope currents onto the continental shelf. *Journal of Physical Oceanography*, 14:1617 – 1621, 1995.

A.E. Hill, A.J. Souza, K. Jones, J.H. Simpson, G.I. Shapiro, R. McCandliss, H. Wilson, and J. Leftley. The malin cascade in winter 1996. *Journal of Marine Research*, 56:87 – 106, 1998.

Jason Holt and Roger Proctor. The seasonal circulation and volume transport on the northwest european continental shelf: A fine resolution model study. *Journal of Geophysical Research*, 113, 2008.

Jason Holt and Lars Umlauf. Modeling the tidal mixing fronts and seasonal stratification of the northwest european continental shelf. *Continental Shelf Research*, 28:887 – 903, 2008.

Jason Holt, Sarah Wakelin, and John Huthnance. Down-welling circulation of the northwest european continental shelf: A driving mechanism for the continental shelf carbon pump. *Geophysical Research Letters*, 36, 2009.

Joanne E. Hopkins, Gordon R. Stephenson Jr., J. A. M. Green, Mark E. Inall, and Matthew R. Palmer. Storms modify baroclinic energy fluxes in a seasonally stratified shelf sea: Inertial-tidal interaction. *Journal of Geophysical Research Oceans*, 119:6863 – 6883, 2014.

Y. Hsueh, Heung-Jae Lie, and Hiroshi Ichikawa. On the branching of the kuroshio west of kyushu. *Journal of Geophysical Research*, 101:3851 – 3857, 1996.

J. M. Huthnance. Slope currents and ”jebar”. *Journal of Physical Oceanography*, 14:795 – 810, 1984.

J.M. Huthnance, H.M. van Aken, M. White, E.D. Barton, B. Le Cann, E.F. Coelho, E.A. Fanjul, P. Miller, and J. Vitorino. Ocean margin exchange-water flux estimates. *Journal of Marine Systems*, 32:107 – 137, 2002.

J.M. Huthnance, J.T. Holt, and S.L. Wakelin. Deep ocean exchange with west-European shelf seas. *Ocean Sciences*, 5:621 – 634, 2009.

D.J. Hydes, A.C. Le Gall, A.E.J. Miller, U. Brockmann, T. Raabe, S. Holley, X. Alvarez-Salgado, A. Antia, W. Balzer, L. Chou, M. Elskens, W. Helder, I. Joint, and M. Orren. Supply and demand of nutrients and dissolved organic matter at and across the nw european shelf break in relation to hydrography and biogeochemical activity. *Depp-Sea Research II*, 48:3265 – 3292, 2001.

M. Inall, T. P. Rippeth, and T. J. Sherwin. Impact of non-linear waves on the dissipation of internal tidal energy at a shelf break. *Journal of Geophysical Research Letters*, 105:8687 – 8705, 2000.

M. Inall, G. I. Shapiro, and T. J. Sherwin. Mass transport by non-linear internal waves on the malin shelf. *Continental Shelf Research*, 21:1449 – 1472, 2001.

M. Inall, D. Aleynik, T. Boyd, M. Palmer, and J. Sharples. Internal tide coherence and decay over a wide shelf sea. *Geophys. Res. Letters*, 38:L23607, 2011.

V.V. Ivanov, G.I. Shapiro, J.M. Huthnance, D.L. Aleynik, and P.N. Golovin. Cascades of dense water around the world ocean. *Progress in Oceanography*, 60:47 – 98, 2004.

J. Klink. Dynmodes.m - ocean dynamic vertical modes. Woods Hole Science Center - SEA-MAT—Matlab tools for oceanographic Analysis, 1999. URL `http://woodshole.er.usgs.gov/operations/sea-mat/index.html`.

Corinne Le Quere, Michael R. Raupach, Josep G. Canadell, Gregg Marland, et al. Trends in the sources and sinks of carbon dioxide. *Nature Geoscience*, 2:831 – 836, 2009.

Mei-Man Lee, David P. Marshall, and Richard G. Williams. On the eddy transfer of tracers: Advective or diffusive? *Journal of Marine Research*, 55: 483 – 505, 1997.

K. K. Liu, L. Atkinson, R. A. Quinones, and L. Talaue-McManus. Biogeochemistry of continental margins in a global context. In K. K. Liu, L. Atkinson, R. A. Quinones, and L. Talaue-McManus, editors, *Carbon and Nutrient Fluxes in Continental Margins: A Global Synthesis*, pages 3 – 24. Berlin Heidelberg: Springer-Verlag, 2010.

R. A. Locarnini, A. V. Mishonov, J. I. Antonov, T. P. Boyer, H. E. Garcia, O. K. Baranova, M. M. Zweng, C. R. Paver, J. R. Reagan, D. R. Johnson, M. Hamilton, and D. Seidov. Volume 1: Temperature. In S. Levitus, editor, *World Ocean Atlas 2013*. NOAA, 2013.

Julius London and Jean Kelley. Global trends in total atmospheric ozone. *Science*, 184:987 – 989, 1974.

Rick Lumpkin and Kevin Speer. Global ocean meridional overturning. *Journal of Physical Oceanography*, 37:2550 – 2562, 2007.

Parker MacCready, Robert D. Hetland, and W. Rockwell Geyer. Long-term isohaline salt balance in an estuary. *Continental Shelf Research*, 22:1591–1601, 2002.

J. A. MacKinnon and M. C. Gregg. Shear and baroclinic energy flux on the summer New England Shelf. *Journal of Physical Oceanography*, 33:1462 – 1475, 2003.

David Marshall. Subduction of water masses in an eddying ocean. *Journal of Marine Research*, 55:201 – 222, 1997.

John Marshall, Daniel Jamous, and Johan Nilsson. Reconciling thermodynamic and dynamic methods of computation of water-mass transformation rates. *Deep-Sea Research Part I*, 46:545–572, 1999.

T.J. McDougall. Parameterizing mixing in inverse models. *Dynamics of Oceanic Internal Gravity Waves, P. Muller and D. Henderson Eds., Proc. Sixth 'Aha Huliko'a Hawaiian Winter Workshop, University of Hawaii at Manoa*, pages 355–386, 1991.

Trevor J. McDougall and Peter C. McIntosh. The temporal-residual-mean velocity. part ii: Isopycnal interpretation and the tracer and momentum equations. *Journal of Physical Oceanography*, 31:1222 – 1246, 2001.

J. F. Middleton and J. W. Loder. Skew fluxes in polarized wave fields. *Journal of Physical Oceanography*, 19:68 – 76, 1989.

Phil Morgan and Lindsay Pender. Seawater library version 3.3, 2010. URL `http://www.cmar.csiro.au`.

J.D. Nash, E.L. Shroyer, S.M. Kelly, M.E. Inall, M.D. Levine, N.L. Jones, and R.C. Musgrave. Are any coastal internal tides predictable? *Oceanography*, 25:80 – 95, 2012.

A. J. G. Nurser, Robert Marsh, and Richard G. Williams. Diagnosing water mass formation from air-sea fluxes and surface mixing. *Journal of Physical Oceanography*, 29:1468–1487, 1999.

J. Nycander. Generation of internal waves in the deep ocean by tides. *Journal of Geophysical Research*, 110:C10028, 2005. doi: 10.1029/2004JC002487.

I. Orlansky. The influence of bottom topography on the stability of jets in a baroclinic fluid. *J. Atmos. Sci.*, 26:1216–1969, 1969.

T. R. Osborn. Estimates of the local rate of vertical diffusion from dissipation measurements. *Journal of Physical Oceanography*, 10:83–89, 1980.

Hsien Wang Ou and Leo Maas. Tidal-induced buoyancy flux and mean transverse circulation. *Continental Shelf Research*, 5:611 – 628, 1986.

Stuart C. Painter, Susan E. Hartman, Caroline Kivimae, Lesley A. Salt, Nicola M. Clargo, Yann Bozec, Chris J. Daniels, Sam C. Jones, Victoria S. Hemsley, Lucie R. Munns, and Stephanie R. Allen. Carbon exchange between a shelf sea and the ocean: The hebrides shelf, west of scotland. *Journal of Geophysical Research: Oceans*, 121:4522 – 4544, 2016.

M. R. Palmer, J. A. Polton, M. E. Inall, T. P. Rippeth, J. A. M. Green, J. Sharples, and J. H. Simpson. Variable behaviour in pycnocline mixing over shelf seas. *Geophysical Research Letters*, 40:161 – 166, 2013.

Matthew R. Palmer, Tom P. Rippeth, and John H. Simpson. An investigation of internal mixing in a seasonally stratified shelf sea. *Journal of Geophysical Research*, 113, 2008.

Daniel Pauly, Villy Christensen, Sylvie Guenette, Tony J. Pitcher, U. Rashid Sumaila, Carl J. Walters, R. Watson, and Dirk Zeller. Towards sustainability in world fisheries. *Nature*, 418:689 – 695, 2002.

R.D. Pingree and B. Le Cann. Celtic and armorican slope and shelf residual currents. *Progress in Oceanography*, 23:303 – 338, 1989.

R.D. Pingree and G. T. Mardell. Solitary internal waves in the celtic sea. *Progress in Oceanography*, 14:431 – 441, 1985.

R.D. Pingree, P. M.Holligan, and G. T. Mardell. The effects of vertical stability on phytoplankton distributions in the summer on the northwest euopean shelf", journal=.

R. A. Plumb and J. D. Mahlman. The zonally averaged transport characteristics of the gfdl general circulation/transport model. *Journal of the Atmospheric Sciences*, 44:298 – 327, 1987.

Roger Proctor, Jason T. Holt, J. Icarus Allen, and Jerry Blackford. Nutrient fluxes and budgets for the north west european shelf from a three-dimensional model. *Science of The Total Environment*, 314:769 – 785, 2003.

Tom P. Rippeth and Mark E. Inall. Observations of the internal tide and associated mixing across the malin shelf. *Journal of Geophysical Research*, 107, 2002.

Tom P. Rippeth, Ben J. Lincoln, Yueng-Djern Lenn, J. A. Mattias Green, Arild Sundfjord, and Sheldon Bacon. Tide-mediated warming of arctic halocline by atlantic heat fluxes over rough topography. *Nature Geoscience*, 8:191 – 194, 2015.

Jo Roberts and Thomas D. Roberts. Use of the butterworth low-pass filter for oceanographic data. *Journal of Geophysical Research: Oceans*, 83:5510–5514, 1978.

Sunke Schmidtko, Karen J. Heywood, Andrew F. Thompson, and Shigeru Aoki. Multidecadal warming of antarctic waters. *Science*, 346:1227 – 1231, 2014.

S.P. Seitzinger and A.E. Giblin. Estimating denitrification in the north atlantic continental shelf sediments. *Biogeochemistry*, 35:235 – 260, 1996.

Jonathan Sharples. Potential impacts of the spring-neap tidal cycle on shelf sea primary production. *Journal of Plankton Research*, 30:183 – 197, 2008.

Jonathan Sharples, C. Mark Moore, and Edward R. Abraham. Internal tide dissipation, mixing, and vertical nitrate flux at the shelf edge of NE New Zealand. *Journal of Geophysical Research*, 106:14069 – 14081, 2001.

Jonathan Sharples, Oliver N. Ross, Beth E. Scott, Simon P. R. Greenstreet, and Helen Fraser. Inter-annual variability in the timing of stratification and the spring bloom in the north-western north sea. *Continental Shelf Research*, 26:733–751, 2006.

Jonathan Sharples, Jacqueline F. Tweddle, J. A. Mattias Green, Matthew R. Palmer, Young-Nam Kim, Anna E. Hickman, Patrick M. Holligan, C. Mark Moore, Tom P. Rippeth, John H. Simpson, and Vladimir Krivtsov. Spring-neap modulation of internal tide mixing and vertical nitrate fluxes at a shelf edge in summer. *Limnology and Oceanography*, 52(5):1735–1747, 2007.

Jonathan Sharples, C. Mark Moore, Anna E. Hickman, Patrick M. Holligan, Jacqueline F. Tweddle, Matthew R. Palmer, and John H. Simpson. Internal tidal mixing as a control on continental margin ecosystems. *Geophysical Research Letters*, 36, 2009.

Jonathan Sharples, Beth E. Scott, and Mark E. Inall. From physics to fishing over a shelf sea tidal bank. *Progress in Oceanography*, 117:14069 – 14081, 2013.

J. Short, T. Doyle, J. Hopkins, J. Wihsgott, E. Dumont, and C. Griffiths. Moorings. In M.E. Inall, editor, *RRS James Cook Cruise JC88, Glasgow to Southampton, FASTNEt Cruise to the Malin Shelf Edge*, number XX in

Internal Report, chapter 13, pages 102 – 130. Scottish Association for Marine Science, 2013.

J.H. Simpson and D.G. Bowers. Models of stratification and frontal movement in shelf seas. *Deep Sea Research*, 28A:727 – 738, 1981.

John H. Simpson and Robin R. McCandliss. "the ekman drain": a conduit to the deep ocean for shelf material. *Ocean Dynamics*, 63:1063 – 1072, 2013.

John H. Simpson and Robin D. Pingree. Shallow sea fronts produced by tidal stirring. In *Oceanic Fronts in Coastal Processes*, chapter 5, pages 29 – 42. 1977.

John H. Simpson and Jonathan Sharples. *Introduction to the Physical and Biological Oceanography of Shelf Seas.* Cambridge University Press, Cambridge, UK, 2012.

Kate Snow, Andrew McC. Hogg, Bernadette M. Sloyan, and Stephanie M. Downes. Sensitivity of antarctic bottom water to changes in surface boyancy fluxes. *Journal of Climate*, 29:313–330, 2016.

A. J. Souza, J. H. Simpson, M. Harikrishnan, and J. Malarkey. Flow structure and seasonality in the hebridean slope current. *Oceanologica Acta*, 24:S63 – S76, 2001.

Kevin Speer and Eli Tziperman. Rates of water mass formation in the north atlantic. *Journal of Physical Oceanography*, 22:93 – 104, 1992.

Gordon R. Stephenson Jr., Joanne E. Hopkins, J. A. M. Green, Mark E. Inall, and Matthew R. Palmer. Baroclinic energy flux at the continental shelf edge modified by wind-mixing. *Geophysical Research Letters*, 42:1826 – 1833, 2015.

Andrew L. Stewart and Andrew F. Thompson. Connecting antarctic cross-slope exchange with southern ocean overturning. *Journal of Physical Oceanography*, 43:1453 – 1471, 2013.

Andrew L. Stewart and Andrew F. Thompson. Eddy-mediated transport of warm circumpolar deep water across the antarctic shelf break. *Geophysical Research Letters*, 42:432 – 440, 2015.

Anders Stigebrandt and Jan Aure. Vertical mixing in basin waters of fjords. *Journal of Physical Oceanography*, 19:917 – 926, 1989.

Fiammetta Straneo and Patrick Heimbach. North atlantic warming and the retreat of greenland's outlet glaciers. *Nature*, 504:36 – 43, 2013.

David A. Sutherland, Fiammetta Straneo, Garry B. Stenson, Fraser J.M. Davidson, Mike O. Hammill, and Aqqalu Rosing-Asvid. Atlantic water variability on the se greenland continental shelf and its relationship to sst and bathymetry. *Journal of Geophysical Research: Oceans*, 118:847 – 855, 2013.

Helmuth Thomas, Yann Bozec, Khalid Elkalay, and Hein J. W. de Baar. Enhanced open ocean storage of co_2 from shelf sea pumping. *Science*, 304: 1005–214, 2004.

A.F. Thompson, K.J. Heywood, S. Schmidtko, and A.L. Steward. Eddy transport as a key component of the Antarctic overturning circulation. *Nature Geosciences*, 7:879–884, 2014.

S A Thorpe. On the shape of progressive internal waves. *Philosophical transcations of the Royal Society of London A*, 263:563 – 614, 1968.

Shizuo Tsunogai, Shuichi Watanabe, and Tetsuro Sato. Is there a "continental shelf pump" for the adsorption of atmospheric co_2? *Tellus*, 51:701 – 712, 1999.

V. Vlasenko, N. Stashchuk, M. E. Inall, and J. E. Hopkins. Tidal energy conversion in a global hotspot: On the 3-D dynamics of baroclinic tides at the Celtic Sea shelf break. *Journal of Geophysical Research Oceans*, 119, 2014. doi: 10.1002/2013JC009708.

Gosta Walin. On the relation between sea-surface heat flow and thermal circulation in the ocean. *Tellus*, 34:187–195, 1982.

Dziga P. Walker, Mark A. Brandon, Adrian Jenkins, John T. Allen, Julian A. Dowdeswell, and Jeff Evans. Oceanic heat transport onto the amundsen sea shelf rhrough a submarine glacial trough. *Geophysical Research Letters*, 34, 2007.

Roland Wollast and Lei Chou. The carbon cycle at the ocean margin in the northern gulf of biscay. *Deep-Sea Research II*, 48:3265 – 3293, 2001.

Carl Wunsch. Note on some reynolds stress effects of internal waves on slopes. *Deep-Sea Research*, 18:583–591, 1971.

Weidong Xu, Peter I. Miller, Graham D. Quartly, and Robin D. Pingree. Seasonality and interannual variability of the european slope current from 20 years of altimeter data compared with in situ measurements. *Remote Sensing of Environment*, 162:196 – 207, 2015.

Andrew Yool and Michael J. R. Fasham. An examination of the “continental shelf pump” in an open ocean general circulation model. *Global Biogeochemical Cycles*, 15:831 – 844, 2001.

Zhongxiang Zhao, Matthew H. Alford, James B. Girton, Luc Rainville, and Harper L. Simmons. Global observations of open-ocean mode-1 m2 internal tides. *Journal of Physical Oceanography*, 46:1657 – 1684, 2016.

M. M. Zweng, J. R. Reagan, J. I. Antonov, R. A. Locarnini, A. V. Mishonov, T. P. Boyer, H. E. Garcia, O. K. Baranova, D. R. Johnson, , D. Seidov, and M. M. Biddle. Volume 2: Salinity. In S. Levitus, editor, *World Ocean Atlas 2013*. NOAA, 2013.

Chapter A1

Appendix

This appendix contains the plots associated with the moorings in Chapter 3 which were not presented within that chapter.

A1.1 Malin Shelf

(a) Potential Density (kg/m^3)

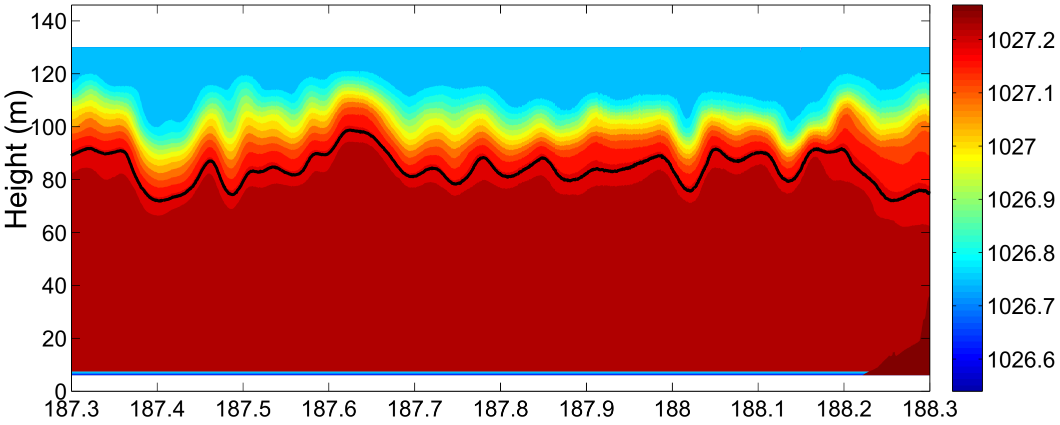

(b) Baroclinic Velocity (m/s)

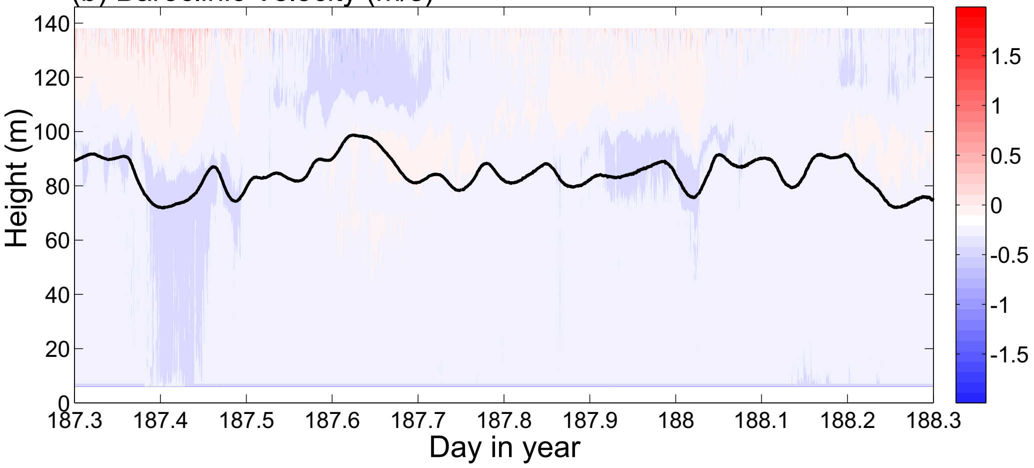

Figure A1.1: Sections of (a) Potential Density and (b) the Across Shelf Baroclinic velocity for mooring SE on the Malin shelf. The black line indicates the isopycnal used to separate the surface and deep layers.

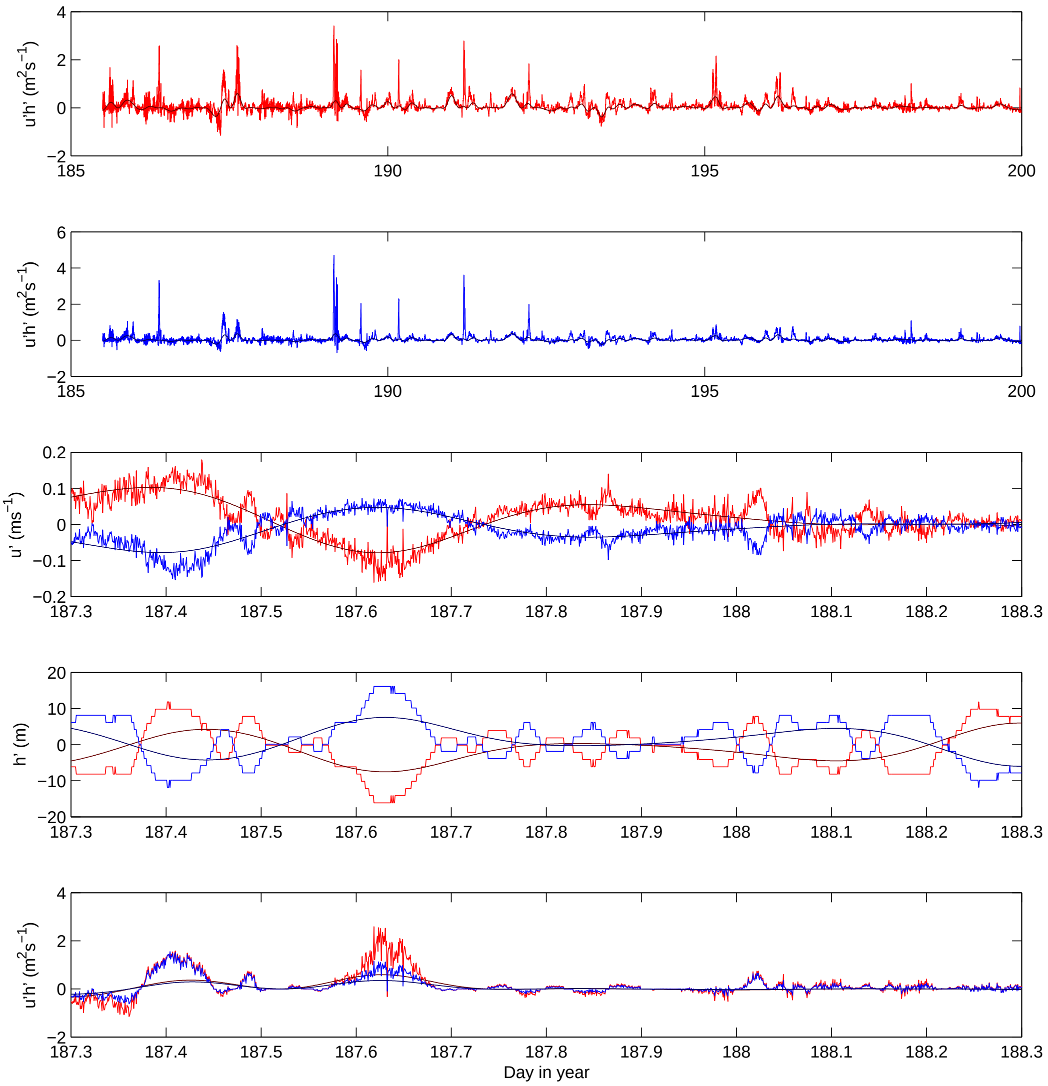

Figure A1.2: Time series from mooring SE on the Malin shelf of (a) and (b) the full record of instantaneous bolus transport for the surface and bottom layers respectively and (c) the velocity perturbations, (d) thickness perturbations and (e) the bolus transport for a selected day. The lighter lines are the full observations and the dark lines are using the 7 hour low pass filtered time series of thickness and velocity.

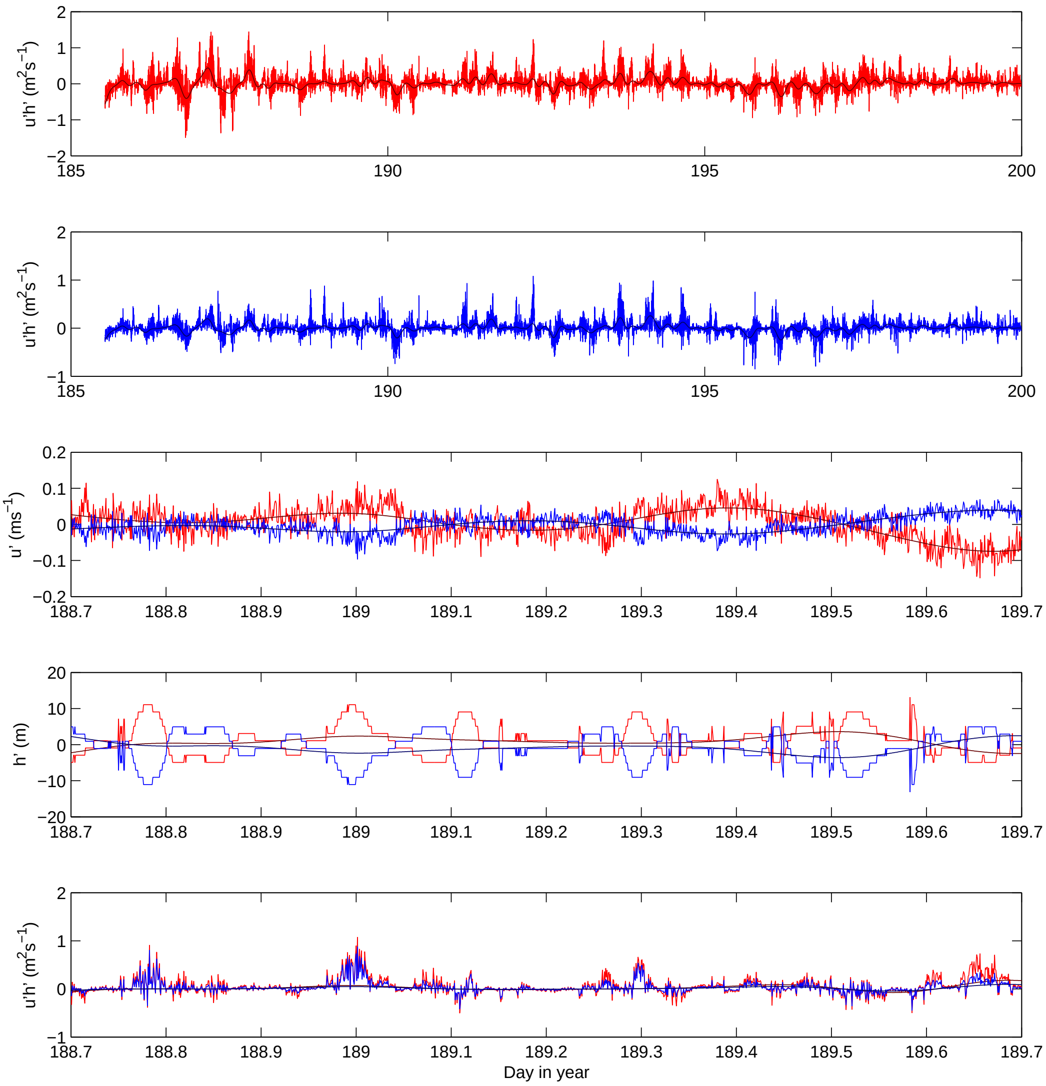

Figure A1.3: Time series from mooring SG on the Malin shelf of (a) and (b) the full record of instantaneous bolus transport for the surface and bottom layers respectively and (c) the velocity perturbations, (d) thickness perturbations and (e) the bolus transport for a selected day. The lighter lines are the full observations and the dark lines are using the 7 hour low pass filtered time series of thickness and velocity.

A1.2 Celtic Sea - ST4 and ST5

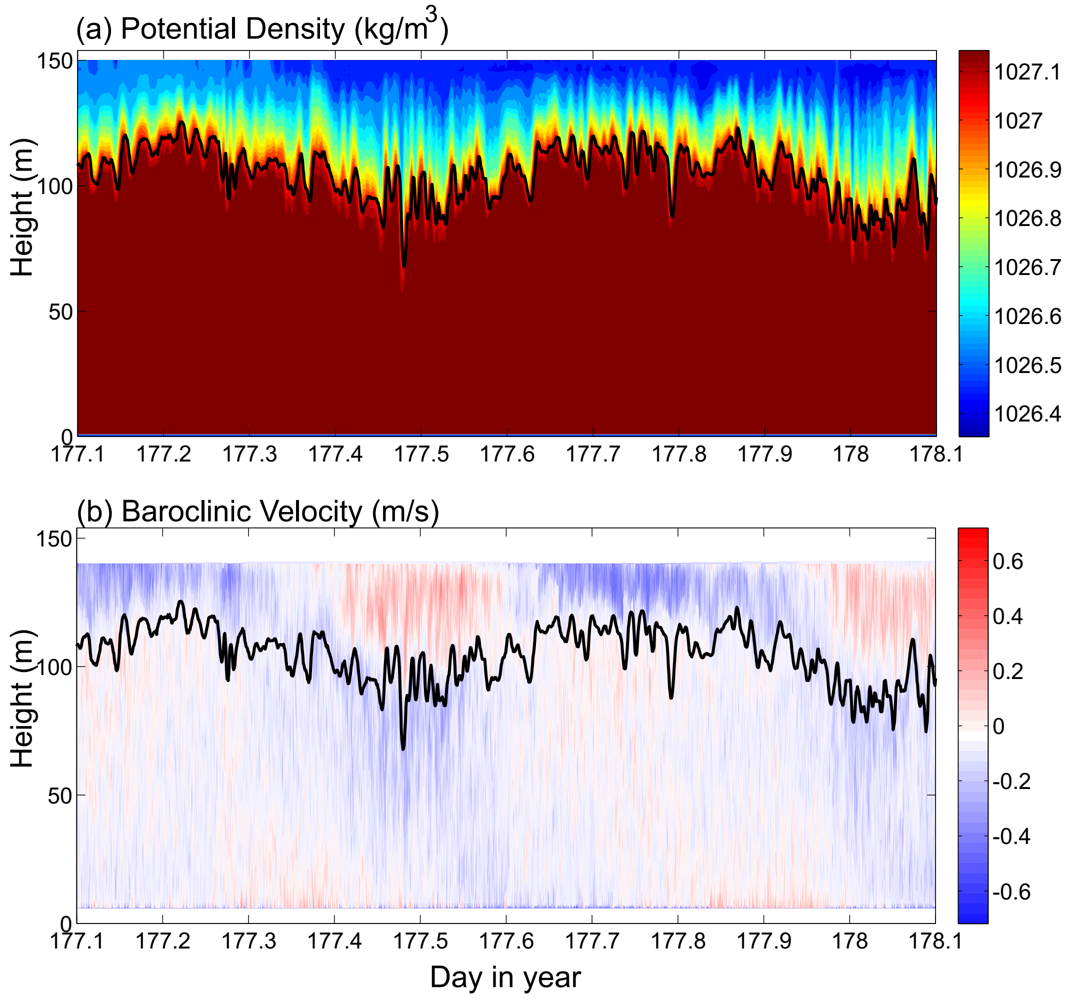

Figure A1.4: Sections of (a) Potential Density and (b) the Across Shelf Baroclinic velocity for mooring ST4 in the Celtic sea. The black line indicates the isopycnal used to separate the surface and deep layers.

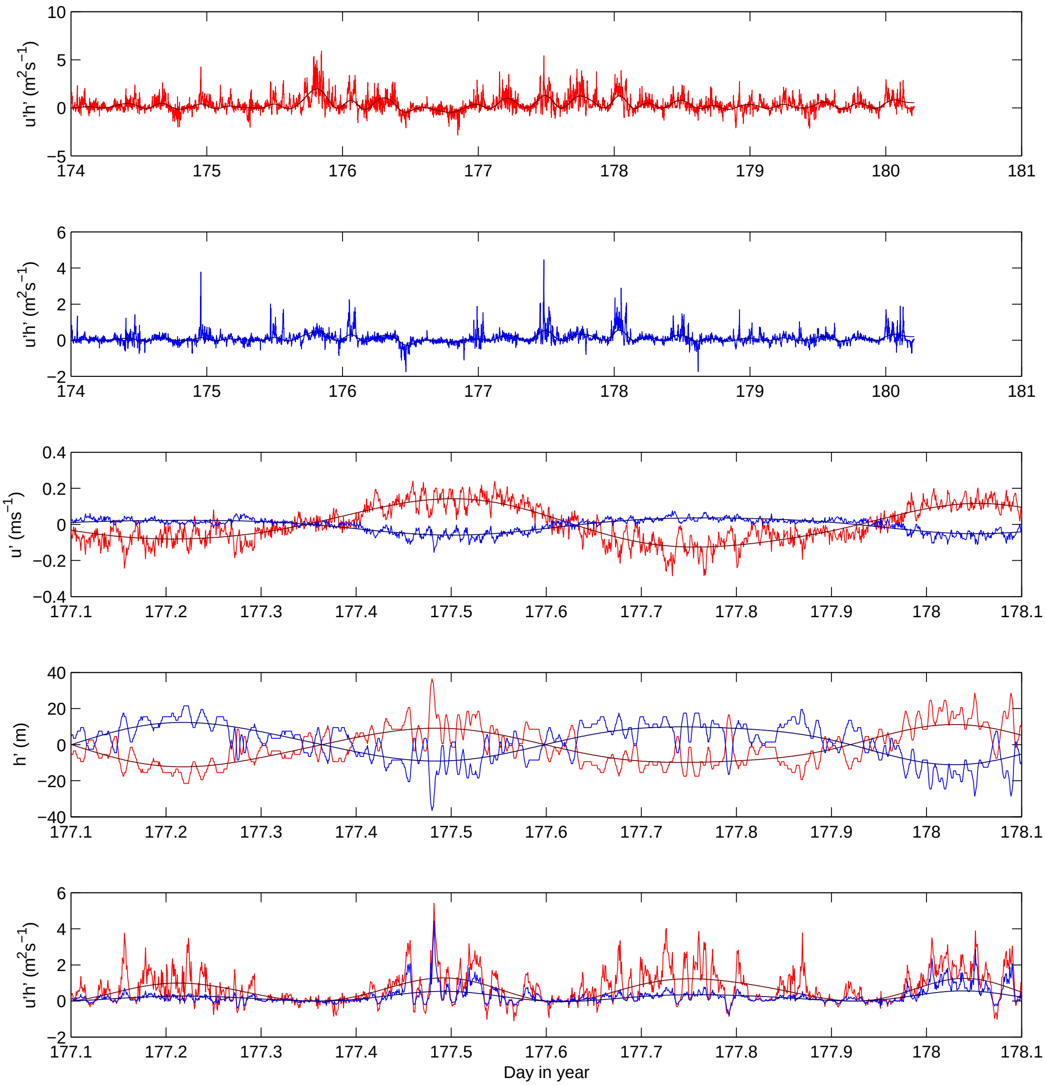

Figure A1.5: Time series from mooring ST4 in the Celtic sea of (a) and (b) the full record of instantaneous bolus transport for the surface and bottom layers respectively and (c) the velocity perturbations, (d) thickness perturbations and (e) the bolus transport for a selected day. The lighter lines are the full observations and the dark lines are using the 7 hour low pass filtered time series of thickness and velocity.

(a) Surface Layer Frequency Spectrum

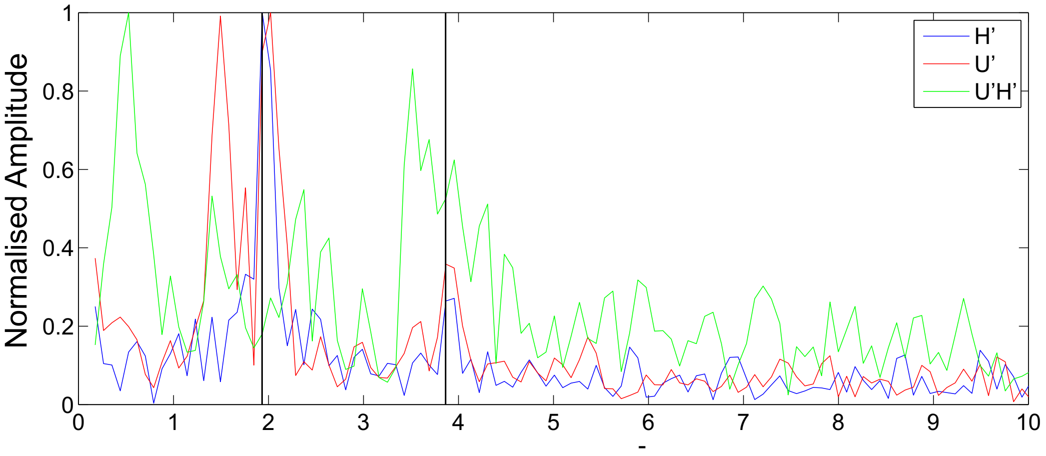

(b) Bottom Layer Frequency Spectrum

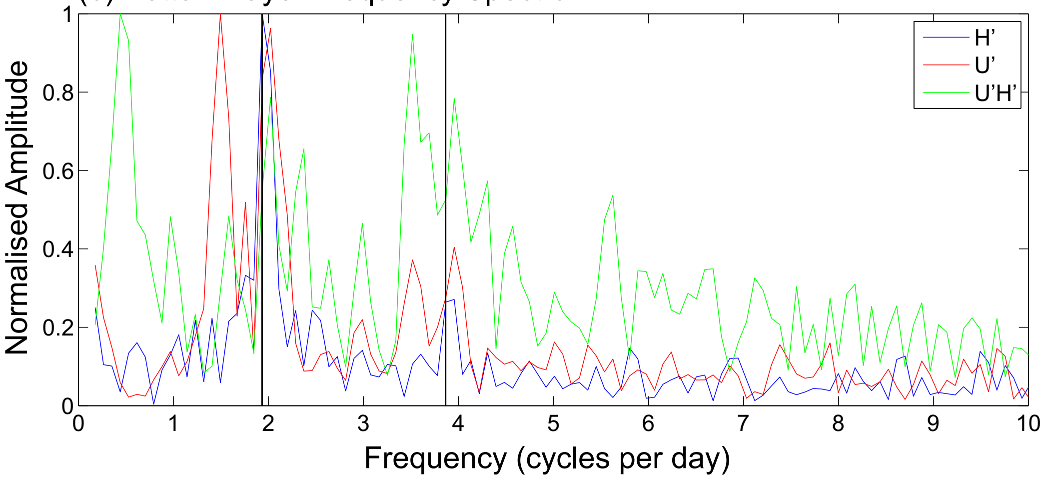

Figure A1.6: Frequency spectra from mooring ST4 in the Celtic sea for (blue) thickness perturbations, (red) velocity perturbations and (green) bolus transport for (a) the surface and (b) the bottom layer.

A1.3 Celtic Sea - IM1 and IM3

Two moorings were located on the Northwest European Celtic Sea as a part of the cruise D352, labelled IM1 and IM3. IM1 was deployed for approximately 13 days in 140 m of water at $49°25.31'N, 8°58.88'W$. IM3 was deployed for approximately 13 days in 136 m of water at $49°22.34'N, 8°54.77'W$.

The mooring at IM1 consisted of two ADCPs: the first an upward looking 150 kHz in a bottom frame and the second a 600kHz mounted subsurface. There was also a string of CTD's and temperature loggers. There were CTD's located at the bottom and at the surface and 14 temperature loggers between the bed and the surface with a variable spacing, between 5 and 15 m.

The mooring at IM3 consisted of one bed-mounted, upward looking 150kHz ADCPand a string of CTD's and temperature loggers. There were 3 CTD's located at the bottom, 55 m, and at the surface and 16 temperature loggers between the bed and the surface with a variable spacing, between 5 and 20 m.

Full water column profiles of salinity were constructed from the 2 - 3 CTDs deployed at each location and used to calculate the density. All measurements were then linearly interpolated onto coincident 1 minute x 4 metre resolution grids.

(a) Potential Density (kg/m^3)

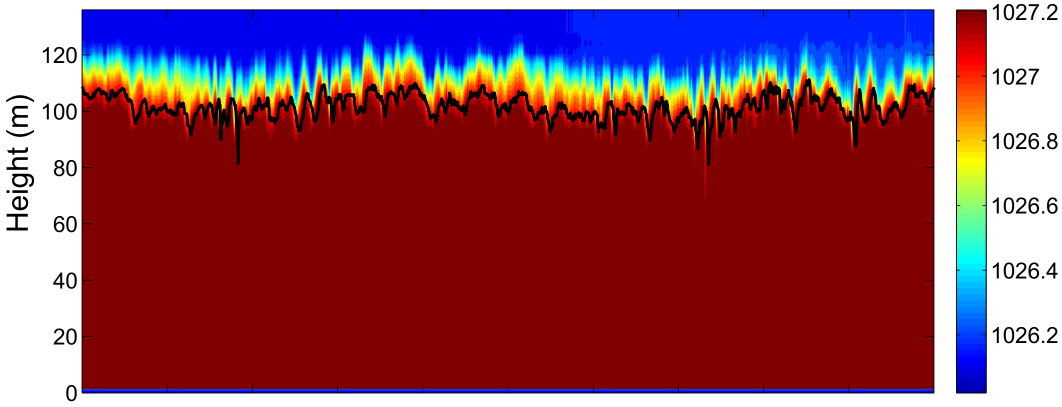

(b) Baroclinic Velocity (m/s)

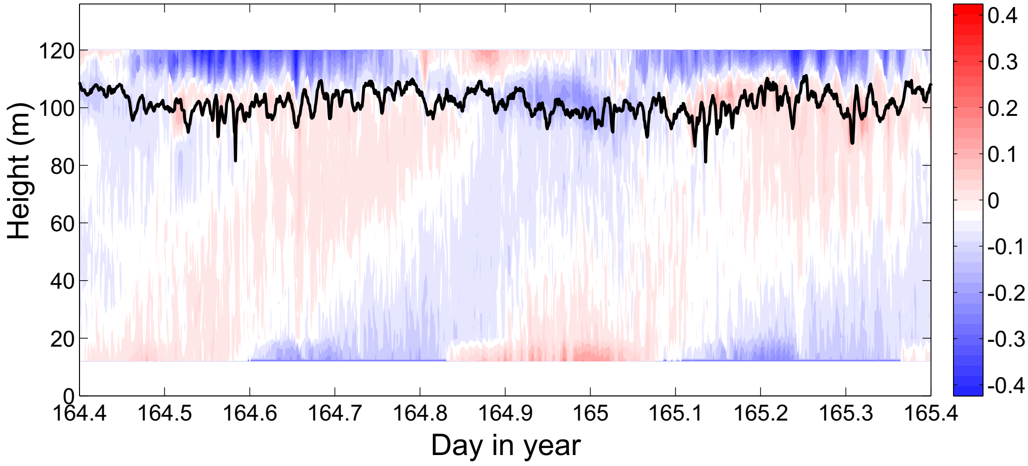

Figure A1.7: Sections of (a) Potential Density and (b) the Baroclinic velocity for mooring IM3 in the Celtic sea. The black line indicates the isopycnal used to separate the surface and deep layers.

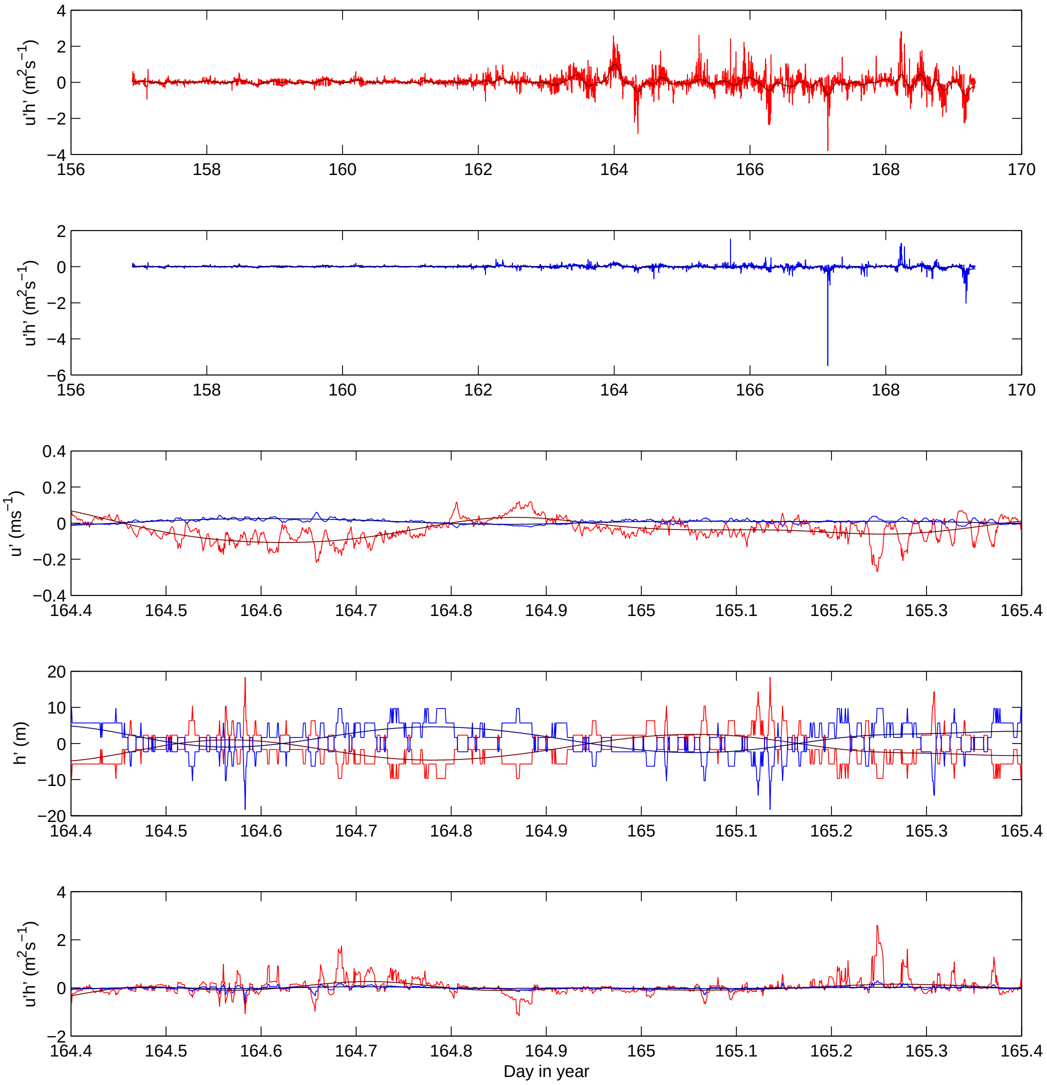

Figure A1.8: Time series from mooring IM3 in the Celtic sea of (a) and (b) the full record of instantaneous bolus transport for the surface and bottom layers respectively and (c) the velocity perturbations, (d) thickness perturbations and (e) the bolus transport for a selected day. The lighter lines are the full observations and the dark lines are using the 7 hour low pass filtered time series of thickness and velocity.

(a) Surface Layer Frequency Spectrum

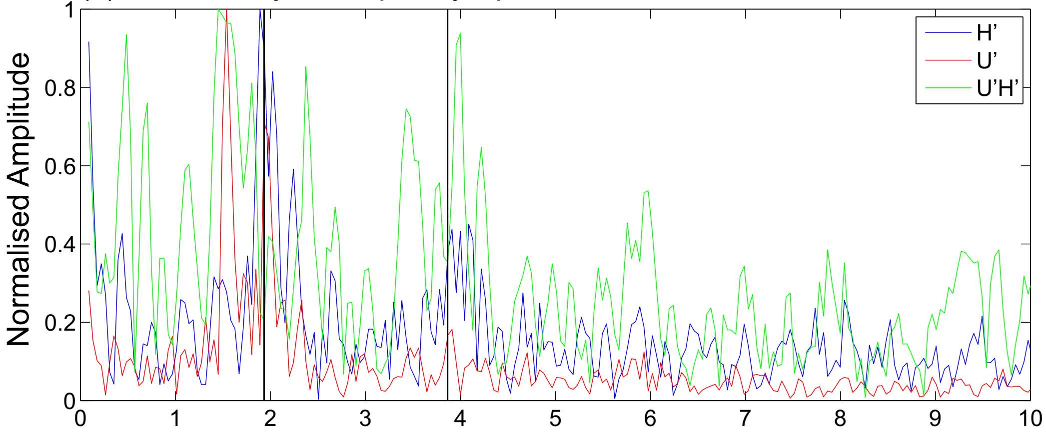

(b) Bottom Layer Frequency Spectrum

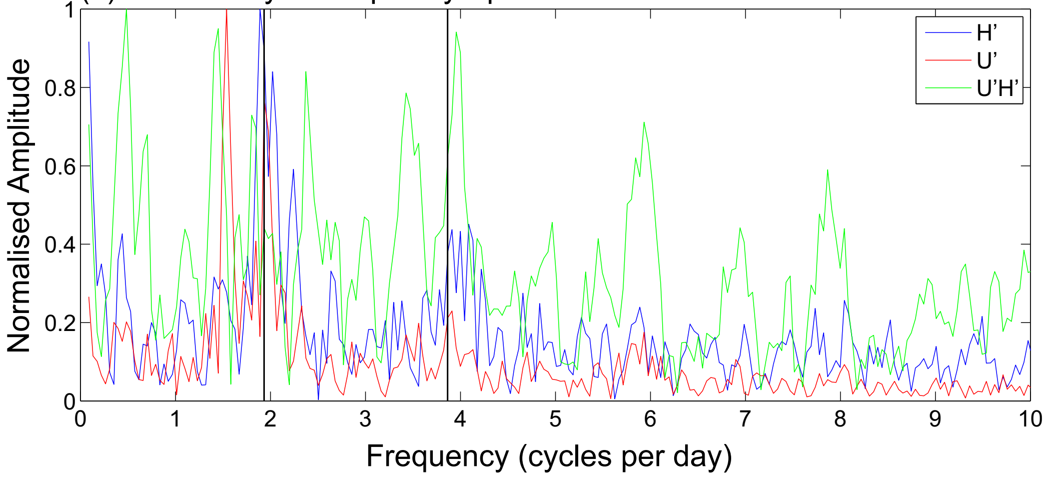

Figure A1.9: Frequency spectra from mooring IM3 in the Celtic sea for (blue) thickness perturbations, (red) velocity perturbations and (green) bolus transport for (a) the surface and (b) the bottom layer.

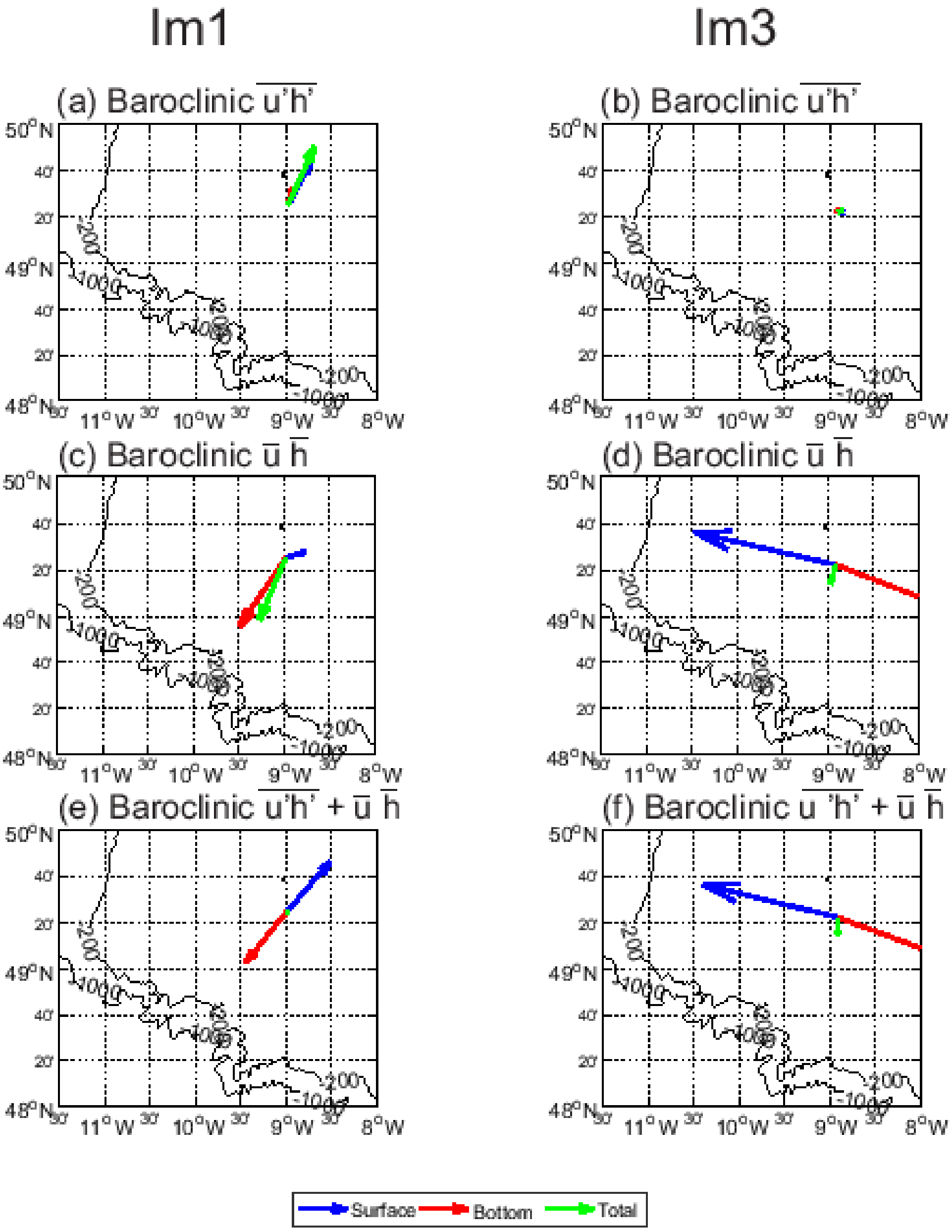

Figure A1.10: Plots showing the direction and relative magnitude of (a and b) the bolus transport driven by the baroclinic velocities, (c and d) the mean transport driven by the baroclinic velocities and (e and f) the total, bolus plus mean, transport driven by the baroclinic velocities i.e (a)+(c)=(e). For the moorings IM1 (a,c and e) and IM3 (b, d and f).